Plasmonics in ultra relativistic regime

Paula Kleij

To cite this version:

Paula Kleij. Plasmonics in ultra relativistic regime. Plasma Physics [physics.plasm-ph]. Institut Polytechnique de Paris, 2023. English. NNT : 2023IPPAX015 . tel-04486180

HAL Id: tel-04486180
https://theses.hal.science/tel-04486180v1

Submitted on 1 Mar 2024

INSTITUT
POLYTECHNIQUE
DE PARIS

NNT : 2023IPPAX015

Thèse de doctorat

Plasmonics in the Ultra Relativistic Regime

Thèse de doctorat de l'Institut Polytechnique de Paris
préparée à l'École Polytechnique

École doctorale n°626 École doctorale de l'Institut Polytechnique de Paris (EDIPP)
Spécialité de doctorat : Optique, Laser et Plasma

Thèse présentée et soutenue à Palaiseau, le 15 février de 2023, par

MADAME PAULA SHERMAN KLEIJ

Composition du Jury :

Jérôme Faure Professeur, Professeur ENSTA Paris (LOA)	Président
Emmanuel d'Humières Professeur, Université de Bordeaux (CELIA)	Rapporteur
Marija Vranić Professeur, Instituto Superior Técnico (GoLP)	Rapporteur
Ondrej Klimo Professeur, Czech Technical University in Prague (FNSPE)	Examinateur
Michèle Raynaud-Brun Directrice de Recherche, CEA/DRF/IRAMIS (LSI)	Directrice de thèse
Caterina Riconda Professeur, Sorbonne Université (LULI)	Co-Directrice de thèse

ECOLE
DOCTORALE

PLASMONICS IN THE ULTRA RELATIVISTIC REGIME

Paula S. Kleij

This project has received funding from the European Union's Horizon 2020 research and innovation programme under grant agreement No 800945 — NUMERICS — H2020-MSCA-COFUND-2017

Simulations were performed on the Irene-SKL machine hosted at TGCC- France, using High Performance Computing resources from GENCI-TGCC (Grant No. 2018-x2016057678) and PRACE (project MIMOSAS).

Contents

Abstract

En français

Une impulsion laser de très haute intensité en interaction avec la matière permet de générer un plasma et des particules chargées relativistes de haute énergie. L'utilisation d'une cible solide possédant une interface modulée périodiquement permet, sous certaines conditions, d'augmenter le couplage laser-plasma et d'exciter des oscillations collectives d'électrons à la surface, appelées ondes plasma de surface (SPW). L'étude et l'exploitation de ces ondes de surface constituent l'un des fondements de la plasmonique. Une des propriétés intéressantes des SPW est leur capacité à induire des champs électromagnétiques extrêmement localisés et intenses, confinées dans le voisinage immédiat de l'interface. Dans un plasma sur-dense, les ondes plasma de surface se propagent avec une vitesse de phase proche de celle de la vitesse de la lumière et sont capables d'accélérer à des fortes énergies des paquets d'électrons le long de la surface de la cible. En outre, le développement et la mise à niveau des installations laser multi-PW à impulsions courtes existantes, telles qu'Apollon et ELI en Europe, avec des lasers atteignant des intensités supérieures à 10^{21} W/cm^2, rend aujourd'hui possible l'exploration de l'excitation des SPW en régimes d'intensité laser de plus en plus élevés. Dans ce contexte, l'extension de l'étude de la plasmonique vers ces régimes de très haute intensité laser, où les effets non linéaires et relativistes entrent progressivement en jeu, est d'un intérêt fondamental pour la physique de l'interaction laser-plasma et la physique des plasmas sur-denses relativistes. En plus, si l'excitation des SPW s'avère encore efficace en régime ultra-relativiste, ce mécanisme d'accélération pourrait offrir de nouvelles possibilités de manipulation et d'exploitation des phénomènes plasmoniques avec des applications potentielles comme les accélérateurs d'électrons compacts ou les spectroscopies d'électrons ultra-rapides.

L'objectif de ce travail de thèse est d'explorer théoriquement et numériquement, au travers de simulations Particle-in-Cell réalisées avec le code SMILEI, la génération de faisceaux d'électrons rapides dans l'interaction laser solide via l'excitation de SPW ou de modes électromagnétiques localisés à la surface dans des régimes laser ultra relativistes. Les résultats originaux de cette thèse sont déclinés à travers trois études complémentaires. Dans un premier temps, nous avons proposé un schéma inédit permettant de piloter la durée et l'intensité du SPW et par conséquent les caractéristiques du faisceau d'électrons. Nous obtenons ainsi des paquets d'électrons ultracourts (quelques fs) ayant une charge de quelques dizaines de pC et des énergies de plusieurs dizaines de MeV. Nous démontrons également que l'utilisation d'un front d'onde laser en rotation (WFR) permet de renforcer l'onde plasma de surface. Ultra-courte et ultra-intense, celle-ci contribue alors à accélérer des paquets d'électrons répartis sur quelques cycles optiques pour atteindre une énergie beaucoup plus élevée qu'en absence de rotation du front d'onde laser. L'excitation par une impulsion laser avec WFR d'une onde plasma de surface sur un substrat structuré apparaît ainsi comme un mécanisme d'accélération prometteur pour générer des faisceaux d'électrons relativistes avec un fort courant et de durée femtoseconde. Dans un deuxième temps, nous avons identifié les paramètres clés pour optimiser le couplage laser-plasma dans le régime ultra-relativiste ($> 10^{21}$ W/cm^2) afin d'assurer l'excitation des électrons par SPW. En effet, l'adoption d'un réseau plus profond et d'une densité de plasma plus importante, permet l'excitation et la survie des SPW dans les régimes d'excitation laser de très haute intensité. Dans ce cas, les paquets d'électrons relativistes de haute charge, produits par le SPW, subissent une forte accélération et émettent de grandes quantités de rayonnement électromagnétique avec des caractéristiques intéressantes. La troisième étude est ainsi consacrée à l'étude de ce rayonnement. Nous montrons que le mécanisme d'accélération par SPW représente également une alternative intéressante de source de lumière car l'énergie perdue par les électrons, en raison de l'émission de rayonnement, est transférée à des photons γ de haute énergie.

En conclusion, l'ensemble de ces résultats ouvre de nouvelles perspectives pour le développement de sources compactes de particules et de rayonnement énergétiques qui pourraient conduire à de nouveaux schémas expérimentaux réalisables sur l'installation Apollon et les lasers multi-PW.

In english

A very high-intensity laser pulse interacting with matter generates a plasma and high-energy relativistic charged particles. The use of a solid target with a periodically modulated surface allows, under certain conditions, to increase the laser-target coupling and to excite collective oscillations of electrons on the surface, known as surface plasma waves (SPW). The study and exploitation of these surface waves is one of the foundations of plasmonics. One of the interesting properties of SPWs is their ability to induce extremely localised and intense electromagnetic fields, confined to the immediate vicinity of the interface. In a very overdense plasma, these waves propagate with a phase velocity close to the speed of light and are capable of accelerating packets of electrons to high energies along the surface of the target. Furthermore, the current capabilities and upgrade of existing short-pulse multi-PW laser facilities, such as Apollon and ELI in Europe, with lasers reaching intensities beyond 10^{21} W/cm^2, are now making it possible to explore the excitation of SPWs at increasingly higher laser intensity regimes. In this context, the extension of the study of plasmonics to these very high laser intensity regimes, where nonlinear and relativistic effects progressively come into play, is of fundamental interest for the physics of laser-plasma interaction and the physics of relativistic overdense plasmas. In addition, if the excitation of SPWs still proves effective in the ultra-relativistic regime, this acceleration mechanism could present novel opportunities for manipulating and harnessing plasmonic phenomena with potential applications in areas such as compact electron accelerators or ultra-fast electron spectroscopy.

The objective of this thesis work is to explore theoretically and numerically, through Particle-in-Cell simulations performed with the SMILEI code, the generation of fast electron beams in solid-state laser interaction via the excitation of SPWs or surface-localized electromagnetic modes in ultra relativistic laser regimes. The original results of this thesis are presented in three complementary studies. Firstly, we proposed a novel scheme to control the duration and intensity of the SPW and consequently the characteristics of the electron beam; thus obtaining ultrashort (few fs) electron packets with a charge of a few tens of pC at energies of several tens of MeV. We demonstrate that the use of a laser pulse with wavefront rotation (WFR) makes it possible to sustain SPW growth. Ultra-short and ultra-intense, these SPW allow accelerating packets of electrons spread over a few optical cycles to reach much higher energy than in the absence of WFR. The excitation by a laser pulse with

WFR of a surface plasma wave on a structured substrate thus appears to be a promising acceleration mechanism for generating relativistic electron beams with a high current and femtosecond duration. Secondly, we identified the key parameters to optimise the laser-plasma coupling in the ultra-relativistic regime ($> 10^{21}$ W/cm^2) to ensure the excitation of electrons by SPW. Indeed, the adoption of a deeper grating and a higher plasma density allows the excitation and survival of SPWs in the very high laser intensity regimes. In this case, the high-charge relativistic electron packets produced by the SPW undergo strong acceleration, emitting large quantities of electromagnetic radiation with interesting characteristics. The third study is thus devoted to this radiation. We show that the SPW acceleration mechanism also constitutes an interesting alternative light source since the energy lost by the electrons due to radiation emission is transferred to high-energy γ photons.

In conclusion, all these results open up new prospects for the development of compact sources of energetic particles and radiation, which could lead to new experimental schemes that could be carried out on the Apollon installation and multi-PW lasers.

Acknowledgments

I have been told that the acknowledgments are the easiest part of writing a thesis. I, however, would like to disagree. Reflecting back on those last couple of years, I realize that I have met far too many people -wonderful people!- to whom I am indebted. Words cannot suffice to articulate my gratitude. Nevertheless, try I must: here is a comprehensive - yet sadly incomplete - list of people I would like to acknowledge.

Foremost, I would like to extend my wholehearted gratitude to two incredible people: my directrice de thèse, Michèle Raynaud, and my co-supervisor, Caterina Riconda. Thank you for your unwavering support, encouragement, and kindness: you always believed in me, even when I stopped believing in myself. Thank you for being my role models, both as brilliant scientists and kind-spirited persons.

I would also like to express my gratitude to Prof. Marija Vranić, Prof. Jérôme Faure, Prof. Emmanuel d'Hummières and Prof. Ondrej Klimo, all of whom agreed to be members of my PhD committee. Thank you for taking the time to read and evaluate my work, as well as for your insightful comments, pertinent questions and interesting remarks. Thanks to you my defense - an otherwise stressful experience - was an enjoyable moment.

My PhD would not have been the same if not for the friendly and stimulating environment in both LSI and LULI. People of LSI at École Polytechnique: thank you for the coffee, snacks, dinners and enjoyable conversations! From bâtiment 83: Lucia Reining, Valérie Véniard, Andrea Cucca, Francesco Sottile, Christine Giorgetti, and Matteo Gatti, thank you for all the convivial moments and words of encouragement when I needed it most. Many thanks to the administrative team, Elodie Dubois and Marylène Raclot, who have always helped me solve any administrative task with a smile and great chat. To "les jeunes": Georg Michelitsch, Rajarshi Sinha Roy, Vitaly Gorelov, Laura Urquiza, Alam Osorio, Abdallah El Sahili, Shalu Rani, Stefano Mazzei, Mark Aichner, Nathalie Saouli, Alexis Meriot, Mariusz Drong, Ayoub Aouina, Jack

Wetherell, Arnaud Lorin and many more for the laughs we've shared together. I extend special regards to two other incredible women in science™: Carolina Garcia Soto <3 and Marie Cherasse, my partners in crime during this endeavor, I'm so proud of you, and can't wait to see what you will accomplish next!

People of TIPS/LULI at Sorbonne Université: you've made the lab feel like a second home. It was a joy working alongside you during these past couple of years. I owe you all a beer! I am deeply indebted to Mickael Grech, thank you for your invaluable help and (lots of) patience. Congratulations to fellow Dr. and jiu-jitsu master Anthony Mercuri-Baron, we've made it! I would like to thank you and Arsenii Mironov for your endless support, friendship, and birthday cakes! I'm extremely grateful to Anna Grassi, a brilliant scientist, and great friend. Also, I would like to pass the baton to Giuseppe Nicotera and Mattys Pouyez, make us proud. Many thanks to Tommaso Vinci, Livia Lancia, Alessandra Benuzzi, Alessandra Ravasio, Sébastien Le Pape, and many more for the warm and cooperative atmosphere and helpful talks. Words cannot express my gratitude to François Amiranoff, an extraordinary person I strive to be like. From physics to photography, the insights and guidance you have provided me with are precious.

This endeavor would not have been possible without Samuel Marini and Meirielen Caetano De Sousa, 'my partners in crime' in the study of SPW. I have greatly enjoyed collaborating with both of you. Samuel, you've been my cornerstone since the beginning of this work! I can't thank you enough for your priceless help and fruitful discussions. Meirie, thank you for your uplifting spirit. Obrigado do fundo do coração.

Vorrei ringraziare i ragazzi del polo Fibonacci: Giulia Cozzani, Sid Fadanelli, Federico "Job" Lavorenti, Manuela Sisti, Francesco Finelli, Francesco Pisani, Giuseppe Arrò, Roberto Manuzzo e il Marchese. Despite being scattered around the world, you've always proven to be there for each other and to celebrate each other achievements. Vi voglio bene e spero rivedervi presto intorno a una torta di Frangioni. Shoutout to Andrea Macchi, per convincermi che ero all'altezza di fare un dottorato e per la tua sana dose di sarcasmo cinico. Un ringraziamento speciale alle Ragazze di Via Mercanti, Francesca Bella (di fatto e di nome) e Gaetano de Marino, il mio fratello napoletano e la mia voce della ragione. La vita senza di voi sarebbe meno pazzeska. Sarò anche eternamente grata a Valeria Grussu, Elisa Paiano e Oriente Plazzi-

Marzotto, siete le amiche che ho sempre desiderato avere. Grazie per essere sempre lì per me, per ascoltarmi quando sono giù e festeggiare i bei traguardi insieme. I would also like to mention a few friends who always believed in me and offered comfort, cocktails and wise words along the way: my brother Raphael Stambollion "Stromboli", Morgane, Alice Fazzini, Alessio Couzzo, Valentina Pepi, Axel Courtat, Laura R.A., Irina M., Ysé G., Chiara B., Mona B., Alessia A.G., and many more. Un agradecimiento especial a Mónica Nicolau, la primera profesora que me mostró el mundo maravilloso de las ciencias. Je suis reconnaissante envers mon grand-père parisien, “Philippe” El Kenje. Je suis également réconnaissante envers Fabien Niel, mon mari de qui je veux divorcer; darling, you can keep the yacht, I'm taking the house - and the dog.

Special thanks to Michele Rech (aka Zerocalcare) for the drawings that appear in this manuscript. If you don't know him, go read Kobane Calling.

L'achèvement de cette thèse n'aurait pas été possible sans l'appui de ma psychologue Anne Delaigue, et de ma psychiatre Florence Robin. Merci pour me munir d'outils qui me seront utiles toute ma vie.

Finally, I would like to dedicate this work to my family. I could not have asked for better parents, I would not be the person I am today if not for you. Aan papa, dankjewel voor je liefde, de steun en de aanmoedigingen tijdens mijn studieproces (ook al hebt je een keer gezegd dat natuurkunde alleen maar een hobby was). A mamá, no sé cómo agradecerte por todo el amor y apoyo que me has dado durante todo este tiempo. Gracias por siempre ser mi ejemplo y obligarme a perseverar cuando quería tirar la toalla. A Lena, sin ti mi vida no tendría sentido. Eres la mejor. À Sartre, qui m'a permis de rester sain d'esprit. A mi familia en México: mi tío Fer, mi tía Assol y mis primos Adrián y Braulio; que a pesar del océano que nos separa, siempre están cerca de mi. A Nena y Opa, que siempre están presentes en mi corazón, hopelijk zijn ze trots op mij.

P.S Je voudrais contre remercier la Covid, qui a annulé tous les conférences et summer schools en personne.

Glossary

List of the most frequently used acronyms used throughout the manuscript:

UHI Ultra High Intensity

SPW Surface Plasma Wave

WFR Wave Front Rotation

FWHM Full Width at Half Maximum

PIC Particle-in-Cell

QED Quantum Electrodynamics

RR Radiation Reaction

MC Monte Carlo

cLL corrected Landau Lifshitz

Nomenclature

SI units are used throughout this manuscript.

Classical parameters

Parameters	Definitions	Numerical values
c	The speed of light in vacuum	3×10^8 ms^{-1}
m_e	The electron rest mass	9.1×10^{-31} kg
e	The electron charge	1.6×10^{-19} C
ϵ_0	Vacuum permittivity	8.85×10^{-12} F/m
μ_0	Vacuum magentic permeability	1.2566×10^{-6} H/m
ω_0^{-1}	Laser normalisation of time	0.531 fs at $\lambda_0 = 1$ μm
$c\omega_0^{-1}$	Laser normalisation of distance	0.159 μm at $\lambda_0 = 1$ μm
$m_e\omega_0 c/e$	Laser normalisation of electric field	3.2×10^{12} V/m at $\lambda_0 = 1$ μm
$m_e\omega_0/e$	Laser normalisation of magnetic field	1.1×10^4 T at $\lambda_0 = 1$ μm
$r_e = e^2/(4\pi\epsilon_0\, m_e c^2)$	Classical radius of the electron	2.82×10^{-15} m
$\tau_e = r_e/c$	Classical time of the electron	9.36×10^{-24} s
$E_{cr} = 4\pi\epsilon_0\, m_e^2 c^4/e^3$	Classical electric field	1.8×10^{20} V/m
$B_{cr} = 4\pi\epsilon_0\, m_e^2 c^3/e^3$	Classical magnetic field	9×10^{11} T
$r_e = e^2/(4\pi\epsilon_0\, m_e c^2)$	Classical radius of the electron	2.82×10^{-15} m

Quantum parameters

Parameters	Definitions	Numerical values
$\hbar$	The reduced Planck constant	1.054×10^{-34} J.s
$\alpha = e^2/(4\pi\epsilon_0\hbar c)$	The fine structure constant	1/137
$\lambda_c = \hbar/m_e c = r_e/\alpha$	The Compton wavelength	$3.86.10^{-13}$ m
$\tau_c = \lambda_c/c$	The Compton time	$3.86.10^{-13}$ m
$E_s = \frac{m_e^2 c^3}{e\hbar} = E_{cr}/\alpha$	The Schwinger field	1.3×10^{18} V/m
I_s	Schwinger intensity	10^{29} W/cm^2

Chapter 1

Introduction

Plasmonics is a rapidly growing field of physics at the frontier of nano-photonics and nano-optics. This relatively young research field is dedicated to the study and application of the interaction of electromagnetic waves with the collective oscillations of electrons in a medium. One cornerstone of plasmonics are *Surface Plasmons*, SP, highly localized electromagnetic field structures with the ability to confine and enhance light in subwavelength regions at the interface between two media whilst propagating along the surface [1–4]. Their unique properties have propelled them as ideal candidates for a plethora of applications across a broad range of scientific disciplines besides physics. Indeed, the enhanced field associated with the tight confinement causes SP's to be extremely sensitive to the surrounding media making them very suitable for bio-chemical sensing [5, 6], plasmon enhanced spectroscopy [7], biomedical imagining [8–10] and solar light harvesting [11, 12]. Moreover, the use of SP circuits makes it possible to decrease the size of current photonic devices bridging the gap between photonics and their microelectronic counterparts [13, 14]. Other applications are outlined in [15] and references within.

The term *surface plasmons*, SP, was first coined by R.H. Ritchie in 1957 when he predicted that the energy losses of fast electrons passing through thin metal films were due to the existence of surface collective electron excitations at the metal surface [16]. Yet the first documented observation of SP dates back to 1902 and is attributed to R.W. Wood who observed a pattern of alternating black and light bands when shining polarized light onto a metal diffraction grating [17]. However, the field really flourished in the 70s with the arrival of new fabrication techniques enabling the production of nano-scale structures. In parallel, laser technology has seen tremendous progress since the realization of the first laser in 1960 by T. H. Maiman [18]. Indeed, the Nobel prize winning CPA (Chirped Pulse Amplification) technique discovered in 1985 [19] has prompted a fast-paced advancement of shorter and more intense laser pulses resulting in the increase of the laser intensity by orders of magnitudes in the last couple of decades.

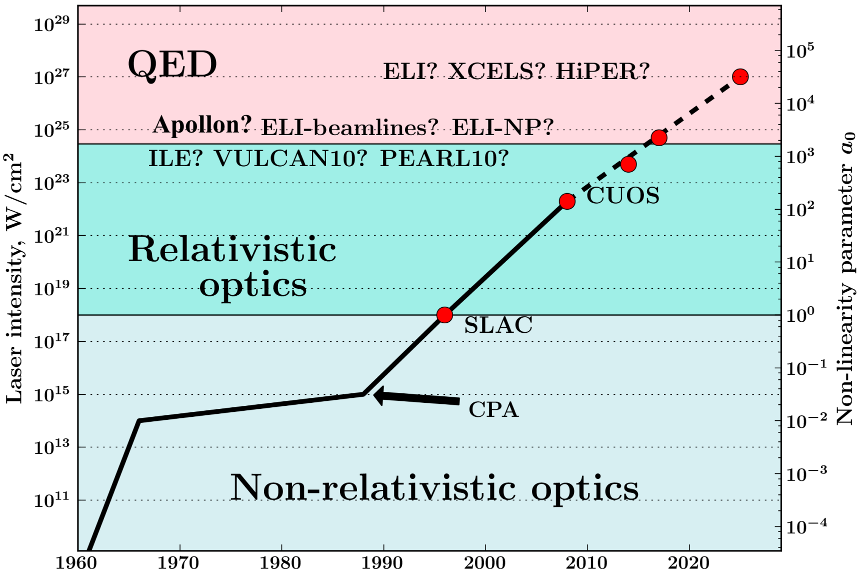

Figure 1.1: Evolution of the laser intensity available in laboratories since 1960. Adapted from [20].

Given the broad range of applications achievable with SP's, it is of utmost importance to control the coupling of the incident electromagnetic wave to SP's. It has been demonstrated that the irradiation of solid structured target [21, 22] by ultra short laser pulses can resonantly excite surface plasmons associated with large localized EM field. In this scenario, high energy transfer from the laser to the target is achieved when the frequency and wavelength of the interacting laser pulse match those given by the SP's dispersion relation [1,23]. In analogy with surface plasmons in solid state physics, the impinging of ultra-high intensity femtosecond lasers on a metallic surface with a periodic engraving can resonantly excite *Surface Plasma Waves* (SPW) [24,25]. In the low laser intensity regime, from few GW/cm^2 to tens of TW/cm^2, SPW have led to harmonic emission [26–28] and the production of photo-electron bunches at energies up to few 100s eV [29, 30].

However, in the ultra-high intensity (UHI) regime ($I_0 \gtrsim 10^{18}$ W/cm^2), any target material quickly turns into a plasma, and electrons reach relativistic quiver-velocities in the intense laser field. The interaction of an intense and short laser pulse with high contrast results in the creation of an over-dense plasma with a sharp density gradient, and can accelerate charged particles to relativistic velocities [31–37]. In the UHI regime, SPW are not only of interest for exploring nonlinear plasma modes, but also for their capability of accelerating electrons. Indeed, since SPW are waves with a longitudinal electric field component and slightly subluminal phase speed, they are able to trap electrons and accelerate them up to high energies along the surface. Previous simulations and experiments have indeed shown that a significant percentage of electrons trapped in the SPW can be accelerated along the surface in the range of $\sim$ 10 MeV [38–42]. High charge electron bunches (up to $\sim$ 650 pC) were also observed [42–46] together with XUV harmonic emission [47].

Furthermore, the imminent arrival of more powerful short-pulse multi-Petawatt laser facilities around the world with intensities up to the order of $10^{22} - 10^{23}$ W/cm^2, such as Apollon [48] (see Fig.1.1), are expected to become widely available to the scientific community in the near future, making the exploration of increasingly higher field regimes plausible. In these regimes, where the electron kinetic energy becomes comparable to or greater than its rest mass $m_e c^2$, relativistic nonlinear effects progressively come into play.

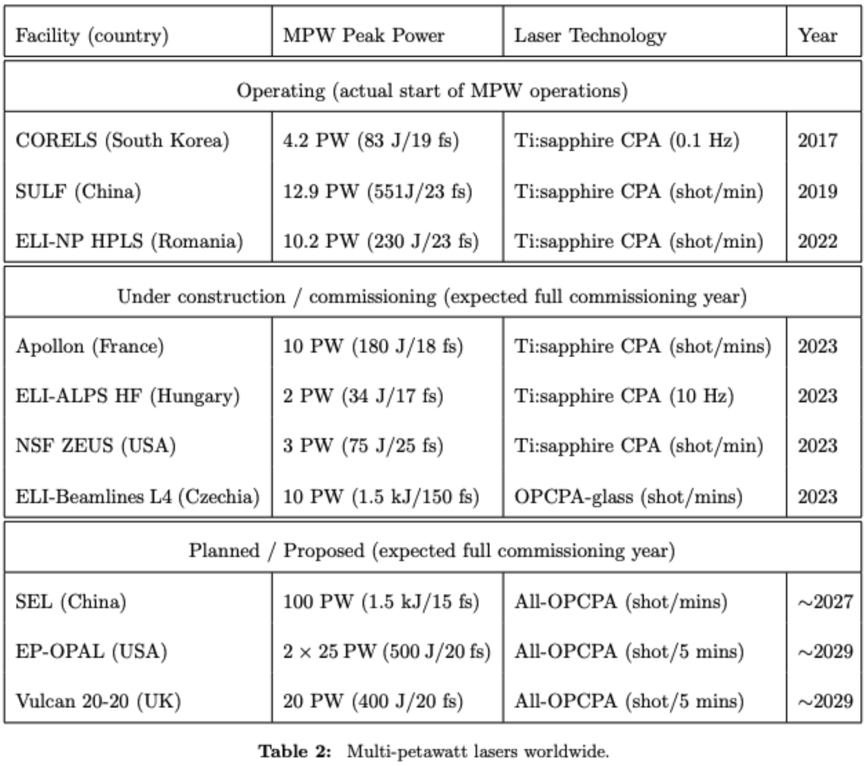

Facility (country)	MPW Peak Power	Laser Technology	Year
Operating (actual start of MPW operations)			
CORELS (South Korea)	4.2 PW (83 J/19 fs)	Ti:sapphire CPA (0.1 Hz)	2017
SULF (China)	12.9 PW (551J/23 fs)	Ti:sapphire CPA (shot/min)	2019
ELI-NP HPLS (Romania)	10.2 PW (230 J/23 fs)	Ti:sapphire CPA (shot/min)	2022
Under construction / commissioning (expected full commissioning year)			
Apollon (France)	10 PW (180 J/18 fs)	Ti:sapphire CPA (shot/mins)	2023
ELI-ALPS HF (Hungary)	2 PW (34 J/17 fs)	Ti:sapphire CPA (10 Hz)	2023
NSF ZEUS (USA)	3 PW (75 J/25 fs)	Ti:sapphire CPA (shot/min)	2023
ELI-Beamlines L4 (Czechia)	10 PW (1.5 kJ/150 fs)	OPCPA-glass (shot/mins)	2023
Planned / Proposed (expected full commissioning year)			
SEL (China)	100 PW (1.5 kJ/15 fs)	All-OPCPA (shot/mins)	~2027
EP-OPAL (USA)	2 × 25 PW (500 J/20 fs)	All-OPCPA (shot/5 mins)	~2029
Vulcan 20-20 (UK)	20 PW (400 J/20 fs)	All-OPCPA (shot/5 mins)	~2029

Table 2: Multi-petawatt lasers worldwide.

Figure 1.2: Summary of the operating, upcoming and planned multi-petawatt laser facilities in the world [49].

Motivated by the upcoming powerful lasers systems (see Figure 1.2), we are interested in extending the study of plasmonics to the ultra relativistic regime, beyond 10^{21} W/cm^2. In this regime, we expect SPW with extremely large amplitudes at the over-dense plasma surface, potentially allowing to obtain unprecedentedly high currents of energetic electrons as well as emitting radiation with interesting characteristics such as directionality, brightness, spectral range, among others. The study of plasmonics in the ultra relativistic regime could present novel opportunities for manipulating and harnessing plasmonic phenomena with potential applications in areas such as high-energy radiation generation, ultra-fast electron diffraction, tabletop electron accelerators, and ultra-fast electron spectroscopy [50–53]. However, the excitation and survival of these SPW in the ultra-relativistic regime remain an open question, as in this limit the plasma grating can evolve on relatively short time scales, and nonlinear effects can affect the dispersion relation in the relativistic regime [54].

Due to the highly non linear nature of this physical scenario, precise numerical modeling via Particle-In-Cell (PIC) codes is necessary. Through a combination of analytical modeling and numerical simulations performed with the PIC code Smilei [55], we will try to shed light on the complex interplay between plasma and lasers, and the rich physics of surface plasma waves. We explore the generation of these fast electron beams in relativistic laser-plasma interaction by using properly structured targets whose surface characteristics allow SPW excitation or local electromagnetic modes in increasingly relativistic laser regimes. In this work we propose an ingenious mechanism to tune SPW and enhance electron acceleration. We then further study the excitation mechanism of SPW in the ultra relativistic regime and the radiation reaction effects that appear when going to even higher laser intensities.

The structure of this manuscript is the following :

- **Chapter 2** gives an overview of the physical processes relevant to this thesis such as the dynamics of an electron in a high field and the generation of SPW.

- **Chapter 3** explains the Particle-In-Cell Smilei code. In this chapter we also propose the implementation of a diagnostic, based on the Lienard Wiechert potentials, complementing the pre-existing radiation modules in SMILEI. The implementation of this radiation is not only interesting for the study of SPW excitation and electron acceleration in the ultra-relativistic regime, but also for the investigation of betatron radiation and high harmonic generation, among others.

- **Chapter 4** presents the first results concerning laser-plasma coupling enhancement through a "smart" grating device. We also propose a novel set-up which permits to tune SPW duration and intensity and consequently the electron bunch characteristics. Indeed, by impinging a laser with wavefront rotation (WFR) on a smart grating design, we both shorten the duration (down to very few optical cycles) and increase the intensity of SPW, thus favoring the production of ultra-short, energetic electron bunches. In the laser-plasma relativistic regime of interaction ($I_0 > 10^{21}$ W/cm^2), we show that such SPW are found to accelerate high-charge (few 10's of pC), high-energy (up to 70 MeV), and ultra-short (few fs) electron bunches.

- **Chapter 5** presents a thorough parametric study on the conditions to improve laser-plasma energy transfer in the ultra-high laser intensity regime as well as to accelerate charged particles through the SPW excitation mechanism as a function of the laser intensity and incidence angle, plasma density and grating depth. We demonstrate a strong correlation between the angle of SPW excitation and the angle of incidence that optimize in the simulations the electron acceleration along the plasma surface. A threshold in the laser strength is also found depending on the density and grating depth of the plasma.

- **Chapter 6** explores the radiation reaction and photon generation in the laser-plasma interaction under extreme conditions, comparing the different radiation models available in SMILEI and different target geometries.

- **Chapter 7** presents a global conclusion to this work and provides outlook and perspectives.

Chapter 2

Theoretical background

Contents

This chapter aims to provide an introduction to the principal notions that will be used throughout this thesis. The first section is dedicated to laser-plasma interaction, showing first how an electron behaves in an electromagnetic field and then how the electromagnetic (EM) wave interacts with plasma. The second section summarizes the generation of surface plasma waves by ultra-high intensity laser pulses, while the last section briefly presents the radiation effects by moving charges.

2.1 Laser-Plasma interaction

In this section, we will recall the fundamental aspects of laser-plasma interaction at relativistic intensities. The interaction of a charged particle with an EM wave is one of the most fundamental physical processes and the subject of many books. We will therefore present a brief overview of the basics: from the single particle motion in the laser field in section 2.1.1 to the propagation of an EM wave in a plasma in 2.1.2. For a more comprehensive review, the reader is referred to dedicated textbooks [56–59].

2.1.1 Dynamics of an electron in an electromagnetic field

At high laser intensities, it is convenient to define the dimensionless laser parameter a_0, also referred to as laser strength, which measures the importance of relativistic effects in the laser-plasma regime. Indeed, an electron at rest can become relativistic within one laser period if the normalized laser amplitude

$$a_0 = \frac{eE_0}{m_e c\omega_0} \gtrsim 1\,, \tag{2.1}$$

where e and m_e are respectively the charge and mass of the electron, c is the speed of light, while E_0 and ω_0 are the amplitude and frequency of the laser. As $a_0 \sim 1$, the electron motion in the laser field becomes relativistic and the response of the electron plasma becomes highly nonlinear due to the presence of the Lorentz factor in the momentum of the particle. In practical unites, a_0 can be expressed in terms of the laser intensity, I, and wavelength, λ, by:

$$a_0 = 0.85\left(\frac{I\lambda^2}{10^{18}\ \mathrm{Wcm^{-2}\mu m^2}}\right)^{1/2}\,. \tag{2.2}$$

The parameter a_0 permits to define the regime where the interaction takes place: when $a_0 \ll 1$ there are no relativistic effects and thus the regime is considered to be non relativistic, as $a_0 \sim 1$ the regime becomes weakly relativistic and when $a_0 \geq 1$ the regime is fully relativistic.

Trajectory in a plane wave

Lets consider a free electron, initially at rest, placed in the path of a plane electromagnetic wave propagating in vacuum. The electron will experience the Lorentz's force due to the electric and magnetic fields and will oscillate in the EM field. The equations for the electron momentum $\mathbf{p}$ and energy $\mathcal{E} = \gamma m_e c^2$ are the following:

$$\frac{d\mathbf{p}}{dt} = -e\left(\mathbf{E} + \mathbf{v} \times \mathbf{B}\right), \tag{2.3}$$

$$\frac{d}{dt}(\gamma m_e c^2) = -e\mathbf{v} \cdot \mathbf{E}, \tag{2.4}$$

with $\mathbf{p} = m_e \gamma \mathbf{v}$ the relativistic momentum of the electron and γ the corresponding Lorentz factor:

$$\gamma = \frac{1}{\sqrt{1 - v^2/c^2}} = \sqrt{1 + \frac{p^2}{m_e^2 c^2}}. \tag{2.5}$$

The first term of Eq.(2.3) represents the linear response of the electron due to $\mathbf{E}$, while the second term leads to a nonlinear response $\mathbf{v} \times \mathbf{B}$ which is responsible for the ponderomotive force $\mathbf{F}_p$. Considering a plane wave, defined by a transverse potential vector $\mathbf{A}(\mathbf{r}, t)$, the electric and magnetic fields are given by

$$\mathbf{E} = -\frac{\partial \mathbf{A}}{\partial t} \quad \text{and} \quad \mathbf{B} = -\nabla \times \mathbf{A}. \tag{2.6}$$

Assuming a wave propagating along the x direction in the vacuum, a particle initially at rest will have [59] :

$$\frac{p_x}{m_e c} = \frac{1}{2}\left(\frac{\mathbf{p}_\perp}{m_e c}\right)^2, \tag{2.7}$$

$$\mathbf{p}_\perp = e\mathbf{A}, \tag{2.8}$$

$$\text{and} \quad \gamma = 1 + \frac{1}{2}\left(\frac{e\mathbf{A}}{m_e c}\right)^2, \tag{2.9}$$

where $\mathbf{p}_\perp$ designates the momentum in the plane transverse to the propagation direction of the wave. The electron is pushed forward by the EM pulse. In the ultra relativistic regime, the electron's velocity is mainly along the axis of propagation. From the Equations (2.7) and (2.8), we deduce that if the electron was initially at rest, the electron will return to the rest state once the EM wave has passed through, effectively displacing the electron by a finite distance along the propagation axis. In a more realistic setting, an electron can escape transversely the laser transverse width with a finite energy gain approximated by the ponderomotive force [60, 61]:

$$\mathbf{F}_p = -\frac{e^2}{2m_e\langle\gamma\rangle}\nabla\langle|\mathbf{A^2}|\rangle \tag{2.10}$$

$$\text{with} \quad \langle\gamma\rangle = \sqrt{1+\frac{\langle p\rangle}{(m_e c)^2}+e^2\frac{\langle|\mathbf{A}|^2\rangle}{(m_e c)^2}}\,. \tag{2.11}$$

with $\langle ... \rangle$ representing the average over a laser period.

Linearly polarized plane wave

Lets assume the case of a linearly polarized wave where

$$\frac{e\mathbf{A}}{m_e c} = a_0 \cos(\omega t)\,\hat{\mathbf{y}}\,, \tag{2.12}$$

The exact trajectory is calculated as following:

$$ky(t) = a_0 \sin(\omega t)\,, \tag{2.13}$$

$$kx(t) = \frac{a_0^2}{8}[2\omega t + \sin(2\omega t)]\,, \tag{2.14}$$

with $k = \omega/c$ the wave number. The trajectory of the electron is represented in Figure 2.1(a). In the laboratory frame, when $a_0 \gg 1$, the electron acquires a drift in the longitudinal direction leading to a drift velocity:

$$v_{drift} = \frac{a_0^2/4}{1+a_0^2/4}c\,, \tag{2.15}$$

where the Lorentz factor is $\gamma_0 = \sqrt{1+a_0^2/2}$. The electron is confined on the xy plane with a drift along $\hat{\mathbf{y}}$. In the drifting frame, meaning a frame of movement with a constant v_{drift} (Figure 2.1(b)), we find the well known 8 figure trajectory of the electron, with:

$$k'y'(t') = \frac{a_0^2}{\sqrt{1+a_0^2/2}}\sin\omega' t'\,, \tag{2.16}$$

$$k'x'(t') = \frac{a_0^2}{8(1+a_0^2/2)}\sin(2\omega' t')\,, \tag{2.17}$$

$$\text{with} \quad \omega' = \frac{\omega}{\sqrt{1+a_0^2/2}}\,. \tag{2.18}$$

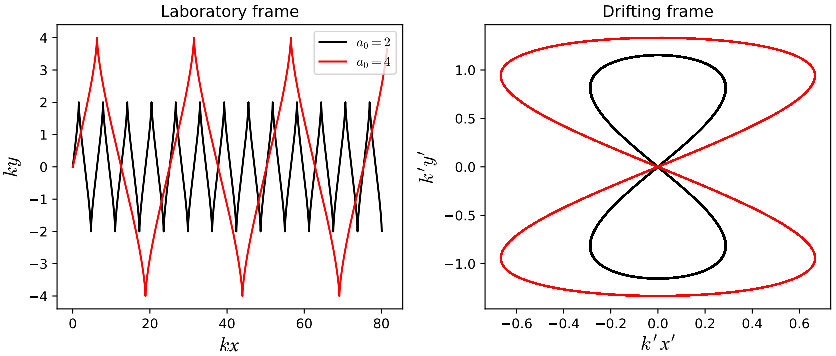

Figure 2.1: Trajectory of an electron in a linearly polarized plane wave in (a) the laboratory frame and (b) the drifting frame.

2.1.2 Relativistic EM Waves propagation in Plasmas

In the ultra-high intensity (UHI) regime $I_0\lambda_0 \gtrsim 10^{18}\mathrm{W/cm^2}\mu\mathrm{m}^2$, any target material quickly turns into a conductive plasma, and electrons reach relativistic quiver-velocities in the intense laser field. Therefore, the study of EM waves in plasma is the natural continuation after having derived the behaviour of a single electron in an intense EM field. For the sake of simplicity, lets consider an unmagnetized, "cold" plasma whose response to high frequency fields is due to electrons only. Here, the ion response is ignored since they are treated as an immobile, homogeneous background.

The equation describing the propagation of an EM wave reads as follows:

$$\left(\nabla^2 - \frac{1}{c^2}\frac{\partial^2}{\partial t^2}\right)\mathbf{E} - \nabla(\nabla\cdot\mathbf{E}) = \mu_0\frac{\partial \mathbf{J}}{\partial t}\,, \tag{2.19}$$

which is obtained from Maxwell's equation by eliminating $\mathbf{B}$. The current density $\mathbf{J} = -en_e\mathbf{v}$ may thus be obtained by the cold fluid equations. Considering the electric field as a plane, monochromatic wave, the linearized electron fluid velocity and corresponding current are then

$$\mathbf{v} = -\frac{e}{i\omega m_e}\mathbf{E}\,, \tag{2.20}$$

$$\mathbf{J} = \frac{n_0 e^2}{i\omega m_e}\mathbf{E} \equiv \sigma\mathbf{E}\,. \tag{2.21}$$

where σ is the conductivity [58,62]. Substituting into Eq.(2.19) we obtain the inhomogeneous Helmholtz equation:

$$\nabla^2\mathbf{E} - \nabla(\nabla\cdot\mathbf{E}) + \frac{\omega^2}{c^2}\varepsilon(\omega)\mathbf{E} = 0 \tag{2.22}$$

where

$$\varepsilon(\omega) = 1 - \frac{\omega_p^2}{\omega^2}\,, \tag{2.23}$$

is the dielectric function of a cold plasma, and ω_p is the plasma frequency defined as:

$$\omega_p = \sqrt{\frac{e^2 n_0}{m_e \epsilon_0}}\,. \tag{2.24}$$

Similarly, the wave equation for the magnetic field is obtained from the Maxwell's equation by eliminating $\mathbf{E}$ [59]:

$$\nabla^2 \mathbf{B} + \frac{1}{\varepsilon} \nabla\varepsilon \times \nabla \times \mathbf{B} + \frac{\omega^2}{c^2}\varepsilon(\omega)\mathbf{B} = 0\,. \tag{2.25}$$

In a homogeneous plasma, $\nabla\varepsilon = 0$, and the Eq.(2.25) for the magnetic field becomes identical to the equation of the electric field. Moreover, $\nabla \cdot \mathbf{E} = 0$ since there is no charge separation in the homogeneous plasma, and the Eq.(2.22) simplifies to:

$$\nabla^2 \mathbf{E} + \frac{\omega^2}{c^2}\varepsilon(\omega)\mathbf{E} = 0\,. \tag{2.26}$$

Imposing fields of type $E(\mathbf{r}) \sim \exp(i\mathbf{k}\cdot\mathbf{r} - i\omega t)$, with k the wave vector, the condition $\nabla \cdot \mathbf{E} = 0$ translated to $\mathbf{k}\cdot\mathbf{E} = 0$ meaning that $\mathbf{k}$ and $\mathbf{E}$ are perpendicular to each other. The derivation of Eq.(2.26) leads to the dispersion relation of EM waves in a plasma :

$$k^2 = \frac{\omega^2}{c^2}\varepsilon(\omega)\,, \tag{2.27}$$

$$\text{or} \quad k^2 c^2 = \omega_p^2 - \omega^2\,. \tag{2.28}$$

The dielectric constant of the medium $\varepsilon(\omega)$ dictates how the incident EM wave behaves. Indeed, the plasma frequency, ω_p, is a cut-off frequency for EM transverse waves meaning that the EM wave is free to propagate in the plasma only when $\omega > \omega_p$. This cut-off condition can also be written as a condition on the plasma density n_0 :

$$n_0 < n_c \equiv \frac{\epsilon_0 m_e \omega^2}{e^2}\,, \tag{2.29}$$

where n_c is the critical density which corresponds to the case when $\omega = \omega_p$. If $n_0 < n_c$, the plasma is said to be underdense and allows the propagation of the EM wave. However, if $n_0 > n_c$ the plasma is overdense and the EM wave cannot propagate into the medium and is reflected. From the definition of n_c we note that ω_p^2/ω^2 is equivalent to n_0/n_c. Furthermore, the EM field experiences an exponential dissipation by $\sim \exp\left(-x/L_s\right)$ with L_s the skin depth

$$L_s = c(\omega_p^2 - \omega^2)^{-1/2}\,, \tag{2.30}$$

which becomes $L_s = c/\omega_p$ when $\omega_p \gg \omega$.

In the presence of high-intensity lasers, and in particular when the normalized vector potential $a_0 \gtrsim 1$, it has been proposed [63–67] to correct the response of the electrons by considering an effective electron mass

$$m_e \to \gamma_0\, m_e\,, \tag{2.31}$$

with γ_0 the Lorentz factor of an electron in a plane wave. It should be noted that for a given frequency ω, relativistic transparency [68] can occur as relativistic effects raise the critical density n_c to γn_c.

2.1.3 Energy absorption

Though in the case of an overdense plasma the laser reflects back into the vacuum side, a non negligible fraction of the laser energy can be transferred to the electrons located at the irradiated surface of the target during the interaction. The energy of these hot electrons can be estimated by the ponderomotive energy and is proportional to a_0:

$$E_{hot} = m_e c^2 (\sqrt{1 + a_0^2/2} - 1)\,. \tag{2.32}$$

Depending on the laser initial conditions and the laser-plasma interaction geometry, the conversion of laser energy into electron kinetic energy can be attributed to different processes. The three most frequently discussed absorption mechanisms (nicely presented in [69]) are resonance absorption, which takes place when the plasma frequency ω_p is equal to the laser frequency ω, vacuum heating and $\mathbf{J} \times \mathbf{B}$ heating.

Vacuum heating

The vacuum heating, also known as Brunel absorption [70], occurs for p-polarized, obliquely incident waves. In this model, for about half a laser period, the electrons on the surface of the plasma are pulled out into the vacuum and then pushed back into the target by the laser electric field component perpendicular to the surface. The electron re-enters the plasma with a velocity of the order of their quiver velocity, acquired during the oscillation in the vacuum region. In the other second half of the laser period, the re-injected electrons are accelerated deep into the target as the laser can only penetrate the plasma up to the skin depth and is unable to drag the electrons back into the vacuum. This mechanism is responsible for the production of hot electrons as bunches.

$\mathbf{J} \times \mathbf{B}$ heating

At high laser intensities, the longitudinal motion of the electrons associated with the $\mathbf{v} \times \mathbf{B}$, term of the Lorentz force exerted on the electron in the laser field, becomes comparable to transverse motion associated with the electric field component. Analogous to the previous case, the electrons are pushed into the plasma and escape the laser field. In this case, the electrons are driven across the vacuum-plasma interface by the magnetic force rather than by the electric field, hence the name $\mathbf{J} \times \mathbf{B}$ heating [33]. This heating mechanism is dominant in the case of a p-polarized normal incident laser wave, for which the vacuum heating gives no contribution.

2.2 Basic introduction to Surface Plasma Waves

Now that we have presented the basics of laser-plasma interaction, we can proceed to present one direct consequence of a laser impinging on a solid target, that is, the excitation of surface plasma waves (SPW). SPW are collective oscillations of the electrons which are confined to the close vicinity of a metal-dielectric interface. These charge oscillations induce an electromagnetic excitation propagating along the surface while remaining confined in a small region across the boundary in the perpendicular direction. Since any dielectric becomes a strongly conductive plasma during the interaction of a laser with intensity above the ionization threshold, we will discuss directly the case of a 2D homogeneous plasma in a (x,y) Cartesian plane where a SPW is able to travel along the plasma-vacuum interface.

2.2.1 SPW excitation in weakly relativistic regime

The dispersion relation

The geometry of the physical system is illustrated in Figure 2.2 where we consider a flat interface between two different media with different dielectric constants (vacuum, ε_1, along $x < 0$ and a plasma, ε_2, along $x > 0$) coinciding with the plane $x = 0$ of the Cartesian coordinate system.

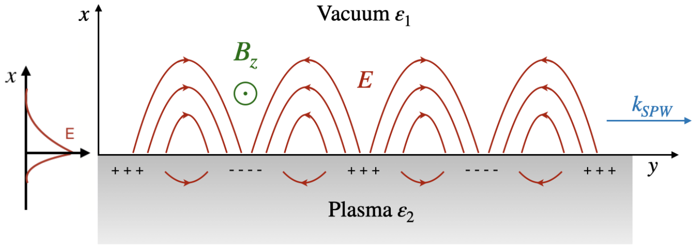

Figure 2.2: Schematic representation of the surface oscillation mode of the electrons at the vacuum-plasma interface.

In this scenario, the SPW propagates along the positive $y-$direction and the system is assumed to be invariant in the $z-$direction. The existence of SPW is ensured if

$$\varepsilon_1 \varepsilon_2 < 0 \quad \text{and} \quad \varepsilon_1 + \varepsilon_2 < 0 \,, \tag{2.33}$$

as explained in [1]. Both conditions are satisfied when considering the case of an interface between a vacuum region, designated by v, hence $\varepsilon_1 = \varepsilon_v = 1$ and an overdense plasma region, designated by p, $\varepsilon_2 = \varepsilon_p = 1 - \omega_p^2/\omega^2$, where ω_p is the plasma frequency, for which $\varepsilon_p < 0$ leading to $\omega_p > \omega$.

Given that there must be a component of the electric field normal to the surface in order to generate waves that travel along the surface, SPW are always transverse magnetic waves (TM). Therefore, the fields are given by:

$$\begin{cases} \mathbf{E}^j & = \left(E_x^j\hat{\mathbf{x}} + E_y^j\hat{\mathbf{y}}\right) e^{-q^j|x|}e^{i(k_y y-\omega t)} \\ \mathbf{B}^j & = B_z^j\hat{\mathbf{z}}e^{-q^j|x|}e^{i(k_y y-\omega t)} \end{cases} \tag{2.34}$$

where $k_y \equiv k_y^j$ is the y component of the wave vector in media $j = v, p$ (vacuum and plasma respectively) parallel to the interface. The transverse wave vector in the two media is defined by $q^j = \sqrt{k_y^2 - \varepsilon_j \frac{\omega^2}{c^2}}$ which gives respectively:

$$q^v = \sqrt{k_y^2 - \frac{\omega^2}{c^2}} \quad \text{and} \quad q^p = \sqrt{k_y^2 - \frac{\omega^2 - \omega_p^2}{c^2}}\,, \tag{2.35}$$

as $\varepsilon_v = 1$ and $\varepsilon_p = 1 - \omega_p^2/\omega^2$. As a result, the fields in the vacuum can be described as:

$$\begin{cases} \mathbf{E}^v & = \left(E_{0x}\hat{\mathbf{x}} + E_{0y}\hat{\mathbf{y}}\right) e^{q^v|x|}e^{i(k_y y-\omega t)}\,, \\ \mathbf{B}^v & = B_{0z}\hat{\mathbf{z}}e^{q^v|x|}e^{i(k_y y-\omega t)}\,. \end{cases} \tag{2.36}$$

While inside the plasma, the fields are given by:

$$\begin{cases} \mathbf{E}^p & = \left(E_{0x}\hat{\mathbf{x}} + E_{0y}\hat{\mathbf{y}}\right) e^{-q^p|x|}e^{i(k_y y-\omega t)}\,, \\ \mathbf{B}^p & = B_{0z}\hat{\mathbf{z}}e^{-q^p|x|}e^{i(k_y y-\omega t)}\,. \end{cases} \tag{2.37}$$

Assuming there are no external sources and that all materials are non-magnetic ($\mu_0 = 1$), we obtain from the Ampère-Maxwell equation that

$$\nabla \times \mathbf{B}^j = \mu_0 \left(\mathbf{J}^j + \varepsilon_j \frac{\partial}{\partial t}\mathbf{E}^j\right) = \frac{-i\omega\varepsilon_j}{c^2}\mathbf{E}^j\,, \tag{2.38}$$

which, when introducing this ansatz in Eq.(2.34), gives the following electric component:

$$\mathbf{E}^j = -\frac{c^2}{i\omega\varepsilon_j}\left(ik_y\hat{\mathbf{y}} \pm q^j\hat{\mathbf{x}}\right) B_{0z}\,. \tag{2.39}$$

The above Eq.(2.39) shows that the electric component is proportional to the $z-$component of the magnetic field. As a consequence, we consider B_{0z} as being representative of the SPW. From henceforth, B_{0z} will be noted B_{SPW}. We can therefore simplify the fields expression in each media as following:

In the vacuum: In the plasma

$$\begin{cases} E_x^v &= -\dfrac{c^2 k}{\omega} B_{\text{SPW}}\,, \\ E_y^v &= \dfrac{c^2 q^v}{i\omega} B_{\text{SPW}}\,, \end{cases} \qquad \begin{cases} E_x^p &= -\dfrac{c^2 k}{\omega \varepsilon_p} B_{\text{SPW}}\,, \\ E_y^p &= -\dfrac{c^2 q^p}{i\omega \varepsilon_p} B_{\text{SPW}}\,. \end{cases} \tag{2.40}$$

The imposed field continuity at the interface $x = 0$ of the electric field parallel to the surface, E_y, leads to:

$$E_y^p = E_y^v = E_y\,, \tag{2.41}$$

which raises the following condition on the evanescence length:

$$\boxed{\frac{q^p}{q^v} = -\varepsilon_p\,.} \tag{2.42}$$

From this condition and knowing the evanescence length for each media (Eq. 2.35), we can derive the dispersion relation:

$$\sqrt{k_y^2 - \frac{\omega^2}{c^2}\varepsilon_p} = -\varepsilon_p \sqrt{k_y^2 - \frac{\omega^2}{c^2}}\,, \tag{2.43}$$

$$\Rightarrow \frac{k_y^2 c^2}{\omega^2} = \frac{\varepsilon_p - \varepsilon_p^2}{1 - \varepsilon_p^2} = \frac{1 - \omega_p^2/\omega^2}{2 - \omega_p^2/\omega^2}\,. \tag{2.44}$$

In conclusion, the SPW's dispersion relation in the non relativistic cold plasma limit [23] is defined as:

$$\boxed{k_y \equiv k_{\text{SPW}}(\omega) = \pm \frac{\omega}{c} \sqrt{\frac{1 - \omega_p^2/\omega^2}{2 - \omega_p^2/\omega^2}}}\,. \tag{2.45}$$

In the limit of $\omega \ll \omega_p$, and expanding in terms of ω/ω_p, the linear approximation yields:

$$\frac{k_y^2 c^2}{\omega^2} = \frac{1 - \omega_p^2/\omega^2}{2 - \omega_p^2/\omega^2} \approx 1 + \frac{\omega^2}{\omega_p^2} + \ldots \quad \text{and} \quad \frac{k_y c}{\omega} \approx 1 + \frac{1}{2}\frac{\omega^2}{\omega_p^2} + \ldots \tag{2.46}$$

Using these approximations in Eq.(2.40), we can compare the proportions of the electric fields near the surface, E_x^v, E_x^p and E_y, with the reference value of the SPW's magnetic field B_{SPW}. The field parallel to the surface thus becomes:

$$E_y \approx c \frac{\omega}{\omega_p} B_{\text{SPW}}\,, \tag{2.47}$$

meaning that $E_y \ll B_{\text{SPW}}$. The fields perpendicular to the interface, which are discontinuous at $x = 0$, become:

$$E_x^v \approx c\left(1+\frac{\omega^2}{\omega_p^2}\right)B_{\text{SPW}} \approx cB_{\text{SPW}}\,, \tag{2.48}$$

$$E_x^p \approx c\frac{1+\omega^2/\omega_p^2}{1-\omega_p^2/\omega^2}B_{\text{SPW}} \approx c\frac{\omega^2}{\omega_p^2}B_{\text{SPW}}\,. \tag{2.49}$$

We obtain therefore that in the limit of $\omega \ll \omega_p$, we have an EM wave whose electric field component parallel to the surface is negligible in the vacuum. Moreover, the electric field perpendicular to the surface is comparable to the magnetic field of the SPW in the vacuum whereas it is negligible inside the plasma.

The coupling problem

The SPW dispersion relation derived in the last subsection 2.2.1,

$$k_{\text{SPW}}(\omega) = \pm\frac{\omega}{c}\sqrt{\frac{1-\omega_p^2/\omega^2}{2-\omega_p^2/\omega^2}}\,,$$

possess a maximum frequency of $\omega_{max} = \omega_p/\sqrt{2}$. When ω tends to the ω_{max} limit, the wave vector k goes to infinity and consequently the group velocity goes to zero, as well as the phase velocity: the mode becomes electrostatic in this region.

In the opposite limit where k lies closer to the light line, the phase velocity of the SPW reaches the speed of light. As shown in Figure 2.3, the SPW's dispersion curve (solid blue line) never intersects the light line given by $\omega = kc$ (dashed black line), indicating that SPW cannot be excited by an EM wave in vacuum. Coupling of the incident EM wave (red solid line) and the SPW occurs when the gap Δk between k_L and k_{SPW} is compensated. In other words, their dispersion curves must overlap. As a consequence, the direct illumination of a flat interface by an EM wave does not excite SPW.

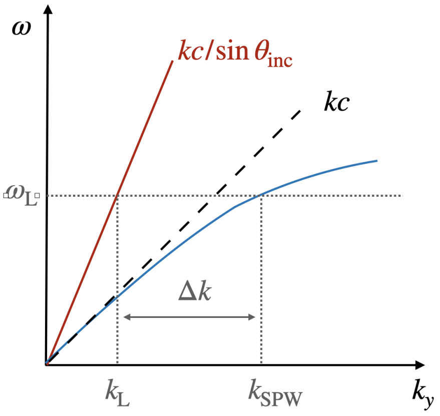

Figure 2.3: Dispersion relation of the SPW (solid blue), the external EM wave (solid red) and the light line (dashed black). The term θ_{inc} denotes the incident angle of the EM wave with respect to the grating.

Different approaches to bridge the gap Δk exist. One way is through the use of a dielectric prism possessing a higher index of refraction than the dielectric of the interface where the SPW is being excited. This method is called attenuated total reflection (ATR) [71,72] and requires three materials with different dielectric constants. However, this method is unsuitable for the study of SPW excitation in high field plasmonics [73] as any dielectric constant turns into plasma when using any laser with $I > 10^{16}$ W/cm^2. In addition, nonlinear effects can appear as soon as the laser intensity is high enough, even before the ionization threshold is attained, which can disturb the pulse. Moreover, the duration of ultra short pulses can be significantly modified when using a prism.

A more suitable technique when going to higher laser intensities, is using a grating coupling. This method consists of adopting a target presenting periodical modulation at the surface with a spatial period d (as in Figure 2.4(a)) instead of a flat target. The grating coupling will be the method used throughout the continuation of this manuscript.

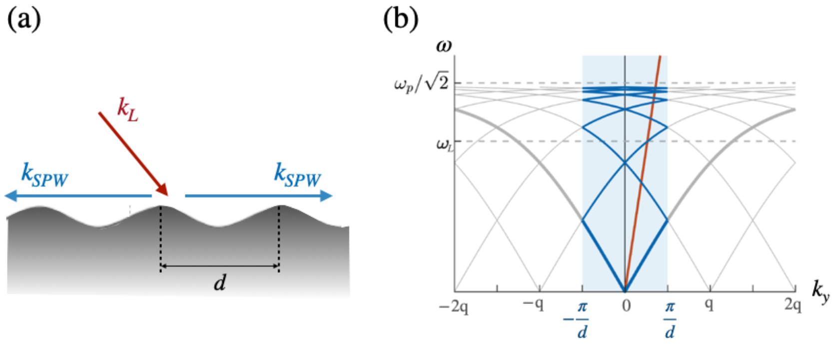

Figure 2.4: (a) Schematic representation of an EM wave on a grating. (b) Taken from [47]: Folding of the dispersion curve of the SPW mode at a periodically modulated interface with period d. The modes are characterized by their frequency and their wave vector q inside the first Brillouin zone (region filled with light blue color). The light line is drawn in red and the folding branches of the dispersion curves are underlined with blue.

In the scenario of a modulated grating, the medium can be considered as periodic. Therefore, as a direct consequence of the Floquet-Bloch theorem, the solutions of the wave equation are given by:

$$\psi_k(y) = e^{iky} u_k(y), \quad \text{with} \quad u_k(y) = u_k(y+d)\,, \tag{2.50}$$

meaning that the solutions take the form of plane waves (term in e^{iky}) multiplied by a periodic function $u_k(y)$ whose periodicity is the same as the grating period d [58]. Subsequently, the solution for the wave equation with wave vector k is periodic with a period of $2\pi/d$. Due to this periodicity, we can restrict the dispersion relation of the SPW to the first Brillouin zone: a region of $\omega - k$ space defined as the interval $[-\pi/d, \pi/d]$. In this region, the SPW can be coupled by incident radiation.

As illustrated in Figure 2.4(b), the SPW dispersion relation is folded around the edges of the Brillouin zone in reciprocal space to the positions corresponding to multiples of the grating vector q = 2π/d. Each branch of the folded SPW curve represents a displaced SPW dispersion curve and shows a pronounced curvature away from the light line. The coupling between the SPW and the incident pulse is once again being given by the overlap between the light line and the folding of a SPW branch.
The phase matching condition is thus given by :

$$\boxed{\omega_{\mathrm{L}} = \omega_{SPW}\,, \quad k_L = k_{SPW} \pm m\mathrm{q}\,,} \tag{2.51}$$

where k_L is the in-plane wave vector of the incident laser pulse, m an integer number ($m = 0$, ± 1,...) and k_{SPW} and q are respectively the wave vectors of the SPW and the grating.

In the previous section, the dispersion relation was calculated for a planar system but it has been demonstrated that it becomes modified when the interface is corrugated. Indeed the correction to the dispersion relation is of $\sim (h/d)^2$ order, with h being the grating depth. Therefore, as long as $h \ll d$, the correction to the SPW's dispersion curve can be considered small. This implies that the k_{SPW} on the grating surface will remain nearly unchanged from the k_{SPW} on the flat surface when the grooves of the gratings are relatively shallow. It is worth mentioning that in the high field case, the gratings are not expected to be extremely shallow. Thereby exciting surface plasmons on the grating surface means satisfying the following equation :

$$k_L \sin\theta_{inc} = k_{SPW} \pm m\mathrm{q}\,, \tag{2.52}$$

which can be obtained by using an appropriately chosen incident angle θ_{inc} for a given q when fixing the values of ω_L, d and m. At the crossing point of two branches of the SPW dispersion curve at the Brillouin zone boundaries, which correspond to the interaction of two diffracted waves, counter-propagating SPW can couple together resulting in two standing wave solutions: one with field extrema at the grating peaks and the other with extrema at the bottom of the valleys. These solutions correspond to different energies and therefore generate a band gap [74]. The band gap in the SPW's dispersion relation depends on the grating depth, with the band gap becoming larger when the gratings are sufficiently deep so that the modulation can no longer be considered as a small perturbation of the planar interface (i.e $h \gg d$). Moreover, the dispersion curve of a shallow grating is always at higher ω than the light line, preventing SPW excitation; however, increasing the grating depth lowers the frequency of the modified SPW dispersion curve enabling matching between the SPW and the laser frequency [3]. The importance of the modulation depth in the laser-plasma coupling is further corroborated in [69] where they observed that decreasing h reduces the importance of the target geometry and increases the importance of the resonant coupling. Decreasing h led to a general decrease in the laser absorption; however, the difference between the case where SPW is excited and the case where the θ_{inc} does not satisfy Eq.2.52 increased for smaller values of h. Nonetheless, an excessively reduced modulation depth is non desirable as the coupling is lost at low laser intensities and significantly reduced for higher intensities. When moving to the UHI regime, the target becomes susceptible to surface deformation due to the laser ablation [54]. As a direct consequence, a deeper grating might be needed to preserve the periodic modulation. This argument will be further discussed in Chapter 5.

In the case where $\omega_p \gg \omega$, which corresponds to the typical condition when working with lasers in the visible and infrared (IR) range, the SPW have a phase and group velocity close to the speed of light (i.e. $v_\phi, v_g \sim c$) and the dispersion relation at low frequency is very small. In this limit, the resonance condition becomes:

$$\sin\theta_{inc} \simeq \pm 1 + m\frac{\lambda}{d}\,. \tag{2.53}$$

This relation may also be viewed as a consequence of the diffraction grating equation, which relates the incidence angle of a monochromatic beam (θ_{inc}) to the emission angles of the diffracted orders (θ_m) and to the grating period (d):

$$\sin\theta_{inc} + \sin\theta_m = m\frac{\lambda}{d}\,. \tag{2.54}$$

Sending a laser pulse at an angle θ_{inc} at a diffraction grating, which is none other than a target with periodic modulation, results in concentrated light at an angle of diffraction where there is constructive interference. Note that Eq.(2.54) results from considering the constructive interference of two or more scattering centers, hence it does not strictly depend on the fact that the grating should be infinite. Moreover, Eq.(2.53) follows from Eq.(2.54) when

$\theta_m = \pm\pi/2$, which means that in this case an interference maximum is sent along the surface in the direction of the SPW's propagation.

The surface corrugation of a diffraction grating enables light scattering, making direct coupling between the incident light and the SPW possible. Indeed, well distributed surface roughness can contain the right vectors to excite SPW [1] given that the wave vector of the incident light is changed by addition or subtraction of an integer multiple of the grating vector q in the direction normal to the grating grooves, allowing it to be momentum matched and thus coupled to the SPW. However, the inverse process of SPW excitation can also occur on the grating, where the SPW propagating along the interface excites in turn an EM wave, which gives rise to radiative losses.

There are many configurations that satisfy the resonance condition given by Eq.(2.53). As shown in Fig.2.5, the incident light, θ_{inc}, is split into a series of different beams at different diffraction angles, also known as diffraction orders. These diffraction orders m only exist when $|m\lambda/d| < 2$ thereby preventing the incident light of wavelength λ from being diffracted in more than a finite number of orders [75]. Indeed, without this restriction, $|\sin\theta_{inc} + \sin\theta_m| > 2$ which is physically meaningless.

The specular reflection ($m = 0$), also known as the zeroth order, always exists and consists of the un-diffracted light leading to the law of reflection $\theta_m = -\theta_{inc}$. The zeroth order is always propagative while the other orders may be propagative or evanescent. When $m \neq 0$, periodic modulations with $d \gg \lambda$ will lead to evanescent orders while $d \ll \lambda$ will lead to a large number of propagative orders [76]. Moreover, the number of orders increases for shorter wavelengths and larger grating periods.

The distinction between the different diffraction orders is summarized as follows :

$$\begin{array}{lrr} \theta_m > -\theta_{inc} & \text{for positive orders} & (m > 0) \\ \theta_m < -\theta_{inc} & \text{for negative orders} & (m < 0) \\ \theta_m = -\theta_{inc} & \text{for specular reflection} & (m = 0) \end{array}$$

Using the sign convention for m where $m > 0$ if the diffracted beam lies left (counter-clockwise side) to the zeroth order ($m = 0$) and $m < 0$ if the beam lies right (clockwise side) to the zeroth order.

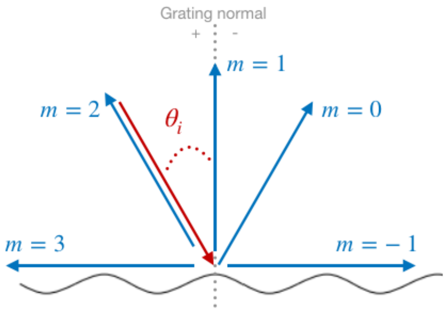

Figure 2.5: Output beams of possible diffraction orders at a diffraction grating.

Excitation of SPW by grating

One way to ensure this coupling is to use structured targets [21, 22], such as periodic grooves, called gratings. In this scenario, see Fig.2.6, a laser pulse impinging on the target interface with a given incidence angle θ_{inc} can excite a SPW provided that the following phase matching conditions are satisfied [1, 23, 25]:

$$\omega_L = \omega_{SPW}\,, \qquad\qquad k_L = k_{SPW} \pm m\frac{2\pi}{d}\,, \tag{2.55}$$

where $\omega_L(= \omega)$ and k_L are the frequency and wave-vector of the laser pulse, k_{SPW} the wave-vector of the SPW, d the grating's period and m the diffraction order.

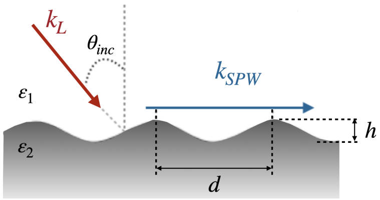

Figure 2.6: Laser-grating coupling illustration where the laser beam is focused thought an angle θ_{inc} over the interface of the plasma target with grating depth h and period d.

For phase-matching to be ensured, the laser dispersion relation becomes:

$$k_L \sin\theta_{inc} = k_{SPW} \pm m\frac{2\pi}{d}\,. \tag{2.56}$$

In the following we restrict our study to the first order mode ($m = 1$) which is the most intense. From the definition of n_c we note that ω_p^2/ω_L^2 is equivalent to n/n_c. Using Eq.(2.45) in Eq.(2.56) we obtain that, in order to resonantly excite a SPW at the vacuum-plasma interface, the laser incidence angle needs to satisfy the following equation:

$$\sin\theta_{inc} = \sqrt{\frac{1-n/n_c}{2-n/n_c}} - \frac{\lambda_0}{d}\,. \tag{2.57}$$

Moreover, for an over-dense plasma ($n \gg n_c$) and the dispersion relation (Eq.(2.45)), the SPW phase and group velocities are slightly subluminal:

$$v_\phi \approx c[1-n_c/(2n)]\,, \qquad v_g \approx c[1-3n_c/(2n)]\,. \tag{2.58}$$

Given that SPW are waves with a longitudinal electric field component and $v_\phi \sim c$, they are optimal for electron acceleration as they can trap electrons and accelerate them up to high energies along the surface [38].

Blazed grating

Blazed gratings (BG) are used to optimize the coupling direction given that they are designed to concentrate a great portion of energy of the incident light in a specific m^{th} diffraction order for a certain wavelength [77,78].

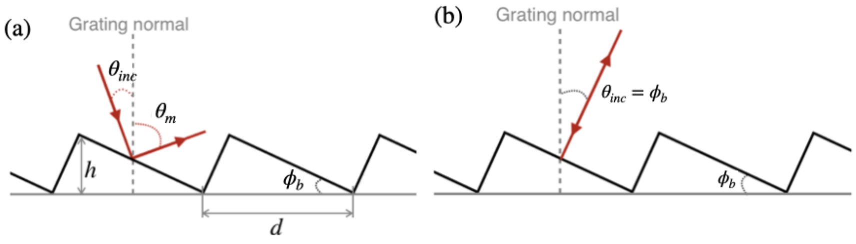

Figure 2.7: Schematic illustrations of (a) the blazed grating and (b) the Littrow mount.

In Fig. 2.7(a), the incident light is directed at the grating at angle θ_{inc} with respect to the grating normal, and is diffracted at angle $-\theta_m$. The blazed grating presents a saw-tooth profile where h denotes the groove's depth, d the distance between the grooves and ϕ_b the angle made by a groove's longer side and the plane of the grating here called "blaze angle". The specular reflection from this blazed grating differs from the flat surface due to surface modulation; in this case, the blaze angle must satisfy the so called blaze condition which implies :

$$\phi_b = \frac{(\theta_{inc}+\theta_m)}{2}\,. \tag{2.59}$$

As a consequence, the grating equation Eq.(2.54) becomes:

$$2 \sin \phi_b \cos (\theta_{inc} - \phi_b) = m \frac{\lambda_B}{d} , \tag{2.60}$$

where λ_B is the "blaze wavelength" which corresponds to the wavelength where the blazed grating should be most efficient.

The blazed grating has some restrictions considering that both the groove's depth and period are fixed. Indeed, h is given by $h = d \cos \phi_b \sin \phi_b$ and d depends on the resonance condition of the desired incident angle. However, BG grant liberty on the blaze angle which determines the grooves shapes allowing the triangular modulation to be either symmetric or asymmetric. These types of gratings are useful because it is possible to know where the diffracted ray goes from where the angle θ_{inc} is incident by exploiting optical geometry. In blazed gratings, one chooses the blazed angle that enables the reflection to coincide with the chosen diffraction angle. The same should apply for the SPW excitation, maximizing the reflection along the propagation direction by the same principle of diffraction. In fact, most commonly used blazed gratings will only scatter the specular ($m = 0$) and the first ($m = -1$) diffraction orders, whereas all other orders will be evanescent [79]. The scattered orders will be excited asymmetrically due to the blazed effect of the slanted grating profile, thereby coupling asymmetrically the incident light to the counter propagating SPW along the periodic direction. When the asymmetrical effect is sufficiently large, the SPW excitation becomes unidirectional [80].

However, most commercial blazed gratings [78, 81, 82] are fabricated in the Littrow configuration (also known as auto-collimation) where the incident and the scattered first order wave are equal, the periodic structure can thus reflect the diffracted light back along the same path as the incident light (see Fig.2.7(b)). In this case $\theta_{inc} = \theta_m = \theta_B$ which reduces the grating equation to:

$$2 \sin \theta_B = m \frac{\lambda_{B(Litt)}}{d} , \tag{2.61}$$

where $\lambda_{B(Litt)}$ is the blaze wavelength in the Littrow mounting [78]. Maximum efficiency is obtained when $\lambda = \lambda_{B(Litt)}$ and decreases when departing from this configuration [77].

Commercially, the use of Littrow configuration is convenient since the minimized angular deviation between the incident and the diffracted light allows the design of very compact systems [76].

2.2.2 SPW excitation in relativistic regime

SPW excitation resulting from high intensity ultra-short laser plasma interaction $\geq 10^{19}$ W/cm^2 and $\leq 100fs$) has been shown to be an efficient way to increase the acceleration of high charge electron bunches along the plasma surface up to $\sim$ 10MeV and $\sim$ 650pC [38–46].

Electron acceleration by SPW

A good analogy to visualize the principle of electron acceleration by a wave is to envisage the electron as a surfer carried along by a sea wave. If the surfer remains still, an incoming wave will only lift them up and down and they will gain no energy in average as the wave passes by. But if the surfer "catches" the wave by paddling to obtain a velocity close to the phase velocity of the wave, the surfer will be pushed along by the wave gaining energy at the wave's expense. Similarly, the energy gain of an electron trapped by the SPW will depend on the electron's initial velocity and position when entering the wave field. In this section, the energy gain will be estimated for a "lucky" electron that satisfies particular and favourable conditions for the acceleration and follows a specific trajectory among many. In reality, the injection of said electron, or the way the electron acquires advantageous initial conditions, are influenced by the presence of a laser pulse. The laser pulse resonantly excites the SPW on the grating and the electron interacting with the SPW field will oscillate with the laser frequency. Given that the local amplitude of the SPW might be higher than that of the incoming laser, the electron's quiver motion will be faster than the electron thermal velocity [38].

This has been proven by previous studies that have shown the generation of highly energetic and collimated bunches of relativistic electrons [42] from the excitation of SPW by the interaction of ultra intense laser pulses ($I > 10^{19}\, Wcm^{-2}$) with grating targets.

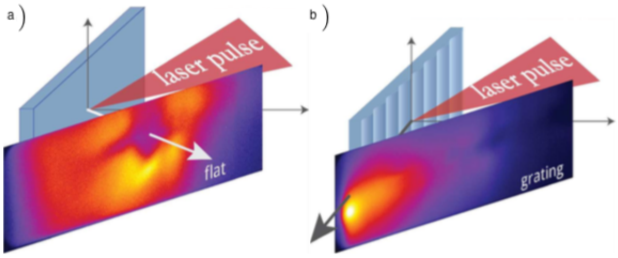

Figure 2.8: Electron acceleration by SPW. a)Image for a flat target, showing a diffuse angular distribution of electrons. b)Image for a grating target irradiated at the resonant angle for SP excitation, showing a highly collimated emission close to the tangent at the target surface. Extracted from [67].

We consider a similar geometry as in section 2.2.1 Fig.2.2 where the SPW propagates in the laboratory frame S at the boundary between vacuum ($x < 0$) and a simple metal or a cold plasma ($x > 0$). We assume the electron density profile to be $n_e = n_0\Theta(x)$ and the SPW a monochromatic plane wave propagating in the y direction [38, 42, 43, 47, 73, 83]. The components of the EM field can thus be written as:

$$\tilde{E}_y = E_{\mathrm{SPW}}\left[\Theta(+x)e^{-q^p x} + \Theta(-x)e^{+q^v x}\right]e^{ik_y y - i\omega t} \tag{2.62}$$

$$\tilde{B}_z = \frac{i\omega/c}{q^v}E_{\mathrm{SPW}}\left[\Theta(+x)e^{-q^p x} + \Theta(-x)e^{+q^v x}\right]e^{ik_y y - i\omega t}\,, \tag{2.63}$$

$$\tilde{E}_x = -ikE_{\mathrm{SPW}}\left[\Theta(+x)\frac{e^{-q^p x}}{q^p} - \Theta(-x)\frac{e^{+q^v x}}{q^v}\right]e^{ik_y y - i\omega t}\,, \tag{2.64}$$

where $q^v = k\left(\omega_p^2/\omega^2 - 1\right)^{-1/2}$ and $q^p = k\left(\omega_p^2/\omega^2 - 1\right)^{1/2}$ are the wave vectors of the vacuum and plasma regions respectively and E_{SPW} is the amplitude of the longitudinal electric field (E_y) component at $x = 0$. Both E_y and B_z are continuous at $x = 0$, however, E_x is discontinuous. Notice that E_{SPW} is the amplitude of the longitudinal field, E_y, parallel to the surface. By the equations above we observe that the perpendicular electric field in vacuum E_x is typically larger by a factor of ω_p/ω and of the same order as the magnetic field.

The field amplitudes can be transformed to a reference frame S' that moves with the SPW along the interface y. The frame S' moves therefore with a velocity equal to the SPW phase velocity $v_\phi = \omega/k$ and we obtain:

$$E'_y = E_y\,, \tag{2.65}$$

$$B'_z = \gamma(B_z + \beta E_x)\,, \tag{2.66}$$

$$E'_x = \gamma(E_x + \beta B_z)\,, \tag{2.67}$$

where β is defined in such a way that $v_\phi = \beta c$ and $\gamma = 1/\sqrt{1-\beta^2}$. In this frame, $ky - \omega t = k'y'$ with $k' = k/\gamma$ and $\omega' = 0$, and the primed fields are static.

Performing the Lorentz transformations listed in Eqs.(2.65-2.67) we get :

$$\tilde{E}'_y = E_{\mathrm{SPW}}\left[\Theta(+x)e^{-q^p x} + \Theta(-x)e^{+q^v x}\right]e^{ik'y'}\,, \tag{2.68}$$

$$\tilde{B}'_z = \frac{i\omega_p^2}{kc\omega}E_{\mathrm{SPW}}\left[\Theta(+x)e^{-q^p x}\right]e^{ik'y'}\,, \tag{2.69}$$

$$\tilde{E}'_x = -\frac{i\gamma k}{q^p}E_{\mathrm{SPW}}\left[\Theta(+x)\frac{e^{-q^p x}}{\omega_p^2/\omega^2 - 1} - \Theta(-x)e^{+q^v x}\right]e^{ik'y'}\,, \tag{2.70}$$

with $q^p = k/\gamma = k'$. The magnetic field B'_z in the moving frame S' vanishes in the vacuum region ($x < 0$) and is discontinuous at the surface. The SPW field is electrostatic in the S' frame for $x < 0$ and is derived from the potential

$$\phi'(x,y) = \frac{i\gamma}{k} E_{\mathrm{SPW}} \left(\Theta(+x)e^{-q^v x} + \Theta(-x)e^{+q^p x}\right) \sin(k'y') \, . \tag{2.71}$$

The acceleration process takes place outside the plasma thus from now on we will only concentrate on the vacuum region.

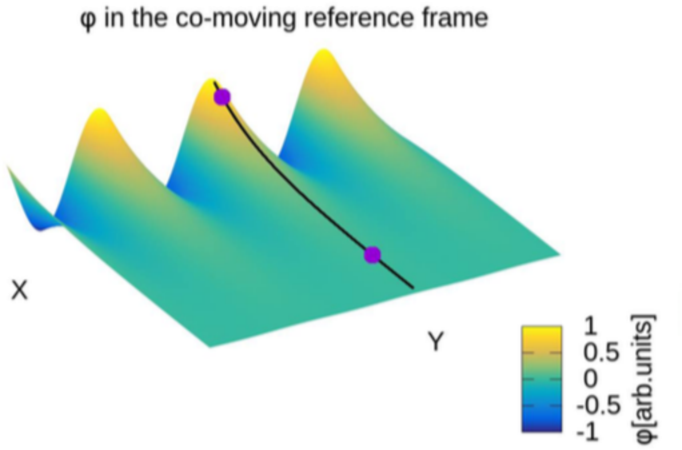

Figure 2.9: Illustration taken from [73] representing the electrostatic potential of the SPW in the boosted frame. The thick line represents the electron's downhill motion.

In this region, the process can be described as the electron going down the 2D potential energy hill $U(x,y) = -e\phi'(x,y)$. As shown in Fig. 2.9, the electron is initially at rest in the moving frame S' at the top of the potential hill ($x = 0$, $y' = \pi/2k'$) with $v'_y = 0$ and descends along the $x = 0$ plane to the region where $U \sim 0$. This is not the only possible trajectory but is the simplest and is given as illustration. Note that $v'_y = 0$ in S' means that the electron moves with an initial velocity v_ϕ in the laboratory frame S. As discussed in [38] this initial velocity that allows the particles to be injected and phase locked in the wave can be given by the $\vec{E}_x \times \vec{B}_z$ motion of the electrons due to the large transverse fields. this mechanism is effective even if the set-up is such that the amplitude of the parallel field is way below the wavebreaking condition.

The final kinetic energy of such an electron in the boosted frame S' will be:

$$W' = W_{max} \equiv 2eE_{\mathrm{SPW}}\gamma/k \, , \tag{2.72}$$

which corresponds to the energy-momentum-four-vector

$$\left(U'_f, \mathbf{p}'c\right) = \left(m_e c^2 + W_{max}, 0, p'_{fy}, 0\right) \ , \tag{2.73}$$

with $U'_f = \left(p'^2_{fy}c^2 + m_e^2 c^4\right)^{1/4}$. Assuming $v_\phi \simeq c$ and $\gamma \sim \omega_p/\omega \gg 1$ the energy gain Eq.(2.72) can be written as :

$$W' \simeq 2m_e c^2 a_{\mathrm{SPW}} \frac{\omega_p}{\omega} \, , \tag{2.74}$$

with $a_{\mathrm{SPW}} \simeq (eE_{SPW}/m_e\omega c)$ a dimensionless parameter. If $a_{\mathrm{SPW}} \sim 1$ the electron becomes relativistic, then $W' \gg m_e c^2$ and in this limit $U'_f \approx W' \simeq p'_{fy}c$.

Transforming back to the laboratory frame S, the energy gain becomes:

$$U_f = \gamma\left(U'_f + \beta p'_{fy}c\right) \simeq 2W'\frac{\omega_p}{\omega} = 4m_e c^2 a_{SPW}\left(\frac{\omega_p}{\omega}\right)^2 \, . \tag{2.75}$$

Considering an electron with the same initial conditions as before but going down the $-x$ direction. This electron will have an energy $W' = W_{max}/2$ and an energy-momentum-four-vector :

$$\left(U'_f, \mathbf{p}'c\right) = \left(m_e c^2 + W_{max}/2, p'_{fx}, 0, 0\right) \ , \tag{2.76}$$

with $U'_f = \left(p'^2_{fx}c^2 + m_e^2 c^4\right)^{1/2}$. In this case, the energy momentum in the laboratory frame S will be:

$$\left(U_f, \mathbf{p}_f c\right) \simeq \left(\gamma U'_f, U'_f, \gamma U'_f, 0\right) \ , \tag{2.77}$$

so that the final energy U_f and emission angle ϕ are given by:

$$U_f = m_e c^2 a_{\mathrm{SPW}} \left(\frac{\omega_p}{\omega}\right)^2 , \tag{2.78}$$

$$\tan\phi = \frac{p_y}{p_x} \sim \gamma \, . \tag{2.79}$$

The more the electrons are energetic, the more they are located along the surface as shown in Fig.2.10

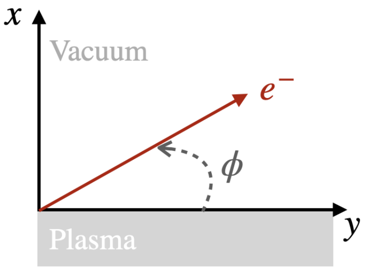

Figure 2.10: Graph of the emission angle ϕ of the electrons with respect to the surface.

2.3 Radiation by moving charges

As discussed in section 2.2.2, we are interested in studying the excitation of SPW at increasingly higher laser intensity regimes for their potential of accelerating highly energetic and high charge electrons. It is a well known fact that accelerated charged particles emit electromagnetic radiation. Therefore we are interested in the eventual radiation emitted by the electrons accelerated via the SPW mechanism. In this section we will discuss the radiation emitted

2.3.1 Classical Radiation Emission

Contrary to a charged particle at rest or at uniform motion, when a charge is accelerated, their surrounding field start to "detach" from the charge and propagate away. This "detachment" represents the radiation emitted. A more detailed physical picture is presented in [84] (paragraph 2.4.1 p27). The emitted radiation can be detected far away from the particles. For any observation direction, the far field radiation can be calculated via the Liénard-Wiechert potentials [85].

Liénard-Wiechert potentials

The electric and magnetic fields around a moving charge are described by the Liénard-Wiechert scalar potential, $\mathbf{\Phi}$, and vector potential, $\mathbf{A}$, in SI units, are written as follows:

$$\mathbf{\Phi}(\mathbf{r},t) = \frac{1}{4\pi\varepsilon_0}\left[\frac{e}{(1-\boldsymbol{\beta}\cdot\mathbf{n})R}\right]_{ret}, \tag{2.80}$$

$$\mathbf{A}(\mathbf{r},t) = \frac{\mu_0 c}{4\pi}\left[\frac{e\boldsymbol{\beta}}{(1-\boldsymbol{\beta}\cdot\mathbf{n})R}\right]_{ret}, \tag{2.81}$$

where $\mathbf{n}$ is an unit vector in direction of the observation point and $\boldsymbol{\beta} = \mathbf{v}/c$. The subscript *ret* indicates that the values inside the square brackets are evaluated at the retarded time:

$$t_{ret} = t - |r - r_0(t_{ret})|/c\,, \tag{2.82}$$

and permits to take into account the relativistic retardation of the fields due to the finite speed of light. We define $\mathbf{n} \equiv \mathbf{R}/R$ with

$$\mathbf{R}(t_{ret}) \equiv |\mathbf{r} - \mathbf{r}_0(t_{ret})|\,, \tag{2.83}$$

where $\mathbf{r}$ is the distance from 0 to the observation point P, $\mathbf{r}_0(t_{ret})$ the distance of the particle on its trajectory from 0, as depicted in Figure 2.11.

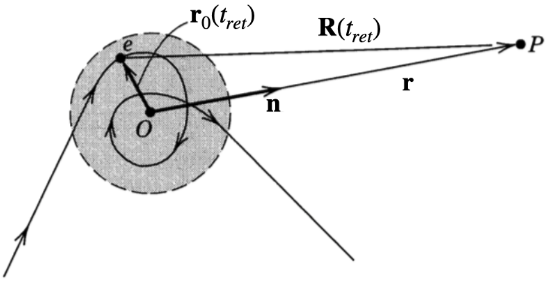

Figure 2.11: Illustration of an electron trajectory, adapted from [85].

From the potentials Eq. (2.81) we find the fields $\mathbf{E}$ and $\mathbf{B}$:

$$\mathbf{E}(\mathbf{r},t) = -\nabla\mathbf{\Phi} - \frac{\partial}{\partial t}\mathbf{A}\,, \tag{2.84}$$

$$\mathbf{B}(\mathbf{r},t) = \nabla\times\mathbf{A}\,. \tag{2.85}$$

The fields due to a point charge e moving with variable velocity $\boldsymbol{\beta}$ are:

$$\mathbf{E}(\mathbf{r},t) = \frac{e}{4\pi\varepsilon_0}\left[\left[\frac{\mathbf{n}-\boldsymbol{\beta}}{\gamma^2(1-\boldsymbol{\beta}\cdot\mathbf{n})^3R^2}\right]_{ret} + \frac{1}{c}\left[\frac{\mathbf{n}\times\{(\mathbf{n}-\boldsymbol{\beta})\times\dot{\boldsymbol{\beta}}\}}{(1-\boldsymbol{\beta}\cdot\mathbf{n})^3R}\right]_{ret}\right]\,, \tag{2.86}$$

$$\mathbf{B}(\mathbf{r},t) = \frac{1}{c}\left[\mathbf{n}\times\mathbf{E}\right]_{ret}\,, \tag{2.87}$$

where $\dot{\boldsymbol{\beta}} = d\boldsymbol{\beta}/dt_{ret}$. The electric field is divided into two separate terms: "velocity fields" and "acceleration fields". The first square bracket represents the velocity field, it does not contain $\dot{\boldsymbol{\beta}}$ and represent the static fields falling off as R^{-2}. On the other hand, the second term denoting the acceleration fields, also known as radiation fields, is proportional to $\dot{\boldsymbol{\beta}}$ and is independent from the first term. Therefore, in the following we will only consider the radiation field:

$$\mathbf{E_a} = \frac{e}{4\pi\varepsilon_0 c}\left[\frac{\mathbf{n}\times\{(\mathbf{n}-\boldsymbol{\beta})\times\dot{\boldsymbol{\beta}}\}}{(1-\boldsymbol{\beta}\cdot\mathbf{n})^3R}\right]_{ret}\,. \tag{2.88}$$

The instantaneous energy flux in the direction $\mathbf{n}$ is given by the Poynting vector

$$\mathbf{S} = \frac{1}{\mu_0}\mathbf{E}\times\mathbf{B} = \frac{1}{\mu_0 c}|\mathbf{E_a}|^2\mathbf{n}\,, \tag{2.89}$$

from which we obtain the radiated power P emitted per unit solid angle $d\Omega$:

$$\frac{dP(t)}{d\Omega} = \left[\mathbf{S}\cdot\mathbf{n}\right]_{ret}R^2\,, \tag{2.90}$$

namely, the energy per unit area per unit time detected at an observation point at time t of radiation emitted by the charge at time t_{ret}.

For relativistic motion the acceleration fields depend on the velocity as well as the acceleration. The radial component of Poynting's vector can be calculated to be :

$$[\mathbf{S}\cdot\mathbf{n}]_{ret} = \frac{e^2}{16\pi^2\varepsilon_0 c}\left[\frac{|\mathbf{n}\times\{(\mathbf{n}-\boldsymbol{\beta})\times\dot{\boldsymbol{\beta}}\}|^2}{(1-\boldsymbol{\beta}\cdot\mathbf{n})^6 R^2}\right]_{ret} . \tag{2.91}$$

From this equation we can deduce two types of effects on the angular distribution: one is the effect of the spatial relationship between $\boldsymbol{\beta}$ and $\dot{\boldsymbol{\beta}}$; and the other effect arises from the transformation from the rest frame of the particle to the observer's frame and manifesting itself by the presence of the factors $(1-\boldsymbol{\beta}\cdot\mathbf{n})$ in the denominator. For ultra-relativistic particles, the latter effect dominates the whole angular distribution.

Since the spectrum is represented in terms of frequencies at a detector, we now consider how the radiated energy is distributed in frequency. The general form of the power radiated per unit solid angle is given by:

$$\frac{dP(t)}{d\Omega} = \frac{e^2}{16\pi^2\varepsilon_0 c}\left[\frac{|\mathbf{n}\times\{(\mathbf{n}-\boldsymbol{\beta})\times\dot{\boldsymbol{\beta}}\}|^2}{(1-\boldsymbol{\beta}\cdot\mathbf{n})^6}\right]_{ret} \equiv |\mathbf{A}(t)|^2 , \tag{2.92}$$

where for simplicity of notation we define

$$\mathbf{A}(t) = \left(\frac{e^2}{16\pi^2\varepsilon_0 c}\right)^{1/2} [R\mathbf{E_a}]_{ret} \tag{2.93}$$

$$= \left(\frac{e^2}{16\pi^2\varepsilon_0 c}\right)^{1/2} \left[\frac{|\mathbf{n}\times\{(\mathbf{n}-\boldsymbol{\beta})\times\dot{\boldsymbol{\beta}}\}|}{(1-\boldsymbol{\beta}\cdot\mathbf{n})^3}\right]_{ret} . \tag{2.94}$$

The Fourier transform $\mathbf{A}(\omega)$ of $\mathbf{A}(t)$ is:

$$\mathbf{A}(t) = \frac{1}{\sqrt{2\pi}}\int_{-\infty}^{\infty}\mathbf{A}(\omega)e^{i\omega t}dt ; \qquad \mathbf{A}(\omega) = \frac{1}{\sqrt{2\pi}}\int_{-\infty}^{\infty}\mathbf{A}(t)e^{-i\omega t}d\omega . \tag{2.95}$$

Using the Fourier integral and its complex conjugate in Eq.(2.92), the power distribution becomes:

$$\frac{dP(t)}{d\Omega} = \frac{1}{2\pi}\int_{-\infty}^{\infty}\mathbf{A}(\omega)e^{-i\omega t}\cdot\mathbf{A}^*(\omega')e^{i\omega' t}d\omega d\omega' . \tag{2.96}$$

Integrating this equation over time t gives the energy radiated per unit solid angle:

$$\frac{dW}{d\Omega} = \int_0^\infty \frac{dP(t)}{d\Omega} dt = \int_{-\infty}^\infty |\mathbf{A}(\omega)|^2 d\omega \tag{2.97}$$

$$= \int_0^\infty \left[|\mathbf{A}(\omega)|^2 + |\mathbf{A}(-\omega)|^2\right] d\omega \,. \tag{2.98}$$

Since $\mathbf{A}(t)$ is real, $\mathbf{A}^*(-\omega) = \mathbf{A}(\omega)$ and so the two terms in the integral are identical:

$$\frac{dW}{d\Omega} = 2\int_0^\infty |\mathbf{A}(\omega)|^2 d\omega \equiv \int_0^\infty \frac{dI}{d\Omega} d\omega \,. \tag{2.99}$$

The integrand $dI/d\Omega$ defines the total radiation received per unit frequency per unit solid angle during the entire pulse of radiation :

$$\frac{d^2 I}{d\Omega d\omega} = 2|\mathbf{A}(\omega)^2| \,, \tag{2.100}$$

where

$$\mathbf{A}(\omega) = \left(\frac{e^2}{32\pi^3 \varepsilon_0 c}\right)^{1/2} \int_{-\infty}^\infty \left[\frac{\mathbf{n}\times\{(\mathbf{n}-\boldsymbol{\beta}) \times \dot{\boldsymbol{\beta}}\}}{(1-\boldsymbol{\beta}\cdot\mathbf{n})^3} e^{i\omega t}\right]_{ret} dt \,. \tag{2.101}$$

In the charge reference frame, with t_{ret} being the charge proper time, the radiation power reads:

$$\frac{dP(t_{ret})}{d\Omega} = (\mathbf{S}\cdot\mathbf{n})\, R^2 \frac{dt}{dt_{ret}} \tag{2.102}$$

$$= (\mathbf{S}\cdot\mathbf{n})\, R^2 (1-\boldsymbol{\beta}\cdot\mathbf{n}) \tag{2.103}$$

$$= \frac{e^2}{16\pi^2 \varepsilon_0 c}\left[\frac{|\mathbf{n}\times\{(\mathbf{n}-\boldsymbol{\beta}) \times \dot{\boldsymbol{\beta}}\}|^2}{(1-\boldsymbol{\beta}\cdot\mathbf{n})^5 R^2}\right] \,. \tag{2.104}$$

Therefore changing the variable of integration from t to t_{ret} we get :

$$\mathbf{A}(\omega) = \left(\frac{e^2}{32\pi^3 \varepsilon_0 c}\right)^{1/2} \int_{-\infty}^\infty \left[\frac{\mathbf{n}\times\{(\mathbf{n}-\boldsymbol{\beta}) \times \dot{\boldsymbol{\beta}}\}}{(1-\boldsymbol{\beta}\cdot\mathbf{n})^2} e^{i\omega(t_{ret}-R(t_{ret})/c)}\right] dt_{ret} \,. \tag{2.105}$$

For the spectrum in the radiation zone ($r \gg r_0$), $\mathbf{n}$ is time-independent and $R(t_{ret}) \simeq r - \mathbf{n}\cdot\mathbf{r_0}(t_{ret})$, then the energy radiated by unit solid angle per unit frequency interval is:

$$\boxed{\frac{d^2 I}{d\omega d\Omega} = \frac{e^2}{16\pi^3 \varepsilon_0 c}\left|\int_{-\infty}^\infty \frac{\mathbf{n}\times\left[(\mathbf{n}-\boldsymbol{\beta}) \times \dot{\boldsymbol{\beta}}\right]}{(1-\boldsymbol{\beta}\cdot\mathbf{n})^2} e^{i\omega(t_{ret}-\mathbf{n}\cdot\mathbf{r_0}(t_{ret})/c)} dt_{ret}\right|^2} \tag{2.106}$$

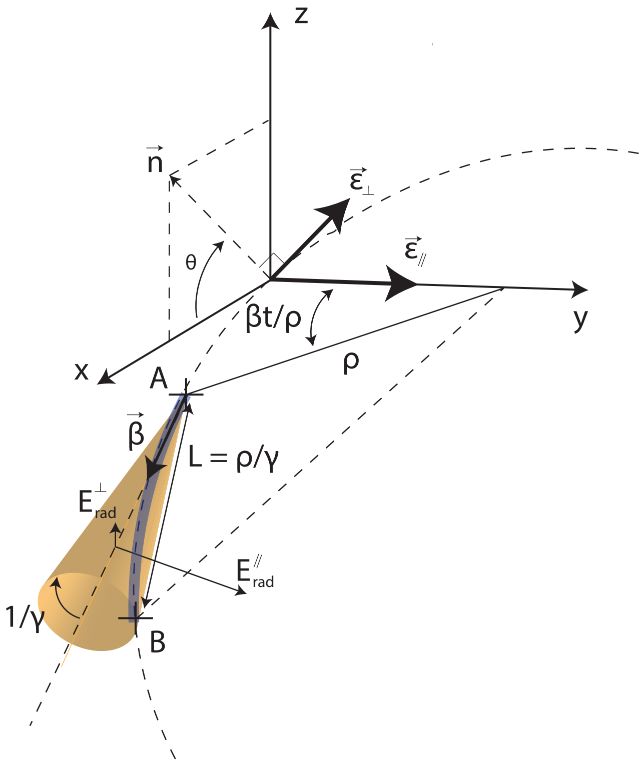

Figure 2.12: Illustration of synchrotron emission [84].

In the case of multiple particles, a sum of amplitudes $\mathbf{A}_k(\omega)$ should be done over all N_e particles with q_k, $\boldsymbol{\beta}_k$, $\mathbf{r}_k$, $\dot{\boldsymbol{\beta}}_k$ being respectively the charge, position, velocity and acceleration of the k^{th} particle: [86]:

$$\mathbf{A}(\omega) = \left(\frac{e^2}{32\pi^3\varepsilon_0 c}\right)^{1/2} \sum_{k=1}^{N_e} \int_{-\infty}^{\infty} q_k \left[\frac{\mathbf{n}\times\{(\mathbf{n}-\boldsymbol{\beta}_k)\times\dot{\boldsymbol{\beta}}_\mathbf{k}\}}{(1-\boldsymbol{\beta}_k\cdot\mathbf{n})^2} e^{i\omega(t_{ret}-\mathbf{n}\cdot\mathbf{r}_k/c)} \right] dt_{ret}\,. \tag{2.107}$$

Unfortunately, the integral in Eq. (2.106) is intractable in practice for most cases. However, it is possible to show that the amount of radiation in the transverse direction exceeds that of the parallel one by the factor of γ^2. Therefore for an ultra-relativistic particle ($\gamma \gg 1$), we can approximate the radiation as coming from a particle on an instantaneous circular path with the curvature $\rho^{-1} = 1/\dot{v}_\perp$ (see fig. 2.12). Moreover, the radiation is emitted in a cone with an opening angle γ. Therefore, for a particle radiating during propagation along a curved trajectory, an observer in a direction $\vec{n}$ will see a burst of radiation, which will not interfere with previously emitted radiation. This yields the so-called synchrotron spectrum

$$\frac{d^2 I^{sync}}{d\omega d\Omega} = \frac{e^2}{12\pi^3\varepsilon_0 c}\left(\frac{\omega\rho}{c}\right)^2 \left(\gamma^{-2}+\theta'^2\right)^2 \left[K_{2/3}^2(\xi) + \frac{\theta'^2}{\gamma^{-2}+\theta'^2}K_{1/3}^2(\xi)\right] , \tag{2.108}$$

with $K_{1/3}$ and $K_{2/3}$ being the modifies Bessel functions of the second kind, θ' the angle between $\mathbf{n}$ and $\boldsymbol{\beta}$, and

$$\xi = \frac{\omega\rho}{3c}\left(\gamma^{-2}+\theta'^2\right)^{3/2} , \tag{2.109}$$

is the normalized frequency. Since the spectrum depends only on ξ, the synchrotron spectrum has the same shape regardless of the particle's energy. The shape of this spectrum depends only on the radius of curvature ρ. Assuming that there is only a magnetic field $\mathbf{B}$, the radius of curvature would be:

$$\rho = \frac{m_e\gamma\beta^2 c}{e\left|\boldsymbol{\beta}\times\mathbf{B}\right|} . \tag{2.110}$$

Due to the properties of the modified Bessels functions, the intensity of radiation is negligible for $\xi \gg 1$. This occurs for larger opening angle: the greater the frequency, the smaller the critical angle beyond which radiation will be negligible. This shows that the radiation is mainly confined in the plane containing particle motion. Radiation can be neglected for all angles at frequencies exceeding the critical value ω_c, defined by $\xi = 1$ and $\theta' = 0$:

$$\omega_c = 3\gamma^3(c/\rho) . \tag{2.111}$$

The use of synchrotron radiation as a model of radiation is only valid for high-energy particles and particle dynamics on timescales shorter than $t \leq \beta c/\rho$.

2.3.2 Radiation Reaction

At extreme laser intensities, charged particles become ultra relativistic and experience strong acceleration. As a consequence, they will emit large amounts of electromagnetic radiation which will lead to an effective friction force on the particle. Said influence of the electron's own radiation emission onto its own motion is called radiation reaction [56] and can become essential in the ultra relativistic regime as it can strongly influence the dynamics of the radiation charges [87]. Indeed, the loss of energy and momentum during the radiation emission causes a radiation reaction force in the opposite direction of motion which can significantly modify the trajectory path of the electron. At laser intensities of $I > 10^{23}$ W/cm^2, the effect of radiation reaction prevails within a single laser period [88]. In the regime where quantum effects are negligible, radiation reaction is best described by the Landau-Lifshitz equation, which reads:

$$\frac{d\mathbf{p}}{dt} = -e(\mathbf{E} + \mathbf{v} \times \mathbf{B}) + \mathbf{F}_{\text{rad}}\,, \tag{2.112}$$

where $\mathbf{F}_{\text{rad}}$ is the radiation reaction force given by:

$$\begin{aligned}\mathbf{F}_{\text{rad}} &= e\,(\mathbf{E} + \boldsymbol{\beta} \times \mathbf{B}) + e\tau_0\,\gamma \left(\frac{d\mathbf{E}}{dt} + \boldsymbol{\beta} \times \frac{d\mathbf{B}}{dt}\right) \\ &+ \tau_0\,[(\boldsymbol{\beta} \cdot \mathbf{E})\,\mathbf{E} - \mathbf{B} \times (\mathbf{E} + \boldsymbol{\beta} \times \mathbf{B})] \\ &- \tau_0\,\gamma^2 \left[(\mathbf{E} + \boldsymbol{\beta} \times \mathbf{B})^2 - (\boldsymbol{\beta} \cdot \mathbf{E})^2\right] \boldsymbol{\beta}\,. \end{aligned} \tag{2.113}$$

where $\tau_0 = \frac{e^2}{6\pi m_e}$. In the ultra-relativistic regime, this simplifies to

$$\frac{d\mathbf{p}}{dt} = \mathbf{F}_L - \frac{2}{3}\frac{e^4\gamma}{m_e^3c^5}\mathbf{p}\left(\mathbf{E}_\perp + \frac{\mathbf{p}}{\gamma m_e c} \times \mathbf{B}\right)^2\,. \tag{2.114}$$

Quantum radiation regime

Quantum radiation effects emerge when the field strength in the emitted particle reference frame gets close to Schwinger limit. This limit is defined by the Schwinger field which is the electric field necessary to bring a work of $2m_ec^2$ over the electron Compton wavelength $\lambda_c = \hbar/m_ec$. It reads

$$E_s = \frac{m_e^2c^3}{e\hbar} \simeq 1.32 \times 10^{18}\ \text{V/m} \tag{2.115}$$

and corresponds to an intensity $I_s \simeq 10^{29}$ W/cm^2. Writing the ratio E/E_s in a Lorentz invariant way, we obtain the quantum dynamical parameter for the electron:

$$\chi = \frac{\gamma}{E_s}\sqrt{(\mathbf{E} + \mathbf{v} \times \mathbf{B})^2 - (\mathbf{v} \cdot \mathbf{E})^2/c^2}\,, \tag{2.116}$$

where $\gamma = \mathcal{E}/(m_ec^2)$. As explained, χ controls for the importance of quantum effects. For $\chi \ll 1$, the interaction between the laser and the particle is purely classical while for $\chi \gtrsim 1$, the interaction is quantum-dominated [89]. The quantum and classical descriptions agree when $\chi \ll 1$.

In the quantum regime, radiation reaction can no longer be described by a classical force. Instead, while propagating in a strong external field, a charged particle has a probability of emitting a high energy photon and experiencing stochastic recoil. This phenomenon is called nonlinear Compton scattering [90] and has a probability given by:

$$\left.\frac{d^2N_{\text{nCs}}}{dtd\gamma_\gamma}\right|_\chi(\gamma_\gamma,\gamma) = \frac{2}{3}\frac{\alpha^2}{\tau_e}\frac{\widetilde{G}(\chi,\chi_\gamma)}{\gamma\gamma_\gamma}\,, \tag{2.117}$$

where $\tau_e = r_e/c$ the time for the light to cross the classical radius of the electron, α the fine-structure constant and:

$$\widetilde{G}(\chi,\chi_\gamma) = \frac{\sqrt{3}}{2\pi}\frac{\chi_\gamma}{\chi}\left[\int_\nu^{+\infty} dy\,\mathrm{K}_{5/3}(y) + \frac{3}{2}\chi_\gamma\nu\,\mathrm{K}_{2/3}(\nu)\right]\,, \tag{2.118}$$

with $\nu = 2\chi_\gamma/[3\chi(\chi-\chi_\gamma)]$ where χ and χ_γ are respectively the quantum parameter for the electron and photon, respectively. The quantum parameter of the photon reads:

$$\chi_\gamma = \frac{\gamma_\gamma}{E_s}\sqrt{(\mathbf{E}+(\boldsymbol{c}\times\mathbf{B})^2-\boldsymbol{c}\cdot\mathbf{E})^2/c^2}\,, \tag{2.119}$$

with $\boldsymbol{c}$ the photon speed and $\gamma_\gamma = \mathcal{E}_\gamma/(m_ec^2)$ where γ is the energy of the radiating electron. Right after the emission of a photon, χ and χ_γ are related as:

$$\frac{\chi_\gamma}{\chi} = \frac{\gamma_\gamma}{\gamma}\,. \tag{2.120}$$

The instantaneous radiated power energy spectrum is then:

$$\frac{dP_{\text{inst}}}{d\gamma_\gamma} = P_\alpha\widetilde{G}(\chi,\chi_\gamma)\,, \tag{2.121}$$

with $P_\alpha = 2\alpha^2m_ec^2/(3\tau_e)$ and P_{inst} the instantaneous radiated power given by:

$$P_{\text{inst}} = P_\alpha\chi^2g(\chi)\,, \tag{2.122}$$

and $g(\chi)$ the quantum correction:

$$g(\chi) = \frac{9\sqrt{3}}{8\pi}\int_0^{+\infty} d\nu\left[\frac{2\nu^2}{(2+3\nu\chi)^2}\mathrm{K}_{5/3}(\nu) + \frac{4\nu(3\nu\chi)^2}{(2+3\nu\chi)}\mathrm{K}_{2/3}(\nu)\right]\,. \tag{2.123}$$

Chapter 3

An introduction to simulating plasmas

Contents

Numerical simulations serve to bridge the gap between theoretical studies and experimental results. Indeed, physical systems, such as plasma, are too complex to be described solely by analytical solutions. A numerical approach is therefore preferable when modeling laser-plasma interaction. Moreover, due to non-linear nature of relativistic laser induced plasma processes, the development of laser-plasma accelerators requires precise numerical modeling.

One effective and universal way to simulate such complex modeling is through the Particle-In-Cell (PIC) method, which gives the kinetic description of a plasma by coupling the Vlasov equation with the Maxwell's equations in order to study the evolution of an ensemble of particles statistically through their distribution function. In particular, we will focus on the SMILEI code (acronym for *Simulation of Matter Irradiated by Light at Extreme Intensitites*) which is a massively parallel open-source PIC code [55]. For a deeper insight into the PIC method, the reader is referred to [91, 92].

3.1 Kinetic description

The kinetic description of a collisionless plasma relies on the knowledge of the position and momentum of each particle composing the plasma. In this approach, each particle species s, charge q_s and mass m_s is defined by a distribution function $f_s(t, \mathbf{x}, \mathbf{p})$ which correlates their position $\mathbf{x}$ and momentum $\mathbf{p}$ distribution in the six dimensional phase space at time t. The distribution f_s obeys the Vlasov equation:

$$\left(\partial_t + \frac{\boldsymbol{p}}{m_s\gamma_s} \cdot \nabla + \boldsymbol{F}_L \cdot \nabla_p\right) f_s(t, \boldsymbol{x}, \boldsymbol{p}) = 0\,, \tag{3.1}$$

where $\gamma_s = \sqrt{1 + \boldsymbol{p}^2/(m_s^2 c^2)}$ is the relativistic Lorentz factor and $\mathbf{F}_L$ the Lorentz force acting on the particles:

$$\mathbf{F}_L = q_s(\mathbf{E} + \mathbf{v} \times \mathbf{B})\,. \tag{3.2}$$

In the Vlasov theory of a plasma, the fields $\mathbf{E}(t, \mathbf{x})$ and $\mathbf{B}(t, \mathbf{x})$ are obtained self-consistently via the Maxwell's equations:

$$\begin{aligned}
\nabla \cdot \boldsymbol{E} &= \rho/\epsilon_0\,, && (3.3)\\
\nabla \cdot \boldsymbol{B} &= 0\,, && (3.4)\\
\nabla \times \boldsymbol{E} &= -\partial_t \boldsymbol{B}\,, && (3.5)\\
\nabla \times \boldsymbol{B} &= \mu_0\left(\boldsymbol{J} + \epsilon_0 \partial_t \mathbf{E}\right)\,. && (3.6)
\end{aligned}$$

with ϵ_0 the vacuum dielectric permittivity and μ_0 the magnetic permeability. The source terms, the charge $\rho(t, \mathbf{x})$ and current $\mathbf{J}(t, \mathbf{r})$ densities, are given by:

$$\begin{aligned}
\rho(t, \mathbf{x}) &= \sum_s q_s n_s(t, \mathbf{x}) && (3.7)\\
\mathbf{J}(t, \mathbf{x}) &= \sum_s q_s n_s(t, \mathbf{x}) \mathbf{V}_s(t, \mathbf{x})\,, && (3.8)
\end{aligned}$$

where the sum runs over all the plasma species. The total density $n_s(t, \mathbf{x})$ in the coordinate space and mean velocity $\mathbf{V}_s(t, \mathbf{x})$ are obtained by integrating over the phase space:

$$\begin{aligned}
n_s(t, \mathbf{x}) &= \int f_s(t, \mathbf{x}, \mathbf{p})\, d\mathbf{p} && (3.9)\\
\mathbf{V}_s(t, \mathbf{x}) &= \frac{1}{n_s} \int \mathbf{v} f_s(t, \mathbf{x}, \mathbf{p})\, d\mathbf{p}\,, && (3.10)
\end{aligned}$$

with $\mathbf{v} = \mathbf{p}/(m_s\gamma)$.

3.2 Fundamental aspects of the PIC algorithm

3.2.1 Macro-particles

The PIC method consists in solving the Vlasov-Maxwell system of equations (3.1)-(3.6) by discretizating of the distribution function $f_s(t, \mathbf{x}, \mathbf{p})$ as a sum of N_s macro-particles.

$$f_\alpha(t, \boldsymbol{r}, \boldsymbol{p}) = \sum_{p=1}^{N_s} \frac{w_p}{V_c} S(\boldsymbol{x} - \boldsymbol{x}_p(t))\delta(\boldsymbol{p} - \boldsymbol{p}_p(t)) \,, \tag{3.11}$$

where V_c is the hypervolume of a cell, $S(x)$ the shape-function of the macro-particle centered in its position $\mathbf{x}_p(t)$, δ the dirac distribution and $\mathbf{x}_p$ and $\mathbf{p}_p$ are the position and momentum of the p-th particle. Each macro-particle represents a statistical sample of the plasma particles. The macro-particle weight w_p is defined as

$$w_p = V_c \frac{n_s(\boldsymbol{x}_p, t = 0)}{N_s(t = 0)} \,, \tag{3.12}$$

with n_s the specified initial density of the plasma at the p-th particle position. From Eq.(3.12) it should be noted that a larger number of particles N_s in the simulation would lead to a more accurate description of the local density variation.

By introducing Eq.(3.11) in the Vlasov Eq.(3.1), we obtain for each macro-particle its relativistic equations of motion:

$$\frac{d\boldsymbol{x}_p}{dt} = \frac{\boldsymbol{p}_p}{m_s \gamma_p} \,, \tag{3.13}$$

$$\frac{d\boldsymbol{p}_p}{dt} = \frac{q_s}{m_s}\left(\boldsymbol{E}_p + \frac{\boldsymbol{u}_p}{\gamma_p} \times \boldsymbol{B}_p\right) \,, \tag{3.14}$$

where $\mathbf{u}_p = \mathbf{p}_p/m_s$ is the reduced momentum and $\gamma_p = \sqrt{1 + \mathbf{u}_p^2}$ their corresponding Lorentz factor. In PIC codes, the Vlasov's equation is thus integrated along the continuous trajectories of these macro-particles. On the other hand, the electromagnetic fields are interpolated at the particle's position:

$$\mathbf{E}_p = \frac{1}{V_c} \int S(\mathbf{x} - \mathbf{x_p})\mathbf{E}(\mathbf{x}) d\mathbf{x} \,, \tag{3.15}$$

$$\mathbf{B}_p = \frac{1}{V_c} \int S(\mathbf{x} - \mathbf{x_p})\mathbf{B}(\mathbf{x}) d\mathbf{x} \,, \tag{3.16}$$

Whilst the electromagnetic fields are discretized onto a staggered grid, the macro-particles are free to move in all directions.

3.2.2 Time and space discretization

In Smilei , the Maxwell equations are solved using the Finite Difference Time Domain (FDTD) technique. This technique, introduced by Kane Yee in 1966 [93], solves the Maxwell equations by discretizing space and time into a structured grid called the Yee lattice where the spaces between consecutive grid points are referred to as cells. The electromagnetic fields (**E**,**B**) are evaluated at each point of the grid, the fields then evolve at discrete time steps making it possible to trace the time evolution.

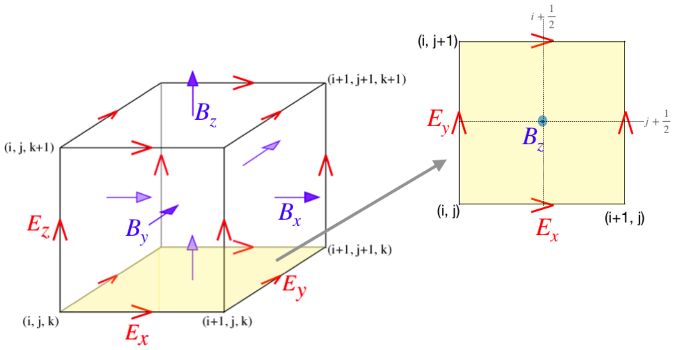

Figure 3.1: Positions of the field components in a unit cell of the Yee's lattice in a 3D staggered grid

Each point on the uniformly spaced rectangular 3D grid (see Figure 3.1) can be expressed by the coordinates:

$$(x, y, z)_{\mathrm{i,j,k}} = (i\Delta x, j\Delta y, k\Delta z)\,,$$

where i, j and k are integers and Δx, Δy and Δz are the space increments along each Cartesian axis. The computational time is similarly uniformly discretized with a Δt time step as $t = n\Delta t$ where n is an integer. An arbitrary function of space and time can be therefore be written as:

$$u(x, y, z; t) = u(i\Delta x, j\Delta y, k\Delta z; n\Delta t) = u^{\mathrm{n}}_{\mathrm{i,j,k}}\,, \tag{3.17}$$

which represents a component of the electromagnetic fields $(E_x, E_y, E_z, B_X, B_y, B_Z)$. Moreover, the temporal and spatial derivatives of these fields are approximated from their Taylor developments to the second order. As a consequence, the temporal derivative of u at a time n and point (i, j, k) is obtained by centered finite difference approximation:

$$\partial_t u\Big|_{i,j,k} = \frac{u^{\mathrm{n+1/2}}_{\mathrm{i,j,k}} - u^{\mathrm{n-1/2}}_{\mathrm{i,j,k}}}{\Delta t} + \Theta\left([\Delta t]^2\right)\,, \tag{3.18}$$

as well as the spatial derivatives of u at the same point :

$$\partial_x u\Big|_{j,k,n} = \frac{u^{\mathrm{n}}_{\mathrm{i+1/2,j,k}} - u^{\mathrm{n}}_{\mathrm{i-1/2,j,k}}}{\Delta x} + \Theta\left([\Delta x]^2\right) \tag{3.19}$$

$$\partial_y u\Big|_{i,k,n} = \frac{u^{\mathrm{n}}_{\mathrm{i,j+1/2,k}} - u^{\mathrm{n}}_{\mathrm{i,j-1/2,k}}}{\Delta y} + \Theta\left([\Delta y]^2\right) \tag{3.20}$$

$$\partial_z u\Big|_{i,j,n} = \frac{u^{\mathrm{n}}_{\mathrm{i,j,k+1/2}} - u^{\mathrm{n}}_{\mathrm{i,j,k-1/2}}}{\Delta z} + \Theta\left([\Delta z]^2\right) . \tag{3.21}$$

As illustrated in Fig. 3.1, the three components of the electric field are sampled at the center of the cube's edges whereas the magnetic field components, which are normal to each grid cell, are sampled at the center of a grid face. This way each magnetic field component is surrounded by four electric field components and conversely each electric field component in turn will be surrounded by four magnetic field components. Furthermore, the computed **E** and **B** fields are staggered with respect to each other in time and space by a half-time and half-spatial step.

For example, taking a closer look to the grid cell layout for a two-dimensional transverse electric polarization mode where **E** field is in the xy plane and **B** field in the $z-$direction.

The finite-difference Maxwell's equations for the electric field become :

$$\frac{E_x|^{n+1}_{\mathrm{i+1/2,j}} - E_x|^{n}_{\mathrm{i+1/2,j}}}{\Delta t} = c\frac{B_z|^{n+1/2}_{\mathrm{i+1/2,j+1/2}} - B_z|^{n+1/2}_{\mathrm{i+1/2,j-1/2}}}{\Delta y} - 4\pi J_x|^{n+1/2}_{\mathrm{i+1/2,j}} \, , \tag{3.22}$$

$$\frac{E_y|^{n+1}_{\mathrm{i,j+1/2}} - E_y|^{n}_{\mathrm{i,j+1/2}}}{\Delta t} = -c\frac{B_z|^{n+1/2}_{\mathrm{i+1/2,j+1/2}} - B_z|^{n+1/2}_{\mathrm{i-1/2,j+1/2}}}{\Delta x} - 4\pi J_y|^{n+1/2}_{\mathrm{i,j+1/2}} \, , \tag{3.23}$$

and the magnetic field on the other hand becomes:

$$\frac{B_z|^{\mathrm{n+1/2}}_{\mathrm{i+1/2,j+1/2}} - B_z|^{\mathrm{n-1/2}}_{\mathrm{i+1/2,j+1/2}}}{\Delta t} = -c\frac{E_y|^{n}_{\mathrm{i+1,j+1/2}} - E_y|^{\mathrm{n}}_{\mathrm{i,j+1/2}}}{\Delta x} + c\frac{E_x|^{n}_{\mathrm{i+1/2,j+1}} - E_x|^{\mathrm{n}}_{\mathrm{i+1/2,j}}}{\Delta y} . \tag{3.24}$$

The electric field **E** is calculated at time step $t = n\Delta t$ and its time evolution from n to $n+1$ is calculated using the magnetic field **B** which has been computed at a previous time step $t = \left(n + \frac{1}{2}\right)\Delta t$. Indeed, Yee's scheme employs the so called *leapfrog* algorithm, a time evolution method in which the interleaved EM fields are solved one after another in an alternating manner. The evolution of these fields in time describes the propagation of an electromagnetic wave in the considered environment.

3.2.3 Initialization

The initialization in SMILEI starts with the user defining the number of macro-particles N_s, the mean velocity $\mathbf{V}_s$, the spatial profiles for the particle density n_s and the initial temperature T_s for each species s. The code will then randomly distribute the particles positions $\mathbf{x}_p$ within each cell, where the density is non null, and randomly sample the particles momentum according to the distribution function requested by the user. Once all the particles have been created, the total charge and current densities are computed by projecting the weight and shape function of each macro particle onto the grid:

$$\rho_{total}(\boldsymbol{x}, t=0) = \sum_s \sum_p \frac{q_s w_p}{V_c} S(\boldsymbol{x} - \boldsymbol{x}_p(t=0)) \, . \tag{3.25}$$

From the initial charge and current distribution, the code computes the initial electromagnetic field as the initial electric fields is obtained by solving the Poisson equation (3.3). At the end of this initialization stage, all the macro particles are created and the fields are computed over the whole simulation grid. The algorithm can then enter the second phase of the PIC code which consists in loop which solves the Maxwell-Vlasov model over a fixed number of time-steps with duration Δt.

3.2.4 The PIC Loop

As illustrated in Figure 3.2, the PIC loop can be essentially decomposed into four main steps:

1. Interpolating the fields from the particle positions.
2. Computing the new positions and velocities of the macro-particles.
3. Projecting the new charge and current densities on the grid.
4. Computing the new electromagnetic fields on the grid.

The fields will then be interpolated once again and so on in a continuous loop. The main steps to advance from time-step n to time-step $n+1$ will be briefly presented in the following, however, for a more in depth and detailed description of each of the four main steps refer to [55, 94] or the online SMILEI documentation.

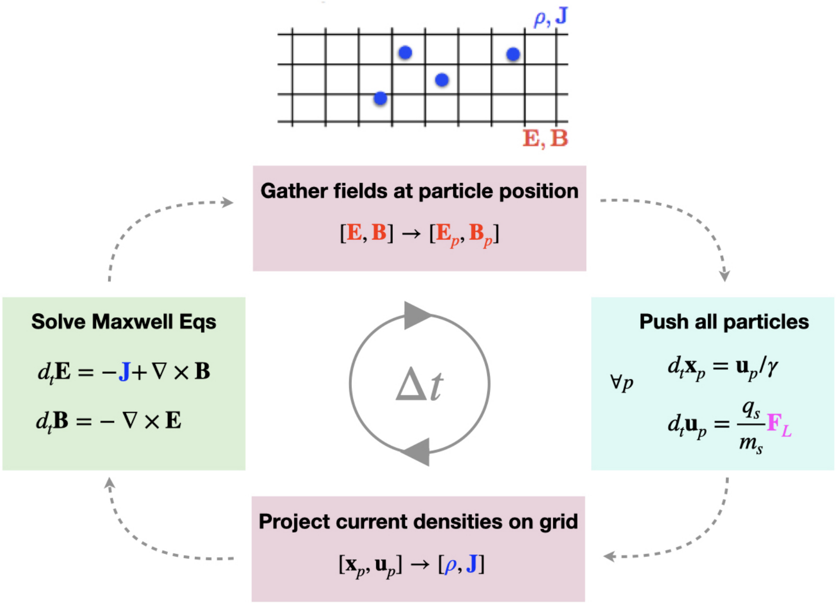

Figure 3.2: Representation of a SMILEI loop.

Step 1: Fields interpolation

As mentioned in section 3.2.2, at time-step n, the fields $\mathbf{E}^n$ and $\mathbf{B}^{(n+1/2)}$ have been calculated on the Yee grid. The particles position are defined at integer time-step n while the velocities are computed at half-integer time-step $n-1/2$. The interpolated fields at time-step n are given by

$$\boldsymbol{E}_p^{(n)} = \frac{1}{V_c}\int \mathrm{d}^3x S(\boldsymbol{x} - \boldsymbol{x}_p^{(n)})\boldsymbol{E}^{(n)}(\boldsymbol{x})\,, \tag{3.26}$$

$$\boldsymbol{B}_p^{(n)} = \frac{1}{V_c}\int \mathrm{d}^3x S(\boldsymbol{x} - \boldsymbol{x}_p^{(n)})\boldsymbol{B}^{(n)}(\boldsymbol{x})\,, \tag{3.27}$$

using the time centered magnetic field at time-step n

$$\boldsymbol{B}^{(n)} = \frac{1}{2}\left(\boldsymbol{B}^{(n-\frac{1}{2})} + \boldsymbol{B}^{(n+\frac{1}{2})}\right)\,. \tag{3.28}$$

Step 2: Particles pusher

From step 1, the new macro-particles momentum and positions can be obtained from the interpolated fields. While different particle pushers are implemented in SMILEI (such as the Boris pusher, the Vay pusher and the Higuera and Cary pusher), they all compute the new particle momentum and position according to:

$$\mathbf{u}_p^{n+\frac{1}{2}} = \mathbf{v}_p^{n-\frac{1}{2}} + \frac{q_s}{m_s}\Delta t \left[E_p^n + \frac{\mathbf{v}_p^{n+\frac{1}{2}} + \mathbf{v}_p^{n-\frac{1}{2}}}{2} \times B_p^n \right] , \tag{3.29}$$

$$\mathbf{x}_p^{n+1} = \mathbf{x}_p^n + \Delta t \frac{\mathbf{u}_p^{n+\frac{1}{2}}}{\gamma_p} , \tag{3.30}$$

with Δt denoting the duration of a time-step.

A comprehensive comparison between the different particle pushers is found in [95] where a discretized version of the above mentioned equation reads:

$$\frac{\mathbf{u}^{n+1} - \mathbf{u}^n}{\Delta t} = \frac{q_s}{m_s} \left[\mathbf{E}^{(n+\frac{1}{2})} + \overline{\mathbf{v}} \times \mathbf{B}^{(n+\frac{1}{2})} \right] . \tag{3.31}$$

where $\overline{\mathbf{v}}$ is the average velocity between two time-steps. The difference between the different approaches to advance particle positions in time lies in the treatment of this average velocity.

The Boris method

The most commonly used scheme is the Boris pusher, which is a classical, second order accurate leapfrog solver. In this method, the average velocity is:

$$\overline{\mathbf{v}} = \frac{\mathbf{u}^{n+1} + \mathbf{u}^n}{2\gamma^{n+1/2}} . \tag{3.32}$$

The Boris pusher conserves the phase space volume of the macro-particles at non-relativistic velocities. However, at relativistic velocities, the Boris method induces numerical error as it causes a change in velocity even when $\mathbf{E} + \mathbf{v} \times \mathbf{B} = \mathbf{0}$.. *The Boris particle pusher is used in the simulations performed in Chapter 4 and Chapter 5.*

The Vay method

In order to overcome the limitation of the Boris method at relativistic velocities since $\mathbf{E} \times \mathbf{B}$ velocity is not preserved, the Vay pusher [96] proposes an adaptation in the Boris algorithm. In this method, the average velocity is defined as

$$\overline{\mathbf{v}} = \frac{\mathbf{u}^n/\gamma^n + \mathbf{u}^{n+1}/\gamma^{n+1}}{2} , \tag{3.33}$$

which effectively means using an averaged velocity instead of an averaged momentum in the calculation of the magnetic field. The Vay method should therefore give more accurate results for relativistic particles. *The Vay particle pusher is used in the simulations performed in Chapter 6.*

Step 3: Current deposition

Once the particles new momentum and positions are updated, the new charge and current distribution are projected on the grid. This current deposition is calculated by a charge-conserving algorithm [97].

Step 4: Advancing electromagnetic field

In order to advance the electromagnetic field, the Maxwell-Ampère equation3.6 is solved first so as to advance the electric field on the grid:

$$\mathbf{E}^{(n+1)} = \mathbf{E}^{(n)} + \Delta t \left[(\nabla \times \mathbf{B})^{(n+1/2)} - \mathbf{J}^{(n+1/2)} \right] . \tag{3.34}$$

Then, the Maxwell-Faraday's equation (3.5) is solved to obtain the advanced magnetic field:

$$\mathbf{B}^{(n+3/2)} = \mathbf{B}^{(n+1/2)} - \Delta t (\nabla \times \mathbf{E})^{(n+1)} . \tag{3.35}$$

In the code the physical quantities are normalized as follows: the mass and momentum of each species are in units of m_e (the electron mass) and $m_e c$ respectively. In our simulations the normalization length corresponds to the laser wave length, λ_0, and the time to the laser period, λ_0/c.

3.3 Radiation treatment in Smilei

As existing and upcoming laser facilities are working on increasing the laser intensity and performing more complex experimental configurations featuring multiple laser and/or particle beams, we approach relatively unexplored, extreme plasma regimes where radiative and QED physics come into play and might affect the plasma dynamics in a nontrivial manner.

In most numerical works performed with Particle-in-cell (PIC) codes, the treatment of electromagnetic fields is dual. A schematic overview is presented in Fig.3.3 which clearly separates two peaks depending on the emitted frequency: a "coherency" peak and a "synchrotron peak".

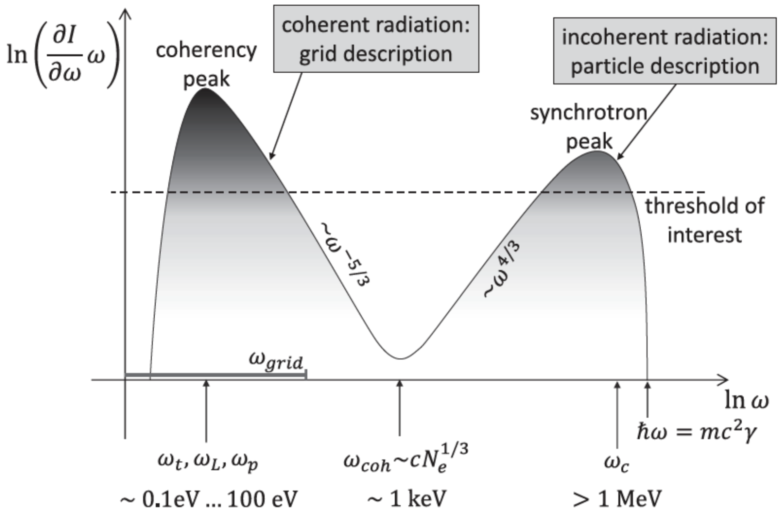

Figure 3.3: Schematic representation of the typical EM-energy deposition. Figure taken from [98].

The coherency peak is situated in the low frequency emissions where a grid based approach is used as the radiation can be directly captured on the simulation grid. However, for high frequency emissions, whose frequencies can no longer be resolved on the grid, a particle approach is used where the radiation is approximated by synchrotron emission or non-linear inverse Compton scattering depending on the importance of quantum effects. In the latter case, the radiation is considered to be purely incoherent.

The pre-existing radiation models implemented in Smilei are only valid for incoherent radiation. The difference lies in the nature of emission: either continuous or discontinuous. The use of different treatments depends on the quantum electron parameter χ (see Chapter 2.3.2) which we will recall in the following:

$$\chi = \frac{\gamma}{E_s}\sqrt{(\mathbf{E}+\mathbf{v}\times\mathbf{B})^2-(\mathbf{v}\cdot\mathbf{E})^3/c^2} \sim \gamma\frac{E}{E_s}$$

3.3.1 Classical to semi classical regime

When $\chi \ll 1$, the interaction between the laser and the particle is purely classical. We remind that the deterministic equation of motion for the electron is

$$\frac{d\mathbf{p}}{dt} = \mathbf{F}_{\mathrm{L}} + \mathbf{F}_{\mathrm{rad}}\,, \tag{3.36}$$

with

$$\mathbf{F}_{\mathrm{rad}} = -P_\alpha \chi^2 g(\chi)\mathbf{u}/(\mathbf{u}c^2)\,. \tag{3.37}$$

There are two models for computing the continuous radiation friction force. For the classical radiation emission regime ($\chi \sim 10^{-3}$), the appropriate model to use is the **Landau-Lifshitz model (LL)** which is computed by taking $g(\chi) = 1$ in Eq.3.37. In this model, the RR is seen as a continuous energy damping.

For the semi classical radiation emission regime ($\chi \sim 10^{-2}$), the RR is more accurately described by the **corrected Landau-Lifshitz model (cLL)** as the LL model can be approximated for high Lorentz factors $\gamma \gg 1$ with a minor quantum correction $g(\chi)$. In addition to the continuous nature of emission, the photons have energies much lower to the electron energies that emit them, $\gamma_\gamma \ll \gamma$.

3.3.2 Moderate to strong quantum regime

When $\chi \gg 1$, the interaction between the laser and the particle is quantum dominated.

In the moderately quantum regime ($\chi \sim 10^{-3} - 10^{-2}$), the stochastic nature of photon emission starts to kick in, however, the energy of the emitted photons is still small compared to the electron energy : $\gamma_\gamma < \gamma$ but the photon energies are no longer negligible $\gamma_\gamma \gg m_e c^2$. In this case, it is possible to model the electron dynamics using a stochastic differential equation [99]:

$$\begin{aligned} d\mathbf{p} &= -e(\mathbf{E}+\boldsymbol{\beta}\times\mathbf{H})dt - mc^2 S(\chi)\,\boldsymbol{\beta}/(c\boldsymbol{\beta}^2)dt \\ &+ mc^2\sqrt{R(\chi,\gamma)}\,dW\,\boldsymbol{\beta}/(c\boldsymbol{\beta}^2)\,. \end{aligned} \tag{3.38}$$

where dW is a Wiener process of variance dt. This is called the **Niel model**.

In the strong quantum regime ($\chi \sim 1$), electrons emit photons with an energy close to the electron energy ($\gamma_\gamma \sim \gamma$). In this case, the emission can no longer be modelled with neither the Landau-Lifshitz equation, nor the previous stochastic differential equation. Instead, we use the **Monte-Carlo (MC)** procedure to sample from the nonlinear Compton scattering probability distribution given in Eq. (2.117):

$$\left.\frac{d^2N_{\mathrm{nCs}}}{dtd\gamma_\gamma}\right|_\chi (\gamma_\gamma, \gamma) = \frac{2}{3}\frac{\alpha^2}{\tau_e}\frac{\widetilde{G}(\chi, \chi_\gamma)}{\gamma\gamma_\gamma}\,, \tag{3.39}$$

with $\widetilde{G}(\chi, \chi_\gamma)$ the quantum emissivity detailed in Chapter 2.3.1. Lets define the variable $\xi' = \chi_\gamma/\chi = \gamma_\gamma/\gamma$. The rate of photon emission can be obtained by integrating Eq. (3.39) over all possible values of γ_γ, i.e. $\xi' = 0$ to 1 :

$$\frac{dN_{nCS}}{dt} \equiv \frac{2\alpha m_e c^2}{3\hbar}\frac{c_0(\chi)}{\gamma}\,, \tag{3.40}$$

where the term c_0 is obtained by integrating by parts the quantum emissivity (see Eq. (2.118)):

$$c_0(\chi) = \frac{\sqrt{3}}{2\pi}\int_0^1 \frac{d\xi'}{1-\xi'}\left[\nu K_{5/3}(\nu) + {\xi'}^2 K_{2/3}(\nu)\right]\,, \tag{3.41}$$

with $\nu = 2\chi_\gamma/[3\chi(\chi - \chi_\gamma)]$. In the Monte-Carlo model, the probability for photon emission to occur in a non elastic event is given by:

$$\mathcal{P} = 1 - \exp\Big(-\frac{dN_{nCS}}{dt}T\Big)\,, \tag{3.42}$$

where T is the time of interaction between particles. The energy of the emitted photon is computed as:

$$\mathcal{E}_\gamma = m_e c^2\gamma\chi_\gamma/\chi\,, \tag{3.43}$$

and the electron momentum directly after emission is then updated in the pusher using momentum conservation and considering forward emission:

$$d\mathbf{p} = -\frac{\mathcal{E}_\gamma}{c}\frac{\mathbf{p}}{\|\mathbf{p}\|}\,, \tag{3.44}$$

which is valid when $\gamma \gg 1$. The resulting force takes into account the recoil experienced by the electron which is induced by the photon emission. As such, the radiation reaction in the MC description is a discrete process. Nevertheless, it is important to note that this implementation does not conserve energy, though the error on energy decreases with increasing electron energy and becomes small for ultra relativistic electrons. Also, in between emission events, the electron dynamics is still governed by the Lorentz force and its momentum updated using the Boris (or Vay) approach.

Finally, the high energy photons obtained from Eq.(3.40) can in turn transform into an electron-positron pair in the high intensity external field. This is the multiphoton Breit-Wheeler pair creation process. However this phenomena is not relevant for this work. The interested reader in a complete overview of the Monte Carlo module implemented in SMILEI is referred to [100].

3.4 Towards Coherent Radiation treatment

As mentioned in section 3.3, a problem in most PIC codes is that they only capture the radiation whose wavelength is resolved by the grid. As depicted in Figure 3.3, the coherency peak and synchrotron peak are well separated yet the coherent radiation is still not well described above a certain energy threshold. In the intermediate regime where the emitted radiation frequencies lie in between the limits of the grid and the particle approach, the coherent radiation that is not accounted for can drastically change the spectral data at lower frequencies which could give an overestimation of the energy emitted at high frequencies. This problem arises when studying laser-plasma interaction at the intermediate laser regime where photons are emitted at low energies and the duration of emission is smaller in comparison with the time it takes for the fields to change. In this case, the probability of photon emission depends on the trajectory of the electron. The low frequency photons have longer wavelengths and take more time to form as the formation of photons no longer depend on the instantaneous values of the electrons. Furthermore, the frequencies are no longer valid in the CFL approximation leading to coherent effects during emission. Another issue is that besides the temporal coherence, the correlation between the distance separating two electrons and the wavelength of the photon formation becomes non negligible. In order to capture this radiation in PIC codes one could for example increase the resolution but this comes at a great computational cost. The goal is therefore obtain the spectral data beyond the resolution limit imposed by the grid resolution of the simulation.

The interest of capturing coherent radiation in PIC codes has been steadily growing in the community with diagnostics already implemented in PIConGPU [101] and in OSIRIS [102]. In PIConGPU, they introduced a form factor formalism that permits to determine the radiation of discrete electron distributions in order to compute coherent and incoherent radiation self-consistently [103]. The OSIRIS code has two different implementations to obtain the coherent radiation: a post-process tool which saves the particle trajectories so as to determine the energy and spectrum of the radiation emitted by these particles [104]; and more recent, a run-time diagnostic that uses the simulation data at each time step to compute the radiation [105]. Inspired by the method featured in [103], we propose the implementation of a diagnostic, based on the Lienard Wiechert potentials (see Chap.2.3.1) complementing the pre-existing radiation modules SMILEI .

3.4.1 Radiation from orbits in a test particle python code

As a first approach we developed a test particle code in python where we treat one single electron (the code is given in Appendix C). Lets assume the trajectory of a relativistic electron as showcased in Figure 3.4, the electron emits radiation at time t and is detected at $t_{ret} = t_{sim} + R/c$ by the detector.

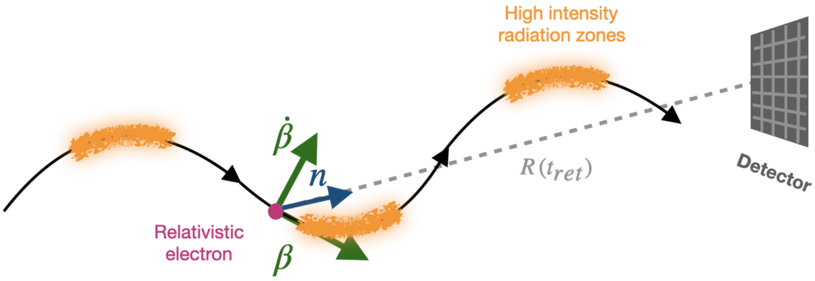

Figure 3.4

For a detector far away, the EM fields associated to the radiation emitted by this accelerated electron can be described by the Liénard-Wiechert potentials as:

$$\mathbf{E}(\mathbf{r},t) = \frac{e}{4\pi\varepsilon_0 c}\left[\frac{\mathbf{n}\times\{(\mathbf{n}-\boldsymbol{\beta})\times\dot{\boldsymbol{\beta}}\}}{(1-\boldsymbol{\beta}\cdot\mathbf{n})^3 R}\right]_{ret} \quad \text{and} \quad \mathbf{B}(\mathbf{r},t) = \frac{1}{c}\left[\mathbf{n}\times\mathbf{E}\right]_{ret}. \tag{3.45}$$

The energy radiated per unit solid angle per unit angular frequency is:

$$\frac{d^2 I}{d\Omega d\omega} = \frac{e^2}{16\pi^3\varepsilon_0 c}\left|\int_{-\infty}^{+\infty}\left[R\mathbf{E}\cdot e^{i\omega t}\right]_{ret} dt\right|^2 . \tag{3.46}$$

In the following, two methods for solving this equation numerically will be presented.

Method 1: post-processing the particle trajectory.

In this method, the emitted radiation is calculated from the electron's position and momentum.

1.- In a first step, we compute the electric field on the detector from the electron's trajectory. This essentially corresponds to calculating $A(t)$ (Eq.(2.92) in Chapter 2.3.1) at the time of the detector:

$$\mathbf{A}(t) = \left(\frac{e^2}{16\pi^2\varepsilon_0 c}\right)^{1/2}\left[\frac{|\mathbf{n}\times\{(\mathbf{n}-\boldsymbol{\beta})\times\dot{\boldsymbol{\beta}}|}{(1-\boldsymbol{\beta}\cdot\mathbf{n})^3}\right]_{ret} .$$

As the electron's momentum is known, we can calculate $\mathbf{E}$ using

$$\boldsymbol{\beta} = \mathbf{u}_p/\gamma \quad \text{and} \quad \dot{\boldsymbol{\beta}} = \frac{1}{\gamma}\dot{\mathbf{u}}_p - \frac{1}{\gamma^2}\mathbf{u}_p\dot{\gamma}\,, \tag{3.47}$$

where the derivatives are obtained by dividing the discrete difference by the timestep dt. The unit vector $\mathbf{n}$ is given by subtracting the electron's known position from the fixed pre-determined position of the detector.

2.-The tricky part is how to overcome the hurdle of the time retardation. Indeed, the fields emitted by each particle will arrive on the detector in the lab frame. However, even if two particles emit at the same time, the lab time differential between two events of emission is not constant and thus the field on the detector is not uniformely spaced. Therefore, we can not sum together the fields from the different electrons using a common time sequence nor effectuate a Fourier transform of the temporal function of the field. One solution is to calculate the retarded time for each point and then perform a high rate interpolating of the field on the grid points of the detector. As a consequence we obtain the radiated energy per unit solid angle at the electron's time of emission $\mathbf{A}(t_{ret})$.

3.- Once we have $\mathbf{A}(t_{ret})$, we perform a fast Fourier Transformation over the whole trajectory. $FFT[\mathbf{A}(t_{ret})]$ from which we obtain the $\mathbf{A}(\omega)$ (see Chapter 2.3.1).

4.- The square modulus of $A(\omega)$ gives the energy as

$$\frac{d^2 I}{d\Omega d\omega} = 2|\mathbf{A}(\omega)|^2\,.$$

The downside of this method is that one would have to store the electrons trajectory which can be very computational costly in terms of memory requirements.

Method 2: computing the far field radiation directly for each timestep.

This method, which is the one that ultimately has been implemented in SMILEI, avoids the storage of the trajectories. Indeed, in this method, we directly calculate the $A(t)e^{i\omega(t_{sim}+R/c)}$ arriving at the detector at the retarded time at each time step. The spectrum is then obtained by plotting the square module of the sum of the field at the detector over the range of frequencies over which the particle radiates.

Example : Electron initially at rest.

Let us assume an elliptically polarized plane wave travelling in the +x direction. The EM fields are written as following:

Electric field: Magnetic field:

$$\begin{cases} E_x &= 0 \\ E_y &= a_0 \delta \sin\phi \\ E_z &= -a_0\sqrt{1-\delta^2}\cos\phi \end{cases} \qquad \begin{cases} B_x &= 0 \\ B_y &= -E_z \\ B_z &= E_y \end{cases} \tag{3.48}$$

where a_0 is the laser strength, δ the laser polarization where $\delta = \pm 1, 0$ renders a linear polarization while $\delta = \pm 1./\sqrt{2}$ a circularly polarization, and $\phi = t - x + \varphi$ with φ a constant phase angle.

The virtual detector position is determined as

$$X_d = R\cos\theta_d \sin\phi_d$$
$$Y_d = R\sin\theta_d \sin\phi_d$$
$$Z_d = R\cos\phi_d$$

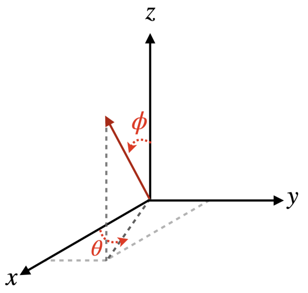

We consider a linearly polarized plane wave propagating in $+x$-direction and polarized in z. The detector is placed along z ($\theta_d = \pi/2$ and $\phi_d = 0$). As shown in Figure 3.5 of the radiated intensity as a function of ω observed at the detector for one electron, both methods (with red representing the outcome of method one and blue of method two) overlap and predict that the radiation is in the xz plane with no emission in $\hat{\mathbf{y}}$.

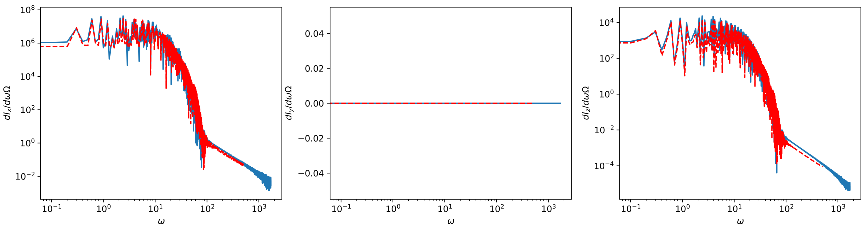

Figure 3.5: The energy radiated per unit solid angle per unit angular frequency as a function of frequency for method 1 (red line) and method 2 (blue line) for $a_0 = 3$.

3.4.2 Implementation in Smilei of in situ radiation calculation

In this section we show the first steps that have been taken for the implementation of an in situ coherent radiation treatment in Smilei which consists in calculating:

$$\frac{d^2I}{d\omega d\Omega} = \frac{e^2\Delta t}{16\pi^3\varepsilon_0 c}\left|\sum_{k=0}^{N_t}\sum_{p=1}^{N_p}\underbrace{\frac{\mathbf{n}\times\left[(\mathbf{n}-\boldsymbol{\beta}_{k,p})\times\dot{\boldsymbol{\beta}}_{k,p}\right]}{(1-\boldsymbol{\beta}_{k,p}\cdot\mathbf{n})^2}}_{\mathbf{A}(t)} e^{i\omega\cdot t_{det}}\right|^2, \tag{3.49}$$

with $t_{det} = \Delta t \times t_{sim} + R_{det}/c$ the time at the detector where t_{sim} is the simulation time and Δt the time resolution. Moreover, $\beta_{k,p}$ and $\dot{\beta}_{k,p}$ respectively the velocity and acceleration of the particle p at time $t = \Delta t \times k$. The integral over time in Eq.2.106 in Chapter 2.3.1 becomes a sum over all macro particles N_p and all sampled times N_t with timestep Δt.

We remind that for each macro particle, the Smilei code saves seven `double`, i.e. their positions (x, y,z), momenta (u_x, u_y, u_z) and their particle weight (w_p). These values are overwritten at each timestep. In order to solve Eq. (3.49) we need β and $\dot{\beta}$ for which we need to save three additional `double` saving the momentum at the previous timestep (see Eq.(3.47)). For each particle species we have a boolean that if true, will save the old momentum for each macro-particle of the selected species. The motion of these selected macro-particles is then calculated by the pusher. For each macro-particle with `bool=True`, the formula for $\mathbf{A}(t)$ will be calculated at each timestep. The radiation contribution is added to the global memory of the simulation. Since the fields are calculated independently from the pusher, the pusher is not modified and therefore this implementation is compatible with all the pusher methods available in Smilei .

In the input file, the user defines the frequency range over which they expect the particle to radiate:

```
nw = 1024
w_crit = 3./2.*gamma**4/np.sqrt(gamma**2-1)
f_max = 10.*w_crit
f_min = 0.1*w_crit
```

with *nw* the number of points. The user also defines the position of the virtual detector. The detector's geometry can be changed.

```
theta_det       = pi/4.
```

```
phi_det        = -pi/2
distance_det   = 1.e3
Xd          = distance_det*np.cos(theta_det)*np.sin(phi_det)
Yd          = distance_det*np.sin(theta_det)*np.sin(phi_det)
Zd          = distance_det*np.cos(phi_det)
```

The radiation model, provisionally named "diag-LW-radiation" is defined in the species block:

```
Species(
    name = 'electron',
  ...
    radiation_model = "diag-LW-radiation" ,
)
```

In order to add the new radiation diagnostic, the block *DiagNewRadiation* must be included:

```
DiagNewRadiation(
    species = ["electron"],
    detector_position = [Xd,Yd,Zd],
    radiation_frequency_extreme = [f_min,f_max,nw]
)
```

For a simple example, we considered an electron in a constant magnetic field. In Figure 3.6 we compared the trajectory (a) and $d^2I/(d\omega d\Omega)$ spectrum in each direction (b) for the outcome of the test particle code (blue) and the SMILEI simulation (red). Both figures overlap and reassures us that the implementation is not giving erroneous results for a simple case.

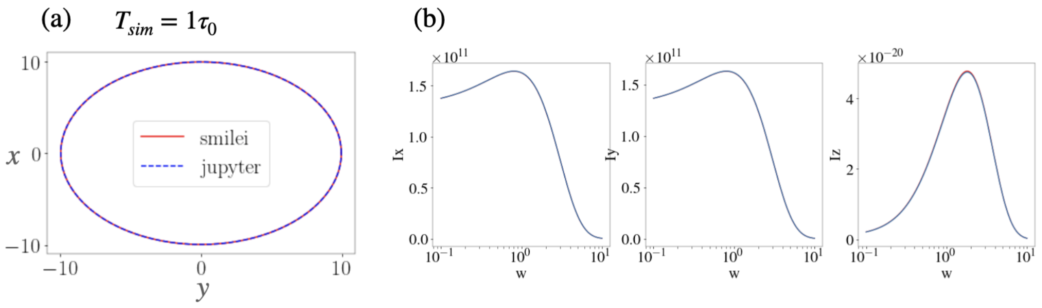

Figure 3.6: (a) Trajectory of a single electron in a constant magnetic field (b) the energy radiated per unit solid angle per unit angular frequency as a function of frequency obtained from SMILEI (red line) and the test particle code (blue line).

3.5 Summary

In this chapter, we have presented briefly the Smilei PIC code, the existing radiation models and the implementation of the coherent radiation model. This implementation is still in the benchmark phase and needs to be further worked on.

Figure 3.7: Even the fictional sidekick of Zerocalcare codes with Smilei .

Chapter 4

Exploiting SPW to obtain short electron bunches

Contents

In order to study the behaviour of Surface Plasma Waves (SPW) in the ultra-relativistic regime, it is useful to understand beforehand how they behave both in the non relativistic and in the relativistic regime.

This chapter initially provides an insight on how to optimize the grating with the aim of improving the laser-plasma coupling, and thus enhancing SPW excitation. Combining said improved grating with a laser possessing Wave Front Rotation (WFR) constitutes the main principle behind the novel scheme for tuning SPW and generating short electron bunches. The subsequent sections discuss the implications of this scheme.

4.1 Optimization of the target for SPW acceleration

Laser pulse parameters have been shown to influence SPW generation [44,66]. However, both the efficient excitation and propagation of SPW strongly depend on the grating and surface properties. Indeed, as mentioned in Chap. 2.2.1, gratings are particularly important for ensuring laser-plasma coupling.

4.1.1 Interaction set-up

Throughout this work, we performed 2D3V PIC simulations using the code presented in the previous chapter, SMILEI. The choice of performing 2D3V simulations is dictated by the physical system as the matching condition for the grating coupling scheme (see Chap. 2.2.1) determines the SPW wave vector, k_{SPW}, which is perpendicular to the grooves on the target surface. The SPW will therefore propagate in a well defined direction. Moreover, 3D simulations performed in preceding work [42] showed minor differences with respect to 2D simulations but are numerically much more expensive which prohibit parametric studies. The use of 2D3V are therefore appropriate to investigate the basics of SPW generation, electron acceleration and interpretation of experiments.

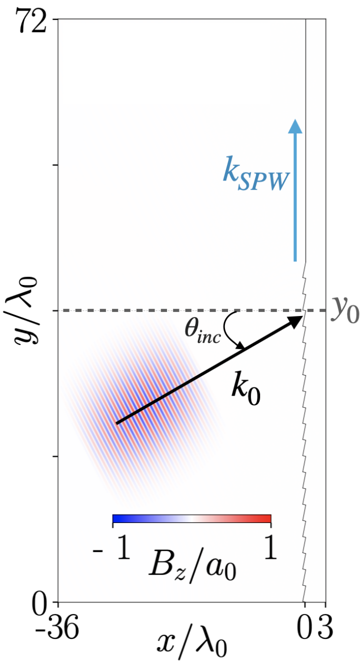

Figure 4.1: Simulation set-up

Parameter	Values
Box size	$39\lambda_0 \times 72\lambda_0$
$\Delta_{x,y}$ Spatial resolution	$\lambda_0/128$
Δ_t Time resolution	$0.95\Delta_{x,y}/\sqrt{2}$
a_0 Laser strength	0.1, 5.
θ_{inc} Incident angle	30°
τ_L Pulse duration	$10\lambda_0/c$
$w_\perp$ Waist	$5.2\lambda_0$
λ_0 Laser wavelength	$0.8\mu m$
n_0 Plasma density	$20n_c$, $100n_c$
m_i/m_e Mass ratio	1836
T_i/T_e Temperature ratio	0.1
T_e Electron temperature	50 eV
Particles per cell	16 electrons/ions

Table 4.1: Main parameters

The interaction set-up is depicted in Figure 4.1 where a laser pulse impinges onto an overdense plasma with density $n_0 \gg n_c$. The simulation box is $39\lambda_0 \times 72\lambda_0$ (in the x-y directions) where the plasma lies in the (x, y) plane for $x \geq 0$ while the vacuum is defined for $x < 0$. Here, the laser pulse impinges the plasma interface through an angle θ_{inc} in relation to the normal surface along the $x-$direction. In this figure, the plasma interface consists of a partially engraved target followed by a flat surface. The description of this mixed grating will be explained in detail in section 4.1.3.

The spatial resolution is set to $\Delta x = \Delta y = \lambda_0/128$ $(= 0.00625\mu\text{m})$, while the temporal resolution is $\Delta t = 0.95\ \Delta x/\sqrt{2}$ so as to satisfy 95% of the Courant– Friedrich– Lewy (CFL) condition for the standard finite-difference time-domain (FDTD) solver [106]. Every simulation cell contains initially 16 randomly distributed particles of each species (electrons and ions). The electromagnetic field boundary conditions are injecting/absorbing in x and periodic in y. The particle boundary conditions in x are reflecting (left) or thermalizing (right), and periodic in y.

The driven laser pulse is a $P-$polarized Gaussian pulse with a waist equal to $w_\perp = 5.2\lambda_0$ $(= 4\mu\text{m})$ and a pulse duration equal to $\tau_L = 10\lambda_0/c$ $(\simeq 27fs)$ [full-width-at-half-maximum (FHWM) in intensity]. The laser transverse profile is Gaussian, $F(y') = \exp(-y'^2/w_\perp^2)$ and its time profile is $\cos^2$: $f(t) = \cos(\pi t/(2\tau_L))$ for $|t| < \tau_L$ and 0 otherwise.

The grating target, of thickness $3\lambda_0$, has an ion to electron mass ratio $m_i/(m_e) = 1836$ and temperature ratio $T_i/(T_e) = 0.1$ with $T_e = 50$eV. It is important to note that when increasing a_0, a higher plasma density should be considered. In our case, for a laser beam with frequency $\lambda_0 = 0.8\mu$m, the plasma critical density is equal to $n_c = 1.5 \times 10^{27} m^{-3}$, meaning that $n_c = 1.5 \times 10^{27}$ electrons m^{-3}. Assuming higher ionization, the density would easily reach values of $n_0 = 100 n_c$ and more. Our chosen values are typical in simulations and experiments on SPW. For example, Refs. [42] and [43] use $n_0 = 50 n_c$ for $a_0 = 5$, while Ref. [45] assumes 4 times ionized gold which corresponds to $n_0 = 139 n_{cr}$. The main simulation parameters are recalled in Table 4.1.

Another advantage of increasing plasma density is that it also increases the SPW phase velocity. From the amplitude of the fields:

$$|B_z| = B_{spw} \,, \tag{4.1}$$

$$|E_y| = \frac{B_{spw}}{v_\phi} \,, \tag{4.2}$$

$$|E_x| = B_{spw} \left(\sqrt{\frac{1}{v_\phi^2} - 1} \right) \,. \tag{4.3}$$

From the ratio of the fields whose relation can be given as

$$\frac{B_z}{E_y} = \frac{B_{spw}}{B_{spw}} v_\phi \tag{4.4}$$

$$\frac{B_z}{E_x} = \frac{B_{spw}}{B_{spw}} \frac{1}{\sqrt{1/v_\phi^2 - 1}} \,, . \tag{4.5}$$

we can evaluate v_ϕ through the ratio B_z/E_x which gives:

$$v_\phi = \frac{B_z/E_x}{\sqrt{1 + (B_z/E_x)^2}} \,. \tag{4.6}$$

For $a_0 \ll 1$ we have:

$$\frac{B_z}{E_y} = \sqrt{\frac{2/\eta - 1}{1/\eta - 1}} \,, \tag{4.7}$$

$$\frac{B_z}{E_x} = \sqrt{\eta} \,, \tag{4.8}$$

with $\eta = n_0/n_c$. Measuring the B_z/E_x ratio for different simulations with $a_0 = 0.1$ where we have increased the plasma density, we compared the phase velocity resulting from this ratio (black triangles) to the theoretical prediction of v_ϕ (solid blue line) in the following figure:

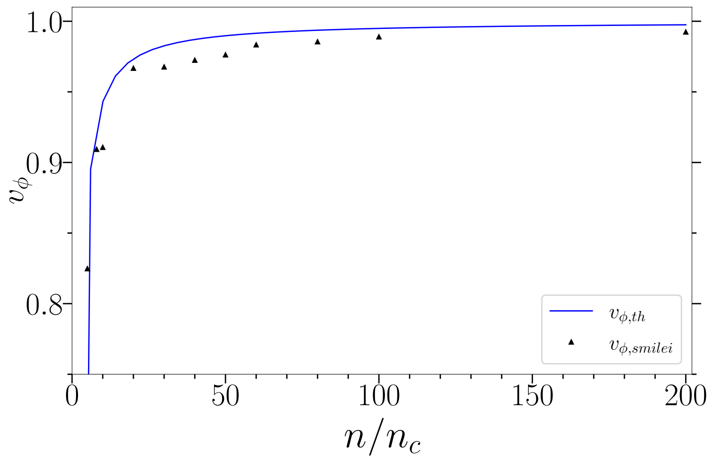

Figure 4.2: Phase velocity as a function of the density n_0/n_c. The solid blue line represents the theoretical prediction of v_ϕ while the black triangles are the v_ϕ obtained via SMILEI simulations for $a_0 = 0.1$

We remind that in order to resonantly excite a SPW at the vacuum-plasma interface using a grating coupling scheme, θ_{inc} is chosen such that:

$$\sin\theta_{inc} = \sqrt{\frac{(n_0/n_c - 1)}{n_0/n_c - 2}} - \frac{\lambda_0}{d} \, ,$$

with d the target periodicity. The resulting SPW is excited at the laser frequency $\omega = \omega_0$, and satisfies the dispersion relation, as given by the non-relativistic cold-fluid model [23]:

$$\frac{c^2 {k_{\text{SPW}}}^2}{\omega^2} = \frac{\omega_p^2/\omega^2 - 1}{\omega_p^2/\omega^2 - 2} \, ,$$

where $\omega_p = \sqrt{e^2 n/(\epsilon_0 m_e)}$ is the electron plasma frequency. Moreover, note that for $n_0 \gg n_c$, the SPW phase and group velocities are slightly subluminal:

$$v_\phi \to c\left[1 - \frac{n_c}{2n_0}\right] \qquad \text{and} \qquad v_g \to c\left[1 - \frac{3n_c}{2n_0}\right] \, ,$$

which makes SPW optimal for electron acceleration.

4.1.2 Adoption of a blazed grating

The grating profile shape plays an important role in the efficiency of the laser-plasma coupling. As a matter of fact we have found, through a previous extensive numerical study of the effect of the target profile on the SPW excitation [107], that the best coupling is obtained for a blazed grating, as also suggested experimentally in [43].

With the aim of determining the efficiency of the blazed grating on laser-plasma coupling, several 2D3V PIC simulations were performed using a laser pulse with $\theta_{inc} = 30°$, impinging onto a solid target, $n_0 = 20n_c$, with varying blazed angles, ϕ_b, ranging from 0° to 30°. A laser intensity of $a_0 = 0.1$ was taken so as to neglect relativistic non linearities. In order to quantify the maximum intensity of SPW, we take the z-component of the magnetic field, noted B_{SPW} or $\hat{B}_{\text{SPW}} = eB_{\text{SPW}}/(m_e\omega_0)$, as representative of the SPW as all the other field components are proportional to it. Indeed, as mentioned in Chap. 2.2.1, when considering a target with $n_0 \gg n_c$, the linear approximation in the vacuum side yields

$$|E_x| \sim c|B_{\text{SPW}}| \qquad \text{and} \qquad |E_y| \sim c|B_{\text{SPW}}|\sqrt{n_c/n_0}\,.$$

The results are shown in Fig. 4.3 where the maximum intensity of B_{SPW} is obtained for a blazed angle of $\phi_b = 13°$. Unless specified otherwise, all values are taken near the end of the simulation, *e.g.* circa 20 cycles after the maximum of the laser has reached the target.

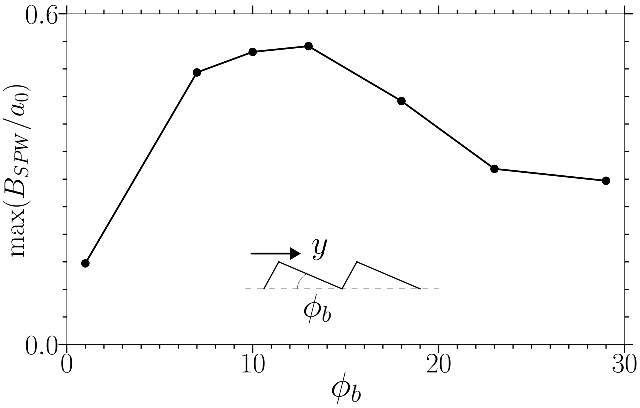

Figure 4.3: SPW intensity as a function of the blazed angle.

This numerical result is coherent with the results in [43] where they observed an increase of up to 30% in the electron beam energy when comparing the results obtained using a blazed target with a blazed angle $\phi_b = 13°$ to those with a sinusoidal grating. Furthermore, note that this particular blazed angle of $\phi_b = 13°$ corresponds to the Littrow ideal configuration for a laser focusing on the target with an incident angle $\theta_i = 30°$ with respect to the normal surface (see Eq. 2.61). Therefore, to optimize the SPW generation, blazed gratings with $\phi_b = 13°$ were adopted for the following simulations.

4.1.3 Mixed target profile

While gratings are primordial for SPW excitation, an additional improvement on the interaction setup was made in an effort to enhance SPW propagation. The proposed structure consists in using a mixed grating composed of a partially engraved target followed by a flat surface. For the modulated grating we use the aforementioned result of a grating with a blazed angle $\phi_b = 13°$, a groove's depth $h = 0.44\lambda_0$ and with a periodicity of $d = 2\lambda_0$. In order to prove the superiority of said set-up, a systematic comparison of 2D3V PIC simulations with different modulated targets have been carried out.

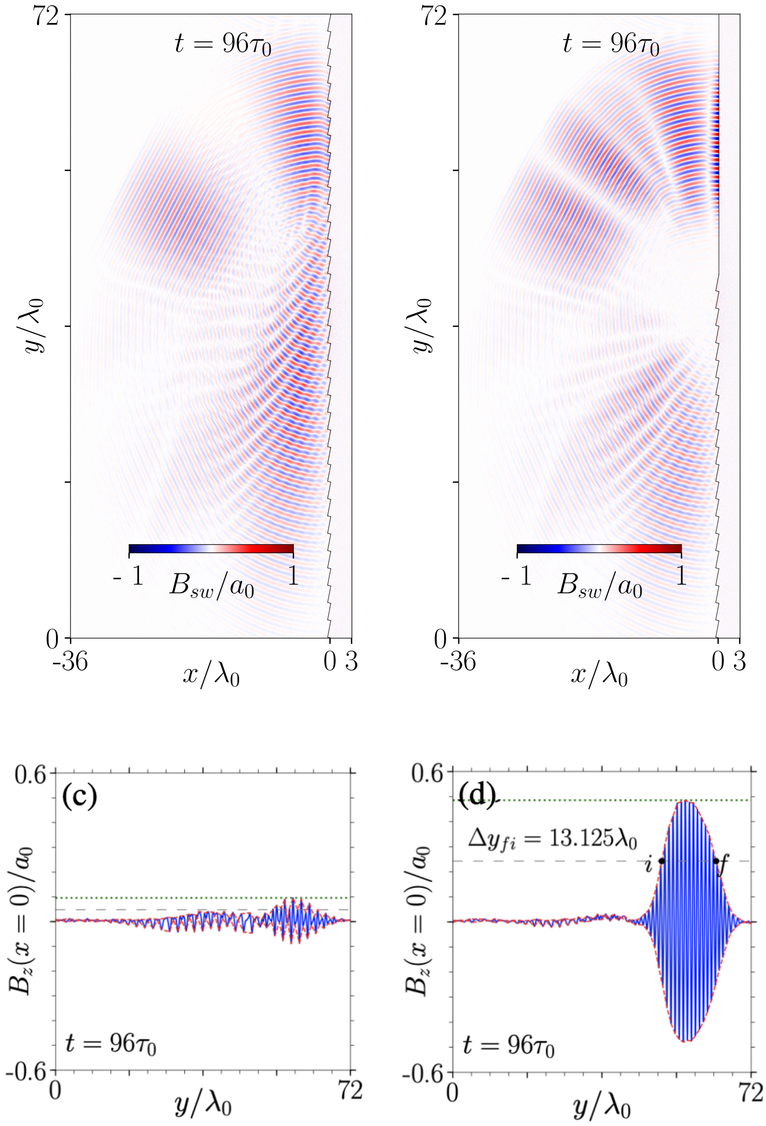

Figure 4.4: The upper panels show the dispersion of the magnetic field for the (a) fully modulated target and (b) mixed grating. The bottom panels (c) and (d) depict a snapshot of SPW magnetic field at the target surface for (a) and (b) respectively. All values are taken at $t = 96\tau_0$ for $a_0 = 0.1$.

A comparison between two of such targets with density $n_0 = 100n_c$ is presented in Fig. 4.4 where the upper row shows the magnetic field dispersion taken at the end of the simulation for (a) a fully modulated blazed target and (b) the mixed grating. Here, the red-blue scale represents the normalized magnetic field amplitude of the laser pulse impinging over the target. The comparison between these two targets suggests that the use of this mixed surface grating allows a better propagation of the SPW along the flat surface as it efficiently mitigates the radiation losses due to scattering of the SPW off the grooves when moving further away from the region where the laser-plasma interaction occurs. Further proof of the mixed grating effectiveness is corroborated by comparing the SPW magnetic field, B_{SPW}/a_0, along the target surface as depicted in the bottom row of Fig. 4.4 for the case with (c) a fully modulated blazed target and (d) the mixed target. In the latter case, Fig. 4.4 (d), the SPW peak amplitude is increased five folds with respect to the fully modulated target case, Fig. 4.4 (c), where a weak signal is observed as the SPW has been dissipated.

Additional simulations reported in Fig. 4.5 for two different laser strengths show that the presence of grooves are only necessary in the laser-irradiated spots. Given that we consider a laser pulse with a waist of $W = 5.2\lambda_0$ (FWHM), the pulse will illuminate the plasma region over a length equal to $\approx 12\lambda_0$, which is equivalent to illuminating 6 ripples as $d = 2\lambda_0$. Lets define $N_{ripples} = 0$ as the number of ripples on the grating at the position where the laser central point reaches the surface of the plasma y_0 (see Fig.4.1). Adding or subtracting ripples from the center will change the topology of the illuminated region and subsequently modify the SPW excitation. As such, $N_{ripples} = -3$ implies that the laser mainly irradiates a flat target whereas $N_{ripples} = 3$ or more implies that gratings will be covering the region illuminated by the laser.

As a first step, we continue to consider $a_0 = 0.1$ and collect in Fig. 4.5(a) the maximum magnetic field over the surface B_{SPW}/a_0 of the excited SPW as a function of the number of ripples in this weakly non linear regime. In the case where only an evanescent signal from the laser pulse illuminates the gratings, $N_{ripples} < -3$, a very weak signal of SPW is noticeable. However, a gradual increase in the SPW signal is observed when adding ripples to the surface until $N_{ripples} = 4$, after which B_{SPW} decreases. The maximum efficiency is thus found for the case where an extra ripple is added after the region where the laser-plasma coupling occurs. Note that adding a ripple after this optimal configuration leads to a reduction of circa 15% of the excited SPW's B_{SPW}

for each additional groove. This reduction can be attributed to the fact that the SPW becomes radiative as a consequence of scattering when propagating along the ripples which leads to a decrease in energy due to radiation losses and wave damping. It is worthy to mention that the amount reduced for each additional ripple depends on the target's shape. These results suggest that in the optimal configuration, to excite SPW in the linear regime, a flat surface follows the grating so that the laser illuminates only the number of ripples corresponding to the projected pulse waist onto the surface.

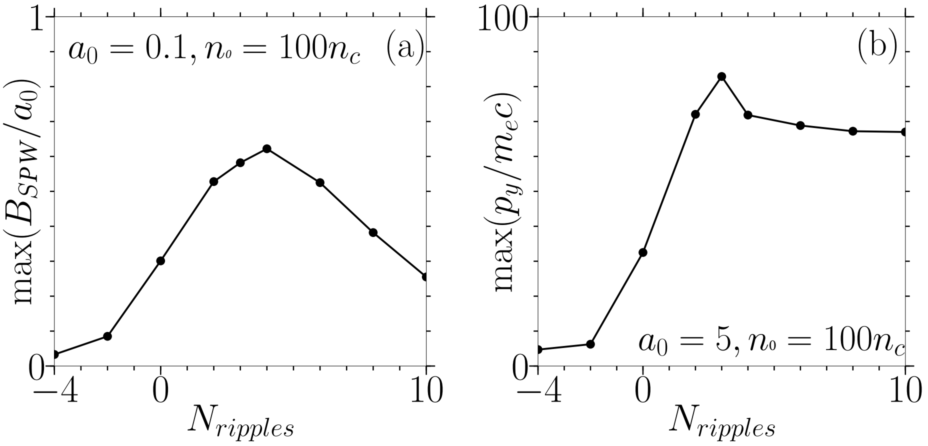

Figure 4.5: (a) Maximum B_{SPW} for $a_0 = 0.1$ and (b) maximum electron momentum for $a_0 = 5$ as a function of the number of ripples starting from the y_0 position.

We now extend this scheme to the Ultra High Intensity (UHI) regime by considering $a_0 = 5$. As mentioned beforehand, the subluminal nature of SPW favours electron acceleration. Therefore, in this nonlinear regime, the SPW will suffer from significant wave damping as a consequence of the energy exchange between the excited SPW and the accelerated particles. Thus, in order to gauge the impact of the topology of the target's surface in the laser irradiated zone in this regime, we will measure the maximum momentum of accelerated electrons p_y instead of the B_{SPW}. The result of this analysis is shown in Fig. 4.5(b), where we notice that the maximum value for the electron momentum increases gradually until the $N_{ripples} = 3$, where the highest value $\max(p_y/m_e c) \equiv p_{max} \approx 80$ is observed. This corresponds to the case in which the laser edge touches the diffraction grating border. Unlike the previous case with $a_0 = 0.1$, here the value $\bar{p}_{max}$ reduces abruptly (about 20%) when adding one extra ripples from the optimal configuration on the plasma interface after which a plateau is formed. This effect is observed because most of the electrons are accelerated at the same time as the SPW is excited and are pushed to the vacuum region as soon as they gain energy. The ripples do not represent therefore an obstacle to the propagation of the accelerated electrons.

We can conclude that the ideal configuration is the one in which the ripples are mainly in the laser-plasma interaction region. Now, to further increase the SPW intensity, let us assume rotational wavefronts.

4.2 Tunable SPW via WFR

Wavefront rotation (WFR) is a technique used on femtosecond lasers to induce a rotation of the successive laser wavefronts, thus leading to a time-varying incidence angle of the laser impinging onto a target [108]. Since WFR are the result of focusing a laser with a pulse front tilt, which is a common spatio-temporal distortion in ultrafast optics [109], they can arise as a side effect when misaligning a grating, or prism (see App.B), in the compressor of a chirped pulse amplification laser leading to pulse front tilt and spatial chirp. Given that this phenomenon decreases the peak intensity at focus, it is often viewed as an undesirable side effect to be avoided during experiments. However, we propose to exploit this effect as it represents a controllable pulse beam parameter. Indeed, it has been showed through electromagnetic simulations, carried out by Pisani *et al.* [110], that the use of WFR on the driving laser pulse could help generate more intense and shorter SPW in the linear optics (low intensity) regime. Since the resonance condition for SPW excitation in the linear regime is met for a well defined value of the laser incidence angle, the use of WFR allows the SPW to be excited for only over a very short time, leading thus to the generation of near single-cycle SPW. It is important to point out that high-field plasmonics involving the nonlinear, relativistic and kinetic behaviour of the plasma is not a straightforward generalisation of the linear regime. For this reason, the study presented in [110] is intrinsically unsuitable for investigating the extension of the plasmonic processes to the UHI regime as their employed technique does not allow to study electron acceleration. For the purpose of identifying the novelties that are only accessible in the UHI regime, we performed several 2D3V PIC simulations to demonstrate how the effects of SPW generation via WFR can be harnessed in the UHI regime to drive tunable, ultrashort, ultra-intense SPW able to generate near single-cycle, highly energetic electron bunches.

4.2.1 Presentation of the novel acceleration scheme

In order to distinguish the SPW signal from the reflected laser, the magnetic field has been filtered selecting values of $k < 2k_{SPW}$. This is due to the fact that SPW are TM-modes, so their signature can be sought by inspecting the Fourier transform of the Bz component of the magnetic field. Taking into account that the SPW and incident/reflected laser waves have different dispersion relations, filtering in (k_x,k_y) Fourier space allows to extract the component associated to the SPW. Then an inverse Fourier transform is done to obtain the Bz component of the SPW magnetic field in the reconstructed real space domain.

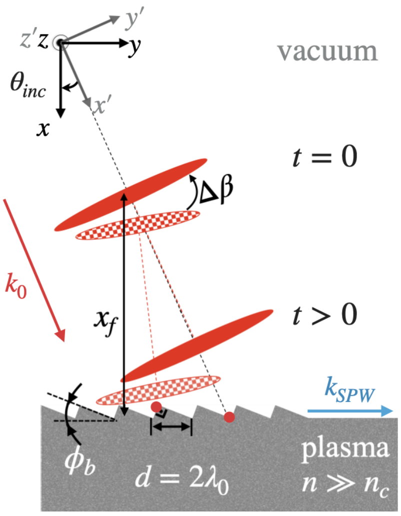

Figure 4.6: Illustration of the setup.

Parameter	Values
$\Delta_{x,y}$ Spatial resolution	$\lambda_0/256$
a_0 Laser strength	$0.1, 5.$
θ_{inc} Incidence angle	31°
$w_\perp$ Laser waist	$5.2\lambda_0$
τ_L Duration	$10\lambda_0/c$
$\Delta\beta$ WFR parameter	$-110 \rightarrow 110$ mrad
n_0 Density	$100n_c$
ϕ_b Blazed angle	13°
h Groove's depth	$0.44\lambda_0$
d Grating periodicity	$2\lambda_0$
Particles per cell	32 electrons/ions

Table 4.2: Main numerical parameters

Identification of control parameters

Using the expressions from [108] as a point of departure, we have that focusing a pulse with tilted wavefronts gives the following electric field profile (in our 2D configuration) as a function of time t and transverse coordinate y':

$$E(y', t) = E_0 \exp\left[-2\frac{t^2}{\tau_f^2} - 2\frac{y'^2}{w_f^2}\right] \exp\left[i\phi(y', t)\right] , \tag{4.9}$$

where E_0 is the maximum electric field and the spatio-temporal phase is

$$\phi(y', t) = 4\,\frac{w_i\xi}{w_f\tau_f\tau_i}\,y't + \omega_0 t\,, \tag{4.10}$$

with ξ the front pulse tilt parameter. The pulse waist and duration before (after) focus are respectively w_i (w_f) and τ_i (τ_f), related by:

$$\frac{\tau_f}{\tau_i} = \frac{w_f}{w_0}\sqrt{1 + \left(\frac{w_i\xi}{\tau_i}\right)^2}\,, \tag{4.11}$$

where $w_0 = 4f/(k_0 w_i)$ is the laser waist with f the focal length and $k_0 = \omega_0/c$. The linear dependence in $y't$ leads to an instantaneous angle of propagation of light

$$\beta(t) \simeq -\frac{c}{\omega_0}\frac{\partial\phi}{\partial y'} = 4\,\frac{w_i\xi}{w_f\tau_f\tau_i}\,t \equiv \Omega_\beta t\,, \tag{4.12}$$

which increases linearly with time. The angular WFR rotation velocity is thus

$$\Omega_\beta \equiv \frac{\partial \beta}{\partial t} = \frac{4 w_i \xi}{k_0 w_f \tau_f \tau_i} \,. \tag{4.13}$$

Using Eq.4.11, we can rewrite this velocity as

$$\Omega_\beta = \frac{w_i^2}{f \tau_i^2} \frac{\xi}{1 + (w_i \xi / \tau_i)^2} \,, \tag{4.14}$$

which corresponds to the equation in [108] where they give Ω_β as a function of the laser parameters before best focus. In Fig.4.6, $\Omega_\beta > 0$ is considered, the angle between two wavefronts are exaggerated for illustration purposes. The main angle of incidence θ_{inc}, defined as that of the central wavefront, is chosen as the resonant angle for exciting the SPW. Successive wavefronts are then shifted by an angle

$$\Delta\beta = \frac{\Omega_\beta \lambda_0}{c} \,, \tag{4.15}$$

henceforth referred to as the WFR parameter. As a result, each successive wavefront will strike the target at a slightly different location along the y-direction. Different to [110], the resonance condition in the UHI regime is broader, and thus different wavefronts will be able to drive the surface wave. For this reason, the laser pulse is focused at a distance x_f from the target as this, together with WFR, allows for a "sliding focus" effect, *i.e.* a displacement in time of the pulse intensity peak along the target surface. In this scenario, the central wavefront excites an SPW while the successive wavefronts will follow the excited SPW.

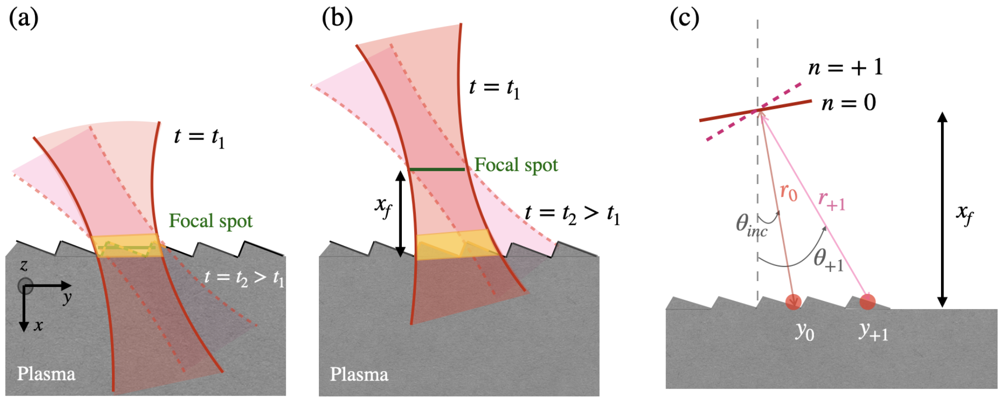

Figure 4.7: Illustration of a laser pulse with WFR with (a) the focal spot on the surface and (b) the best focus at a certain distance from the grating. The yellow zone designs the irradiated spot.

The effect of the laser focal spot placement on the excitation of the SPW is further illustrated in Fig.4.7. Indeed, in figure (a), when the pulse is focused directly on the grating, the laser irradiated spot (highlighted in yellow) remains unchanged in time. However, when the focal spot is further away from the grating, as shown in figure (b), the illuminated region shifts along the y direction between $t = t_1$ and subsequent timesteps. If the sliding focus velocity $v_{\rm sl}$ is close to the SPW velocity, the latter will be driven more efficiently.

To estimate the effective velocity $v_{\rm sl}$ of the projected waist onto the target, we consider the geometrical approach depicted in Fig.4.7(c) where the solid line $n = 0$ represents the central wavefront, and the dashed line $n = +1$ a succeeding wavefront, striking the target at y_0 and y_{+1} respectively. The point at which the center of each wavefront impinges the target, y_n, and their distance from the best focus, r_n, is given by:

$$y_j = x_f \tan\theta_j \,, \tag{4.16}$$

$$r_j = \frac{x_f}{\cos\theta_j} \,, \tag{4.17}$$

where $\theta_n = \theta_{inc} + n\Delta\beta$ is the propagation angle.
For arbitrary value of n, we obtain the following velocity

$$v_{n+\frac{1}{2}} = \frac{y_{n+1} - y_n}{\lambda_0 + r_{n+1} - r_n}\, c \,, \tag{4.18}$$

with

$$\begin{aligned} y_{j+1} - y_j &\simeq x_f \Delta\beta (1 + \tan^2\theta_{inc}) \,, \\ r_{j+1} - r_j &\simeq x_f \Delta\beta \frac{\tan\theta_{inc}}{\cos\theta_{inc}} \,. \end{aligned}$$

The resulting apparent velocity is thus a constant independent of time. For ultra-short pulses and/or the central wavefronts, we find the following constant sliding velocity:

$$v_{\rm sl} \approx \frac{1 + \tan^2\theta_{inc}}{\lambda_0/(x_f\Delta\beta) + \tan\theta_{inc}/\cos\theta_{inc}}\, c \,, \tag{4.19}$$

$$\simeq \frac{\Delta\beta\, x_f/\lambda_0}{\cos^2\theta_{inc} + \sin\theta_{inc}\,\Delta\beta\, x_f/\lambda_0}\, c \,. \tag{4.20}$$

This velocity depends on the WFR parameter, $\Delta\beta$, the target-to-waist distance, x_f and the laser's incidence angle, θ_{inc}. In order to test the theoretical prediction of $v_{\rm sl}$ against PIC simulations, we fix $\Delta\beta = 33$mrad, and vary the laser θ_{inc} for $x_f = 25\lambda_0$ (black) and $x_f = 50\lambda_0$ (pink). The results are amassed in Fig. 4.8 where the solid lines represent the theoretical $v_{\text{sl,th}}$ predicted by Eq.4.20, while the symbols (triangles for $x_f = 50\lambda_0$ and circles for $x_f = 25\lambda_0$) are the $v_{\text{sl,PIC}}$ obtained from the PIC simulations by locating the position of the maximum laser field amplitude as a function of time at the target surface and time-averaging over the laser high-frequency. Eq. (4.20) is found to be in good agreement with measurements from PIC simulations as both v_{sl} overlap.

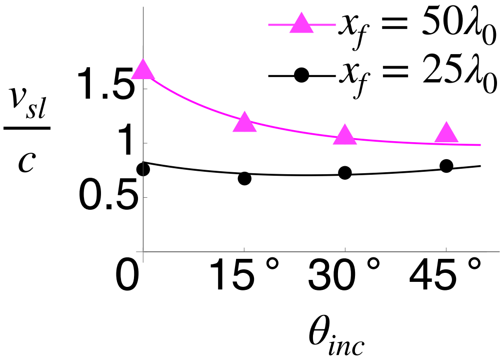

Figure 4.8: Sliding velocity as a function of the laser incidence angle comparing the theoretical prediction from Eq.4.20 (solid lines) and the results from PIC simulations for $x_f = 50\lambda_0$ (pink triangles) and $x_f = 25\lambda_0$ (black circles).

Returning our attention to the WFR parameter, the sign and value of $\Delta\beta$ affects the duration and amplitude of the excited SPW [111]. Indeed, when the sliding velocity is along the direction of propagation of the SPW, the excited wave can increase its amplitude while maintaining a short duration. On that account, additional tunability can be obtained by calculating an optimal value of the WFR parameter $\Delta\beta_{\text{opt}}$ such that the sliding velocity v_{sl} coincides with the SPW velocity $v_{\text{SPW}} \simeq c$. Therefore solving $v_{\text{sl}} = c\,(1 - n_c/n_0)$ leads to:

$$\Delta\beta_{\text{opt}} \simeq \frac{\lambda_0}{x_f}\,(1 + \sin\theta_{inc})\ . \tag{4.21}$$

The importance of the parameter x_f is demonstrated by Eq. (4.21) as $\Delta\beta_{\text{opt}}$ decreases when increasing the distance between the target and best focus, which would permit to relax the experimental constraint of obtaining large WFR velocity [108]. However, there is an energy trade off since at larger values of x_f, the intensity of the laser at the surface decreases. Indeed, when comparing $x_f = 50\lambda_0$ to $x_f = 25\lambda_0$, whose $\Delta\beta_{\text{opt}}$ are respectively 30mrad and 60mrad, we noticed an 8% decrease on the laser field amplitude on target.

Thanks to our model, we have identified the parameters relevant to WFR: the phase front rotation, $\Delta\beta$, and the distance between the target and the pulse focal spot, x_f. In the following section we will present a parametric study varying only these parameters.

4.2.2 Exploiting WFR in a weakly non linear regime for short SPW generation

We first consider $a_0 = 0.1$, for which relativistic non-linearities can be neglected, so as to assess the coupling efficiency of our proposed set-up and identify the optimal parameters for SPW excitation.

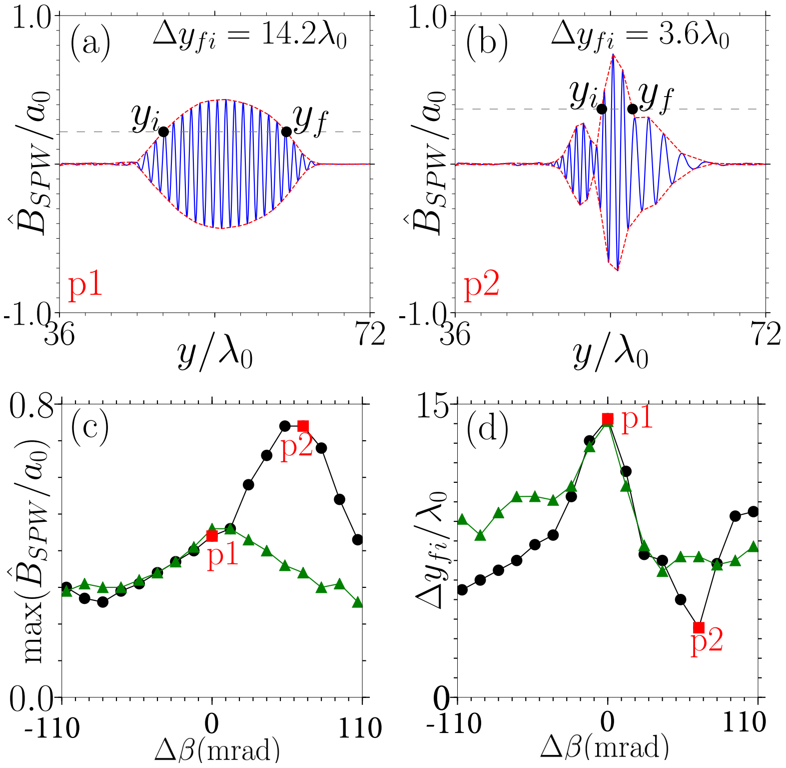

Figure 4.9: SPW magnetic field at the target surface for (a) $\Delta\beta = 0$ and (b) $\Delta\beta =$ 67mrad with $a_0 = 0.1$ and $x_f = 25\lambda_0$. (c) Maximum SPW field amplitude and (d) duration (FWHM) versus the WFR parameter $\Delta\beta$ for $x_f = 0$ (green triangles) and $x_f = 25\lambda_0$ (black circles). Markers p1 and p2 indicate the cases shown in panels (a) and (b).

In the upper row of Fig. 4.9, we show a snapshot of $\hat{B}_{\text{SPW}}$ along the target surface for $x_f = 25\lambda_0$, (a) $\Delta\beta = 0$ and (b) $\Delta\beta = 67$mrad. More concretely, we compare the case where no WFR has been applied to the driven laser pulse to the case for which we have found the most intense and shortest SPW in our simulations. The duration of the excited SPW, measured as the signal FWHM, is estimated from the SPW spatial width through the relation $\Delta\tau_{fi} \simeq \Delta y_{fi}/c$. We effectively see that using this optimal $\Delta\beta$ increased the SPW peak amplitude by $\sim 65\%$ with respect to the case without WFR, and reduced the SPW duration fourfold from 14.2 to $3.6\lambda_0/c$.

The deformity of the SPW pulse seen in Fig. 4.9(b) could be due to a radial chirp effect. Qualitatively, if we consider the wavelength as the distance between two wavefronts, the chirp in the laser will be along the radius instead of along the axis of propagation. As such, the distance between the wavefront varies with the radius and thus each extremity of the wavefront will impinge on the grating at different instants of time. The SPWs are then excited at slightly different frequencies (within resonance width) and at different points on the grating at different instants. This delay of the arrival of each part of the wavefronts could lead to the spatial chirp observed in Fig. 4.9(b).

The two previously presented cases correspond to the red markers $p1$ and $p2$ showed in the bottom row of Fig.4.9 depicting (c) the maximum value of $\hat{B}_{\text{SPW}}$ and (d) the measured SPW duration as a function of a parametric scan of $\Delta\beta$ for $x_f = 0$ (laser pulse focus is on the target, green triangles) and $x_f = 25\lambda_0$ (laser pulse focus is at a distance of $25\lambda_0$ form the target, black circles). At $x_f = 0$ the WFR has little impact on SPW excitation: the most intense SPW is found for $\Delta\beta = 0$ and using a non-zero $\Delta\beta$ decreases the duration of the SPW but also its maximum amplitude. Instead for $x_f = 25\lambda$, $\Delta\beta$ acts as a tuning parameter allowing both to shorten the SPW and to increase its amplitude. We observe the shortest and most intense SPW for $\Delta\beta \simeq 67$mrad. This numerical result is in good agreement with our theoretical prediction from Eq. (4.21), where $\Delta\beta_{\text{opt}} \simeq 60$mrad for $x_f = 25\lambda_0$. In panel (c) we note a smooth trend around this optimal value; the point directly on the left of $p2$ corresponds to $\Delta\beta = 53$mrad. Interestingly, even though the on-target laser intensity is reduced when increasing x_f to $25\lambda_0$, a significant increase of the SPW amplitude is still obtained using the optimal WFR parameter. A parametric scan considering $x_f = 50\lambda_0$ (not shown here) leads to an optimal WFR parameter $\Delta\beta \simeq 33$mrad also in good agreement with $\Delta\beta_{\text{opt}} = 30$mrad from Eq. (4.21). As expected, positive values of $\Delta\beta$, for which the sliding velocity is along the SPW propagation direction, give a maximal effect. In contrast, for negative $\Delta\beta$, the SPW is still of a shorter duration but with a reduced amplitude, roughly that obtained when placing the target at $x_f = 0$.

4.2.3 Exploiting WFR in a relativistic regime for short electron bunch generation

We now turn our attention to the second series of simulations performed in the UHI regime with $a_0 = 5$ to study electron acceleration.

Fig. 4.10 shows (a) the maximum electron momentum parallel to the surface and (b) the characteristic width of the accelerated electron bunch as a function of $\Delta\beta$, considering $x_f = 0$ (green triangles) and $x_f = 25\lambda_0$ (black circles). Both panels exhibit very similar features than observed at low intensity. Placing the target at focus ($x_f = 0$) the accelerated electron bunch maximum energy and duration are marginally affected by WFR. In contrast, for $x_f = 25\lambda_0$, WFR significantly impacts electron acceleration: taking $\Delta\beta > 0$ leads to more energetic, shorter electron bunches. By comparing the case for which the target is at focus ($x_f = 0$) with $\Delta\beta = 0$ and that with the target at $x_f = 25\lambda_0$ for $\Delta\beta = 67$mrad, we find in panel (a) an increase of 62% in the maximum electron momentum going from $\max(p_y) \simeq 80m_ec$ to $\simeq 130m_ec$. The optimum value $\Delta\beta = 67$mrad found for electron acceleration in the UHI regime is the same as found earlier for efficient, ultrashort SPW excitation at lower intensity.

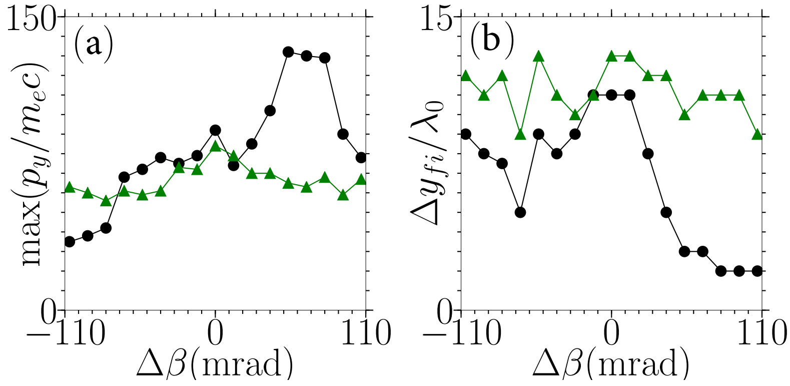

Figure 4.10: For $a_0 = 5$, (a) maximum electron momentum along the surface (p_y) and (b) electron bunch duration (FWHM) versus $\Delta\beta$ for $x_f = 0$ (green triangles), $x_f = 25\lambda_0$ (black circles).

Fig. 4.11 gives further insights into the acceleration process. The electron phase-space and SPW magnetic field at the target surface are shown at two different times and $x_f = 25\lambda$, for $\Delta\beta = 0$ and $\Delta\beta = 67$mrad. In both cases the duration of the electron bunch is proportional to the duration of the SPW, the shortest SPW obtained for $\Delta\beta = 67$mrad leading to the shortest electron bunch. For $\Delta\beta = 0$, the SPW is strongly damped at $t = t_0 + 20\lambda_0/c$: the electron bunch has reached its parallel momentum $\max(p_y) \simeq 90m_ec$ and has a width (measured from the FWHM in momentum) $\Delta y_{fi} = 11\lambda_0$. Instead, for $\Delta\beta = 67$mrad, at $t = t_0 + 10\lambda_0/c$, two periods after the laser has left the surface, we can see in Fig. 4.11(c) that the magnetic field is intense, $\hat{B}_{\text{SPW}} \simeq 1.2\,a_0$, and the most energetic electrons have already reached momentum up to $\max(p_y) \simeq 70 m_e c$. Ten periods later (Fig. 4.11(d)), a narrow, $\Delta y_{fi} = 3\lambda_0$, and energetic, $\max(p_y) \simeq 130 m_e c$, electron bunch is obtained, while the SPW has been significantly damped.

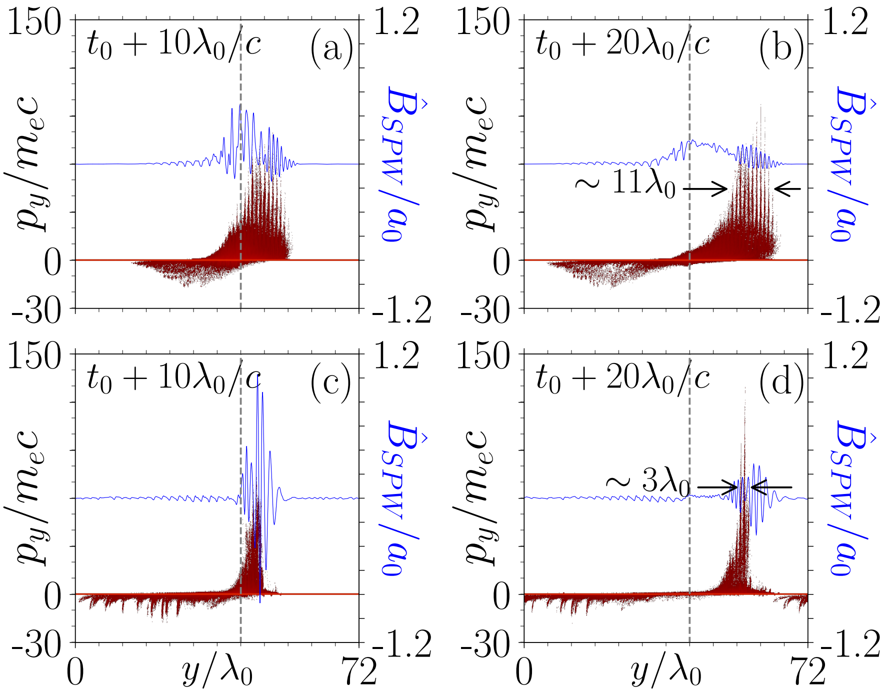

Figure 4.11: Electron phase-space (red) and SPW field amplitude (blue line, right scale) for $a_0 = 5$ at times, $t = t_0 + 10\lambda_0/c$ and $t = t_0 + 20\lambda_0/c$. (a)-(b): $\Delta\beta = 0$, and (c)-(d): $\Delta\beta = 67$mrad. The gray line indicates the end of the grating and beginning of the flat region.

Similar observations can be drawn from Fig. 4.12, where (a) the electron energy distribution as a function of the emission angle is shown. We notice that the most energetic electrons are mainly accelerated along the target's surface (situated at 90°) and in the $y > 0$-direction (*i.e.* in the SPW direction of propagation). Panel (b) reports the energy distribution of the electron as a function of the electron energy, for different values of $\Delta\beta$: positive $\Delta\beta = 67$mrad (solid red line), $\Delta\beta = 0$ (blue dashed line) and negative $\Delta\beta = -40$mrad (green dotted line). As expected from Fig. 4.11, the highest energy is obtained for the positive $\Delta\beta$ with a cutoff electron energy of about 70 MeV. Without WFR, the electron energy cutoff is circa 50 MeV, which decreases to around 35 MeV when applying a negative $\Delta\beta$. In the latter scenario, the drop of electron energy can be explained by the fact that a negative $\Delta\beta$ leads to a v_{sl} travelling in the opposite direction of the excited SPW, therefore the central wavefront will excite a shorter SPW but the consecutive wavefronts will not "follow" the SPW nor sustain its growth.

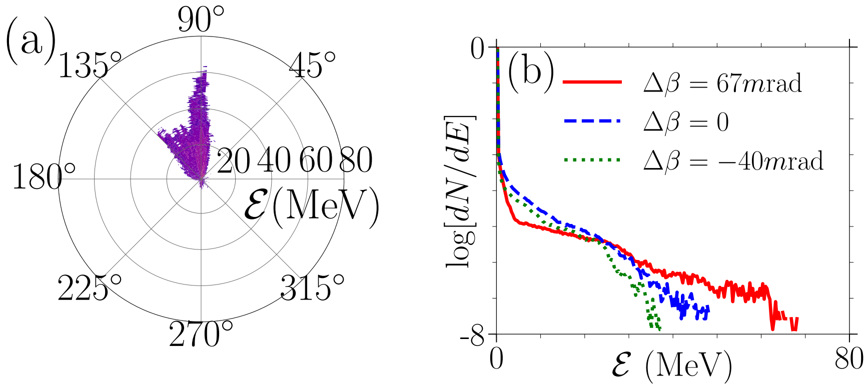

Figure 4.12: (a) Electron energy distribution in MeV as a function of the emission angle $\phi = \tan^{-1}(p_y/p_x)$ for $\Delta\beta = 67$mrad and $a_0 = 5$. (b) Electron energy distribution for $\Delta\beta = 67$mrad (red), $\Delta\beta = 0$ (blue) and $\Delta\beta = -40$mrad (green).

A particle tracking of the most energetic electrons permits a further insight into the acceleration process. The upper row of Fig. 4.13 shows their electron gain energy, $\Delta\mathcal{E}$, along the surface while the bottom row depicts the longitudinal field E_y acting on the most energetic particle as a function of the distance for: (a)-(c) $\Delta\beta = 0$ and (b)-(d) $\Delta\beta = 67$mrad. The red line in panel (c) and (d) correspond to the trajectory-averaged value of the longitudinal field $\langle E_y\rangle$. In the case without WFR we find $\Delta\mathcal{E} \simeq 90 m_e c^2$ and $\langle E_y\rangle \simeq -1.0\, m_e c\omega_0/e$. When using the optimal $\Delta\beta$ we obtain $\Delta\mathcal{E} \simeq 130 m_e c^2$ and $\langle E_y\rangle \simeq -1.4\, m_e c\omega_0/e$. In the latter case, the electrons seem to remain trapped and accelerated in the SPW for longer. Through evaluating $\langle E_y\rangle$, we can define the following acceleration length:

$$l_{\text{acc}} = \frac{\Delta\mathcal{E}}{|e\,\langle E_y\rangle|}\,, \tag{4.22}$$

which for both cases leads to an acceleration length $l_{acc} \sim 15\lambda_0$, consistent with the observed particle trajectories. Note that this l_{acc} exceeds the laser spot size of $\approx 12\lambda_0$, and corresponds roughly to the length over which the SPW decreases its amplitude significantly (see $\hat{B}_{\text{SPW}}$ in Fig. 4.11). This confirms the electrons are accelerated by the SPW as it propagates along the target surface.

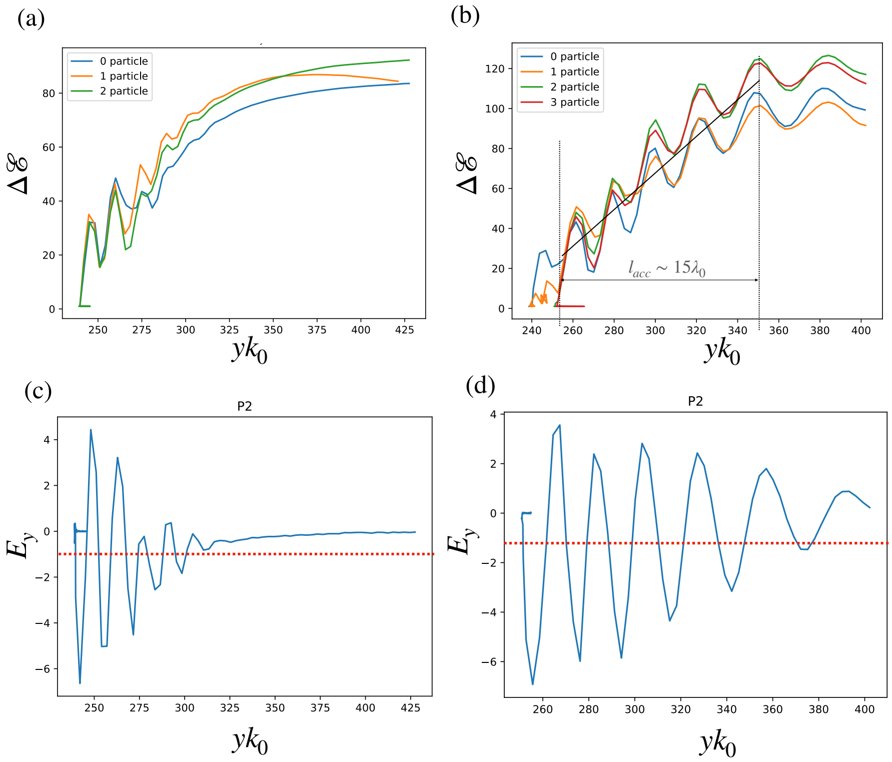

Figure 4.13: The upper row shows the energy gain $\Delta\mathcal{E}$ of the four most energetic electrons and the bottom row the longitudinal field E_y of the most energetic particle, $P2$, as a function of the distance for the case (a)-(c) without WFR and (b)-(d) with $\Delta\beta = 67$mrad.

These results and in particular the increase of the maximum electron energy (equivalent to the electron momentum) are consistent with what one expects from the increase of the SPW amplitude by use of the WFR driving pulse. Indeed, an upper limit of the electron energy gain in the SPW has been derived in [38] by generalizing the results of laser wakefield acceleration (LWFA) [91, 112, 113] leading to

$$\Delta\mathcal{E} \sim \chi' \gamma_\phi \max|\hat{B}_{\text{SPW}}| m_e c^2 \tag{4.23}$$

so that $\Delta\mathcal{E}$ is proportional to the SPW field amplitude. Here $\gamma_\phi = (1 - v_\phi^2/c^2)^{-1/2}$ and χ' is a constant of order one, reaching at most 4 [38]. In our simulations, the magnetic field of the SPW (time-averaged over the wave period) reached at most $\max|\hat{B}_{\text{SPW}}| \sim 3.8$ when $\Delta\beta = 0$ and $\max|\hat{B}_{\text{SPW}}| \sim 7.0$ when $\Delta\beta = 67$mrad. Considering that $\gamma_\phi \simeq 10$ for $n_0 = 100n_c$, if $\Delta\beta = 0$, we then obtain the upper limit equal to $\Delta\mathcal{E} \simeq 154 m_e c^2$ and if $\Delta\beta = 67$mrad, then $\Delta\mathcal{E} \simeq 280 m_e c^2$. These predictions overestimate the electron energy as they assume i) no wave decay over the distance required for acceleration, ii) optimal electron injection and iii) acceleration exactly parallel to the target surface, while it has been observed that electrons are deflected in the perpendicular direction [42]. While the electron acceleration in SPW is not yet at the level of LWFA in terms of maximum electron energy (up to 8 GeV in recent works [114]), our proposed scheme benefits from improved control of maximum energy and duration, and can thus offer an alternative route toward compact multi-MeV electron sources. In addition, since SPWs are excited at the vicinity of very dense plasmas, one can expect to achieve higher charge with this technique than with LWFA. Indeed, experiments carried out by Cantono *et al.* in [43], have demonstrated accelerated charges up to 660pC with table-top laser systems. These experiments were done without WFR nor the optimized grating. In our 2D simulations, with $\Delta\beta = 67$mrad, the highest energy particles form a bunch with duration of $\simeq 3\lambda_0/c$ and total charge $\simeq 10\text{pC}/\lambda_0$. Assuming a bunch width (in the z-direction) of the order of the laser pulse with $w_\perp = 5.2\lambda_0$ and $\lambda_0 = 0.8\mu$m, one could expect few cycles electron bunches with a charge of ~ 52 pC.

Considering similar laser parameters (without WFR) and electron energies to the SPW experiment in [43], the the LWFA experiment described in [115] measured short, high-charge electron bunches with energy 85 MeV (21 MeV energy spread), charge 15 ± 7 pC and duration 4.4 fs. The charge obtained with LWFA is noticeably smaller to the one obtained experimentally with SPW. As a consequence, the electron beams obtained with SPW are potentially competitive with cutting-edge laser wakefield electron beams from under dense plasmas in terms of emitted current.

An other important point when discussing the beam quality of plasma accelerators is the emittance. An asset of LWFA is their ability to generate electron beams with low energy spread and small transverse emittance of around 0.1 mm mrad [116–118]. In the case of SPW, selecting particles with energies in the range of 30 to 70 MeV (study not presented in this manuscript), the emittance is smaller when using WFR ($\sim 10\mu m$). This result is due to the fact that the fast particles are predominantly accelerated along the target's parallel direction (90°), without dispersing. Instead, the less energetic particles are susceptible to be accelerated by different mechanisms and can thus be accelerated to random directions, which compromises the beam quality. In such case, the electron beam disperses and the emittance grows. Without WFR, the efficiency in generating fast particles is smaller resulting in bigger beam emittance. Similar to LWFA, further improvement on our proposed set-up should aim to produce low emittance and low energy spreads.

In conclusion, the highlight of our proposed set-up of SPW electron acceleration, is that we are able to accelerate an electron beam with an important charge. However, a trade off when considering highly-charged beam is that space-charge effects could play a role in the long term on the electron bunch properties. Nonetheless, this is true not only for our scheme, but for any electron source. Complementary techniques exists to transport and/or collimate non-neutral beams, but this issue is beyond the scope of our work.

4.3 Summary

In this work we have extended the study of ultrashort SPW generation via WFR to electron acceleration and are the subject of a published paper in Physical Review E [46].

Innovative approaches which exploit spatio-temporal laser couplings and pulse chirping to improve applications are present in other fields of study such as the implementation of a "flying focus" effect (similar to our "sliding focus") in Raman amplification [119], control of laser pulses for broadband extreme ultraviolet generation [120] and for high harmonic generation from solid targets [108]. In our work we employed WFR in the completely novel context of high field plasmonics.

We have highlighted and modeled the "sliding focus" effect induced by WFR and its dependence on the target-to-waist distance. We showed that, despite the defocusing, the sliding focus leads to a strong enhancement of the SPW amplitude and control of its duration. This allowed us to introduce the control parameter $\Delta\beta$ and x_f, which combined with an appropriately tailored plasma target, showed a significant improvement to what proved in a similar situation without WFR and for non optimized targets. Such enhancement has a major impact on electron acceleration by the SPW in the nonlinear, relativistic regime, and is pivotal to the production of high charge, ultrashort electron bunches with features that go beyond current limits of LWFA, and provides important and clear guidelines for forthcoming experiments where one may simply smoothly tune such parameters until the optimal condition is found.

Chapter 5

Extension of the resonance condition for SPW excitation to ultra high intensity

Contents

Whilst SPW are proven to be optimal for electron acceleration, there has been little quantitative analysis of their survival when increasing the laser intensity beyond the UHI regime. In this limit, the plasma grating can evolve on relatively short time scales, and nonlinear effects can affect the dispersion relation in the relativistic regime. Therefore, the excitation and survival of SPW beyond UHI remains an open question. In order to bridge this gap, we performed a series of 2D Particle-In-Cell (PIC) simulations for laser intensities ranging from 10^{16} to 10^{22} W/cm^2 to determine the conditions for improving laser-plasma energy transfer as well as accelerating charged particles by the SPW excitation mechanism in an over-dense plasma with a grating, in the ultra relativistic regime.

This chapter is organized as follows: the first section describes the PIC simulation setup with parameters closely corresponding to recent experiments [42, 43]. Section 5.2 analyses SPW excitation as a function of laser incidence and intensity. The results are then compared to analytical values obtained by the dispersion relation for cold SPWs and a heuristic relativistic correction. The importance of considering high density plasma to maintain SPW excitation in the ultra relativistic regime is shown. Section 5.3 studies the behavior of accelerated electrons along the plasma surface. A strong correlation is demonstrated between the angle of SPW excitation and the laser's angle of incidence that optimizes electron acceleration along the plasma surface. The section 5.4 investigates the influence of the grating depth at higher laser intensities. Then, in the last section our conclusions are presented.

5.1 Set-up

The geometry of the 2D3V simulations are depicted in Fig. 5.1 where the plasma lies in the (x, y) plane for $x \geq 0$, its surface being along the y direction.

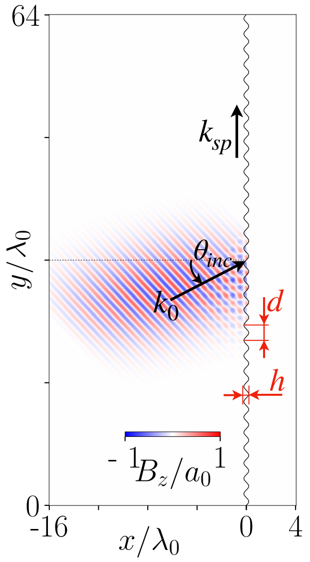

Figure 5.1: Simulation set-up.

Parameter	Values
Box size	$20\lambda_0 \times 64\lambda_0$
$\Delta_{x,y}$ Spatial resolution	$\lambda_0/128$
Δ_t Time resolution	$0.95\Delta_{x,y}/\sqrt{2}$
a_0 Laser strength	$0.1 \rightarrow 50.$
θ_{inc} Incidence angle	$28° \rightarrow 50°$
$w_\perp$ Laser waist	$5\lambda_0$
τ_L Duration	$10\lambda_0/c$
n_0 Density	$100n_c$,$200n_c$
h Groove's depth	$0.1\lambda_0$, 0.4λ
d Grating periodicity	$2\lambda_0$
Particles per cell	16 electrons/ions

Table 5.1: Main parameters

The laser beam is focused thought an angle θ_{inc} over the interface of the plasma target with electron density n_0, grating depth h and period d. Here, the red-blue scale represents the magnetic field amplitude of the laser pulse impinging over the target.

The main parameters of the driven $P-$polarized Gaussian laser pulse and the plasma properties are given in the table 5.1. The plasma grating presents a sinusoidal-modulated vacuum-plasma interface located at $x_g(y) = (h/2)\,\sin(2\pi y/d)$. In all cases studied, we considered $d = 2\lambda_0$ $(= 1.6\mu\text{m})$, however, in order to determine the influence of the grating depth on SPW excitation we have used either $h = 0.1\lambda_0$ $(= 0.08\mu\text{m})$ or $0.4\lambda_0$ $(= 0.32\mu\text{m})$. The plasma consists of electrons with a small initial temperature of $T_e = 50\text{eV}$ as well as a neutralizing background of ions free to move in the space with initial temperature $T_i/(ZT_e) = 0.1$, where $Z = 1$ is the atomic number.

In the systematic study we have performed, we selected two values for the plasma density: $n_0 = 100n_c$ and $n_0 = 200n_c$. These are typical values on the plasma density and corresponds to about three and six times ionized gold $(\sim 104n_c$ and $\sim 208n_c)$ [42, 43, 45]. In prospect of the evolution of the experimental techniques to increase the laser's contrast (ex. [121]), we assumed a step density plasma in our simulations. The pre-plasma effect is well analysed in the article by X. M. Zhu *et al.*, Ref. [45].

The simulations were run until particles or radiation got to the position $y = 60\lambda_0$ $(= 48\mu\text{m})$, which determines the final simulation time $t = t_f$. Notice that t_f varies according to the laser incidence angle and it gets larger as θ_{inc} increases.

5.2 Resonance condition for SPW excitation at high intensity

In order to evidence the condition for SPW excitation as function of the laser intensity, we perform a set of simulations with intensity corresponding to a_0 varying from $a_0 = 0.1$ to $a_0 = 50$ as may be reached on forthcoming multi-petawatt laser systems, see *e.g.* Refs. [48,122]. For any given (n_0, a_0), we have performed a parametric scan varying the incidence angle of the laser from typically $\theta_{\text{inc}} = 28°$ to $\theta_{\text{inc}} = 50°$ in order to extract the optimal condition for SPW excitation. The plasma grating period and depth are kept constant.

In the presence of high-intensity lasers plasma interaction, and in particular when the normalized vector potential $a_0 \gtrsim 1$, it has been proposed [63–67] to correct the response of the electrons by considering an effective electron mass

$$m_e \to \gamma_0\, m_e\,,$$

with $\gamma_0 \simeq \sqrt{1 + a_0^2/2}$ the Lorentz factor of an electron in a plane wave (see Chap. 2.1.1). We consider that the SPW is excited by the laser, if $\omega = \omega_L$. Also we consider the heuristic correction $\omega \to \gamma_0\omega$. In the case of SPW excitation by the laser, we thus consider a heuristic correction to the dispersion relation (Eq.(2.45)) by replacing

$$\frac{\omega_p^2}{\omega^2} \equiv \frac{\omega_p^2}{\omega_0^2}\,,$$

with $\omega_0^2 = (\gamma_0\,\omega)^2$. As a consequence, correcting the phase-matching condition leads a a_0-dependent optimal angle of incidence for the surface plasma wave excitation:

$$\theta_{\text{opt}}(a_0) = \arcsin\left(\sqrt{\frac{n_0/(\gamma_0 n_c) - 1}{n_0/(\gamma_0 n_c) - 2}} - \frac{\lambda_0}{d}\right). \tag{5.1}$$

This results in an optimal angle, θ_{opt} that increases with the amplitude of the SPW field. For $a_0 \gg 1$ it depends on the parameter $n_0/(\gamma_0 n_c) \sim \sqrt{2} n_0/(a_0 n_c)$. In order to verify the validity of this scaling, we considered two electron densities, $n = 100 n_c$ and $200 n_c$.

Initially, the depth is chosen as $h = 0.1\lambda_0$, so that corrections to the dispersion relation due to finite depth are negligible. As detailed in the following, we find in simulations that at high intensity the resonance is quite broad. For values of $n/(a_0 n_c) \lesssim 10$ the correction to the dispersion relation can improve the coupling of the laser with plasma. We notice no further improvement for higher value of a_0, and the resonance angle becomes roughly independent of a_0. We can then conclude that Eq. (5.1) does not hold at ultra-high intensity.

The time evolution of the maximum amplitude of the SPW B_z field normalized to a_0 for a typical case ($a_0 = 20$, $n_0 = 200n_c$, $h = 0.1\lambda_0$ and different values of the laser incidence angle between 30° and 45°) is reproduced in Fig. 5.2. The field component reaches a maximum around $t = 12\lambda_0/c$ for an incidence angle of 33°, named hereafter θ_{opt} with $t = 0$ corresponding to the time when the laser pulse reaches the plasma surface. We notice that the SPW field amplitude does not become larger than the laser field a_0, as opposed to what has been found for longer pulses and lower intensities [25]. In this short pulse regime ($\simeq 27$ fs) the SPW excitation does not have time to reach the stationary regime. From the figure we can also see that the resonance condition is not sharp. A laser incident at angles close to the optimal values excites a field with very similar behaviour to the optimal one. This is also due, as discussed in Ref. [44], to the fact that the width of the incident laser transverse profile induces a spectral mode distribution of the SPW which induces an angular width for the θ_{opt} equals here to $\sim 4°$.

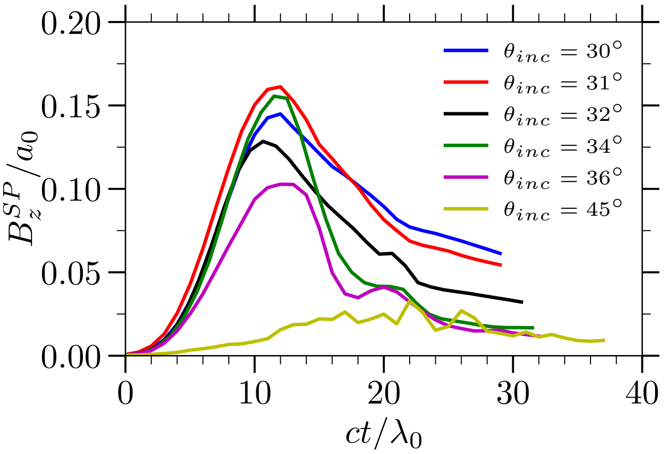

Figure 5.2: SPW B_z field amplitude evolution for $a_0 = 20$, $n_0 = 200n_c$ and $h = 0.1\lambda_0$, and laser incidence angle in between 30° and 45°, $t = 0$ corresponds to the instant of time when the laser pulse reaches the plasma.

In Fig. 5.3 we report the optimum laser incidence θ_{opt} (red dots) as a function of a_0 for the two plasma densities considered. The θ_{opt} is obtained by considering for each a_0 the angle that corresponds to the peak value of SPW B_z in time, namely we follow the same procedure that is illustrated in Fig. 5.2.

As a_0 increases, and in particular for $a_0 \gtrsim n/(10n_c)$, the incertitude in determining the optimum angle of the SPW B_z becomes large since many angles correspond more or less to the same maximum value of the field. Moreover, when increasing a_0, the normalised amplitude of the field B_z^{SP}/a_0 decreases. We notice that going from $a_0 \sim 1$ to $a_0 \sim n/(10n_c)$ results in a reduction of the field amplitude of $\approx 45\%$. Further increasing a_0 and taking $a_0 \sim n/(4n_c)$ results in a field amplitude reduction of $\approx 60\%$ in relation to the field observed when $a_0 = 1$.

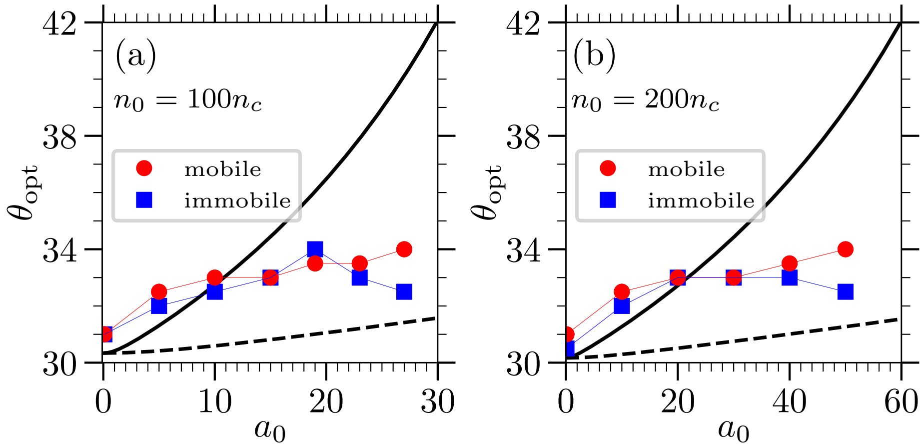

Figure 5.3: In red (points), laser angle of incidence that optimizes the SPW B_z field amplitude as a function of the laser strength parameter a_0 for (a) $n_0 = 100n_c$, and (b) $n_0 = 200n_c$. In blue (squares) we report the results from simulations assuming immobile ions. In both cases, $h = 0.1\lambda_0$. The solid (dashed) black line represents the expected value obtained using the dispersion relation for the cold SPW limit with the heuristic relativistic correction as a function of a_0 ($a_0/5$). Note small variations on the optimal condition also results in small variations on the SPW B_z field amplitude.

In Fig. 5.3 we also plot in black the expected value obtained using Eq. (5.1). As anticipated, while at first the values obtained in the simulations fit the equation, for larger values of a_0 the resonance angle becomes roughly independent of a_0. The threshold, noted $a_{0,T}$ in the following, is about $a_{0,T} = 10$ in the case when $n_0 = 100n_c$ and increases up to 20 when $n_0 = 200n_c$ (or, equivalently, $n_0/(a_{0,T}n_c) \sim 10$). As we can see, even if Eq. (5.1) does not hold, the parameter $n_0/(a_0 n_c)$ is a relevant quantity to describe the laser plasma coupling and the SPW excitation. More importantly, this parameter shows the importance of considering higher density plasma to maintain SPW excitation in the ultra relativistic regime. In Eq. (5.1) the heuristic correction to the dispersion relation is obtained using the laser parameter a_0. In the present simulations, the SPW maximum field amplitude is always smaller than a_0, and typically, as shown in Fig. 5.2, of the order of $a_0/5$. Therefore, for reference we also report in dashed black line in Fig. 5.3 the result from Eq. (5.1) considering $a_0/5$ instead of a_0 in the γ_0 function.

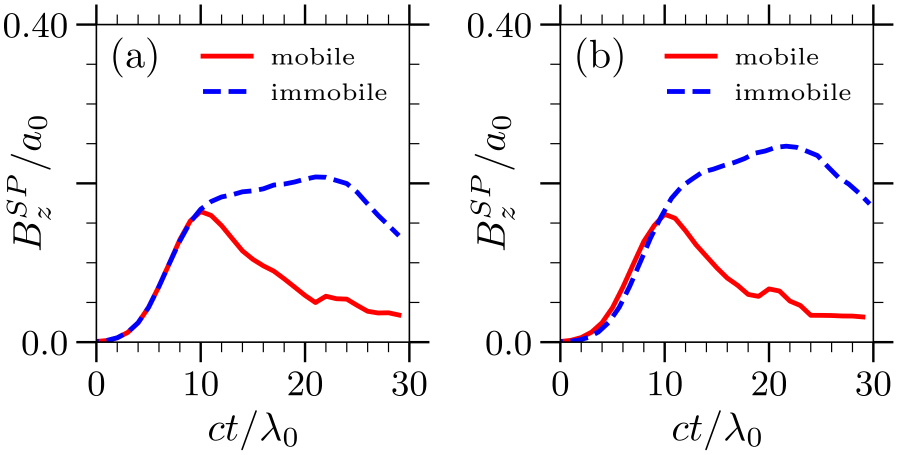

Figure 5.4: SPW B_z field amplitude evolution at $\theta_{inc} = 33°$ with time for (a) $n_0 = 100n_c$, $a_0 = 27$, and (b) $n_0 = 200n_c$, $a_0 = 50$. $t = 0$ corresponds to the instant of time when the laser pulse reaches the plasma.

Increasing a_0 increases the laser pressure, which may alter the grating and suppress the SPW excitation. To check the importance of this effect and to verify if the relativistic correction of the dispersion relation (Eq. (5.1)) is recovered, we also performed a set of simulations with immobile ions (represented by blue squares in Fig. 5.3 and a blue dashed line in Fig. 5.4). As we can see, the optimal angle is barely modified when the ions are immobile. However, as shown in Fig. 5.4 where we plot the SPW field amplitude evolution with time for two densities and $a_0 > a_{0,T}$, in the case of immobile ions the SPW field survives a longer time and peaks to higher values. This means that the grating deformation affects the SPW field on time scales larger than few laser periods ($\sim 12\lambda_0/c$ here). Above $a_{0,T}$ the damping of the SPW by the electrons is large, resulting in strong electron acceleration along the surface trapped in the SPW [38, 42, 44]. In the next section of this chapter we consider the SPW evolution as related to the electron dynamics along the grating.

5.3 Electron acceleration along the plasma surface

Using the same laser intensities and plasma densities as in the previous section, we will first analyze the maximum energy of the electrons that propagate along the plasma surface as a function of the laser angle of incidence. The results are summarized in Fig. 5.5 where we report the optimal laser's angle of incidence, θ^e_{opt} (which optimizes the formation of high energetic electron bunches propagating along the plasma surface) as a function of the laser strength parameter a_0 for (a) $n_0 = 100n_c$, and (b) $n_0 = 200n_c$ (case $h = 0.1\lambda_0$). To identify the electrons that propagate along the surface, we have defined the emission angle $\phi_e = \tan^{-1}(p_y/p_x)$ and selected electrons with $\phi_e = 90° \pm 3°$. The height of the bars indicates the range of angles of the laser incidence giving the highest electron energy. The error bars were determined by analyzing the energy spectrum of the electrons propagating along ($\phi_e = 90° \pm 3°$) the plasma surface.

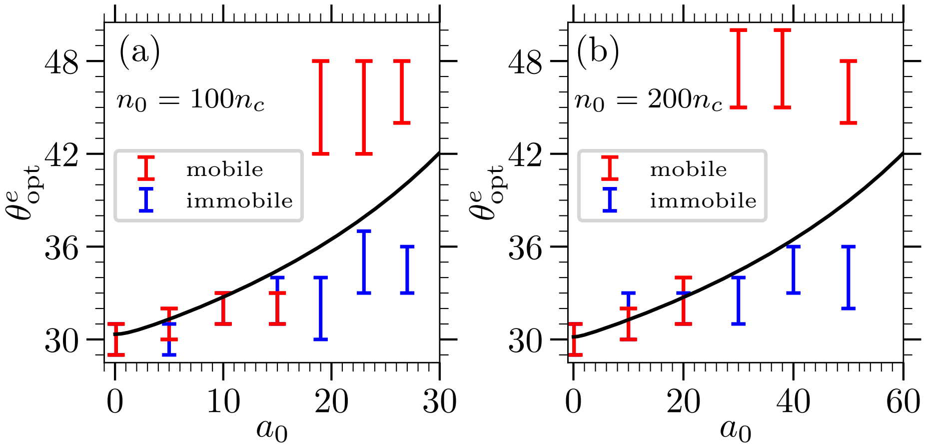

Figure 5.5: In red (bars), angle of incidence of the laser that optimizes electron bunches energy propagating along the plasma surface (θ^e_{opt}) as a function of the laser strength parameter a_0 for (a) $n_0 = 100n_c$, and (b) $n_0 = 200n_c$. In blue (bars) is reported results from simulations assuming immobile ions. In both cases, $h = 0.1\lambda_0$. The solid black line reports the optimal angle of SPW excitation obtained using the dispersion relation for cold SPW with the heuristic relativistic correction (see the discussion in the text).

As before, we have considered both mobile and immobile ions with the same color code as in Fig. 5.3 (red - mobile, blue -immobile). Comparing Fig. 5.3 and Fig. 5.5 we find at low laser intensity a strong correlation between the optimum angle of SPW excitation and the laser angle of incidence that optimizes the electron acceleration along the plasma surface. The optimum angle giving the highest energy of the electron bunch propagating along the surface is $\sim 31°$ for $a_0 \sim 1$ and increases slightly up to $\sim 33°$ with a_0 until it reaches $a_{0,T}$. It confirms the robustness of the SPW excitation in this range of intensity.

Above $a_{0,T}$, we observe for the realistic simulations (mobile ions) that the laser incidence angle that optimizes the electron bunch energy propagating along the surface is no longer the same one that optimizes the SPW field. The transition occurs for a_0 around 20 if the plasma density is $n = 100n_c$, and around 30 if $n = 200n_c$. However when considering simulations with immobile ions (blue bars) we recover the result of the previous Fig. 5.3: the optimal angle for electron acceleration coincides with the optimal angle for SPW excitation. This shows that the electrons dynamic is sensitive to the grating deformation.

It is clear that above $a_{0,T}$, electron acceleration by the SPW will be in competition with other acceleration mechanisms along the surface [83]. As discussed in more detail in the next section, the analysis of the electron phase space confirms this hypothesis, since above $a_{0,T}$ the electron velocity distribution does not show the characteristic behaviour of the acceleration by SPW, namely bunches with periodicity equal to the SPW wavelength, and directionality along the surface [123]. Indeed, we checked the effect of the laser on the plasma surface examining the spatial ion density distribution in two different time scales. Both an increase in plasma density due to the radiation pressure and an expansion of the plasma is observed. In the short time interval, comparable to the laser pulse duration, the diffraction grating is distorted and the plasma is pushed, which results in a large increase in the local plasma density. In the second and long scale that happens few cycles after the laser-plasma interaction, the plasma expansion creates an under-dense region in front of the target. That also might have a major effect on the laser absorption mechanism and to define the optimal angle to the electron acceleration. The effect of under-dense sheet in front of the plasma surface has been investigated in Ref. [45].

To overcome the possible limitation of SPW-laser coupling at high laser intensity, we now consider the influence of the target grating depth that, when chosen appropriately, can significantly improve the acceleration by SPW.

5.4 Recovery of SPW acceleration by adapting the grating depth

In laser-solid interaction and also at high laser intensity where plasma is created, it is well known that the ratio between the target grating depth and the grating periodicity plays a major role in the SPW excitation [66, 124]. Thus here, in order to find the optimum grating parameters for SPW excitation in the ultra high laser intensity regime ($a_0 \geq 25$), we have redone the PIC simulations increasing the grating depth of the plasma to $h = 0.4\lambda_0$.

In Fig. 5.6 we compare the optimal angle of incidence of the laser that optimizes electron bunches energy propagating along the plasma surface (bars) found in the previous section for $h = 0.1\lambda_0$ (in red) with the one found for $h = 0.4\lambda_0$ (in green) keeping unchanged the other parameters. As we can see in the case $h = 0.4\lambda_0$ the optimum angle for particle acceleration remains between 30° and 36° and coincides with the optimum angle for SPW excitation as presented in Fig. 3. As in section III the best laser incidence angle to excite highly energetic electron bunches stay roughly constant and does not scale with the laser strength. This is illustrated as an example by the simulations at $a_0 = 30$.

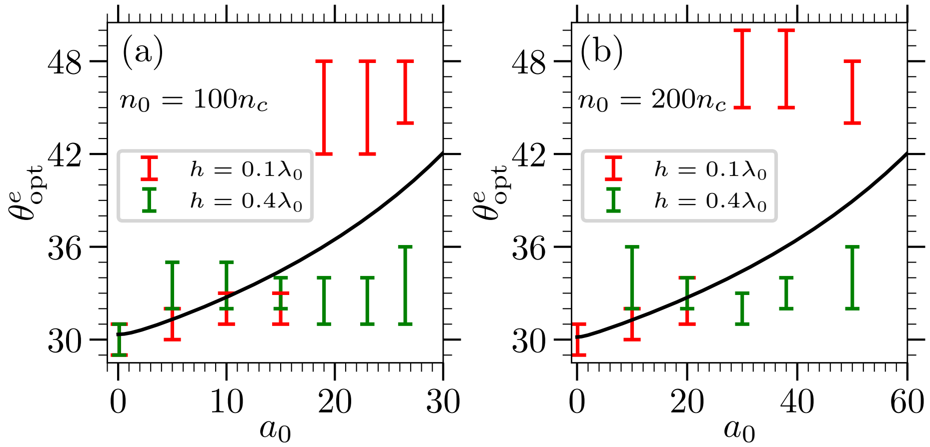

Figure 5.6: Optimal angle of incidence of the laser that optimizes electron bunches energy propagating along the plasma surface (θ^e_{opt}) as a function of the laser strength parameter a_0 for (a) $n_0 = 100n_c$, and (b) $n_0 = 200n_c$ (case $h = 0.1\lambda_0$ in red and $h = 0.4\lambda_0$ in green). The black line reports the expected value obtained using the dispersion relation for cold SPW with the heuristic relativistic correction (see the discussion in the text).

In Fig. 5.7 we plot the maximum B_z field amplitude evolution in time for different values of laser incidence angle. The time evolution of the field is quite similar to that observed in Fig. 5.2 where $a_0 = 20$ and $h = 0.1\lambda_0$, but the value of the field amplitude is larger and the optimal angles $(31^\circ - 33^\circ)$ coincide with the optimal angles for electron acceleration in Fig. 5.6 (b). As a consequence with the deeper grating we expect both that the electrons are mainly accelerated by the SPW and that the maximum energy gained by the electrons is higher than if the grating is shallow.

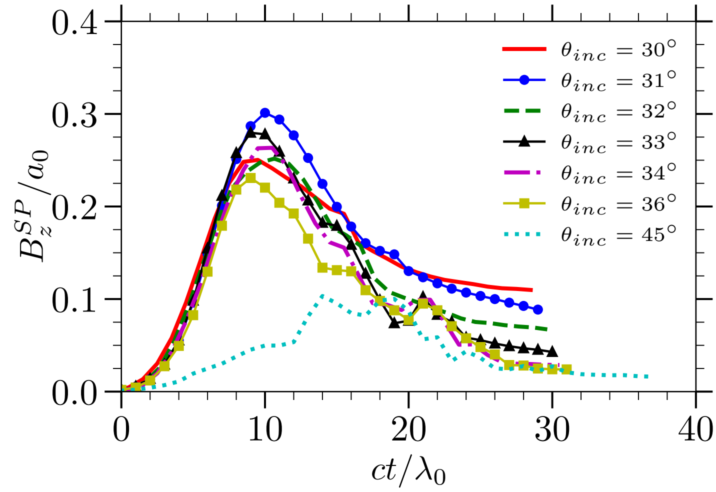

Figure 5.7: SPW B_z field amplitude evolution with time for $a_0 = 30$, $n_0 = 200n_c$ and $h = 0.4\lambda_0$ and laser incidence angle in between 30° and 45°. $t = 0$ corresponds to the instant of time when the laser pulse reaches the plasma.

In Fig. 5.8 we show the maximum value of the gamma factor, γ_f along the target's surface, for the electrons observed at the end of simulation as a function of the laser strength parameter a_0, taking $\theta_{inc} = \theta^e_{opt}$ and the parameters used in the Fig. 5.6. As expected we observe that the energy transfer is better when the gratings are deeper ($h = 0.4\lambda_0$) than when they are shallow ($h = 0.1\lambda_0$) in the high-intense regime. The red dotted line is the function $\gamma_f = 1 + 5.1a_0$ that fits the data when $h = 0.1\lambda_0$ and the green dashed curve is the function $\gamma_f = 1 + 9.3a_0$ that fits the data when $h = 0.4\lambda_0$.

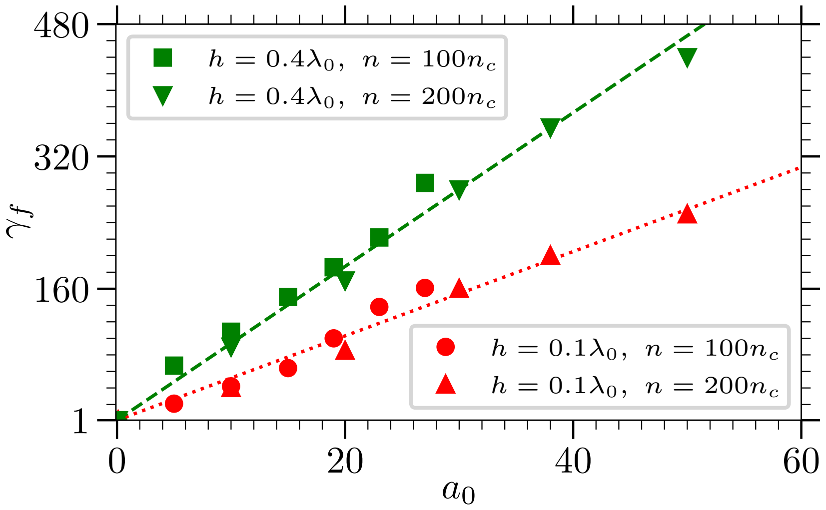

Figure 5.8: Maximum value of gamma factor, γ_f along the target's surface, observed at the end of simulation as a function of the laser strength parameter a_0 for (a) $n_0 = 100n_c$, and (b) $n_0 = 200n_c$ (case $h = 0.1\lambda_0$ in red and $h = 0.4\lambda_0$ in green). The dashed lines represents the general tendency of the results.

A more detailed analysis of the electron dynamics can be inferred from their energy distributions as a function of the propagation angle and from their phase space (p_y/m_ec,y/λ_0). If $h = 0.4\lambda_0$ and $\theta_{inc} = 33°$, a large amount of highly energetic electrons propagates along the surface $\phi_e = 90°$ (Fig. 5.9(a)), and the phase space shows bunches distanced by a wavelength (Fig. 5.9(b)), consistent with the SPW acceleration mechanism.

This is very different from the case with $h = 0.1\lambda_0$, and $\theta_{inc} = 33°$ reported in Fig. 5.9 (c) and (d) or $h = 0.1\lambda_0$, and $\theta_{inc} = 45°$ reported in Fig. 5.9 (e) and (f). We observe for these last two parameters sets that the faster electrons are accelerated mainly along the direction of the incident and reflected laser beam and fewer electrons are found propagating along the surface at 90°. Moreover a large amount of fast electrons are pushed inside the plasma. It is worth to point out that although the peak energy is reduced in this configuration, the laser plasma coupling is still large so that this configuration might be a way to enhance TNSA at the rear of the thin target [125]. In such a limit, the SPW field when present (Fig. 5.9 (c) and (d)) is weak and the SPW wave is no longer the predominant acceleration mechanism. This might be attributed to the grating deformation due to laser pressure which prevents laser-SPW coupling. We can thus conclude that a deeper grating allows to recover the exciting of SPW in the ultra high intensity laser regime and acceleration along a preferential direction. This effect is evident in Fig. 5.9 (g) when comparing the electron's spectra (selecting only the ones emitted parallel to the target

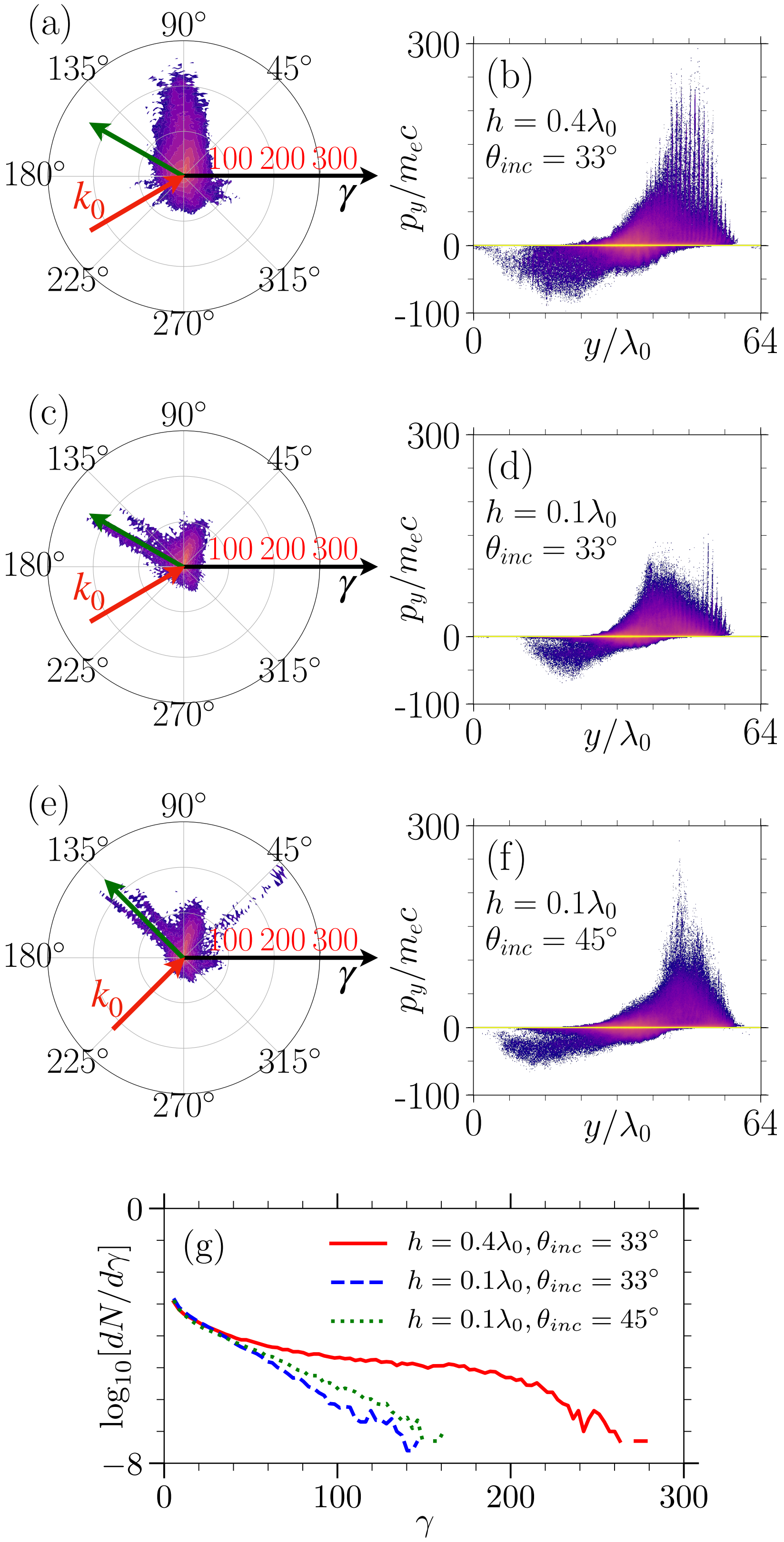

Figure 5.9: For $\theta_{inc} = 33°$, $a_0 = 30$, $n_0 = 200n_c$ and $h = 0.4\lambda_0$, (a) electron energy distribution at $t = t_f$. The plasma surface is along 90°, the red arrow shows the direction of the incident laser beam and the green arrow the reflected one; (b) phase space (p_y/m_ec,y/λ_0) of the electrons in the simulation box; the panels (c) and(d) [(e) and (f)] represent the same as the panels (a) and (b) for $h = 0.1\lambda_0$ and $\theta_{inc} = 33°$ [$\theta_{inc} = 45°$]; (g) spectrum of the electron bunches along the surface for the three parameter sets discussed.

$\phi_e = 90° \pm 6°$) for $h = 0.1\lambda_0$ (in blue) and $h = 0.4\lambda_0$ (in red), with $\theta_{inc} = 33°$ in both cases. The electron energy obtained when increasing the grating depth is increased by a factor of two for the deepest grating and the optimal angle. Instead for $h = 0.1\lambda_0$ the energy spectrum changes very little between $\theta_{inc} = 33°$ and 45° (in green), even if, when comparing the phase space p_y/m_ec,y/λ_0 for both incident angles (Fig. 5.9 (d) and (f)) we observe a small signature of the SPW excitation (bunching of the phase space), that is lost at 45°.

To conclude this section we verified that for $h = 0.4\lambda_0$, the SPW is still excited even at significantly higher laser intensities. In Fig. 5.10 the electrons emission spectrum assuming two extreme laser conditions (a) $a_0 = 100$, and (b) 200 is shown. There, the plasma density is equal to $n_0 = 200n_c$. From the panels, we observe a large increase of the electron energy achieving $\gamma_f/a_0 \sim 7, 8$ ($\gamma_f \approx 800$ for $a_0 = 100$ and $\gamma_f \approx 1600$ for $a_0 = 200$), even if for the largest laser strength $a_0 = 200$ (Fig. 5.10 (b)), the angular distribution of the electrons tends to increase. Our results show that, even in the very high-intensity regime of interaction, there is good evidence that SPW excitation and the consequent electron acceleration are still present when the diffraction grating is correctly chosen. However, they do not account for additional processes that may set at extreme intensities, such as radiation reaction or quantum effects which will be further explored in the next chapter.

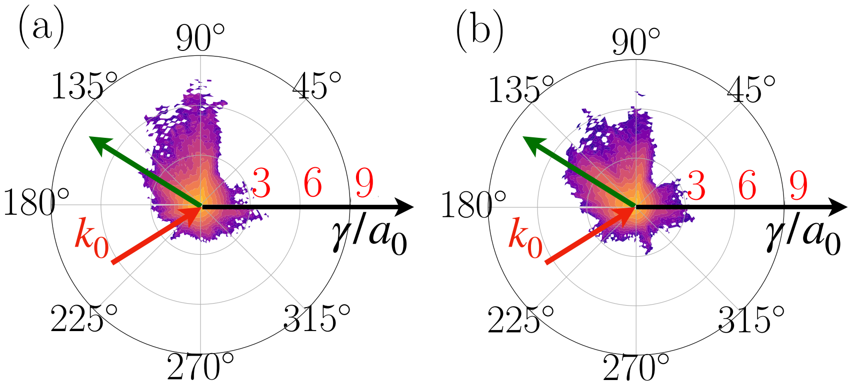

Figure 5.10: Electron energy distribution at $t = t_f$, $\theta_{inc} = 33°$ and $h = 0.4\lambda_0$ and, $a_0 = 100$ (a) and $a_0 = 200$ (b). The plasma surface is along 90°, the red arrow indicates the direction of the incident laser beam, and the green arrow, the reflected one. Note that although the ratio γ/a_0 is about the same in both panels, γ_f is about 800 in (a) and 1600 in (b).

5.5 Summary

These results are part of a published paper in Physics of Plasmas [54].

In this work, we consider a laser pulse impinging on an over dense plasma, whose surface presents a periodic modulation (grating), in order to generate large amplitude Surface Plasma Waves (SPWs). Key parameters were obtained for optimising laser-plasma coupling in the ultra-relativistic regime ($\sim 10^{22}$ W/cm^2). A systematic study in function of the laser incidence angle and intensity, a_0, showed that at ultra high laser intensities ($a_0 \geq 30$) the SPW resonance angle becomes roughly independent of a_0. A strong correlation was also observed between the optimum SPW excitation angle and the laser's angle of incidence that optimizes electron acceleration along the plasma surface. The production of high energetic electron bunches is analysed as well as the appropriate values of plasma density and surface shape to ensure SPW survival at ultra-high laser intensity. Furthermore, the parameter $n/(a_0 n_c)$ is shown as crucial for describing laser plasma coupling and SPW excitation, as it highlights the importance of the prior consideration of higher density plasma to maintain SPW excitation in the ultra relativistic regime. Finally, as a high-intensity laser illuminating the grating inevitably distort it, increasing the grating's depth provides a more robust condition for SPW excitation. This may be a way to obtain unprecedentedly high currents of energetic electrons as well as emitting radiation with interesting characteristics thereby paving the way to new experiments on forthcoming multi-petawatt laser systems. The radiation signatures in this regime will be discussed in the following chapter.

Chapter 6

From electron acceleration to radiation reaction and photon production

Contents

The findings presented in the previous chapter provide evidence that SPW excitation survives in the ultra relativistic regime ($a_0 \geq 30$). The electrons experience strong acceleration with SPW, thus we expect them to emit large amounts of electromagnetic radiation. This strong emission results in a radiation reaction (RR) force that can significantly impact the particle dynamics. As the radiation effects become increasingly more important at ultra high intensities, we investigated how RR affects the accelerated electron bunches generated by the SPW. Moreover, the emitted radiation is interesting per se. For example when lasers with intensities above 10^{22} W/cm^2 ($a_0 \approx 68$ when $\lambda_0 = 0.8\ \mu$m) interact with plasmas, it was shown that a fraction of the laser pulse energy is converted into photon emission in the multi-MeV energy range [126]. The generation of x-ray and γ-rays through laser-plasma interaction paves the way for an interesting and cost efficient complementary alternative to synchrotrons and other sources based on radio frequency accelerators [127, 128]. This chapter is organized as follows: the first section is dedicated to the electron acceleration at increasingly higher intensities whilst the second section focuses on the photon emission.

6.1 Set-up

The 2D3V simulations geometry is the same as in the previous chapters where the plasma lies in the (x, y) plane for $x \geq 0$ and its surface is along the y direction. The main parameters of the driven $P-$polarized Gaussian laser pulse and the plasma properties are given in table 6.1. The laser waist and duration parameters remain unchanged from the previous chapter 5.

Parameter	Values
Box size	$42\lambda_0 \times 72\lambda_0$
$\Delta_{x,y}$ Spatial resolution	$\lambda_0/256$
a_0 Laser strength	$0.1 \rightarrow 200$
θ_{inc} Incidence angle	$32°$
$w_\perp$ Laser waist	$5\lambda_0$
τ_L Duration	$10\lambda_0/c$
n_0 Density	$200n_c$
h Groove's depth	$0.4\lambda_0$
d Grating periodicity	$2\lambda_0$
Plasma thickness	$6\lambda_0$
Particles per cell	32 electrons/ions
Ions	mobile

Table 6.1: Recapitulation of the main parameters used in this chapter.

Indeed, in the following, we have used a mixed target consisting of a sinusoidal grating followed by a flat target after the laser impact zone. The flat region after irradiation zone allows to reduce the energy losses due to scattering of the gratings (as presented in Chapter 4) and focus on the electrons energy loss due to radiation reaction. For the sinusoidal grating we have opted for a groove depth of $h = 0.4\lambda_0$ as the previous Chapter 5 showed that deeper gratings allow to recover SPW excitation in the ultra relativistic regime. Moreover, the simulation box size has been increased from $20\lambda_0 \times 64\lambda_0$ in Chapter 5 to $42\lambda_0 \times 72\lambda_0$ in Chapter 6 in order avoid boundary conditions effects.

We perform a set of simulations with laser intensities varying from $I = 10^{16}$ to 10^{23} W/cm^2 (i.e. a_0 from 0.1 to 200 when $\lambda_0 = 0.8\,\mu$m). In Figure 6.1 we show the maximum electron energy $\mathcal{E}_f$ (in MeV) observed along the target as a function of a_0, similar to Figure 5.8 but focusing only on the case where $h = 0.04\lambda_0$ and $n_0 = 200n_c$ only (green triangles in Figure 5.8), extending the laser intensity up to $a_0 = 200$.

The data points for $\mathcal{E}_f$ in the figure below correspond to the electron energy spectrum cut-off at $t = 76\tau_0$ which roughly corresponds to circa 20 optical cycles after the laser first impinges the target (at $y = 36\lambda_0$) and the particles reach $y = 64\lambda_0$ ($= 51.2\mu$m).

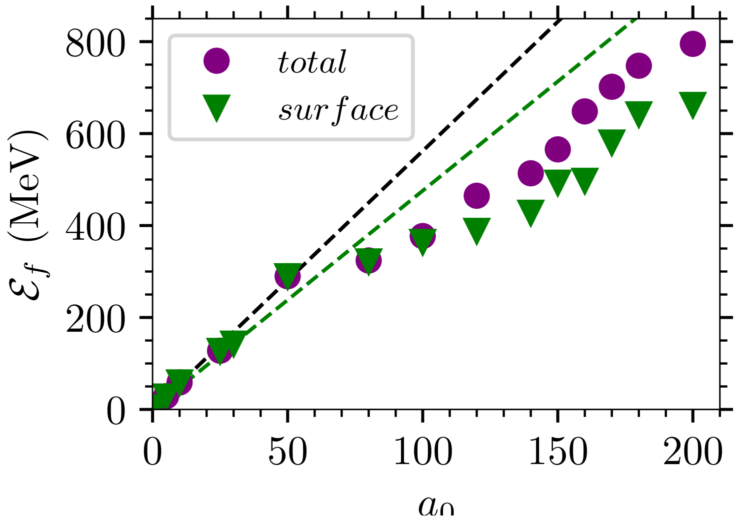

Figure 6.1: Maximum value the electron energy $\mathcal{E}_f$ in MeV ($t = 76\tau_0$) as a function of the laser strength parameter a_0. The energy of the electrons along the target (green triangles) or in the whole simulation box (purple circles). The green dashed line represents the general tendency of the results depicted in Figure 5.8 ($\mathcal{E}_f = \gamma_f m_e c^2 = (1 + 9.3a_0)m_e c^2$) and the black dashed line designates the scaling for electron acceleration via SPW ($\mathcal{E}_{f,SPW} \sim \gamma_\phi \max|\hat{B}_{\text{SPW}}| m_e c^2|$).

In the interest of consistency, we maintained the same symbol and colour code as previously. The green triangles indicate the maximum electron energy at $t = 76\tau_0$ for electrons propagating along the surface (selecting only the electrons propagating at $\phi_e = 90° \pm 6°$). The green dashed line indicates the scale $\mathcal{E}_f = \gamma_f m_e c = (1 + 9.3a_0)m_e c$ which fitted the data in Figure 5.8 with $h = 0.4\lambda_0$ and $n_0 = 200n_c$. We notice that the slope of the function no longer accurately predicts the tendency of $\mathcal{E}_f$ when a_0 increases beyond 50, as the green triangles are well below the slope. Superposed on the figure, we show the maximum $\mathcal{E}_f$ of the electrons in the whole simulation box as purple circles. Up until $a_0 = 100$, the total maximum $\mathcal{E}_f$ of electrons coincides with the energy of the electrons observed along the surface. This overlap implies that up to a threshold, the electrons are mainly accelerated through the SPW acceleration mechanism. The black dashed line represents an upper limit of the electron energy gain in the SPW obtained from [38] and used in Chapter 4 (see Eq.(4.23)):

$$\mathcal{E}_{f,SPW} \sim \chi' \gamma_\phi \max|\hat{B}_{\text{SPW}}| m_e c^2 \tag{6.1}$$

where $\chi' = 1$ is a constant of order one, and $\gamma_\phi = (1 - v_\phi^2/c^2)^{-1/2}$. We notice that up until $a_0 = 50$, the maximum electron energies agree well with the upper limit of the electron energy gain in the SPW. Beyond $a_0 = 100$, we observe a discrepancy. However, for this value of a_0 and above, RR effects (not turned on here) might be important, so we defer the interpretation to a more complete analysis. In the following, we will refer to these points without RR as the control case.

6.2 Energy loss due to radiation reaction

As pointed out in the Chapter 2.3.2, radiation can be the dominant reason for energy loss for ultra-relativistic particles. In order to gauge the importance of RR for increasingly higher values of a_0, we first compare the different radiation treatments implemented in Smilei (briefly presented in Chapter 2) and compare them with the control case where no RR is included.

6.2.1 Comparison between radiation models

In Figure 6.2, we contrast the maximum $\mathcal{E}_f$ as a function of a_0 obtained for the control case (purple circle) with those obtained from simulations where the RR was accounted for by a "corrected" classical model (upward orange triangle) and by a quantum model (red square). With "corrected" classical model we intend simulations performed with the corrected Landau Lifshitz (cLL) and for quantum model those done with Monte-Carlo (MC). For clarity, we will only show the comparison between the three different set of simulations for $a_0 = 50$, 100, 150 and 200.

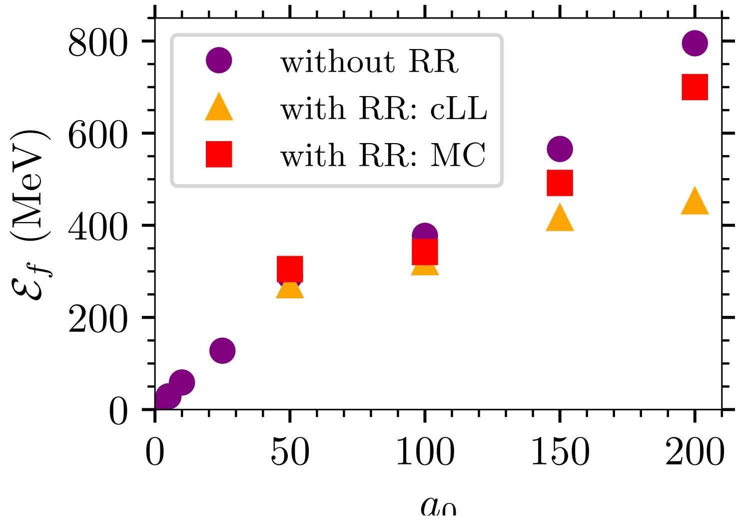

Figure 6.2: Maximum of electron energy $\mathcal{E}$ in MeV as a function of the laser strength a_0 observed at $t = 76\tau_0$ in the whole simulation box when neglecting radiation reaction (purple circle), when considering classical radiation reaction with corrected Landau Lifshitz (orange triangle) and when taking into account quantum radiation correction with Monte Carlo (red square).

For $a_0 < 100$, the loss of energy due to radiation reaction effects is negligible compared to the acquired energies. However, from $a_0 = 100$ onward, we notice that the energy loss by radiation becomes more apparent as a_0 increases. Furthermore, we notice a stark difference between the two radiation models when $a_0 \geq 150$. For $a_0 = 150$, we obtain a 26.4% decrease in the maximum electron energy when using cLL and 13% with the MC model if we compare these points to the control case. While the percentage of energy loss by radiation estimated with MC simulations remains nearly the same when increasing the laser intensity to $a_0 = 200$ (12%) the energy loss increases up to circa 43.1% when using cLL. As a result, the $\mathcal{E}_f$ obtained when using cLL only changes slightly from circa 416 MeV for $a_0 = 150$ to 452 MeV for $a_0 = 200$. A possible reason for the discrepancy between the models might be due to the nature of emission, which will be subsequently discussed.

Figure 6.3 shows the electron energy spectra for each a_0; maintaining the same colour code as before: with purple orange and red representing respectively the simulations performed without RR, with the classical radiation model (cLL) and with the quantum radiation model (MC).

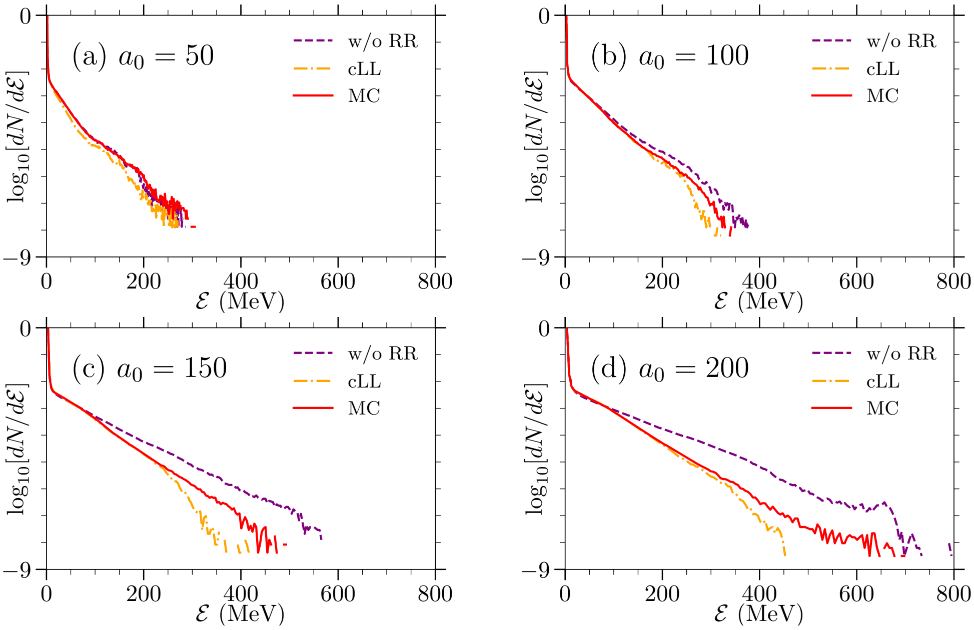

Figure 6.3: Electron energy spectra in MeV for $n_0 = 200n_c$ taken at $t = 76\tau_0$ for a) $a_0 = 50$, b) $a_0 = 100$, c) $a_0 = 150$ and d) $a_0 = 200$. when using a classical radiation model (corrected Landau Lifshitz, cLL, dashed orange), a quantum radiation model (Monte-Carlo, MC, solid red) and without radiation reaction (dotted purple).

We notice in Figure 6.3(a) that the three spectra are nearly indistinguishable for $a_0 = 50$. While a slight difference can already be noted in panel (b) for $a_0 = 100$, the distinction between the three models becomes more evident when further increasing a_0. Indeed, when comparing the spectra obtained from the simulations with the classical and quantum models of RR against the control case for $a_0 = 150$ and 200, we see that the electron energy is largely overestimated when the RR is not included. However, we observe an energy difference between the cLL and MC spectra very clearly visible at $a_0 = 200$. Already in panel (c) for $a_0 = 150$ we see that very few electrons have energies above 400 MeV when using cLL, but the cut off energy is closer to the cut-off energy of the MC spectra than to the control case. In contrast, for $a_0 = 200$ (panel (d)), the cut-off energy of the MC spectra approaches the energies obtained from the simulation where RR was not accounted for. These findings suggest that, above a certain a_0, an overestimation of the radiation emitted via the cLL model results in an energy cut-off which does not increase significantly with a_0 when considering a classical radiation model. In this case, stochasticity becomes more important when increasing a_0. Indeed, the cLL model, considering a continuous emission, overpredicts the energy loss. On the other hand, the quantum description of photon emission consists of a series of discrete events determined stochastically by emission probabilities. The electron recoil after a discrete photon emission results in a discontinuous RR force. Due to the discrete nature of quantum emissions, there is a non null probability in MC simulations that some electrons do not emit photons, and therefore reach higher energies similar to those obtained in simulations where RR was not included [99, 129]. This phenomena, called quantum quenching, might explain the reason behind the high electron energies obtained with MC for $a_0 = 200$ as seen in panel d of Figure 6.3. Another possible explanation is that, during the process stochastic MC emission, an electron can embark on a new trajectory which is even more favourable for acceleration.

The preceding figure depicted the electron energy spectra over the whole simulation box at $t = 76\tau_0$. In Figure 6.4, we confront the total spectra (solid lines) with the spectra obtained when considering only the electrons accelerated along the surface (dotted black line), $\phi_{e,surface} = 90° \pm 6°$, and in the specular direction (green dashed line), $\phi_{e,specular} = 148° \pm 10°$. The left column correspond to $a_0 = 150$ and the right column to $a_0 = 200$. All three spectra are presented for the case where (a)-(d) there is no RR, (b)-(e) with the cLL model, and (c)-(f) with the MC model.

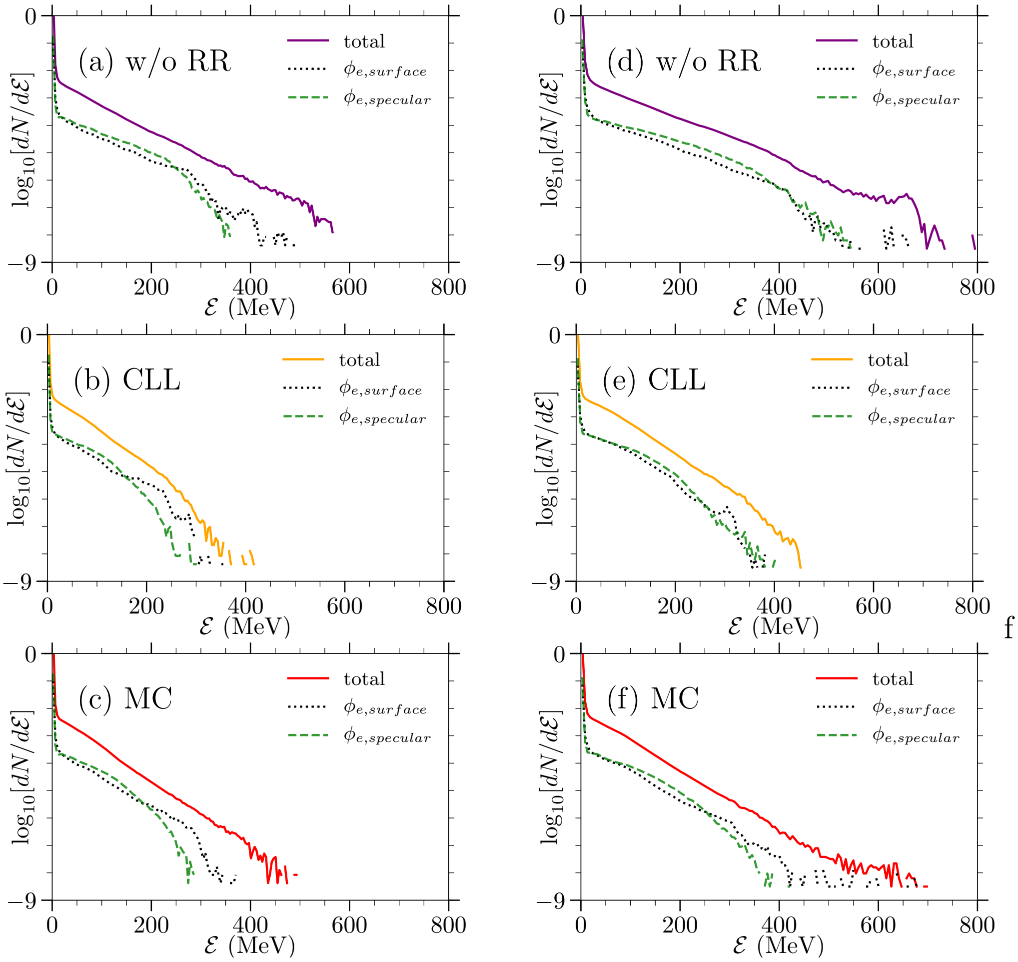

Figure 6.4: Electron energy spectra in MeV taken at $t = 76\tau_0$ for $n_0 = 200n_c$ (a)-(c) $a_0 = 150$ and (d)-(f) $a_0 = 200$. The solid coloured line corresponds to the total spectra observed in the simulation code (purple, orange and red are respectively for the simulations performed without RR, with cLL and MC), the black dotted line represents the spectrum of the detected electrons along the surface ($\phi_{e,surface}$) and the green dashed line the electrons detected in the specular direction ($\phi_{e,specular}$).

For $a_0 = 150$, the spectrum shape for the electrons accelerated in the reflected direction of the laser pulse remains similar, albeit with a lower cut-off energy of around 300 MeV (instead of 350 MeV) with cLL and 280 MeV when using MC. Conversely, the cut-off energy of the electrons accelerated parallel to the plasma surface decreases from around 500 MeV in the control case to approximately 350 MeV when including RR. The fastest electrons, accounted for by the continuous line, correspond to a collimated bunch propagating at an angle $\phi_e = 20°$ with respect to the target's interface (i.e. $\phi = 90°$) that after acceleration excited the surface wave. The left column panels suggest that regardless of the RR model, there are electrons accelerated along the surface over a large angle and the fastest electrons have already left the surface at $t = 76\tau_0$.

For $a_0 = 200$, we obtain a similar result: the spectra of both directions of observation (i.e. along the surface and in the specular direction) overlap when (d) not including RR and (e) including classical RR although, once again, the fastest electrons have already left the surface. However, contrary to the $a_0 = 150$, a small quantity of electrons still on the surface are accelerated to energies close to the maximum value when including quantum RR.

Based on this analysis, we now want to focus on the higher a_0 case so as to investigate the high energy photon emission processes. **In the remaining part of this chapter, all simulations that include RR effects are henceforth performed with the MC model.**

6.2.2 Effect of RR on the electron energy distribution

Figure 6.5 provides a recap of the electron energy spectra for increasing laser intensities a_0 when including the radiation reaction with the MC model (solid lines) and without RR (faded dashed line). At $a_0 = 50$, the discontinuous emission as described by the MC model has no effect and only comes into play from $a_0 \geq 100$ forwards.

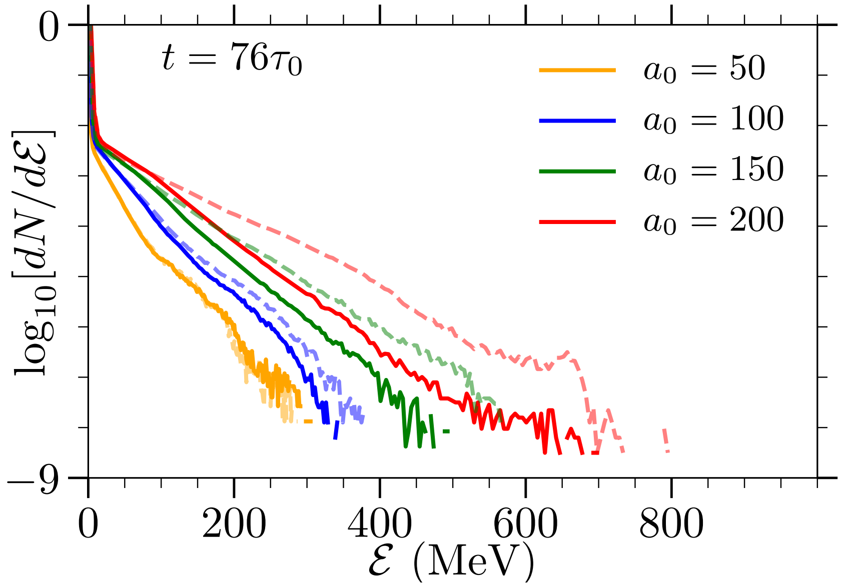

Figure 6.5: Electron energy spectrum (in MeV) for different a_0 for simulations performed with Monte Carlo (solid line) and without radiation reaction (faded dashed line) at $t = 76\tau_0$ and for $n_0 = 200n_c$.

In Figure 6.6 we show respectively the electron energy distribution and the electron phase space in the y-direction parallel to the surface at $t = 76\tau_0$ for (a)-(b) $a_0 = 100$, (c)-(d) $a_0 = 150$ and (e)-(f) $a_0 = 200$. As reminder, in the figures depicting the electron energy distribution, $\phi_e = 90°$ designates the interface between the vacuum (left) and the plasma (right). The red arrow represents the incident direction of the laser pulse while the green arrow shows specular direction.

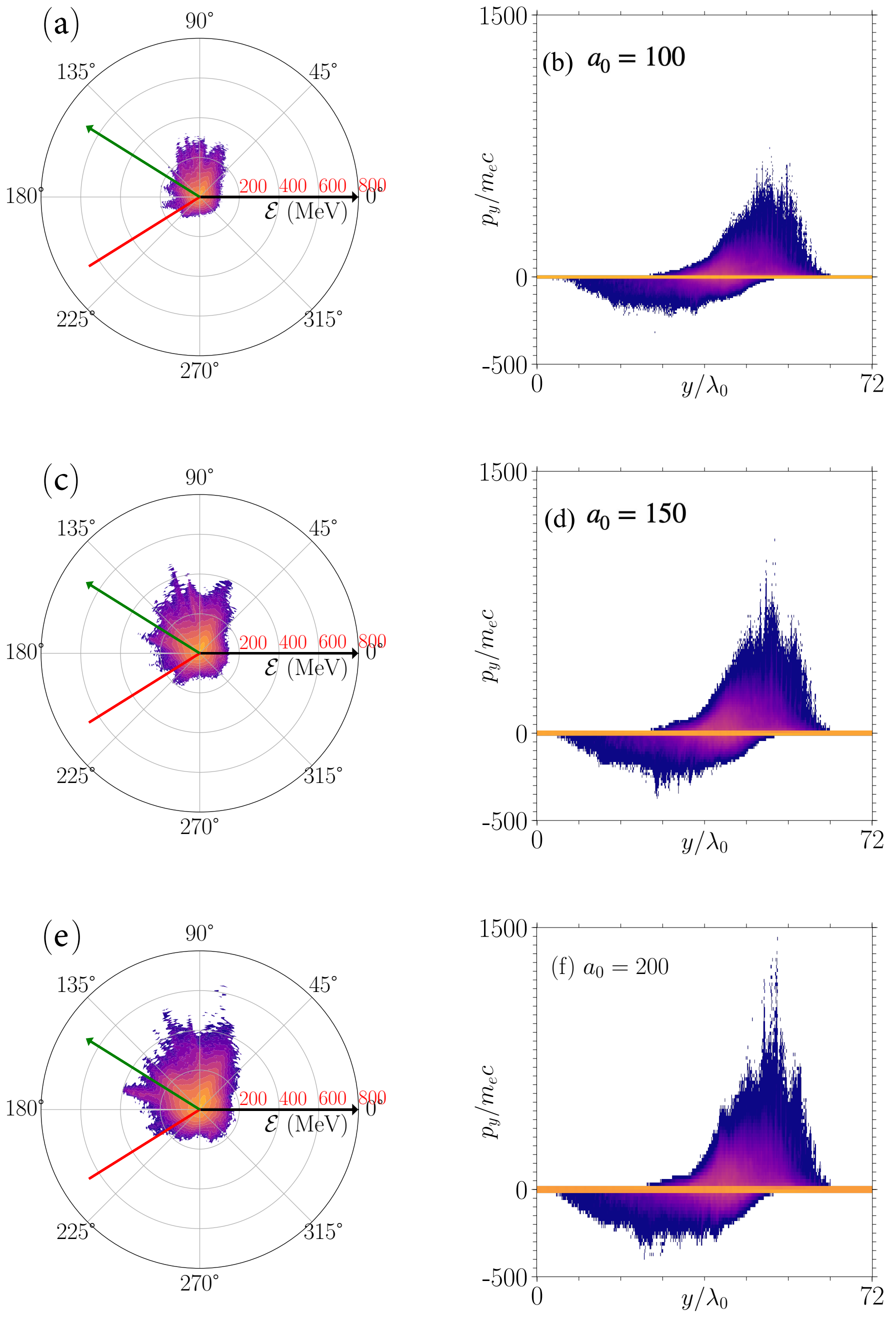

Figure 6.6: The left column represent the electron energy distribution at $t = 76\tau_0$ with 90° being the plasma surface and the direction of the incident and reflected laser beam indicated by the red and green arrow respectively; the right column correspond to the phase space $(p_y/m_ec, y/\lambda_0)$ of the electrons in the simulation at $t = 76\tau_0$. The upper row (a)-(b) are for $a_0 = 100$, the middle row (c)-(d) for $a_0 = 150$ and the bottom row (e)-(f) for $a_0 = 200$ and $n_0 = 200n_c$. All simulations are performed with the MC model.

Notice that in Chapter 5, the same simulation without RR for $a_0 = 100$ is presented in Figure 5.10(a), where the snapshot of the electron energy distribution corresponds to an earlier time in the simulation ($t = 72\tau_0$) and the energy axis is in γ. Increasing a_0 leads to higher electron energies but also to a broader distribution. When presenting the electron energy distribution in chapter 4 and chapter 5 for $a_0 = 5$ and $a_0 = 30$, we showed that for those intensities the most accelerated electrons were predominantly along the surface and collimated in said direction. In Figure 6.6 (a)-(d) however, the electron energies in the specular direction and at a larger angle with respect to the surface (i.e $\phi_e = 90° \pm 20°$) increases with a_0 as well.
The corresponding phase spaces (p_y/m_ec,y/λ_0) are plotted in Figure 6.6(b)-(f), in order to identify more precisely the different acceleration mechanisms at play. The figures show areas where more important bunching of electrons reaching higher values of p_y/m_ec are obtained when increasing a_0. However, the periodicity of the electron bunches, which is a characteristic signature of electron acceleration by SPW, even if still visible, is smoothed out implying the presence of other acceleration mechanisms.

It highlights the importance of taking into account radiation reaction mechanisms in the ultra high interaction laser plasma regime. Moreover we show that there is a limitation to the efficiency of this process. With the aim of obtaining very high energy electron bunches, the increase of a_0 when keeping SPW excitation in the considered configuration reaches limits. That's why we next vary geometrical parameters of the target looking for a more appropriate configuration.

6.2.3 Comparison between different target geometries

In order to assess the interest of using resonant gratings in the ultra relativistic regime, we compare in this subsection different target geometries for $a_0 = 200$ and $n_0 = 200n_c$ using MC in order to take into account RR effects.

In a first time, we compare a flat target against the optimized sinusoidal grating presented in section 6.1. Figure 6.7 presents the electron energy spectrum detected throughout the simulation box for the sinusoidal grating (red line) and the flat target (green line). With a flat target, the cut-off energy ($\mathcal{E}_f \sim 1000$) surpasses the electron energy reached with the resonant sinusoidal grating ($\mathcal{E}_f \sim 700$).

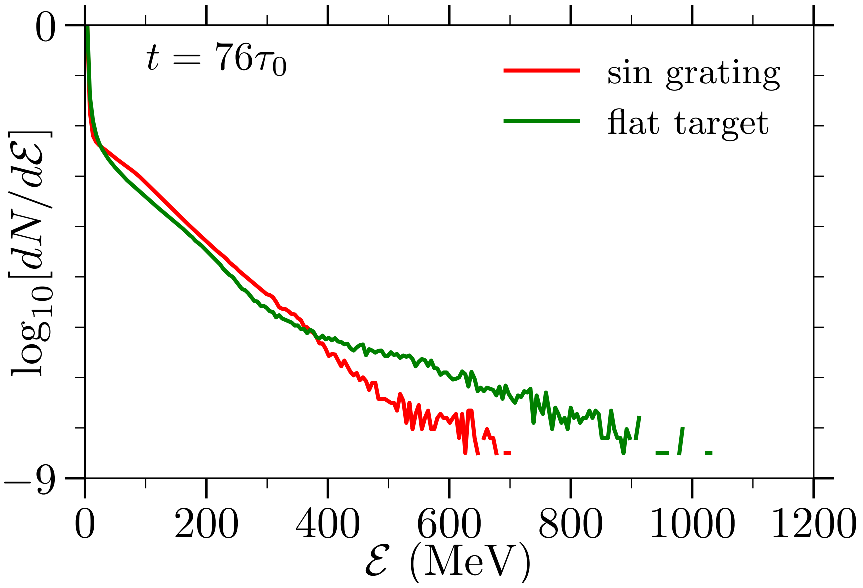

Figure 6.7: Electron energy spectrum in MeV where the green line corresponds to the case using the flat target geometry and the red line when using the optimized sinusoidal grating (as defined in section 6.1) at $t = 76\tau_0$ for $a_0 = 200$ and $n_0 = 200n_c$.

While the electrons reach higher energies with a flat target, the corresponding electron energy distribution featured in 6.8(a) shows that the most energetic electrons are predominantly accelerated in the vacuum, focused along a direction close to of the reflected laser pulse as a result of vacuum laser acceleration. Due to the surface deformation, the target acts as a focalizing mirror increasing its intensity in the vacuum which explains the large electron energies obtained.

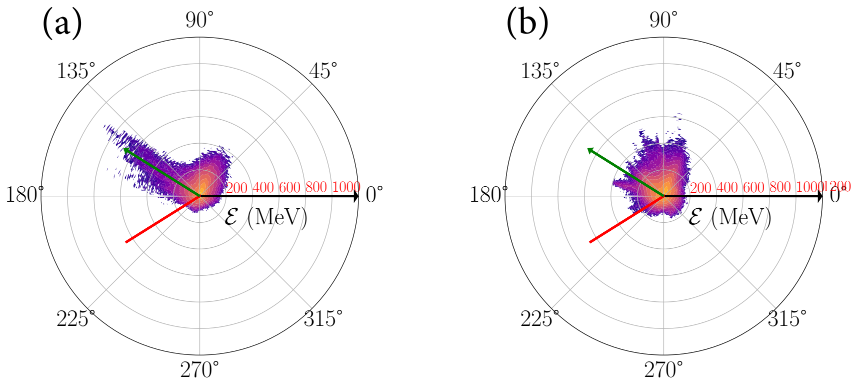

Figure 6.8: Electron energy distribution in MeV at $t = 76\tau_0$ for $a_0 = 200$ and $n_0 = 200n_c$ when using a (a) flat target and (b) sinusoidal grating as defined in section 6.1. Note that 90° being the plasma surface and the direction of the incident and reflected laser beam indicated by the red and green arrow respectively.

Without RR (not shown here), the electrons are accelerated exactly in the specular direction ($\phi_e = 148°$). However, when taking into account the RR effects provided by the MC model, the fastest electrons propagate in a slightly altered direction ($\phi_e = 141°$).

Confronting side by side the magnetic field B_z/a_0 in the real space and a close up of the electron charge density in Figure 6.9 we can clearly see that in the case of sinusoidal grating, the electrons are mainly found in bunches along the surface while in the flat target case we can discern electrons accelerated in the vacuum in the same direction of the self focused laser beam. The self focusing of the laser results from the relativistic local increase in electron mass and to plasma density redistribution under the action of the ponderomotive force [130] occurring during ultra relativistic laser pulse–plasma interaction. Indeed, the plasma becomes a concave mirror due to the surface deformation. In the case of a resonant sinusoidal target, the electrons have higher charge density ($\rho_e \sim 5n_0$) than in the plasma mirror case where electrons reach higher energies but with small charge density ($\rho_e \sim 0.1n_0$). This point might have importance for applications.

Sinusoidal target

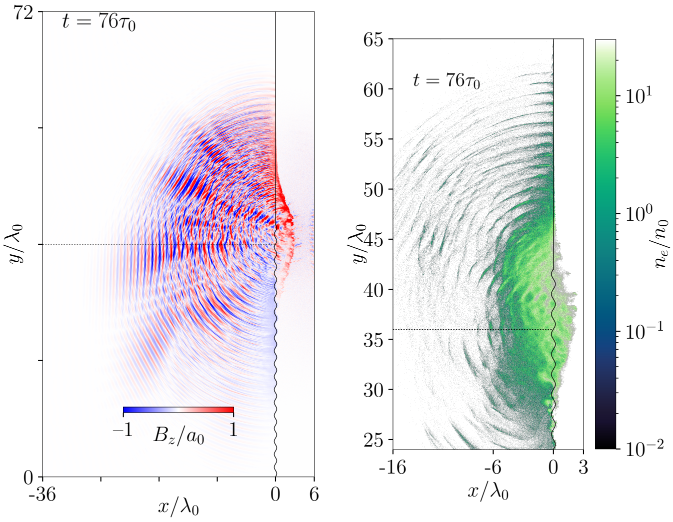

Flat target

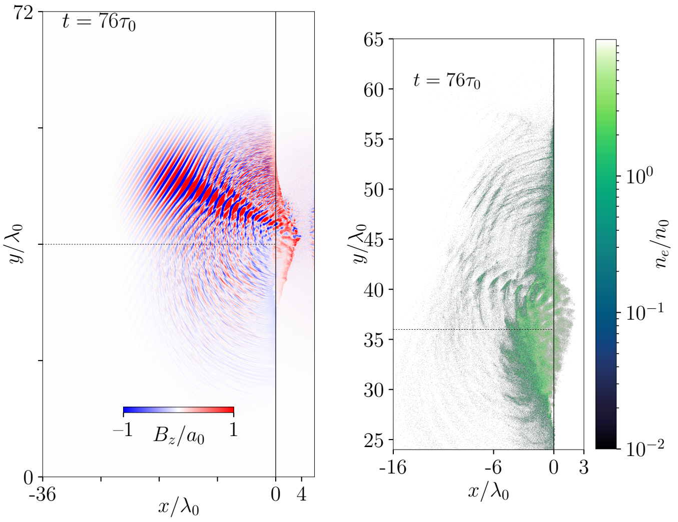

Figure 6.9: For $a_0 = 200$ and $n_0 = 200n_c$: Upper row: magnetic field B_z/a_0 and electron charge density when using sinusoidal target as defined in section 6.1. The different orders seen in the upper left panel are due to sinusoidal grating. Bottom row correspond to the same diagnostics with a flat target. The light gray dotted line indicates the spot of impact where the maximum of the laser pulse arrives.

Wave front rotation (WFR) at ultra high intensity

Let us recall the setup from Chapter 4.1.1 consisting in a tailored target with blazed grating and a flat surface short after the interaction zone. Our findings provided strong evidence that the use of a laser pulse with WFR focused at a certain distance from the surface permitted to tune SPW amplitude and the resulting electron bunches in the relativistic regime ($a_0 = 5$). In this subsection we show that our proposed scheme also enhances electron acceleration in the ultra relativistic regime. In the following, we have used a blazed grating with $\phi_b = 13°$ ($h = 0.44\lambda_0$) instead of the sinusoidal grating while maintaining the parameters of Tab. 6.1 and $a_0 = 200$ and using MC in order to take into account RR effects. For the simulations with WFR, the laser is focused at a distance $x_f = 25\lambda_0$ from the target and the WFR parameter is $\Delta\beta = 67$ mrad, which corresponds to the optimal parameter for $\theta_{inc} = 30°$ in Chapter 4.

In Figure 6.10 we add onto Figure 6.7 the electron energy spectrum for this tailored target with WFR (blue solid line) and without WFR (faded blue dashed line).

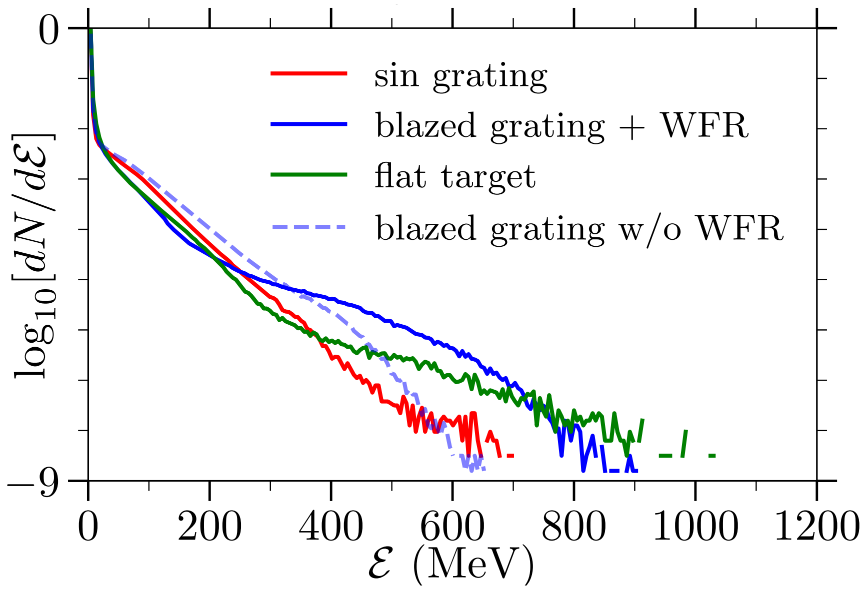

Figure 6.10: Electron energy spectrum in MeV for different surface geometry at $t = 76\tau_0$ for $a_0 = 200$ and $n_0 = 200n_c$.

Without WFR, the optimized blazed grating does not increase the cut-off energy with respect to the sinusoidal target although it does increase the quantity of electrons accelerated. With WFR, a large improvement is observed as more electrons are accelerated to much higher energies, up to $\mathcal{E} \sim 900$ MeV, close to those obtained with our plasma mirror.

The evolution in time of the electron energy distribution of both the flat target case and our WFR scheme, featured in Figure 6.11, provides further insight into the electron dynamics. At $t = 64\tau_0$ the laser is still interacting with the overdense plasma. At $t = 74\tau_0$ the laser pulse is already completely reflected while $t = 84\tau_0$ designates the end of the simulation, well after the laser impinged on the target. In the case of the flat surface (upper row), the electrons are accelerated into the vacuum along the specular direction of the laser. In the case of the optimized target and WFR, while we observe a broadening of the distribution along the surface, we notice near the end of the simulation energetic electron bunches still along the interface.

Evolution in time with the flat target

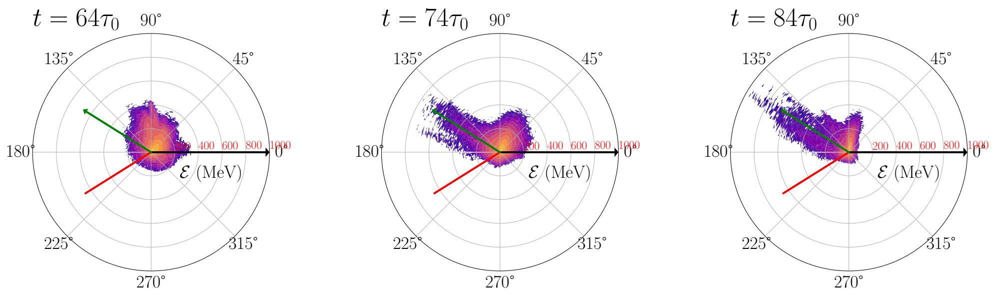

Evolution in time with the optimized target and WFR

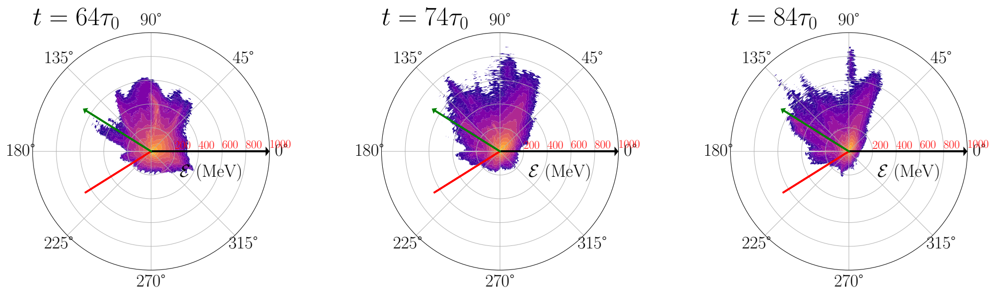

Figure 6.11: Electron energy distribution at $t = 76\tau_0$ for $a_0 = 200$ and $n_0 = 200n_c$, with 90° being the plasma surface and the direction of the incident and reflected laser beam indicated by the red and green arrow respectively.

It should be noted that electrons accelerated along the surface are characteristic of SPW excitation. Even though the resonance conditions broadens in the UHI regime of laser-plasma interaction, the use of a laser with WFR ensures that the SPW resonance condition is satisfied for one or more of the wavelength sweeping across the grating at slightly different incident angles.

Grating deformation

The close up in Figure 6.12 of the ion charge density for $a_0 = 200$ and $n_0 = 200n_c$ using the optimized sinusoidal grating, the optimized blazed grating and the former with WFR early in the interaction (at $t = 66\tau_0$) sheds a light on the apparent improvement in electron acceleration when using WFR. We remind that in the case of WFR, the laser is focused at a distance from the target which induces an apparent sliding velocity along the surface with the wavefronts striking the target at different points in time. The ion charge density is normalized to n_0 so as to make the local plasma compression more visible for each scenario. A strong local plasma compression is observed with the optimized sinuoidal grating in Figure 6.12a) and with the optimized blazed gratinging in Figure 6.12 b) amounting to three times the electron charge density. The seemingly forward shifted location of the plasma compression when using the blazed grating without WFR might be due to the fact that this grating increases the value of the diffraction along the surface, increasing the laser-plasma coupling in that particular direction. While the grating is not completely destroyed, the plasma compression affects the laser absorption. Panel c) of Figure 6.12 also yields an interesting result as the use of WFR permits to decrease the laser ablation and preserves the grating periodicity for longer. Thanks to the WFR, instead of the maximum of the laser amplitude impinging on one specific spot of the target, each individual wavelength will strike the target at different points in time. Interestingly enough, in this scenario there seems to be plasma filamentation though this should be further investigated.

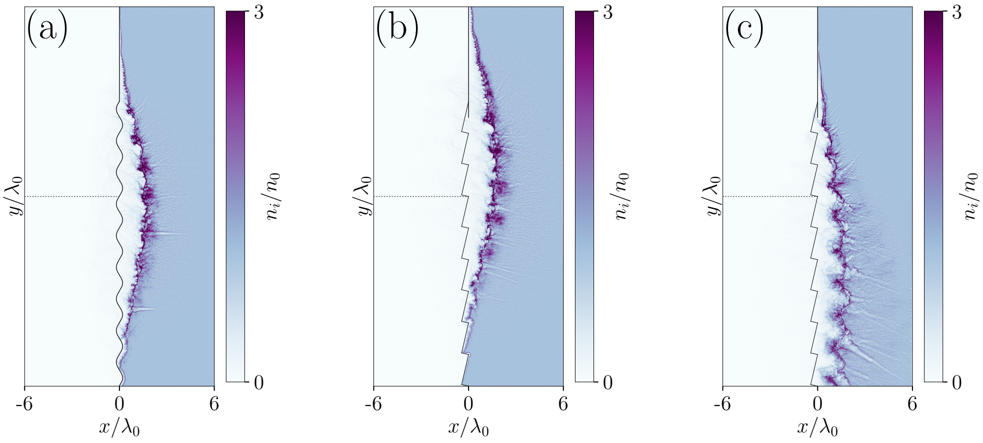

Figure 6.12: Ion charge density normalized to the electron charge density for $a_0 = 200$ and $n_0 = 200n_c$ at $t = 66\tau_0$ when using (a) the optimized sinusoidal grating, (b) the optimized blazed grating and (c) the former with WFR.

6.3 Photon emission

As mentioned in the introduction of this chapter, a large fraction of the laser light may be transformed into higher frequencies photons up to γ-ray and beyond for high enough laser intensities [126, 131]. Studies have shown that the stochastic nature of photon emission electron can greatly affect the electron energy distribution [132]. Therefore, in order to complete the investigation of the electron acceleration in the previous section, we will now focus taking the Radiation reaction into account via Monte Carlo model on the resulting photon emission and compare the efficiency of γ-ray generation between different a_0 and target geometries. It should be noted that in our simulations, the produced photons are "frozen" for the rest of the simulation time. Once emitted, the photons are frozen in time which will aid to understand at which time and position they are mostly emitted.

6.3.1 Impact of increasing a_0

Considering the configuration of a laser impinging on the optimized sinusoidal plasma target with $n_0 = 200n_c$, we present in Figure 6.13 the photon energy angular distribution, $\mathcal{E}_\gamma$ for (a) $a_0 = 50$, (b) $a_0 = 100$, (c) $a_0 = 150$ and (d) $a_0 = 200$ at $t = 76\tau_0$. In order to improve the visualization, the energy scaling of the upper row has been limited to $\mathcal{E}_\gamma = 200$ MeV while the energy scaling of the bottom row goes up to 600 MeV. The photons are considered to be high energy when $\mathcal{E}_\gamma > 2m_ec^2$. Moreover, we assume the plasma to be transparent to the high-energy photons.

The (a)-(d) photon energy distribution and their respective (e) energy spectrum show the maximum energy of photons detected throughout the simulation box. Not surprisingly, we see that increasing the laser intensity increases the probability of emitting photons up to higher energies as well. In our scenario, the total photon energy is proportional to the electron energy by $\mathcal{E}_\gamma \propto \mathcal{E}/2$. Given that ultra-relativistic electrons emit at a small angle $1/\gamma$ (see the discussion in section 2.3.1), we assume that the photons are emitted along the electron velocity at the time of emission.

We stated beforehand that the generated photons are collected once emitted, therefore the figures at $t = 76\tau_0$ shows the integral of all the produced photons emitted up a given timestep. For all these cases, the laser arrives on the target around $t = 56\tau_0$ and the most energetic photons are emitted around $t = 66\tau_0$ after which some photons are still emitted at lower energies but becomes quasi indiscernible in the energy distribution due to the presence of the photon emitted earlier. Keeping in mind that the laser pulse has a duration of $10\lambda_0$, we conclude that most photons are generated during the laser plasma interaction.

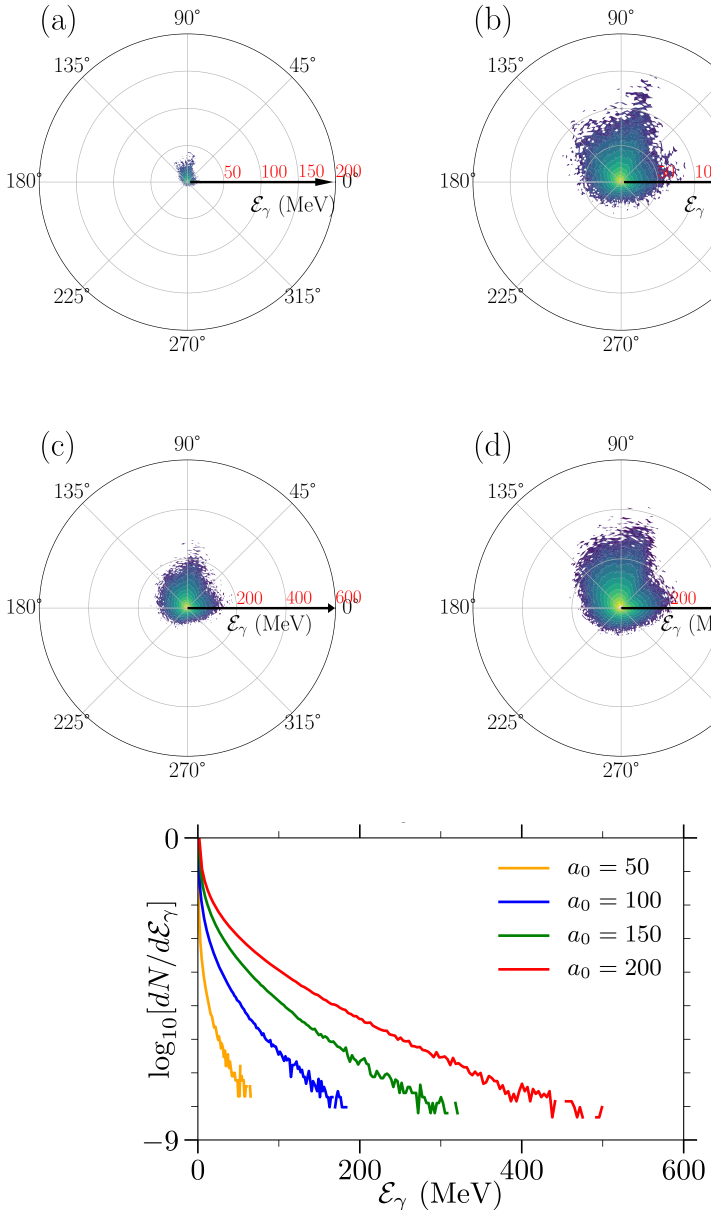

Figure 6.13: For $n_0 = 200n_c$ at $t = 76\tau_0$: photon energy distribution $\mathcal{E}_\gamma$ as a function of the emission angle for a) $a_0 = 50$, b) $a_0 = 100$, c) $a_0 = 150$ and d) $a_0 = 200$ with $n_0 = 200n_c$ and $\phi_e = 90°$ representing the interface between vacuum (left) and plasma (right); (e) is the photon energy spectra in MeV for the different a_0 described above.

We recall the definition of the quantum parameters of electrons and high energy photons:

$$\chi = \frac{\gamma}{E_s}\sqrt{(\mathbf{E}+\mathbf{v}\times\mathbf{B})^2-(\mathbf{v}\cdot\mathbf{E})^2/c^2}\,, \tag{6.2}$$

$$\chi_\gamma = \frac{\gamma_\gamma}{E_s}\sqrt{(\mathbf{E}+(\boldsymbol{c}\times\mathbf{B})^2-\boldsymbol{c}\cdot\mathbf{E})^2/c^2}\,, \tag{6.3}$$

where **c** is the photon velocity, **E** and **B** are the local fields experienced by the particle. These values are calculated for each macro particle in the PIC code. Right after the emission of a high energy photon, the above mentioned quantities are related by:

$$\gamma_\gamma/\gamma = \chi_\gamma/\chi \tag{6.4}$$

with $\gamma = \mathcal{E}/(m_e c^2)$ and $\gamma_\gamma = \mathcal{E}_\gamma/(m_e c^2)$ the electron and photon energies, respectively. When electrons have $\chi \sim 0.1$, the emitted photons can attain energies superior to the electron mass at rest and stochastic effects become non negligible [99]. The distribution of the χ of the electrons is depicted in Figure 6.14 for two different times.

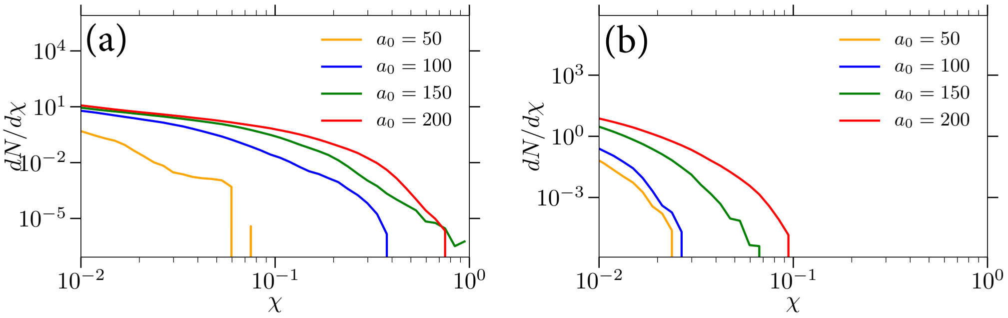

Figure 6.14: Electron quantum parameter χ spectrum at (a) $t = 66\tau_0$ and (b) $t = 76\tau_0$ for different a_0 and $n_0 = 200n_c$.

We notice that at (a) $t = 66\tau_0$, which corresponds to the time where the end of the laser is interacting with the plasma, the maximum of the χ parameter approaches ~ 0.07 for $a_0 = 50$ and $\chi > 0.1$ when increasing a_0. Using $a_0 = 100$ leads to $\chi \sim 0.4$ while $a_0 = 150$ and 200 lead to $\chi \sim 0.8-0.9$ respectively. Ten optical cycles after, χ decreases by nearly an order of magnitude yet for $a_0 = 150$ and 200 the quantum parameter remains close to $\chi \sim 0.1$. This result corroborates the idea that for our scheme with an oblique incident laser impinging on a resonant grating, $\mathcal{E}_\gamma$ increases with a_0 because the ultra-relativistic electrons can achieve higher χ values. Higher values of χ also translates to a more important difference between the classical and quantum predictions of RR [133] which explains the increasing difference in energy spectrum and cut-off energies between the radiation models from $a_0 = 150$ onward in Figure 6.3. In the regime where $a_0 \gg 1$ and $\chi \leq 1$, the quantum radiation reaction can be attributed to the electron recoil due to the spontaneous emission of multiple incoherent photons [134]. Given that in our scenario, the quantum parameter χ of the electrons is below one, the χ_γ right after emission will also be inferior to one and thus we can neglect eventual decay of the photons emitted by the electrons into electron-positrons pairs.

6.3.2 Photon emission in different geometries

In the following we compare the photon emission resulting from the interaction of a laser pulse with $a_0 = 200$ impinging on an over-dense plasma, $n_0 = 200 n_c$, presenting different target geometries as described in section 6.2.3. The photon energies distributions as function of the emission angle for each case are gathered in Figure 6.15 where (a) represents the case with a flat target, (b) with the optimized sinusoidal grating as before and (c)-(d) with the tailored blazed grating, respectively with WFR null $\Delta\beta = 0$ (c) and with WFR $\Delta\beta = 67$ mrad (d).

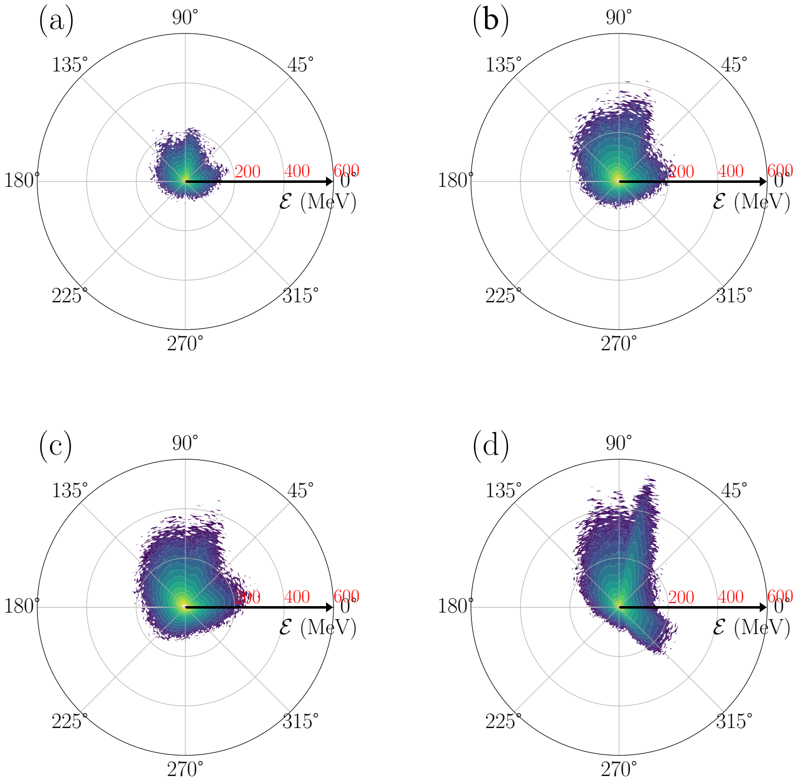

Figure 6.15: Photon energy distribution $\mathcal{E}_\gamma$ taken at $t = 76\tau_0$ for a a laser pulse $a_0 = 200$ impinging on a) a flat target, b) an optimized sinusoidal grating and c)-d) a tailored blazed grating. The laser pulse has c) no wavefront rotation and d) wavefront rotation with WFR $\Delta\beta = 67$ mrad. In all simulations $n_0 = 200 n_c$.

These figures suggest that using a resonant grating that allows SPW excitation enhances the emission of photons as $\mathcal{E}_\gamma$ doubles with respect to the flat target case. For instance, we find photons with energies extending as high as $\sim$ 400 MeV for both resonant gratings in (b) and (c) while for the flat the maximum is found for $\sim$ 200 MeV. Interestingly enough, while using the sinusoidal or the blazed grating results in roughly the same maximum energy attainable by the photons, more photons with energies above 300 MeV are emitted along the surface at the vacuum side when using the smartly tailored blazed grating. This effect could be due to the enhancement of laser-plasma coupling when using blazed gratings as explained in Chapter 4.

Furthermore, when using the blazed grating in combination with a pulse with WFR focused at a certain distance from the target's surface, we observe in panel (d) an additional net increase of $\mathcal{E}_\gamma$. Indeed, while the maximum $\mathcal{E}_\gamma$ along the target is $\sim$ 350 MeV for the previous two cases, we find $\sim$ 500 MeV when using WFR with the resonant grating, amounting to a 42.8% increase in photon energy. When comparing the photon energy distribution of the resonant grating to the electron energy distributions for the same situations presented in the previous section, we notice that the most energetic photons are mainly emitted forward with an angle $< 10°$ with respect to the surface. The narrower angular distribution of the photons observed in panel (d) could be a direct consequence of using WFR.

Contrary to the resonant targets, the flat target case does not emit photons in the direction of the most energetic electrons which are accelerated in the specular direction. In fact, the photon emission only takes place when the laser beams comes into contact with the target. The photons are emitted during the duration of the laser pulse and are mainly emitted by the electrons quivering in the laser field.

The time evolution of the electron quantum parameter χ in Fig.6.16 offers an insight of the probability of emitting photons during the different moments of interaction. When comparing the χ spectrum at the beginning of the laser pulse interacting with the target (panel a), near the the end of the laser-plasma interaction (panel b), ten optical cyles after when the laser has already been reflected (panel c) and near the end of the simulation (panel d) we notice that the use of WFR (blue solid line) permits to maintain higher maximum χ along the surface for longer duration. This is coherent with the observation of a "large" field along the surface at later times. Initially, the configurations with a resonant grating (red and blue lines) surpass $\chi = 0.1$ while the planar target (green line) reaches $\chi = 0.05$. Ten cycles after the initial interaction, the three different target geometries reach $\chi > 0.5$ at $t = 66\tau_0$ (panel b). However, at $t = 76\tau_0$, the χ for both the sinusoidal and planar target fall to 0.1 and further decreases to $\chi \sim 0.03$ at $t = 84\tau_0$. These results support the hypothesis that the majority of photons are emitted during the first ten laser cycles. In contrast, the use of the blazed grating preserves χ as even without the use of WFR (faded blue dashed lines) χ remains slightly higher than 0.1 at $t = 76\tau_0$. In addition, the use of WFR permits to prolong the duration of the laser-plasma interaction as the maximum amplitude of each wavefront strike the target at different points in time and space. The extension of the interaction also translates into the conservation of higher χ along the surface with $\chi = 0.5$ at $t = 76\tau_0$ and 0.3 near the end of the simulation. Moreover, in this scenario, the emission of γ-photon by the electrons is also enhanced as the electrons do not co-propagate in the same direction of the laser and therefore radiate more. These preliminary results provide evidence in favor of studying plasmonics in the ultra relativistic regime as they could present a interesting alternative for photon sources.

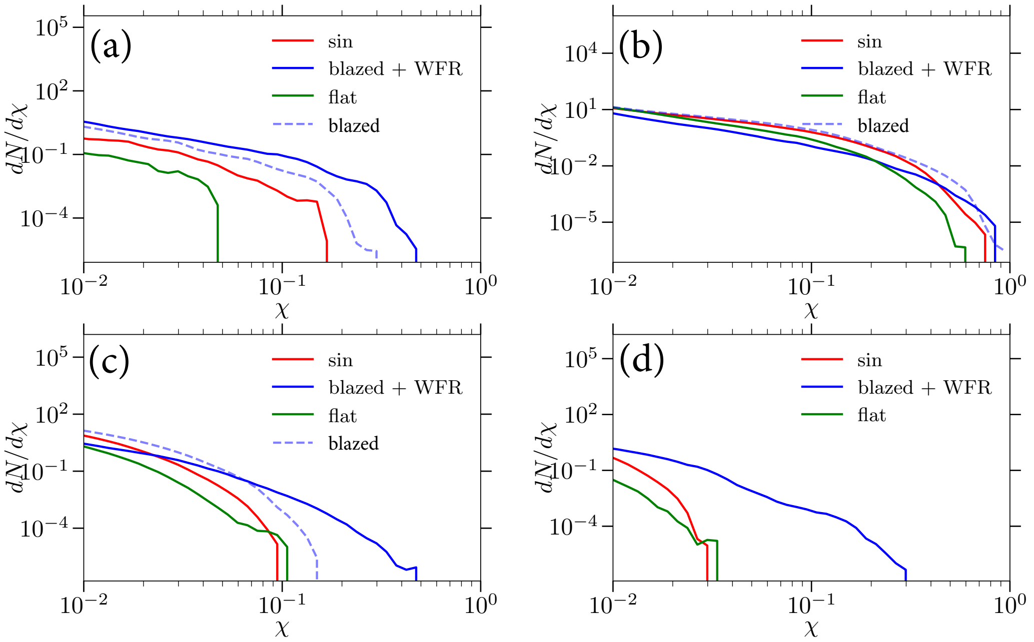

Figure 6.16: For $a_0 = 200$ and $n_0 = 200n_c$, we show the distribution of the χ parameter of the electrons for the different target geometries at different times with a) $t = 56\tau_0$ (near the beginning of the laser-plasma interaction) , b) $t = 66\tau_0$ (near the end of the laser-plasma interaction) , c) $t = 76\tau_0$ (ten optical cyles after when the laser has already been reflected) and d) $t = 84\tau_0$ (ear the end of the simulation). The different targets are distinguished by the colour: (green solid line) a flat target , (red solid line) an optimized sinusoidal grating and (blue dashed line) the optimized blazed grating with WFR.

6.4 Summary

In this preliminary work, we proved evidence that extending the study of a laser pulse impinging on an over-dense plasma with a periodically modulated surface to higher laser intensities ($a_0 > 50$) represents an interesting alternative of light source as the energy lost by electrons due to radiation emission is transferred to high-energy γ photons.

Moreover, we compared the electron acceleration and photon conversion efficiency for different target shapes and the results are summarized in Figure 6.17 where the stars represent the maximum $\mathcal{E}_\gamma$ attainable by the photons for the sinusoidal grating (red), flat target (purple) and mixed blazed grating with WFR (blue).

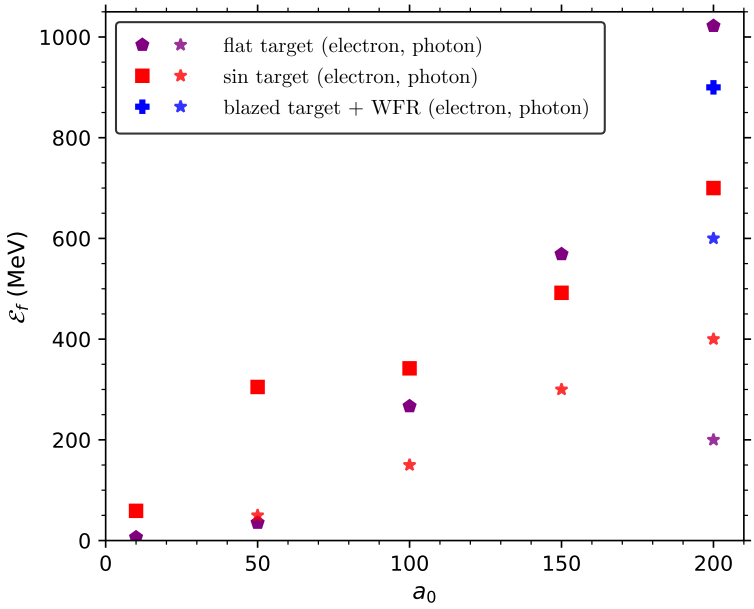

Figure 6.17: Recapitulation of the maximum electron energy at $t = 76\tau_0$ for increasing a_0 in the case of a flat target (purple pentagons), sinusoidal target (red squares) and a blazed grating (blue cross, only for $a_0 = 200$). Throughout these simulations $n_0 = 200n_c$. The faded coloured stars represent the maximum photon energy.

Depending on the desired outcome, one may opt for one target geometry or another. For example, at $a_0 = 200$, the flat target, which turns into a concave plasma mirror under our parameters, excites electrons up to higher energies but does not prove to be an efficient γ beam source. Instead, a resonant grating favours electron acceleration along the surface, we obtain less energetic electrons but with a more important charge density. In addition, the conversion into γ-photon is enhanced as the electrons do not co-propagate in the same direction of the laser and therefore radiate more. Furthermore, the idea of using a laser with WFR coupled with a tailored blazed grating, as explained in Chapter 4, is also effective when going to the ultra-relativistic regime. Indeed, thanks to this mechanism, we obtain more energetic and collimated electron bunches and improved photon emission. This scheme permits to enhance the emission and acceleration of the electrons along the surface. To go further, the finding of a scaling law as in [135] but for the electron acceleration along the surface could be investigated. Futhermore, photon beams in the MeV range are useful for many applications, including nuclear, atomic and material physics. The γ beams obtained in our mechanism could become a tool for high energy density imaging and absorption spectroscopy. On the other hand, for medical and biomedical applications, photons in the XUV or X-ray range ($<$100 keV) are preferred. Our study shows that the Monte Carlo simulation is not efficient in this limit as low photon energies in the XUV or X ray range results in a large increase of the number of photons produced and significantly slows down the simulations. For experiments with lower a_0 we need to include the treatment of coherent radiation in SMILEI for the study of surface plasma waves in the intermediate laser-plasma regime of interaction. This is also of interest for betatron radiation and high harmonic generation problems among many others, and will be the subject of future studies.

Chapter 7

Conclusion

Contents

7.1 Summary of results

The analytical and numerical work presented in this thesis has been motivated by the current capabilities and upgrade of existing multi-PW laser facilities, such as Apollon and ELI in Europe, with lasers reaching intensities beyond 10^{21} W/cm^2. Since Surface Plasma Waves (SPW) already exhibit interesting properties in the low intensity regime, manipulating and harnessing plasmonic phenomena in the ultra relativistic regime reveal promising prospects of using SPW for the obtention of high-energy particle and radiation sources using the next generation of multi-PW lasers.

The control of laser-plasma interaction can be improved using structured targets. Indeed, in Chapter 4, we consider a laser pulse impinging on an overdense plasma, whose surface presents a periodic modulation which is tailored so as to favour the generation of large amplitude SPW. Our proposed target consists in a mixed grating composed of a partially engraved target followed by a flat surface. This grating optimization allows for a better propagation of the SPW along the flat surface as it mitigates the radiation losses due to scattering of the SPW off the grooves when moving further away from the region where the laser-plasma interaction occurs. In addition, in the completely novel context of high field plasmonics, we couple this smart grating with a laser pulse with wavefront rotation (WFR). We have highlighted and modeled the "sliding focus" effect induced by WFR and its dependence on the target-to-waist distance. We showed that, despite the defocusing, the sliding focus leads to a strong enhancement of the SPW amplitude and control of its duration. This allowed us to introduce the control parameters $\Delta\beta$, the angle between two wavefronts, and x_f, the distance between the laser best focus and the target. Combining both control parameters with an appropriately tailored plasma target, showed a significant improvement to what observed in a similar situation without WFR and for non optimized targets. Such enhancement has a major impact on electron acceleration by the SPW in a relativistic regime ($a_0 = 5$), and is pivotal to the production of high charge (few 10's of pC), high energy (up to 70 MeV), ultrashort electron bunches (~ 3.6 laser periods). It provides important and clear guidelines for forthcoming experiments where one may simply smoothly tune such parameters until the optimal condition is found.

In order to ensure the excitation of electrons by SPW when using increasingly higher laser amplitudes, we provide in Chapter 5 the key parameters for optimising laser-plasma coupling in the ultra-relativistic regime ($\sim 10^{22}$ W/cm^2). A systematic study based on the laser incidence angle and intensity, a_0, showed that at ultra high laser intensities ($a_0 \geq 30$) the SPW resonance angle becomes roughly independent of a_0. A strong correlation was also observed between the optimum SPW excitation angle and the laser's angle of incidence that optimizes electron acceleration along the plasma surface. The production of high energetic electron bunches is analysed as well as the appropriate values of plasma density n_0 and surface shape to ensure SPW survival at ultra-high laser intensity. Furthermore, it is shown that the parameter $n_0/(a_0 n_c)$ is crucial for describing laser-plasma coupling and SPW excitation, as it highlights the importance of the prior consideration of higher density plasma to maintain SPW excitation in the ultra relativistic regime. Finally, as high-intensity laser illuminating the grating inevitably distorts it, we demonstrate that increasing the grating's depth provides a more robust condition for SPW excitation. This may be a way to obtain unprecedentedly high currents of energetic electrons as well as emitting radiation with interesting characteristics thereby paving the way to new experiments on forthcoming multi-PW laser systems.

In Chapter 6, we propose a new source of γ radiation based on ultra-high intensity laser ($a_0 > 50$) impinging on an over-dense plasma with periodically modulated surface, such that accelerated electrons emit high-energy photons during the interaction. Using a resonant grating favouring SPW generation enhances the acceleration and emission of the electrons along the surface. Furthermore, the idea of using a laser with WFR coupled with a tailored blazed grating, as explained in Chapter 4, is also effective when going to the ultra-relativistic regime. Indeed, owing to this mechanism, it is possible to obtain more energetic and collimated electron bunches and improved photon emission. The obtained high energy γ-photon beams could become a tool for high energy density imaging and absorption spectroscopy. However, for medical and biomedical applications, photons in the XUV or X-ray range are preferred. In order to investigate the emission of X-photon beams in experiments in the intermediate laser regime ($a_0 < 50$), we need to include the treatment of coherent radiation in SMILEI for the study of SPW in the corresponding laser-plasma regime of interaction. The implementation of said treatment in SMILEI is discussed in Chapter 3.

In a nutshell, the study of plasmonics in the ultra relativistic regime paves the way to experimentally explore alternative sources of ultrahigh energetic electron and photon sources.

At last, it should be noted that during the thesis we have studied an alternative mechanism for vacuum acceleration that develops when a relativistically intense laser irradiates the wedge of an over-dense plasma. This induces a diffracted electromagnetic wave with a significant longitudinal electric field that accelerates electrons from the plasma over long distances to relativistic energies. Since this work is not in line with the rest of the manuscript, it is not discussed in the thesis, however the full text article is included in appendix A.3.

7.2 Outlook and Perspectives

The electrons excited via the SPW mechanism could be used as an electron source with huge potential in a variety of applications such as ultra-fast electronic spectroscopy, which could lead to better understanding of potential screening and high-field effects occurring during UHI laser-plasma interaction. Moreover, this alternative electron acceleration mechanism could be of interest for injecting high charge electron beams into accelerators. Another relevant potential use for high charge electron sources, regardless of the angle-energy correlation, is heating targets for inertial fusion. On this point, it might be interesting to explore other configurations, such as a cone target with a corrugated surface inside in order to favour SPW excitation and fast electron production. In addition, ultra-intense MeV photon beams are of interest in a huge variety of research fields, from nuclear, atomic and material science to medical and biophysical applications. Also, the generation of γ-rays has the potential to offer complementary alternatives to synchrotrons [128].

Extending the study to much higher laser intensities of $I > 10^{23}$ W/cm^2, the possibility of exotic physics such as e^-e^+ pair creation and other phenomena of quantum electrodynamics (QED) can be explored [136]. Future research involves the possibility of considering electron–positron pair creation via the Breit–Wheeler mechanism [137] and confront the results with the different configurations proposed in the comparative study presented in Ref. [138, 139].

Figure 7.1: Disclaimer: not an accurate depiction of how the defense went down.

Appendices

Appendix A

Scientific contributions

A.1 Articles in peer reviewed journals

- S. Marini, **P. S. Kleij**, F. Pisani, F. Amiranoff, M. Grech, A. Macchi, M. Raynaud, and C. Riconda, "Ultrashort high energy electron bunches from tunable surface plasma waves driven with laser wavefront rotation" Phys. Rev. E. 103, L021201 (2021)
- S. Marini, **P. S. Kleij**, F. Amiranoff, M. Grech, C. Riconda and M. Raynaud, "Key parameters for surface plasma wave excitation in the ultra-high intensity regime", Physics of Plasmas 28, 073104 (2021)
- S. Marini, **P. S. Kleij**, M. Grech, M. Raynaud and C. Riconda, "Electron acceleration scheme by laser plasma wedge interaction", Physical Review Research (2023) (accepted for publication on the 10th of January)

P. S. Kleij, S.Marini, M.Grech, C.Riconda and M.Raynaud ,"Photon emission and Radiation reaction effects in surface plasma waves in ultra high intensities." *In preparation.*

A.2 Public presentations

- **P. S. Kleij**, A. Grassi, M. Grech, C. Riconda and M. Raynaud
  High Frequency Incoherent and Coherent Radiation in SMILEI: application to XUV emission from electrons accelerated in surface waves
  48th European Physical Society Conference on Plasma Physics, online (2022). **Poster presentation**

- **P. S. Kleij**, S. Marini, M. Grech, F. Pisani, F. Amiranoff, M. Raynaud, A. Macchi, and C. Riconda,
  Laser wavefront rotation as a way to control intense localized surface plasma waves and obtain ultra energetic electron bunches
  11ème Forum Lasers et Plasmas, Belambra (2021). **Oral presentation**

- **P. S. Kleij**, S. Marini, M. Grech, F. Pisani, F. Amiranoff, M. Raynaud, A. Macchi, and C. Riconda,
  Ultra-short electron bunches from tunable surface plasma wave excitation by laser with wavefront rotation
  47th European Physical Society Conference on Plasma Physics, online (2022).**Poster presentation**
  *** Winner of PPCF/EPS/IUPAD PhD Poster Prize (BPIF)**

- **P. S. Kleij**, S. Marini, M. Grech, F. Pisani, F. Amiranoff, M. Raynaud, A. Macchi, and C. Riconda,
  Ultra-short electron bunches from tunable surface plasma wave excitation by laser with wavefront rotation
  47th Conference on Plasma Physics Satellite Meeting, Online (2021). **Poster Presentation.**
  *** Winner of the ELI Poster Prize**

A.3 Full article texts

The full text of the published articles, in their journal layout, are included in the succeeding pages by order of apparition. The results of the first paper are discussed in Chapter 4 while the second paper is the object of Chapter 5. The work of the third paper is not included in the thesis discussion as it presents an alternative acceleration mechanism that does not involve SPW.

PHYSICAL REVIEW E **103**, L021201 (2021)

Letter

Ultrashort high energy electron bunches from tunable surface plasma waves driven with laser wavefront rotation

S. Marini,[1,2] P. S. Kleij,[1,2,3] F. Pisani,[3] F. Amiranoff,[2] M. Grech,[2] A. Macchi,[4,3] M. Raynaud,[1] and C. Riconda[2,*]

[1]*LSI, CEA/DRF/IRAMIS, CNRS, École Polytechnique, Institut Polytechnique de Paris, F-91128 Palaiseau, France*

[2]*LULI, Sorbonne Université, CNRS, CEA, École Polytechnique, Institut Polytechnique de Paris, F-75252 Paris, France*

[3]*Enrico Fermi Department of Physics, University of Pisa, largo Bruno Pontecorvo 3, 56127 Pisa, Italy*

[4]*National Institute of Optics, National Research Council (CNR/INO), Adriano Gozzini laboratory, 56124 Pisa, Italy*

(Received 31 July 2020; revised 22 September 2020; accepted 15 January 2021; published 15 February 2021)

We propose to use ultrahigh intensity laser pulses with wave-front rotation (WFR) to produce short, ultraintense surface plasma waves (SPW) on grating targets for electron acceleration. Combining a smart grating design with optimal WFR conditions identified through simple analytical modeling and particle-in-cell simulation allows us to decrease the SPW duration (down to a few optical cycles) and increase its peak amplitude. In the relativistic regime, for $I\lambda_0^2 = 3.4 \times 10^{19}$ W/cm^2 μm^2, such SPW are found to accelerate high charge (few 10 s of pC), high energy (up to 70 MeV), and ultrashort (few fs) electron bunches.

DOI: 10.1103/PhysRevE.103.L021201

Surface plasmon polaritons, also known as surface plasma waves (SPW) in free electron media, are highly localized electromagnetic field structures with the ability to confine and enhance light in subwalength regions at the interface between two media [1–4]. Their unique properties have made them ideal candidates for applications in a broad range of research fields, from biochemical sensing [5,6] to the design of small photonic devices [7,8].

The excitation of SPW by micrometric wavelength ($\lambda_0 = 0.8\,\mu$m) femtosecond (fs) laser pulses irradiating solid targets has been demonstrated as a strategy to enhance secondary emission of radiation and particles. In the low intensity regime, from few GW/cm^2 to tens of TW/cm^2, surface plasmon polaritons have led to harmonic emission [9–11] and the production of photoelectron bunches at energies up to few 100s eV [12,13]. The advent of table-top, 10s TW, fs lasers allowed on-target irradiance $I_0\lambda_0^2 \gtrsim 10^{18}$ W/cm^2 μm^2. In this ultrahigh intensity (UHI) regime, any target material quickly turns into a plasma, and electrons reach relativistic quiver velocities in the intense laser field. SPW then become of interest not only as unexplored nonlinear plasma modes but also for their capability of accelerating electrons, being waves with a longitudinal electric field component and slightly subluminal phase speed. Simulations and experiments have indeed shown that relativistic SPW can accelerate high charge, ultrashort electron bunches along the target surface [14–25], with energies largely exceeding their quiver energy and spatiotemporal correlation with extreme ultraviolet (XUV) harmonic emission [26].

In a recent paper, Pisani *et al.* [27] showed through electromagnetic simulations in the linear optics (low intensity) regime that using wave-front rotation (WFR) on the driving laser pulse could help generate more intense, shorter SPW. WFR is a technique used on fs lasers to induce a rotation of the successive laser wave fronts, thus leading to a time-varying incidence angle of the laser impinging onto a target. Since SPW on a grating are excited for a well-defined value of this angle, using WFR allows for the SPW excitation only over a very short time, leading to the generation of near single-cycle SPW; an enhancement of the excited SPW was also found.

In this Letter, we demonstrate how these effects can be harnessed in the UHI regime, and WFR can be used to drive tunable, ultrashort, ultraintense SPW able to generate near single-cycle, highly energetic electron bunches. The optimal WFR conditions are identified using both analytical modeling and kinetic (particle-in-cell, PIC) simulations. They allow for a significant increase of both the SPW amplitude and the electron energy by up to 65% with respect to the case without WFR. A careful design of the grating target allows for an additional increase (by 25%) of the electron maximum energy. Electron bunches with several 10s of MeV energy and 10s of pC charge are predicted considering currently available table-top laser parameters.

The interaction setup considered throughout this work is depicted in Fig. 1. A UHI laser pulse impinges onto an overdense plasma with density $n \gg n_c$, with $n_c = \epsilon_0 m_e \omega_0^2/e^2$ being the critical density at the laser frequency $\omega_0 = 2\pi c/\lambda_0$, c the vacuum speed of light, ϵ_0 the vacuum permittivity, and m_e and $-e$ the electron mass and charge. To resonantly excite a SPW at the vacuum-plasma interface, the target surface is partially modulated, and the laser incidence angle (θ_0) is chosen such that $\sin\theta_0 = \sqrt{(n/n_c - 1)/(n/n_c - 2)} - \lambda_0/d$, with d being the target periodicity [1]. The resulting SPW is excited at the laser frequency $\omega = \omega_0$ and satisfies the dispersion relation (nonrelativistic cold-fluid model [28]) $c^2 k_{\text{SPW}}{}^2/\omega^2 = (\omega_p^2/\omega^2 - 1)/(\omega_p^2/\omega^2 - 2)$, with k_{SPW} being the SPW wave number and $\omega_p = \sqrt{e^2 n/(\epsilon_0 m_e)}$ the electron plasma frequency. For $n \gg n_c$, the SPW phase and group velocities are

---

[*] caterina.riconda@sorbonne-universite.fr

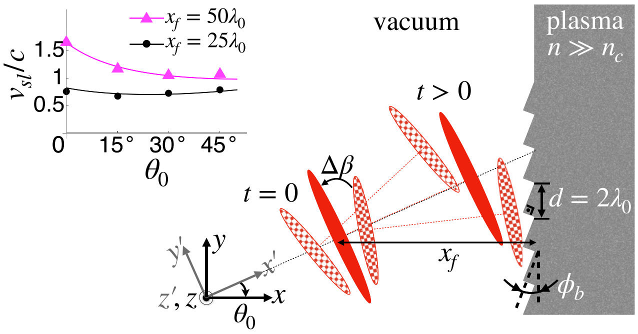

FIG. 1. Interaction setup: the central laser wave fronts are shown at best focus ($t = 0$) and striking the target ($t > 0$). Due to WFR, setting the target at a distance x_f from best focus leads to a "sliding focus" effect, with the maximum on-target intensity sliding in the y direction at a velocity v_{sl}. The upper left insert compares v_{sl} from Eq. (3) (solid lines) with measures from PIC simulations (symbols) for $x_f = 25\lambda_0$ (black circles) and $x_f = 50\lambda_0$ (magenta triangles).

slightly subluminal: $v_\phi \to c[1 - n_c/(2n)]$ and $v_g \to c[1 - 3n_c/(2n)]$.

As shown in Fig. 1, the target is located at a distance x_f from the laser best focus, which together with WFR allows for a "sliding focus" effect, i.e., a displacement in time of the pulse intensity peak along the target surface. If the sliding focus velocity v_{sl} is close to the SPW velocity, the latter will be driven more efficiently. To estimate v_{sl}, let us recall that at focus, the electric field of a pulse with WFR can be written as [29]

$$E(y', t) = E_0\, f(t)\, F(y')\, \exp[i\phi(y', t)]\,. \tag{1}$$

Here E_0 is the maximum electric field, $f(t)$ and $F(y')$ are the electric field temporal and transverse (in our two-dimensional [2D] configuration) spatial envelope, and the spatiotemporal phase is

$$\phi(y', t) = \omega_0 t(1 - \Omega_\beta\, y'/c). \tag{2}$$

The linear dependence in $y't$ leads to an instantaneous angle of propagation of light $\beta(t) \simeq -(c/\omega_0)\partial\phi/\partial y' = \Omega_\beta t$ increasing linearly with time, with Ω_β being the WFR velocity. In Fig. 1, $\Omega_\beta > 0$ is considered, only the central wave fronts are represented, and angles are exaggerated for illustration purposes. The main angle of incidence θ_0, defined as that of the central wavefront, is chosen as the resonant angle for exciting the SPW. Successive wave fronts are then shifted by an angle $\Delta\beta = \Omega_\beta\lambda_0/c$ henceforth referred to as the WFR parameter. As a result, each successive wave front will strike the target at a slightly different location along the y direction, leading to the apparent sliding velocity of the pulse on the target. For ultrashort pulses and/or the central wave fronts, we obtain a constant sliding velocity:

$$v_{\text{sl}} \simeq \frac{\Delta\beta\, x_f/\lambda_0}{\cos^2\theta_0 + \sin\theta_0\, \Delta\beta\, x_f/\lambda_0}\, c\,. \tag{3}$$

As shown in the insert of Fig. 1 (for $\Delta\beta = 33$ mrad), Eq. (3) is found to be in good agreement with measurements from PIC simulations.[1]

The sign and value of the WFR parameter $\Delta\beta$ affects the duration and amplitude of the excited SPW [27]. Indeed, when the sliding velocity is along the direction of propagation of the SPW, the excited wave can increase its amplitude while maintaining a short duration. Additional tunability can be obtained by calculating an optimal value of the WFR parameter $\Delta\beta_{\text{opt}}$ such that the sliding velocity v_{sl} coincides with the SPW velocity $\simeq c$; this leads to

$$\Delta\beta_{\text{opt}} \simeq \frac{\lambda_0}{x_f}\,(1 + \sin\theta_0)\,. \tag{4}$$

Equation (4) depends on x_f: $\Delta\beta_{\text{opt}}$ decreases when increasing the distance between the target and best focus. This allows us to relax the experimental constraint of obtaining large WFR velocity [30]. However, there is a trade-off since at larger values of x_f the intensity of the laser at the surface decreases. For the largest value we investigate, $x_f = 50\lambda_0$ [where Eq. (4) gives $\Delta\beta_{\text{opt}} \simeq 30$ mrad], the laser field amplitude on target is decreased by 8% with respect to the configuration studied below, $x_f = 25\lambda_0$ where $\Delta\beta_{\text{opt}} \simeq 60$ mrad.

An additional improvement on the interaction setup was made by considering that both the efficient excitation and propagation of SPW strongly depend on the grating and surface properties. By an extensive numerical study of the effect of the target profile on the SPW excitation [31], we have found that the best coupling is obtained for a blazed grating, as also suggested experimentally in Ref. [21]. A systematic comparison between targets fully modulated or only partially engraved showed that a partially engraved target (with grooves only in the laser-irradiated spot) efficiently mitigates radiation losses due to scattering of the SPW off the grating. The use of this mixed surface grating allows a better propagation of the SPW along the flat surface. In our simulations (not shown), we observed an increase of 25% of the maximum electron energy using such targets.

To test our claims, two series of 2D3V PIC simulations were performed with the code SMILEI [32] considering different laser field strengths $a_0 = eE_0/(m_e c\omega_0)$. First, a nonrelativistic laser intensity $a_0 = 0.1$ allows us identify the optimal parameters for SPW excitation. Then, the UHI regime of interaction $a_0 = 5$ and electron acceleration along the target surface are considered. In both cases, the general setup of the simulation is given in Fig. 1 with numerical parameters.[2] The grating target, of thickness $3\lambda_0$, has density $n = 100\, n_c$, ion to electron mass ratio $m_i/(m_e) = 1836$, and temperature ratio $T_i/(T_e) = 0.1$ with $T_e = 50$ eV. The periodicity of the

---

[1] In PIC simulations, v_{sl} is measured by locating the position of the maximum laser field amplitude as a function of time at the target surface and time averaging over the laser high frequency.

[2] The simulation box is $39\lambda_0 \times 72\lambda_0$ (in the x-y directions), with 9984×18432 cells (spatial resolution $\Delta = \lambda_0/256$), and time resolution $\Delta t = 0.95\Delta/\sqrt{2}$. Electromagnetic field boundary conditions are injecting and absorbing in x and periodic in y. Particle boundary conditions in x are reflecting (left) or thermalizing (right), and periodic in y. There are 32 macroparticles per species per cell.

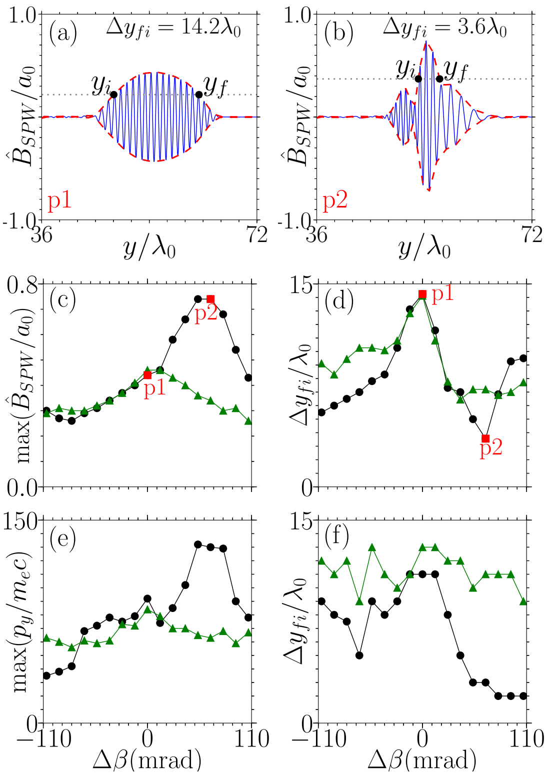

FIG. 2. SPW magnetic field at the target surface for (a) $\Delta\beta = 0$ and (b) $\Delta\beta = 67$ mrad with $a_0 = 0.1$ and $x_f = 25\lambda_0$. (c) Maximum SPW field amplitude and (d) duration (FWHM) vs the WFR parameter $\Delta\beta$ for $a_0 = 0.1$. Markers p1 and p2 indicate the cases shown in panels (a) and (b). (e) Maximum electron momentum along the surface (p_y) and (f) electron bunch duration (FWHM) vs $\Delta\beta$ for $a_0 = 5$. In panels (c) to (f), $x_f = 0$ (green triangles) and $x_f = 25\lambda_0$ (black circles).

grating is $d = 2\lambda_0$ with groove depth $h = 0.44\lambda_0$ and blazed angle $\phi_b = 13^\circ$. A flat surface (at $y > 42\lambda_0$) follows the grating so that the laser illuminates only the number of ripples corresponding to the projected pulse waist onto the surface. The driving laser is a *p*-polarized Gaussian pulse with transverse size $w_\perp = 5.2\lambda_0$, duration [full width at half maximum (FWHM) in intensity] $T = 10\lambda_0/c$.[3] The laser pulse impinges onto the grating target at the resonant angle $\theta_0 = 31^\circ$. The simulation is run up to time $t_0 + 20\lambda_0/c$, with t_0 being the time when the peak of the pulse reaches the target. Unless specified otherwise, all values are taken at the end of the simulation.

We first consider $a_0 = 0.1$ for which relativistic nonlinearities can be neglected. The z component of the magnetic field,[4] noted B_{SPW} [or $\hat{B}_{\text{SPW}} = eB_{\text{SPW}}/(m_e\omega_0)$], is taken as representative of the SPW, with all the other field components being proportional to it. For $n \gg n_c$, and in the vacuum side, the linear approximation yields $|E_x| \sim c|B_{\text{SPW}}|$ and $|E_y| \sim c|B_{\text{SPW}}|\sqrt{n_c/n}$.

In Fig. 2, we show a snapshot of $\hat{B}_{\text{SPW}}$ (blue solid line) and its envelope (red dashed line) along the target surface for $x_f = 25\lambda_0$, (a) $\Delta\beta = 0$, and (b) $\Delta\beta = 67$ mrad. The latter case corresponds to the most intense and shortest SPW found in our simulations, $\Delta\beta_{\text{opt}} = 60$ mrad. With this optimal WFR parameter, the SPW peak amplitude is increased by $\approx$65% with respect to the case without WFR and its duration, measured as the signal FWHM, is reduced by four from 14.2 to $3.6\lambda_0/c$.

Figures 2(c) and 2(d) show the maximum value of $\hat{B}_{\text{SPW}}$ and the measured SPW duration as the result of a parametric scan of $\Delta\beta$ for $x_f = 0$ (target at focus, green triangles) and $x_f = 25\lambda_0$ (target off-focus, black circles). At focus, WFR has a small impact on the SPW excitation: The most intense SPW is obtained for $\Delta\beta = 0$, and using nonzero $\Delta\beta$ decreases the duration of the SPW but also its maximum amplitude. Instead, for $x_f = 25\lambda_0$, $\Delta\beta$ acts as a tuning parameter, allowing both to shorten the SPW and to increase its amplitude. We observe the shortest and most intense SPW for $\Delta\beta \simeq 67$ mrad. This is in good agreement with the optimal prediction from Eq. (4), $\Delta\beta_{\text{opt}} \simeq 60$ mrad. Note a smooth trend around this optimal value; the point directly on the left of p2 corresponds to $\Delta\beta = 53$ mrad. Interestingly, even though the on-target laser intensity is reduced when increasing x_f to $25\lambda_0$, a significant increase of the SPW amplitude is still obtained using the optimal WFR parameter. A parametric scan considering $x_f = 50\lambda_0$ (not shown) leads to an optimal WFR parameter $\Delta\beta \simeq 33$ mrad also in good agreement with $\Delta\beta_{\text{opt}} = 30$ mrad from Eq. (4). Finally, as expected positive values of $\Delta\beta$, for which the sliding velocity is along the SPW propagation direction, give a maximal effect. In contrast, for negative $\Delta\beta$, the SPW is still of a shorter duration but with a reduced amplitude, roughly that obtained when placing the target at best focus.

We now turn our attention to the second series of simulations performed in the UHI regime ($a_0 = 5$) and electron acceleration. The bottom row in Fig. 2 shows [Fig. 2(e)] the maximum electron momentum parallel to the surface and [Fig. 2(f)] the characteristic width[5] of the accelerated electron bunch as a function of $\Delta\beta$, considering $x_f = 0$ (green triangles) and $x_f = 25\lambda_0$ (black circles). Both panels exhibit very similar features to those observed at low intensity. Placing the target at focus ($x_f = 0$), the accelerated electron bunch maximum energy and duration are marginally affected by WFR. In contrast, for $x_f = 25\lambda_0$, WFR significantly impacts electron acceleration: Taking $\Delta\beta > 0$ leads to more energetic, shorter electron bunches. By comparing the case for which the target is at focus with $\Delta\beta = 0$ and that with the target at $x_f = 25\lambda_0$ with $\Delta\beta = 67$ mrad, one finds an increase of the maximum electron momentum by 62% [from $\max(p_y) \simeq 80m_ec$ to $\simeq 130m_ec$] and much shorter bunches when the optimal (positive) WFR parameter is considered and target is off focus. The optimum value $\Delta\beta = 67$ mrad found for electron acceleration in this regime is the same as found earlier for efficient, ultrashort SPW excitation at lower intensity.

---

[3] The laser transverse profile is Gaussian, $F(y') = \exp(-y'^2/w_\perp^2)$ with $w_\perp = 5.2\lambda_0$ and its time profile is $\cos^2$: $f(t) = \cos(\pi t/(2T))$ for $|t| < T$ (0 otherwise), with $T = 10\lambda_0/c$.

[4] B_{SPW} is collected at $t = t_0 + 20\lambda_0/c$, on flat surface far from the laser-plasma interaction zone. The magnetic field has been filtered, selecting values of $k > 2k_{\text{SPW}}$.

[5] The duration of the electron bunch is estimated from its spatial width through the relation $\Delta\tau_{fi} \simeq \Delta y_{fi}/c$.

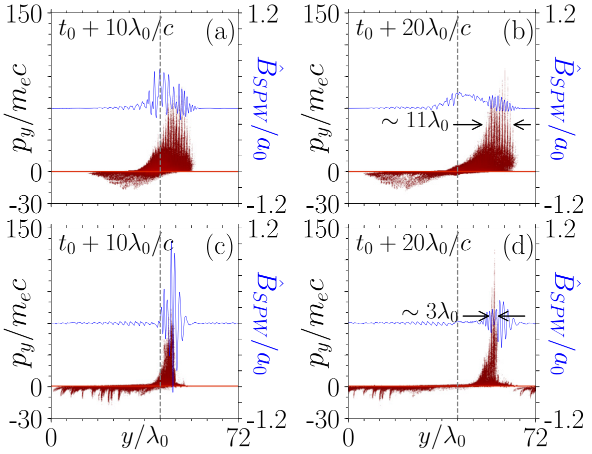

FIG. 3. Electron phase-space (red dots) and SPW field amplitude (blue line, right scale) for $a_0 = 5$ at times, $t = t_0 + 10\lambda_0/c$ and $t = t_0 + 20\lambda_0/c$. [(a), (b)] $\Delta\beta = 0$ and [(c), (d)] $\Delta\beta = 67$ mrad. The gray vertical dashed line indicates the end of the grating and beginning of the flat region.

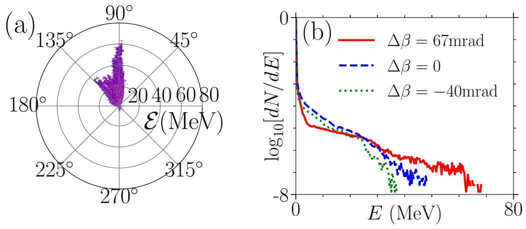

FIG. 4. (a) Electron energy distribution in MeV as a function of the emission angle $\phi = \tan^{-1}(p_y/p_x)$ for $\Delta\beta = 67$ mrad and $a_0 = 5$. (b) Electron energy distribution for $\Delta\beta = 67$ (red solid line), $\Delta\beta = 0$ (blue dashed line), and $\Delta\beta = -40$ mrad (green dotted line).

Figure 3 gives further insights into the acceleration process. The electron phase space and SPW magnetic field at the target surface ($x_f = 25\lambda_0$) are shown at two different times, for [Figs. 3(a) and 3(b)] $\Delta\beta = 0$ and [Figs. 3(c) and 3(d)] $\Delta\beta = 67$ mrad (optimal condition). In both cases, the duration of the electron bunch is proportional to the duration of the SPW, the shortest SPW obtained for $\Delta\beta = 67$ mrad leading to the shortest electron bunch. For $\Delta\beta = 0$ [Figs. 3(a) and 3(b)], the SPW is strongly damped at $t = t_0 + 20\lambda_0/c$: The electron bunch has reached its parallel momentum $\max(p_y) \simeq 90 m_ec$ and has a width (measured from the FWHM in momentum) of $\Delta y_{fi} = 11\lambda_0$. The acceleration process is more efficient using the optimal WFR parameter $\Delta\beta = 67$ mrad [Figs. 3(c) and 3(d)]. At $t = t_0 + 10\lambda_0/c$, two periods after the laser has left the surface, the magnetic field is intense ($\hat{B}_{\text{SPW}} \simeq 1.2\, a_0$) and the most energetic electrons have already reached momentum up to $\max(p_y) \simeq 70 m_ec$. Ten periods later, a narrow ($\Delta y_{fi} = 3\lambda_0$) and energetic [$\max(p_y) \simeq 130 m_ec$] electron bunch is obtained, while the SPW has been significantly damped.

Similar observations can be drawn from Fig. 4. In Fig. 4(a), the electron distribution in energy and direction (the angle is defined in the simulation plane with respect to the x axis) is shown, demonstrating that the most energetic electrons are accelerated mainly along the target's surface and in the $y > 0$ direction (i.e., in the SPW direction of propagation). Figure 4(b) shows the energy distribution of the electron, for different values of $\Delta\beta$.

These results and in particular the increase of the maximum electron energy (equiv. momentum) are consistent with what one expects from the increase of the SPW amplitude by use of the WFR driving pulse. Indeed, an upper limit of the electron energy gain in the SPW has been derived in Ref. [18] by generalizing the results of wake-field acceleration [33,34], leading $\Delta\mathcal{E} \sim \chi\, \gamma_\phi \max|\hat{B}_{\text{SPW}}| m_ec^2$ so that $\Delta\mathcal{E}$ is proportional to the SPW field amplitude. Here $\gamma_\phi = (1 - v_\phi^2/c^2)^{-1/2}$ and χ is a constant of order one, reaching at most 4 [18]. In our simulations, the magnetic field of the SPW (time-averaged over the wave period) reached at most $\max|\hat{B}_{\text{SPW}}| \approx 3.8$ for $\Delta\beta = 0$ and $\max|\hat{B}_{\text{SPW}}| \approx 7.0$ for $\Delta\beta = 67$ mrad. Considering that $\gamma_\phi \simeq 10$ for $n = 100 n_c$, we then obtain the upper limit $\Delta\mathcal{E} \simeq 154 m_ec^2$ for $\Delta\beta = 0$ and $\Delta\beta = 67$ mrad for $\Delta\mathcal{E} \simeq 280 m_ec^2$. These predictions overestimate the electron energy as they assume (i) no wave decay over the distance required for acceleration, (ii) optimal electron injection, and (iii) acceleration exactly parallel to the target surface, while it has been observed that electrons are deflected in the perpendicular direction [19].

To gain further insight into the acceleration process, we performed a particle tracking of the most energetic electrons and evaluated the trajectory-averaged value of the longitudinal field $\langle E_y \rangle$ acting on the particle. This allows to define an acceleration length $l_{\text{acc}} = \Delta\mathcal{E}/|e\langle E_y \rangle|$. From the particle track, we found $\Delta\mathcal{E} \simeq 90 m_ec^2$ and $\langle E_y \rangle \simeq -1.0\, m_ec\omega_0/e$ for $\Delta\beta = 0$, and $\Delta\mathcal{E} \simeq 130 m_ec^2$ and $\langle E_y \rangle \simeq -1.4\, m_ec\omega_0/e$ for $\Delta\beta = 67$ mrad. In both cases, this leads to an acceleration length $l_{acc} \sim 15\lambda_0$, consistent with the observed particle trajectories. This length largely exceeds the laser spot size and is close to the length over which the SPW decreases its amplitude significantly (see, e.g., Fig. 3). This confirms the electrons are accelerated by the SPW as it propagates along the target surface.

In the optimal case, the highest energy particles (in the range 30–70 MeV) form a bunch with duration of $\simeq 3\lambda_0/c$ [$\sim$8 fs for $\lambda_0 = 0.8\ \mu$m] and total charge $\simeq 10$ pC/λ_0 (in our 2D simulations). Assuming a bunch width (in the z direction) of the order of the laser pulse with $w_\perp = 5.2\lambda_0$, one could expect few cycles of electron bunches with a charge of $\approx$52 pC. These results are competitive with cutting-edge laser wake-field electron beams from underdense plasmas. Considering similar laser parameters and electron energies, short, high-charge electron bunches were obtained with energy 85 MeV (21 MeV energy spread), total charge 15 pC, and duration 4.4 fs [35].

In conclusion, a laser with WFR and an appropriately tailored plasma target allow us to control the duration and amplitude of SPW in the linear and relativistic regime. As a consequence, ultrashort (near single cycle), energetic and highly charged electron bunches are generated. The optimal parameters are clearly identified; since they are well within the capabilities of current UHI installations, this work opens new prospects and provide guidelines for forthcoming experiments.

Financial support from Grant No. ANR-11-IDEX-0004-02 Plas@Par is acknowledged. Simulations were performed on the Irene-SKL machine hosted at TGCC- France, using High Performance Computing resources from GENCI-TGCC (Grant No. 2018-x2016057678) and PRACE (Project MIMOSAS). P.S.K. was supported by the CEA NUMERICS program, which has received funding from the European Union's Horizon 2020 research and innovation program under the Marie Sklodowska-Curie Grant agreement No. 800945.

---

[1] H. Raether, *Surface Plasmons on Smooth and Rough Surfaces and Gratings* (Springer-Verlag, Berlin, 1988).
[2] W. Barnes, A. Dereux, and T. Ebbesen, Nature (London) **424**, 824 (2003).
[3] S. A. Maier, *Plasmonics: Fundamentals and Applications* (Springer-Verlag, Berlin, 2007).
[4] J. M. Pitarke, V. M. Silkin, E. V. Chulkov, and P. M. Echenique, Rep. Prog. Phys. **70**, 1 (2007).
[5] P. K. Jain, X. Huang, I. H. El-Sayed, and M. A. El-Sayed, Acc. Chem. Res. **41**, 1578 (2008).
[6] K. C. Y. Huang, M.-K. Seo, T. Sarmiento, Y. Huo, J. S. Harris, and M. L. Brongersma, Nat. Photon. **8**, 244 (2014).
[7] E. Ozbay, Science **311**, 189 (2006).
[8] T. Chung, S.-Y. Lee, E. Y. Song, H. Chun, and B. Lee, Sensors **11**, 10907 (2011).
[9] G. S. Agarwal and S. S. Jha, Solid State Commun. **41**, 499 (1982).
[10] J. L. Coutaz, M. Neviere, E. Pic, and R. Reinisch, Phys. Rev. B **32**, 2227 (1985).
[11] P. Jatav and J. Parashar, Phys. Plasmas **26**, 022301 (2019).
[12] J. Kupersztych, P. Monchicourt, and M. Raynaud, Phys. Rev. Lett. **86**, 5180 (2001).
[13] J. Zawadzka, D. A. Jaroszynski, J. J. Carey, and K. Wynne, Appl. Phys. Lett. **79**, 2130 (2001).
[14] M. Raynaud, J. Kupersztych, C. Riconda, J. C. Adam, and A. Héron, Phys. Plasmas **14**, 092702 (2007).
[15] T. Ceccotti, V. Floquet, A. Sgattoni, A. Bigongiari, O. Klimo, M. Raynaud, C. Riconda, A. Heron, F. Baffigi, L. Labate *et al.*, Phys. Rev. Lett. **111**, 185001 (2013).
[16] A. Bigongiari, M. Raynaud, C. Riconda, and A. Héron, Phys. Plasmas **20**, 052701 (2013).
[17] Y. Tian, J. Liu, W. Wang, C. Wang, A. Deng, C. Xia, W. Li, L. Cao, H. Lu, H. Zhang *et al.*, Phys. Rev. Lett. **109**, 115002 (2012).
[18] C. Riconda, M. Raynaud, T. Vialis, and M. Grech, Phys. Plasmas **22**, 073103 (2015).
[19] L. Fedeli, A. Sgattoni, G. Cantono, D. Garzella, F. Réau, I. Prencipe, M. Passoni, M. Raynaud, M. Květoň, J. Proska *et al.*, Phys. Rev. Lett. **116**, 015001 (2016).
[20] L. Fedeli, A. Sgattoni, G. Cantono, and A. Macchi, Appl. Phys. Lett. **110**, 051103 (2017).
[21] G. Cantono, A. Sgattoni, L. Fedeli, D. Garzella, F. Réau, C. Riconda, A. Macchi, and T. Ceccotti, Phys. Plasmas **25**, 031907 (2018).
[22] A. Macchi, Phys. Plasmas **25**, 031906 (2018).
[23] M. Raynaud, A. Héron, and J.-C. Adam, Plasma Phys. Controlled Fusion **60**, 014021 (2018).
[24] X. M. Zhu, R. Prasad, M. Swantusch, B. Aurand, A. A. Andreev, O. Willi, and M. Cerchez, High Power Laser Sci. Eng. **8**, 15 (2020)
[25] M. Raynaud, A. Héron, and J.-C. Adam, Sci. Rep. **10**, 13450 (2020).
[26] G. Cantono, L. Fedeli, A. Sgattoni, A. Denoeud, L. Chopineau, F. Réau, T. Ceccotti, and A. Macchi, Phys. Rev. Lett. **120**, 264803 (2018).
[27] F. Pisani, L. Fedeli, and A. Macchi, ACS Photon. **5**, 1068 (2018).
[28] P. K. Kaw and J. B. McBride, Phys. Fluids **13**, 1784 (1970).
[29] H. Vincenti and F. Quéré, Phys. Rev. Lett. **108**, 113904 (2012).
[30] F. Quéré, H. Vincenti, A. Borot, S. Monchocé, T. J. Hammond, K. T. Kim, J. A. Wheeler, C. Zhang, T. Ruchon, T. Auguste *et al.*, J. Phys. B: At. Mol. Opt. Phys. **47**, 124004 (2014).
[31] P. S. Kleij, M.Sc. thesis, Università di Pisa, Sorbonne Université, France, 2019, https://etd.adm.unipi.it/t/etd-09022019-103844/.
[32] J. Derouillat, A. Beck, F. Pérez, T. Vinci, M. Chiaramello, A. Grassi, M. Flé, G. Bouchard, I. Plotnikov, N. Aunai *et al.*, Comput. Phys. Commun. **222**, 351 (2018).
[33] T. Tajima and J. M. Dawson, Phys. Rev. Lett. **43**, 267 (1979).
[34] P. Mora and F. Amiranoff, J. Appl. Phys. **66**, 3476 (1989); P. Mora, Phys. Fluids **4**, 1630 (1992).
[35] O. Lundh, J. Lim, C. Rechatin, L. Ammoura, A. Ben-Ismaïl, X. Davoine, G. Gallot, J.-P. Goddet, E. Lefebvre, V. Malka, J. Faure *et al.*, Nat. Phys. **7**, 219 (2011).

Physics of Plasmas

Key parameters for surface plasma wave excitation in the ultra-high intensity regime

Cite as: Phys. Plasmas **28**, 073104 (2021); https://doi.org/10.1063/5.0052599
Submitted: 31 March 2021 • Accepted: 23 June 2021 • Published Online: 19 July 2021

S. Marini, P. S. Kleij, F. Amiranoff, et al.

Phys. Plasmas **28**, 073104 (2021); https://doi.org/10.1063/5.0052599 **28**, 073104

Physics of Plasmas ARTICLE scitation.org/journal/php

Key parameters for surface plasma wave excitation in the ultra-high intensity regime

Cite as: Phys. Plasmas **28**, 073104 (2021); doi: 10.1063/5.0052599
Submitted: 31 March 2021 · Accepted: 23 June 2021 ·
Published Online: 19 July 2021

S. Marini,[1,2,a)] P. S. Kleij,[1] F. Amiranoff,[2] M. Grech,[2] C. Riconda,[2] and M. Raynaud[1,b)]

AFFILIATIONS

[1]LSI, CEA/DRF/IRAMIS, CNRS, École Polytechnique, Institut Polytechnique de Paris, F-91120 Palaiseau, France
[2]LULI, Sorbonne Université, CEA, CNRS, École Polytechnique, Institut Polytechnique de Paris, F-75252 Paris, France

[a)]Author to whom correspondence should be addressed: samuel.marini@polytechnique.edu
[b)]Electronic mail: michele.raynaud-brun@polytechnique.edu

ABSTRACT

Ultra-short high-power lasers can deliver extreme light intensities ($\geq 10^{20}$ W/cm^2 and ≤ 30 fs) and drive large amplitude Surface Plasma Wave (SPW) at over-dense plasma surface. The resulting current of energetic electron has great interest for applications, potentially scaling with the laser amplitude, provided that the laser–plasma transfer to the accelerated particles mediated by SPW is still efficient at ultra-high intensity. By means of particle-in-cell simulations, we identify the best condition for SPW excitation and show a strong correlation between the optimum surface plasma wave excitation angle and the laser's angle of incidence that optimize the electron acceleration along the plasma surface. We also discuss how plasma density and plasma surface shape can be adjusted in order to push to higher laser intensity the limit of surface plasma wave excitation. Our results open the way to new experiments on forthcoming multi-petawatt laser systems.

I. INTRODUCTION

The interaction of an intense laser pulse with an over-dense plasma, possessing a sharp density gradient, can result in accelerate charged particles with relativistic velocities.[1–8] The irradiation of structured targets,[9,10] such as periodic grooves (gratings) on a metal surface, by ultra-short laser pulses, is of particular interest for generating intense Surface Plasma Waves (SPWs), which can store the laser energy and efficiently accelerate electrons.

In this scenario, high energy transfer from the laser to the plasma is achieved when the frequency and wavelength of the interacting laser pulse match those given by the SPW's dispersion relation.[12–14] The high intensity and ultra-short laser–plasma interaction regime ($\leq 10^{19}$ W/cm^2 and ≤ 100 fs) showed that a significant percentage of electrons trapped in the SPW can be accelerated along the surface in the range of $\sim$10 MeV.[15–20] High charge electron bunches (up to $\sim$650 pC) were also observed[20–24] with applications, including the generation of bright sources of ultra-short pulsed x-rays, ultra-fast electron diffraction, tabletop electron accelerators, and ultra-fast electron spectroscopy.[25–28] Recently, a scheme exploiting to date laser techniques was proposed for controlling the duration and amplitude of SPWs by which a laser with an intensity of a few 10^{19} W/cm^2 and a pulse duration of a few tens of fs should be able to accelerate electrons up to $\sim$70 MeV.[21] Surprisingly, in these experiments and simulations, the non-relativistic cold dispersion relation successfully defined the conditions of the SPW excitation with laser beam intensity up to $\sim 10^{19}$ W/cm^2.

Extending the regime of ultra-high laser intensity interaction beyond 10^{21} W/cm^2 can result in surface waves with extremely large amplitudes at the over-dense plasma surface, potentially allowing one to obtain unprecedentedly high currents of energetic electrons as well as emitting radiation with interesting characteristics. However, the excitation and survival of these SPWs in the ultra-high laser intensity regime remain an open question, as in this limit the plasma grating can evolve on relatively short time scales, and nonlinear effects can affect the dispersion relation in the relativistic regime.

In this paper, we determine the conditions for improving laser–plasma energy transfer as well as accelerating charged particles by the SPW excitation mechanism in an over-dense plasma with a grating, in the ultra-high laser intensity regime of interaction. We employed 2D Particle-In-Cell (PIC) simulations for laser intensities ranging from 10^{16} to 10^{22} W/cm^2, for various angles of incidence. The influence of both the plasma density and the grating depth of the modulated plasma surface was investigated since previous studies identified them as important parameters in SPW excitation.[20–24]

The paper is organized as follows: Sec. II describes the PIC simulation setup with parameters closely corresponding to recent experiments.[20,22] Section III analyses SPW excitation as a function of laser incidence and intensity. The results are then compared to analytical values obtained by the dispersion relation for cold SPWs and a heuristic relativistic correction. The importance of considering high density plasma to maintain SPW excitation in the ultra-relativistic regime is shown. Section IV studies the behavior of accelerated electrons along the plasma surface. A strong correlation is demonstrated between the angle of SPW excitation and the laser's angle of incidence that optimizes electron acceleration along the plasma surface. Sec. V investigates the influence of the grating depth at higher laser intensities. Then, in Sec. VI, our conclusions are presented.

II. PARAMETER OF THE SIMULATIONS

2D3V PIC simulations have been performed with the open-source code SMILEI.[29] The geometry is depicted in Fig. 1 where the plasma lies in the (x, y) plane for $x \geq 0$, its surface being along the y direction.

The driven laser is a $P-$polarized Gaussian pulse with a waist equal to $5\lambda_0$ $(=4\,\mu\text{m})$ and a pulse duration equal to $\tau_L = 10\lambda_0/c$ $(\simeq 27$ fs) full width at half maximum (FHWM), where c is the speed of light in vacuum and $\lambda_0 = 0.8\,\mu\text{m}$ is the chosen laser wavelength. The laser pulse impinges the plasma interface through an angle θ_{inc} in relation to the normal surface along the $x-$direction. The plasma grating has constant electron density n_0 with a sinusoidal-modulated vacuum–plasma interface located at $x_g(y) = (h/2)\,\sin(2\pi y/d)$ where h is the grating depth and d is the period. In all cases studied, we considered $d = 2\lambda_0$ $(=1.6\,\mu\text{m})$ and we used $h = 0.1\lambda_0$ $(=0.08\,\mu\text{m})$ or $0.4\lambda_0$ $(=0.32\,\mu\text{m})$ for the grating depth. The plasma consists of electrons with a small initial temperature of $T_e = 50$ eV as well as a neutralizing background of ions free to move in the space with initial temperature $T_i/(ZT_e) = 0.1$, where $Z = 1$ is the atomic number.

In the systematic study, we have performed, we selected two values for the plasma density: $n_0 = 100n_c$ and $n_0 = 200n_c$ where $n_c = \epsilon_0 m_e \omega_0^2/e^2$ (ω_0 is the laser frequency, and ϵ_0 is the vacuum permittivity). These values are chosen in order to study the theoretical dependence on the plasma density and are compatible with the plasma density obtained in experiments by ionizing solid gratings.[15,20,22,24] Additionally, we varied the laser field strength [normalized vector potential $a_0 \equiv eE_0/(m_e c\,\omega_0)$] from $a_0 = 0.1$ $(\sim\times 10^{16}\ \text{W/cm}^2)$ to $a_0 = 50$ $(\sim 4 \times 10^{21}\ \text{W/cm}^2)$ as may be reached on forthcoming multi-petawatt laser systems, see, e.g., Refs. 30 and 31. For any given (n_0, a_0), we have performed a parametric scan varying the incidence angle of the laser from typically $\theta_{\text{inc}} = 28°$ to $\theta_{\text{inc}} = 50°$ in order to extract the optimal condition for SPW excitation.

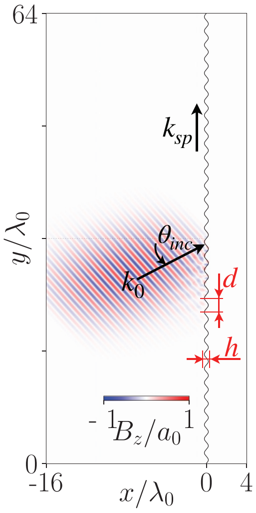

FIG. 1. Simulation setup: the laser beam is focused thought an angle θ_{inc} over the interface of the plasma target with constant electron density n_0, grating depth h and period d. Here, the red–blue scale represents the magnetic field amplitude of the laser pulse impinging over the target.

In these simulations, the box extends over $20\lambda_0$ $(=16\,\mu\text{m})$ in the x-direction [roughly $16\lambda_0$ $(=12.8\,\mu\text{m})$ of vacuum and $4\lambda_0$ $(=3.2\,\mu\text{m})$ of plasma], and $64\lambda_0$ $(=51.2\,\mu\text{m})$ in the y-direction. The spatial resolution was set to $\Delta x = \Delta y = \lambda_0/128$ $(=0.006\,25\,\mu\text{m})$. The simulation time step is chosen to be $\Delta t = 0.95\,\Delta x/\sqrt{2}$ that corresponds to 95% of the Courant–Friedrich–Lewy (CFL) condition for the standard finite-difference time-domain (FDTD) solver.[32] Every cells contain initially 16 randomly distributed particles of each species (electrons and ions). Electromagnetic field boundary conditions are injecting/absorbing in x and periodic in y. Particle boundary conditions in x are reflecting (left) or thermalizing (right) and periodic in y. The simulations were run over until particles or radiation gets the position $y = 60\lambda_0$ $(=48\,\mu\text{m})$, which determines the final simulation time $t = t_f$. Notice that t_f varies according to the laser incidence angle and it gets larger as θ_{inc} increases.

III. RESONANCE CONDITION FOR SPW EXCITATION AT HIGH INTENSITY

In order to evidence the condition for SPW excitation as a function of the laser intensity, we perform a set of simulations with intensity corresponding to a_0 varying from $a_0 = 0.1$ to $a_0 = 50$ and incident angle ranging from $\theta_{inc} = 28°$ to $50°$. The plasma grating period and depth are kept constant. Initially, the depth is chosen as $h = 0.1\lambda_0$, so that corrections to the dispersion relation due to finite depth are negligible. The SPW dispersion relation in the cold plasma nonrelativistic limit is[13]

$$\frac{c^2k^2}{\omega^2} = \frac{\omega_p^2/\omega^2 - 1}{\omega_p^2/\omega^2 - 2}, \tag{1}$$

k and ω are the SPW wavelength and the frequency and ω_p is the plasma frequency. In the presence of high-intensity lasers plasma interaction, and in particular, when the laser electric field E_0 becomes of the order of $m_e c\omega_0/e$ [i.e., for a normalized vector potential $a_0 \equiv eE_0/(m_e c\,\omega_0) \gtrsim 1$], it has been proposed[33–37] to correct the response of the electrons by considering an effective electron mass $m_e \to \gamma_0\, m_e$, with $\gamma_0 \simeq \sqrt{1 + a_0^2/2}$ the Lorentz factor of an electron in a plane wave with normalized vector potential a_0. In the case of SPW excitation by the laser, we, thus, consider a heuristic correction to the dispersion relation by replacing $\omega_p^2/\omega^2 \equiv \omega_p^2/\omega_0^2$ by $\omega_p^2/(\gamma_0\,\omega_0^2)$. As a consequence, correcting the phase-matching condition leads a a_0-dependent optimal angle of incidence for the surface plasma wave excitation:

$$\theta_{\text{opt}}(a_0) = \arcsin\left(\sqrt{\frac{n_0/(\gamma_0 n_c) - 1}{n_0/(\gamma_0 n_c) - 2}} - \frac{\lambda_0}{d}\right). \tag{2}$$

This results in an optimal angle, θ_{opt}, that increases with the amplitude of the SPW field. For $a_0 \gg 1$, it depends on the parameter $n_0/(\gamma_0 n_c) \sim \sqrt{2} n_0/(a_0 n_c)$. In order to verify the validity of this scaling, we considered two electron densities, $n_0 = 100n_c$ and $200n_c$.

As detailed in the following, we find in simulations that at high intensity the resonance is quite broad. Although for values of $n_0/(a_0 n_c) \lesssim 10$, the correction to the dispersion relation can improve the coupling of the laser with plasma. We notice no further improvement for higher value of a_0, and the resonance angle becomes roughly independent of a_0. We can then conclude that Eq. (2) does not hold at ultra-high intensity.

To show this let us recall that SPW is TM-modes, so their signature can be sought by inspecting the Fourier transform of the B_z component of the magnetic field. Taking into account that the SPW and incident/reflected laser waves have different dispersion relations, filtering in (k_x, k_y) Fourier space allows one to extract the component associated with the SPW. Then, an inverse Fourier transform is done to obtain the B_z component of the SPW magnetic field in the reconstructed real space domain.

The time evolution of the maximum amplitude of the SPW B_z field normalized to a_0 for a typical case ($a_0 = 20$, $n_0 = 200n_c$, $h = 0.1\lambda_0$ and different values of the laser incidence angle between 30° and 45°) is reproduced in Fig. 2. The field component reaches a maximum around $t = 12\lambda_0/c$ for an incidence angle of 33°, named hereafter θ_{opt} with $t = 0$ corresponding to the time when the laser pulse reaches the plasma surface. We notice that the SPW field amplitude does not become larger than the laser field a_0, as opposed to what has been found for longer pulses and lower intensities.[14] In this short pulse regime ($\simeq$27 fs), the SPW excitation does not have time to reach the stationary regime. From the figure, we can also see that the resonance condition is not sharp. A laser incident at angles close to the optimal values excites a field with very similar behavior to the optimal one. This is also due, as discussed in Ref. 23, to the fact that the width of the incident laser transverse profile induces a spectral mode distribution of the SPW, which induces an angular width for the θ_{opt} equals here to ~4°.

In Fig. 3, we report the optimum laser incidence θ_{opt} (red dots and error bar) as a function of a_0 for the two plasma densities considered. The θ_{opt} is obtained by considering for each a_0 angle that corresponds to the peak value of SPW B_z in time (following the same procedure that is illustrated in Fig. 2). In the panels, the error bars measure the uncertain measuring the peak value of SPW B_z, while the gray shadow identifies the region where $\max|B_z^{SP}| \gtrsim 0.85\max|B_z^{SP}|$. As a_0 increases, and in particular, for $a_0 \gtrsim n_0/(10n_c)$, the incertitude in determining the optimum angle of the SPW B_z becomes large since many angles correspond more or less to the same maximum value of the field. Moreover, when increasing a_0, the normalized amplitude of the field B_z^{SP}/a_0 decreases. We notice that going from $a_0 \sim 1$ to $a_0 \sim n_0/(10n_c)$ results in a reduction of the field amplitude of ≈45%. Further increasing a_0 and taking $a_0 \sim n_0/(4n_c)$ result in a field amplitude reduction of ≈60% in relation to the field observed when $a_0 = 1$ (not shown here).

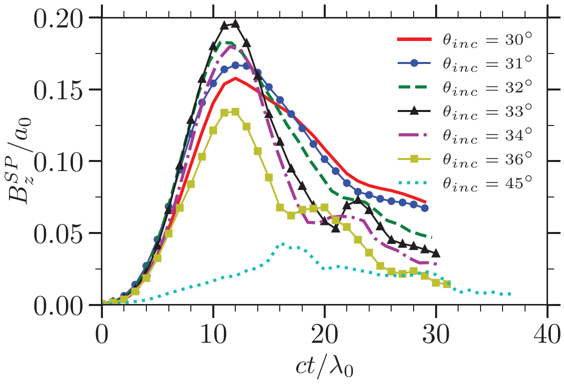

FIG. 2. SPW B_z field amplitude evolution for $a_0 = 20$, $n_0 = 200n_c$, and $h = 0.1\lambda_0$, and laser incidence angle in between 30° and 45°, $t = 0$ corresponds to the instant of time when the laser pulse reaches the plasma.

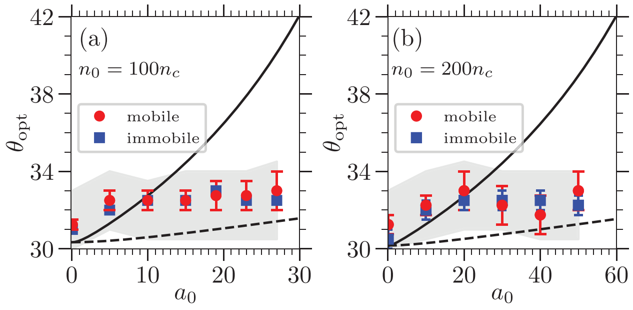

FIG. 3. In red (rounds) laser angles of incidence that optimizes the SPW B_z field amplitude as a function of the laser strength parameter a_0 for (a) $n_0 = 100n_c$ and (b) $n_0 = 200n_c$. The gray region represents the laser angles of incidence where $\max|B_z^{SP}| \gtrsim 0.85\max|B_z^{SP}|$. In blue (squares), we report the results from simulations assuming immobile ions. In both cases, $h = 0.1\lambda_0$. The solid (dashed) black line represents the expected value obtained using the dispersion relation for the cold SPW limit with the heuristic relativistic correction as a function of a_0 ($a_0/5$) (see the discussion in the text).

In Fig. 3, we also plot in black the expected value obtained using Eq. (2). As anticipated, while at first the values obtained in the simulations fit the equation, for larger values of a_0 the resonance angle becomes roughly independent of a_0. The threshold, noted $a_{0,T}$ in the following, is about $a_{0,T} = 10$ in the case when $n_0 = 100n_c$ and increases up to 20 when $n_0 = 200n_c$ [or, equivalently, $n_0/(a_{0,T} n_c) \sim 10$]. As we can see, even if Eq. (2) does not hold, the parameter $n_0/(a_0 n_c)$ is a relevant quantity to describe the laser–plasma coupling and the SPW excitation. More importantly, this parameter shows the importance of considering higher density plasma to maintain SPW excitation in the ultra-relativistic regime.

In Eq. (2), the heuristic correction to the dispersion relation is obtained using the laser parameter a_0. In the present simulations, the SPW maximum field amplitude is always smaller than a_0, and typically, as shown in Fig. 2, of the order of $a_0/5$. Therefore, for reference, we also report in dashed black line in Fig. 3 the result from Eq. (2) considering $a_0/5$ instead of a_0 in the γ_0 function.

Increasing a_0 increases the laser pressure, which may alter the grating and suppress the SPW excitation. To check the importance of this effect and to verify if the relativistic correction of the dispersion relation [Eq. (2)] is recovered, we also performed a set of simulations with immobile ions (represented by blue squares in Fig. 3 and a blue dashed line in Fig. 4). As we can see, the optimal angle is barely

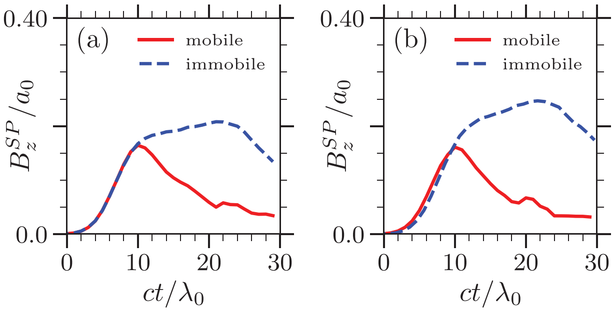

FIG. 4. SPW B_z field amplitude evolution at $\theta_{inc} = 33°$ with time for (a) $n = 100n_c$, $a_0 = 27$ and (b) $n = 200n_c$, $a_0 = 50$. $t = 0$ corresponds to the instant of time when the laser pulse reaches the plasma.

modified when the ions are immobile. However, as shown in Fig. 4 where we plot the SPW field amplitude evolution with time for two densities and $a_0 > a_{0,T}$, in the case of immobile ions the SPW field survives a longer time and peaks to higher values. This means that the grating deformation affects the SPW field on time scales larger than few laser periods ($\sim 12\lambda_0/c$ here).

Above $a_{0,T}$ the damping of the SPW by the electrons is large, resulting in strong electron acceleration along the surface trapped in the SPW.[16,20,23] In Sec. IV of this paper, we consider the SPW evolution as related to the electron dynamics along the grating.

IV. ELECTRON ACCELERATION ALONG THE PLASMA SURFACE

As mentioned in the introduction, SPW excitation resulting from high intensity ultra-short laser–plasma interaction ($\leq 10^{19}$ W/cm^2 and ≤ 100 f s) has been shown to be an efficient way to increase the acceleration of high charge electron bunches along the plasma surface up to $\sim$10 MeV and $\sim$650 pC.[16–24] Using the same laser intensities and plasma densities as in Sec. III, we will first analyze the maximum energy of the electrons that propagate along the plasma surface as a function of the laser angle of incidence. The results are summarized in Fig. 5 where we report the optimal laser's angle of incidence, θ^e_{opt} (which optimizes the formation of high energetic electron bunches propagating along the plasma surface) as a function of the laser strength parameter a_0 for (a) $n_0 = 100n_c$, and (b) $n_0 = 200n_c$ (case $h = 0.1\lambda_0$). To identify the electrons that propagate along the surface, we have defined the emission angle $\phi_e = \tan^{-1}(p_y/p_x)$ and selected electrons with $\phi_e = 90° \pm 3°$. The bars indicate the range of angles of the laser incidence giving the highest electron energy. This was determined by analyzing for each angle the energy spectrum of the electrons propagating along the plasma surface ($\phi_e = 90° \pm 3°$). Notice that for the angles considered in the error bar the electron peak energy is about the same within a percentage of up to 10%.

As before, we have considered both mobile and immobile ions with the same color code as in Fig. 3 (red—mobile, blue—immobile). Comparing Figs. 3 and 5, we find at low laser intensity a strong correlation between the optimum angle of SPW excitation and the laser angle of incidence that optimize the electron acceleration along the plasma surface. The optimum angle giving the highest energy of the electron bunch propagating along the surface is $\sim 31°$ for $a_0 \sim 1$ and increases slightly up to $\sim 33°$ with a_0 until it reaches $a_{0,T}$. It confirms the robustness of the SPW excitation in this range of intensity.

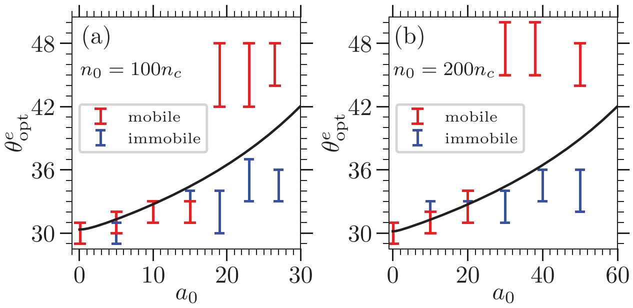

FIG. 5. In red (bars), angle of incidence of the laser that optimizes electron bunches energy propagating along the plasma surface (θ^e_{opt}) as a function of the laser strength parameter a_0 for (a) $n_0 = 100n_c$ and (b) $n_0 = 200n_c$. Blue (bars) shows the results from simulations assuming immobile ions. In both cases, $h = 0.1\lambda_0$. The solid black line reports the optimal angle of SPW excitation obtained using the dispersion relation for cold SPW with the heuristic relativistic correction (see the discussion in the text).

Above $a_{0,T}$, we observe for the realistic simulations (mobile ions) that the laser incidence angle that optimize the electron bunch propagating along the surface is no longer the same one that optimize the SPW field. The transition occurs for a_0 around 20 if the plasma density is $n_0 = 100n_c$, and around 30 if $n_0 = 200n_c$. However, when considering simulations with immobile ions (blue bars) we recover the result of the previous Fig. 3: the optimal angle for electron acceleration coincides with the optimal angle for SPW excitation. This shows that the electrons dynamic is sensitive to the grating deformation. Other acceleration mechanisms along and across the surface have been suggested associated with the laser absorption:[39] indeed, we find that above $a_{0,T}$ acceleration by SPW is not the main mechanism of electron acceleration, and the fast electron's angular distribution is much wider. This will be discussed in more detail in Sec. V, but we can anticipate that the analysis of the electron phase space confirms this hypothesis, since above $a_{0,T}$ the electron velocity distribution does not show the characteristic behavior of the acceleration by SPW, namely, bunches with periodicity equal to the SPW wavelength, and directed along the surface.[40] Finally, we checked the effect of the laser on the plasma surface examining the spatial ion density distribution in two different time scales. Both an increase in plasma density due to the radiation pressure and an expansion of the plasma are observed (not reported here). In the short time interval (comparable to the laser pulse duration), the diffraction grating is distorted and the plasma is pushed, which results in a large increase in the local plasma density. In the second and long scale that happens few cycles after the laser–plasma interaction, the plasma expansion creates an under-dense region in front of the target that also might have a major effect on the laser absorption mechanism and to define the optimal angle to the electron acceleration. The effect of under-dense sheet in front of the plasma surface has been investigated in Ref. 24.

To overcome the possible limitation of SPW–laser coupling at high laser intensity, we now consider the influence of the target grating depth that, when chosen appropriately, can significantly improve the acceleration by SPW.

V. RECOVERY OF SPW ACCELERATION BY ADAPTING THE GRATING DEPTH

In the laser–solid interaction and also at high laser intensity where plasma is created, it is well known that the ratio between the target grating depth and the grating periodicity plays a major role in the SPW excitation.[36,38] Thus, here, in order to find the optimum grating parameters for SPW excitation in the ultra-high laser intensity regime ($a_0 \geq 25$), we have redone the PIC simulations increasing the grating depth of the plasma to $h = 0.4\lambda_0$.

In Fig. 6, we compare the optimal angle of incidence of the laser that optimize electron bunches energy propagating along the plasma surface (bars) found in Sec. IV for $h = 0.1\lambda_0$ (in red) with the one found for $h = 0.4\lambda_0$ (in green) keeping unchanged the other parameters. As we can see in the case $h = 0.4\lambda_0$, the optimum angle for particle acceleration remains between 30° and 36° and coincides with the optimum angle for SPW excitation as presented in Fig. 3. As in Sec. III, the best laser incidence angle to excite highly energetic electron bunches stay roughly constant and does not scale with the laser strength. This is illustrated as an example by the simulations at $a_0 = 30$. In Fig. 7, we plot the maximum B_z field amplitude evolution in time for different values of laser incidence angle and $h = 0.1\lambda_0$ (a) and $h = 0.4\lambda_0$ (b). Comparing Fig. 7(a), where $a_0 = 30$ and $h = 0.1\lambda_0$, the time evolution of the field is quite similar to that observed in Fig. 2 where $a_0 = 20$ and $h = 0.1\lambda_0$. However, when we increase the grating's depth, the value of the field amplitude is larger and the optimal angles ($31^\circ - 33^\circ$) coincide with the optimal angles for electron acceleration in Fig. 6(b). As a consequence with the deeper grating, we expect both that the electrons are mainly accelerated by the SPW and that the maximum energy gained by the electrons is higher than if the grating is shallow.

In Fig. 8, we show the maximum value of the gamma factor, γ_f along the target's surface, for the electrons observed at the end of simulation as a function of the laser strength parameter a_0, taking $\theta_{inc} = \theta^e_{opt}$ and the parameters used in Fig. 6. As expected we observe that the energy transfer is better when the gratings are deeper ($h = 0.4\lambda_0$) than when they are shallow ($h = 0.1\lambda_0$) in the high-intense regime. The red dotted line is the function $\gamma_f = 1 + 5.1a_0$ that fits the data when $h = 0.1\lambda_0$, and the green dashed curve is the function $\gamma_f = 1 + 9.3a_0$ that fits the data when $h = 0.4\lambda_0$.

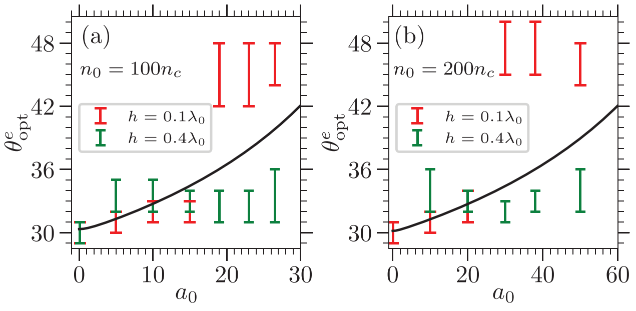

FIG. 6. Optimal angle of the incidence of the laser that optimize electron bunches energy propagating along the plasma surface (θ^e_{opt}) as a function of the laser strength parameter a_0 for (a) $n_0 = 100n_c$ and (b) $n_0 = 200n_c$ (case $h = 0.1\lambda_0$ in red and $h = 0.4\lambda_0$ in green). The black line reports the expected value obtained using the dispersion relation for cold SPW with the heuristic relativistic correction (see the discussion in the text).

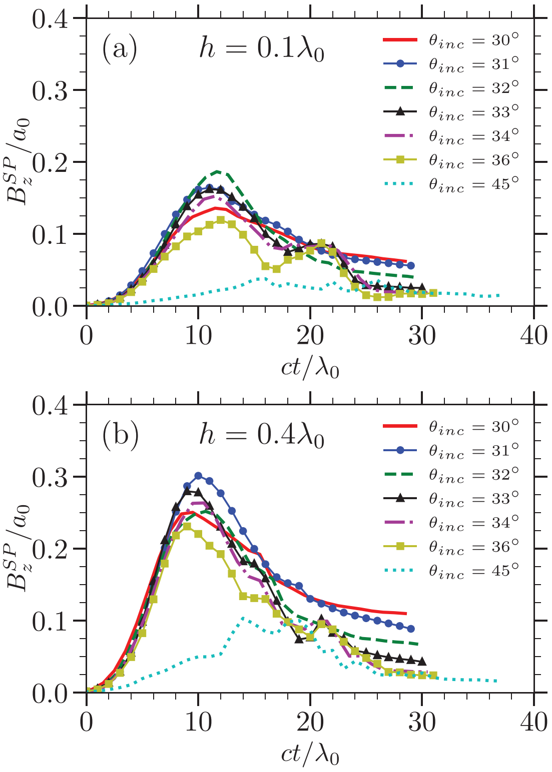

FIG. 7. SPW B_z field amplitude evolution with time for $a_0 = 30$, $n_0 = 200n_c$, laser incidence angle in between 30° and 45°, and $h = 0.1\lambda_0$ (a) and $h = 0.4\lambda_0$ (b). $t = 0$ corresponds to the instant of time when the laser pulse reaches the plasma.

A more detailed analysis of the electron dynamics can be inferred from their energy distributions as a function of the propagation angle and from their phase space (p_y/m_ec, y/λ_0). If $h = 0.4\lambda_0$ and $\theta_{inc} = 33^\circ$, a large amount of highly energetic electrons propagates along the surface $\phi_e = 90^\circ$ [Fig. 9(a)], and the phase space shows bunches distanced by a wavelength [Fig. 9(b)], consistent with the SPW acceleration mechanism.

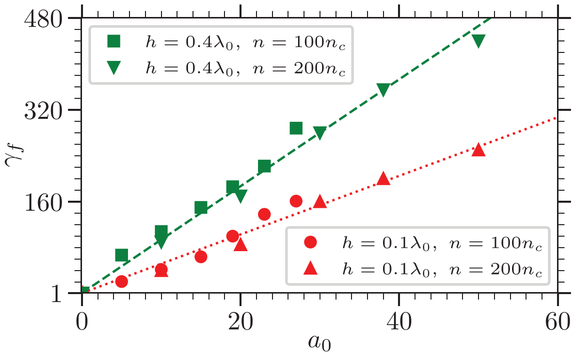

FIG. 8. Maximum value of gamma factor, γ_f, along the target's surface, observed at the end of simulation as a function of a function of the laser strength parameter a_0 for $n_0 = 100n_c$ and $n_0 = 200n_c$ (case $h = 0.1\lambda_0$ in red and $h = 0.4\lambda_0$ in green). The dashed lines represents the general tendency of the results.

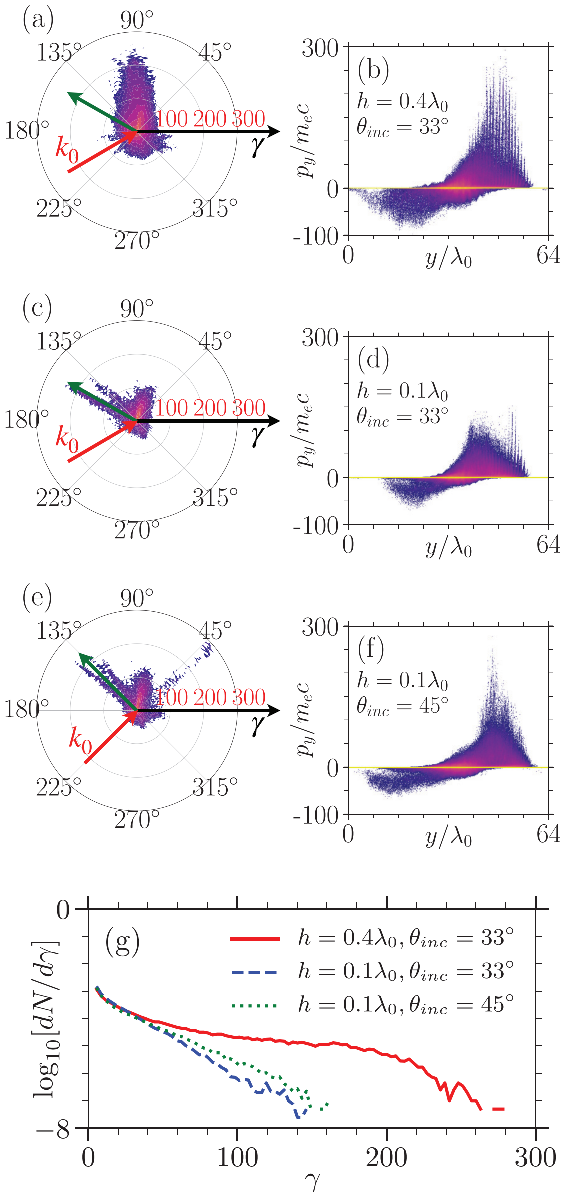

FIG. 9. For $\theta_{inc} = 33°$, $a_0 = 30$, $n_0 = 200n_c$, and $h = 0.4\lambda_0$: (a) electron energy distribution at $t = t_f$. The plasma surface is along 90°, the red arrow shows the direction of the incident laser beam, and the green arrow shows the reflected one; (b) phase space ($p_y/m_e c$, y/λ_0) of the electrons in the simulation box; the panels (c) and (d) [(e) and (f)] represent the same as the panels (a) and (b) for $h = 0.1\lambda_0$ and $\theta_{inc} = 33°$ ($\theta_{inc} = 45°$); (g) spectrum of the electron bunches along the surface for the tree parameter sets discussed.

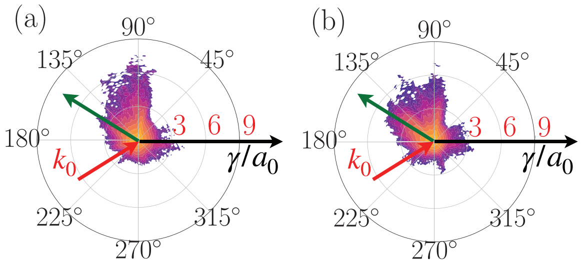

FIG. 10. Electron energy distribution at $t = t_f$, $\theta_{inc} = 33°$, and $h = 0.4\lambda_0$: $a_0 = 100$ (a) and $a_0 = 200$ (b). The plasma surface is along 90°, the red arrow indicates the direction of the incident laser beam, and the green arrow shows the reflected one. Note that although the ratio γ/a_0 is about the same in both panels, γ_f is about 800 in (a) and 1600 in (b).

This is very different from the case with $h = 0.1\lambda_0$, and $\theta_{inc} = 33°$ reported in Figs. 9(c) and 9(d) or $h = 0.1\lambda_0$, and $\theta_{inc} = 45°$ reported in Figs. 9(e) and 9(f). We observe for these last two parameters sets that the faster electrons are accelerated mainly along the direction of the incident and reflected laser beam, and fewer electrons are found propagating along the surface at 90°. Moreover, a large amount of fast electrons are pushed inside the plasma. It is worth to point out that although the peak energy is reduced in this configuration, the laser–plasma coupling is still large so that this configuration might be a way to enhance the target normal sheath acceleration (TNSA) at the rear of the thin target.[11] In such a limit, the SPW field when present [Figs. 9(c) and 9(d)] is weak and the SPW wave is no longer the predominant acceleration mechanism. This might be attributed to the grating deformation due to laser pressure, which prevents the laser–SPW coupling.

We can, thus, conclude that a deeper grating allows one to recover the exciting of SPW in the ultra-high intensity laser regime and acceleration along a preferential direction. This effect is evident in Fig. 9(g) when comparing the electron's spectra (selecting only the ones emitted parallel to the target $\phi_e = 90° \pm 6°$) for $h = 0.1\lambda_0$ (in blue) and $h = 0.4\lambda_0$ (in red), with $\theta_{inc} = 33°$ in both cases. The electron energy obtained when increasing the grating depth is increased by a factor of two for the deepest grating and the optimal angle. Instead for $h = 0.1\lambda_0$, the energy spectrum changes very little between $\theta_{inc} = 33°$ and 45° (in green), even if, when comparing the phase space $p_y/m_e c$, y/λ_0 for both incident angles [Figs. 9(d) and 9(f)], we observe a small signature of the SPW excitation (bunching of the phase space), that is lost at 45°.

To conclude this section, we verified that for $h = 0.4\lambda_0$, the SPW is still excited even at significantly higher laser intensities. In Fig. 10, the electrons emission spectrum assuming two extreme laser conditions (a) $a_0 = 100$ and (b) 200 is shown. Therefore, the plasma density is equal to $n_0 = 200n_c$. From the panels, we observe a large increase in the electron energy achieving $\gamma_f/a_0 \sim 7, 8$ ($\gamma_f \approx 800$ for $a_0 = 100$ and $\gamma_f \approx 1600$ for $a_0 = 200$), even if for the largest laser strength $a_0 = 200$ [Fig. 10(b)], the angular distribution of the electrons tends to increase. Our results show that, even in the very high-intensity regime of interaction, there is good evidence that SPW excitation and the consequent electron acceleration still present when the diffraction grating is correctly chosen. However, they do not account for additional processes that may set at extreme intensities, such as radiation reaction or quantum effects (like pair creation).[41] These processes are under investigation and remain beyond the scope of this work.

VI. CONCLUSION

In this work, we consider a laser pulse impinging on an over dense plasma, whose surface presents a periodic modulation (grating), in order to generate large amplitude Surface Plasma Waves (SPWs). Key parameters were obtained for optimizing laser–plasma coupling in the ultra-relativistic regime ($\sim 10^{22}$ W/cm^2). A systematic study in the function of the laser incidence angle and intensity, a_0, employing the SMILEI particle-in-cell simulations, showed that at ultra-high laser intensities ($a_0 \geq 30$), the SPW resonance angle becomes roughly independent of a_0. A strong correlation was also observed between the optimum SPW excitation angle and the laser's angle of incidence that optimizes electron acceleration along the plasma surface. The production of high energetic electron bunches is analyzed as well as the appropriate values of plasma density and surface shape to ensure SPW survival at ultra-high laser intensity. Furthermore, the parameter $n_0/(a_0 n_c)$ is shown as crucial for describing laser–plasma coupling and SPW excitation, as it highlights the importance of the prior consideration of higher density plasma to maintain SPW excitation in the ultra-relativistic regime. Finally, as high-intense lasers illuminating the grating inevitably distorts it, increasing the grating's depth provides a more robust condition for SPW excitation. This may be a way to obtain unprecedentedly high currents of energetic electrons as well as emitting radiation with interesting characteristics, thereby paving the way to new experiments on forthcoming multi-petawatt laser systems.

ACKNOWLEDGMENTS

P.S.K. was supported by the CEA NUMERICS program, which has received funding from the European Union's Horizon 2020 research and innovation program under the Marie Sklodowska-Curie Grant Agreement No. 800945. Financial support from Grant No. ANR-11-IDEX-0004-02 Plas@Par is acknowledged. Simulations were performed on the Irene-SKL machine hosted at TGCC-France, using High Performance Computing resources from GENCI-TGCC (Grant No. 2018-x2016057678). The authors acknowledge PRACE for awarding access to Irene-SKL. Technical support from the SMILEI dev-team was also greatly appreciated.

DATA AVAILABILITY

The data that support the findings of this study are available from the corresponding author upon reasonable request.

REFERENCES

[1] W. L. Kruer and K. Estabrook, Phys. Fluids **28**, 430 (1985).
[2] F. Brunel, Phys. Rev. Lett. **59**, 52 (1987).
[3] F. Brunel, Phys. Fluids **31**, 2714 (1988).
[4] W. L. Kruer, *The Physics of Laser-Plasma Interaction* (Addison-Wesley, 1988).
[5] S. C. Wilks, W. L. Kruer, M. Tabak, and A. B. Langdon, Phys. Rev. Lett. **69**, 1383 (1992).
[6] S. C. Wilks and W. L. Kruer, IEEE J. Quantum Electron. **33**, 1954 (1997).
[7] C. Ren, M. Tzoufras, J. Tonge, W. B. Mori, F. S. Tsung, M. Fiore, R. A. Fonseca, L. O. Silva, J.-C. Adam, and A. Heron, Phys. Plasmas **13**, 056308 (2006).
[8] F. N. Beg, A. R. Bell, A. E. Dangor, C. N. Danson, A. P. Fews, M. E. Glinsky, B. A. Hammel, P. Lee, P. A. Norreys, and M. Tatarakis, Phys. Plasmas **4**, 447 (1997).
[9] T. Kluge, S. A. Gaillard, K. A. Flippo, T. Burris-Mog, W. Enghardt, B. Gall, M. Geissel, A. Helm, S. D. Kraft, T. Lockard, J. Metzkes, D. T. Offermann, M. Schollmeier, U. Schramm, K. Zeil, M. Bussmann, and T. E. Cowan, New J. Phys. **14**, 023038 (2012).
[10] S. Jiang, A. G. Krygier, D. W. Schumacher, K. U. Akli, and R. R. Freeman, Phys. Rev. E **89**, 013106 (2014).
[11] A. Héron, J.-C. Adam, and P. Mora, Phys. Plasmas **27**, 013103 (2020).
[12] H. Raether, *Surface Plasmons on Smooth and Rough Surfaces and Gratings* (Springer-Verlag, 1988).
[13] P. K. Kaw and J. B. McBride, Phys. Fluids **13**, 1784 (1970).
[14] A. Bigongiari, M. Raynaud, C. Riconda, A. Héron, and A. Macchi, Phys. Plasmas **18**, 102701 (2011).
[15] T. Ceccotti, V. Floquet, A. Sgattoni, A. Bigongiari, O. Klimo, M. Raynaud, C. Riconda, A. Heron, F. Baffigi, L. Labate *et al.*, Phys. Rev. Lett. **111**, 185001 (2013).
[16] C. Riconda, M. Raynaud, T. Vialis, and M. Grech, Phys. Plasmas **22**, 073103 (2015).
[17] N. Naseri, D. Pesme, and W. Rozmus, Phys. Plasmas **20**, 103121 (2013).
[18] L. Willingale, P. M. Nilson, A. G. R. Thomas, J. Cobble, R. S. Craxton, A. Maksimchuk, P. A. Norreys, T. C. Sangster, R. H. H. Scott, C. Stoeckl, C. Zulick, and K. Krushelnick, Phys. Rev. Lett. **106**, 105002 (2011).
[19] L. Willingale, A. G. R. Thomas, P. M. Nilson, H. Chen, J. Cobble, R. S. Craxton, A. Maksimchuk, P. A. Norreys, T. C. Sangster, R. H. H. Scott, C. Stoeckl, C. Zulick, and K. Krushelnick, New J. Phys. **15**, 025023 (2013).
[20] L. Fedeli, A. Sgattoni, G. Cantono, D. Garzella, F. Reau, I. Prencipe, M. Passoni, M. Raynaud, M. Kveton, J. Proska, A. Macchi, and T. Ceccotti, Phys. Rev. Lett. **116**, 015001 (2016).
[21] S. Marini, P. S. Kleij, F. Pisani, F. Amiranoff, M. Grech, M. Raynaud, A. Macchi, and C. Riconda, Phys. Rev. E **103**, 21201 (2021).
[22] G. Cantono, A. Sgattoni, L. Fedeli, D. Garzella, F. Reau, C. Riconda, A. Macchi, and T. Ceccotti, Phys. Plasmas **25**, 031907 (2018).
[23] M. Raynaud, A. Héron, and J.-C. Adam, Sci. Rep. **10**, 13450 (2020).
[24] X. M. Zhu, R. Prasad, M. Swantusch, B. Aurand, A. A. Andreev, O. Willi, and M. Cerchez, High Power Laser Sci. Eng. **8**, E15 (2020).
[25] Y. Azamoum, V. Tcheremiskine, R. Clady, A. Ferré, L. Charmasson, O. Utéza, and M. Sentis, Sci. Rep. **8**, 4119 (2018).
[26] J. S. Liu, C. Q. Xia, W. T. Wang, H. Y. Lu, C. Wang, A. H. Deng, W. T. Li, H. Zhang, X. Y. Liang, Y. X. Leng, X. M. Lu, C. Wang, J. Z. Wang, K. Nakajima, R. X. Li, and Z. Z. Xu, Phys. Rev. Lett. **107**, 035001 (2011).
[27] S. Tokita, M. Hashida, S. Inoue, T. Nishoji, K. Otani, and S. Sakabe, Phys. Rev. Lett. **105**, 2015004 (2010).
[28] M. Lupetti, J. Hengster, T. Uphues, and A. Scrinzi, Phys. Rev. Lett. **113**, 013903 (2014).
[29] J. Derouillat, A. Beck, F. Pérez, T. Vinci, M. Chiaramello, A. Grassi, M. Flé, G. Bouchard, I. Plotnikov, N. Aunai, J. Dargent, C. Riconda, and M. Grech, Comput. Phys. Commun. **222**, 351 (2018).
[30] B. Cros, B. S. Paradkar, X. Davoine, A. Chancé, F. G. Desforges, S. Dobosz-Dufrénoy, N. Delerue, J. Ju, T. L. Audet, G. Maynard, M. Lobet, L. Gremillet, P. Mora, J. Schwindling, O. Delferrière, C. Bruni, C. Rimbault, T. Vinatier, A. Di Piazza, M. Grech, C. Riconda, J. R. Marquès, A. Beck, A. Specka, P. Martin, P. Monot, D. Normand, F. Mathieu, P. Audebert, and F. Amiranoff, Nucl. Instrum. Methods Phys. Res., Sect. A **740**, 27 (2014).
[31] T. M. Jeong and J. Lee, Ann. Phys. **526**, 157 (2014).
[32] R. Nuter, M. Grech, P. Gonzalez de Alaiza Martinez, G. Bonnaud, and E. d'Humières, Eur. Phys. J. D **68**, 177 (2014).
[33] A. I. Akhiezer and R. N. Polovin, Sov. Phys. JETP **3**, 696 (1956), available at http://www.jetp.ac.ru/cgi-bin/e/index/e/3/5/p696?a=list.
[34] A. Macchi, F. Cornolti, F. Pegoraro, T. V. Liseikina, H. Ruhl, and V. A. Vshivkov, Phys. Rev. Lett. **87**, 205004 (2001).
[35] E. Siminos, M. Grech, S. Skupin, T. Schlegel, and V. T. Tikhonchuk, Phys. Rev. E **86**, 056404 (2012).
[36] M. Raynaud, A. Héron, and J.-C. Adam, Plasma Phys. Controlled Fusion **60**, 014021 (2018).
[37] A. Macchi, Phys. Plasmas **25**, 031906 (2018).
[38] M. C. Hutley and D. Maystre, Opt. Commun. **19**, 431 (1976), available at https://www.sciencedirect.com/science/article/abs/pii/0030401876901164.
[39] A. Macchi, A. Grassi, F. Amiranoff, and C. Riconda, Eur. Phys. J. Plus **134**, 420 (2019).
[40] M. Raynaud, J. Kupersztych, C. Riconda, A. Héron, and J.-C. Adam, Phys. Plasmas **14**, 092702 (2007).
[41] F. Niel, C. Riconda, F. Amiranoff, M. Lobet, J. Derouillat, F. Pérez, T. Vinci, and M. Grech, Plasma Phys. Controlled Fusion **60**, 094002 (2018).

PHYSICAL REVIEW RESEARCH **5**, 013115 (2023)

Electron acceleration by laser plasma wedge interaction

S. Marini,[1,2] M. Grech,[3] P. S. Kleij,[2] M. Raynaud,[2] and C. Riconda[1,*]
[1]*LULI, Sorbonne Université, CNRS, CEA, École Polytechnique, Institut Polytechnique de Paris, F-75252 Paris, France*
[2]*LSI, CEA/DRF/IRAMIS, CNRS, École Polytechnique, Institut Polytechnique de Paris, F-91128 Palaiseau, France*
[3]*LULI, CNRS, CEA, Sorbonne Université, École Polytechnique, Institut Polytechnique de Paris, F-91120 Palaiseau, France*

(Received 14 February 2022; accepted 10 January 2023; published 15 February 2023; corrected 17 March 2023)

An electron acceleration mechanism is identified that develops when a relativistically intense laser irradiates the wedge of an overdense plasma. This induces a diffracted electromagnetic wave that carries a significant longitudinal electric field and that accelerates electrons from the plasma over long distances to relativistic energies. Well collimated, highly charged (nC) electron bunches with energies up to hundreds of MeV are obtained using a laser beam with $I\lambda_0^2 = 3.5 \times 10^{19}$ Wμm^2/cm^2. Multidimensional particle-in-cell simulations, supported by a simple analytical model, confirm the efficiency and robustness of the proposed acceleration scheme.

DOI: 10.1103/PhysRevResearch.5.013115

I. INTRODUCTION

The interest in developing novel compact energetic particle and radiation sources via ultraintense laser-plasma interaction mechanisms has steadily increased over the last decade as they are useful for a large variety of applications ranging from image generation [1] to proton therapy [2], passing through space propulsion [3]. With this aim, various schemes were proposed and studied in detail, either involving the broad category of laser wakefield acceleration [4] or the interaction of a laser with an overdense plasma [5–24], in which our work is inscribed.

Among the mechanisms relying on overdense plasma, electron acceleration by resonantly excited relativistic surface plasma waves (SPWs) [7–13,25,26] has been demonstrated, leading to high charge, ultrashort bunches along the target surface, reaching energies largely above their quiver energy and correlated in time and space with extreme ultraviolet harmonic emission [10]. Advanced methods to control the duration and energy of the electron bunches have been proposed [12].

A compelling alternative, which draws attention by its seemingly simple concept, is the acceleration of electrons in the vacuum by a laser through straight energy transfer, known as vacuum laser acceleration [5,6,27–31]. Ideas to improve such a scheme have been proposed, like plasma mirror injectors [19,20], in which the electrons "surf" the reflected electromagnetic wave along a distance proportional to the Rayleigh length. The resulting bunches of nC charge reach energies of the order of MeV for a laser intensity $\sim 10^{19}$W/cm^2.

Alternatively, direct laser acceleration involves the nonresonant interaction of a laser with a solid target [5,21,22,32]. In particular, the use of a microstructured hollow-core target has been suggested that both guides and confines the laser pulse, resulting in an enhanced and superluminal longitudinal electric field [23,24].

II. ELECTRON ACCELERATION BY A DIFFRACTED FIELD

In this paper, an electron acceleration mechanism is unraveled that develops when an ultrahigh intensity p-polarized laser pulse irradiates the wedge of an overdense plasma target. We therefore propose an acceleration scheme that, considering an ultrashort ($\sim$25 fs), ultraintense ($\sim 10^{19}$ W/cm^2) laser pulse (assuming micrometric wavelengths), allows us to produce electron beams with hundreds of MeV energy, nC charge, and very small (a few degrees) angular aperture.

The scheme is depicted in Fig. 1, where the laser pulse propagates in the horizontal ($x > 0$) direction. It is focused onto the wedge of the target, where the latter consists of an overdense plasma slab occupying the regions $x > 0$ and $y < 0$ and extended over several laser wavelengths in the z direction.

Electron acceleration occurs at the ($y = 0$)−target surface which is irradiated by the laser at grazing incidence. In the following, we will identify the key role of the electromagnetic wave diffracted at the plasma wedge [see Fig. 1(b)] in accelerating the electrons. For a right-angle wedge, this diffracted wave propagates cylindrically, from the wedge outward, in all vacuum directions (from $\theta = 0$ to $\theta = 3\pi/2$). Most importantly, this wave carries a radial or longitudinal electric field which is responsible for the observed electron acceleration. This longitudinal field is maximum for small angles pointing in the direction of propagation of the incident laser, and it is shown to decay with the inverse square root of the distance from the wedge. We will demonstrate the effectiveness of this acceleration scheme capable of sustaining

---

[*] caterina.riconda@upmc.fr

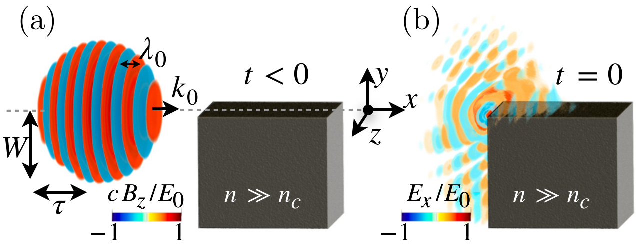

FIG. 1. (a) Laser-plasma interaction scheme. (b) Electric field E_x extracted from the 3D PIC simulation at the time $t = 0$, at which the normalized laser amplitude $a_0 = 5$ is maximum on the plasma edge (here $n = 100n_c$).

sub-mm acceleration lengths both through 3D particle-in-cell (PIC) simulations and through an analytical model showing that the electron energy increases with the square root of the acceleration distance and scales linearly with the laser maximum electric field amplitude.

III. 3D SIMULATIONS OF THE ELECTRON ACCELERATION AT THE WEDGE SURFACE

Simulations have been performed with the open source PIC code Smilei [33]. In the simulations, the laser pulse has a maximum normalized vector potential $a_0 = eE_0/(m_e c\omega_0) = 5$ ($I\lambda_0^2 = 3.5 \times 10^{19}$ Wμm^2/cm^2, with I the laser intensity and λ_0 its wavelength) a Gaussian transverse profile with waist $\sigma_0 = 6\,\lambda_0$, duration $\tau = 8\,\lambda_0/c$ (full width at half maximum in intensity), and maximum electric field amplitude E_0. It is focused onto a cold plasma with electron density $n = 100\,n_c$, $n_c = \epsilon_0 m_e \omega_0^2/e^2$ being the critical density beyond which the plasma is opaque to an incident laser pulse with angular frequency $\omega_0 = 2\pi c/\lambda_0$ (ϵ_0 is the vacuum permittivity, m_e and $-e$ the electron mass and charge, respectively, and c the speed of light in vacuum). The details of the numerical set up are given in Appendix A. Figure 2 gives an example of a 3D simulation result. It reports in color scale the E_x component of the diffracted wave (normalized to E_0) at time $t = 18\lambda_0/c$, $t = 0$ denoting the time at which the maximum of the laser pulse reaches the edge of the target. In gray scale is the electron density. Electrons accelerated by the diffracted wave are clearly visible as bunches propagating with the longitudinal field, right above the target surface. The resulting electron energy spectrum is reported at different instants of time in Fig. 3(a), and the electron angular-energy distribution is reported at time $t = 54\lambda_0/c$ in Fig. 3(b), where $\phi_e = \arctan(p_y/p_x)$.

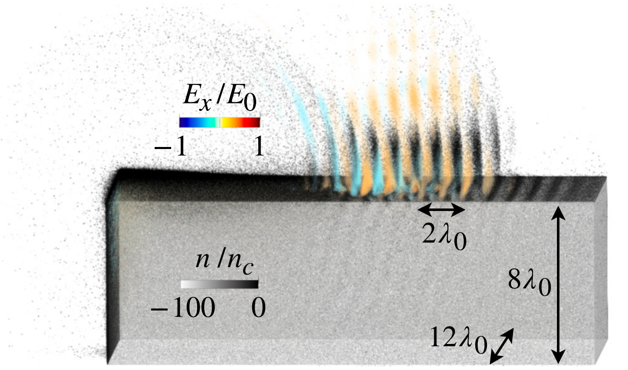

FIG. 2. Electric field E_x (in color, normalized to the maximum laser field strength E_0) and plasma density n/n_c (in gray scale) at $t = 18\lambda_0/c$. Results from the 3D PIC simulation with $a_0 = 5$ and $n = 100n_c$.

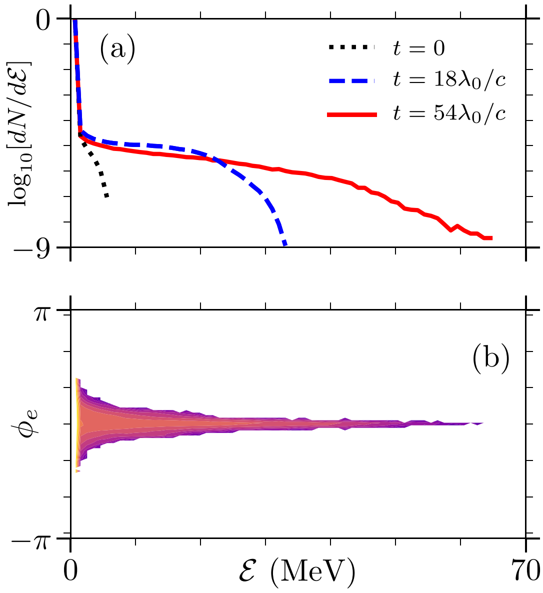

FIG. 3. (a) Electron energy ($\mathcal{E}$) spectrum at different times and (b) electron energy-angular distribution at $t = 54\lambda_0/c$. Results from the 3D PIC simulation with $a_0 = 5$ and $n = 100n_c$.

After only a few tens of optical cycles of interaction, the electrons have already reached energy of several tens of MeV, and carry substantial charges. When considering only electrons with energy above half the maximum energy (i.e., above 30 MeV at time $t = 54\lambda_0/c$) and assuming $\lambda_0 = 0.8\,\mu$m, we obtain a total charge of 0.8 nC, emitted within an angle ∼80 mrad and normalized emittance $\epsilon_{n,\perp} \sim 4.5$ mm.mrad [34]. Similar charge levels were reported considering vacuum laser accelerators [19,23], but the present scheme allows us to obtain much higher electron energies at given laser intensity and duration.

IV. FIELDS IN THE WEDGE CONFIGURATION

Understanding how electrons are accelerated requires a deeper insight into the laser pulse diffraction at the plasma wedge, which can be drawn from previous theoretical [35,36] and numerical works [37]. In particular, the different electromagnetic field components are present in the electron acceleration region ($x > 0, y > 0$), and can be distinguished as (i) the incident electromagnetic wave, (ii) a (small amplitude) SPW propagating along with the vacuum-target interface, and (iii) the electromagnetic wave diffracted at the plasma wedge [35–37].

In the proposed scheme, electron acceleration is governed by the diffracted wave. A key element for efficient electron acceleration is that, due to the nonperfectly conducting nature of the plasma, the diffracted wave carries a nonzero radial

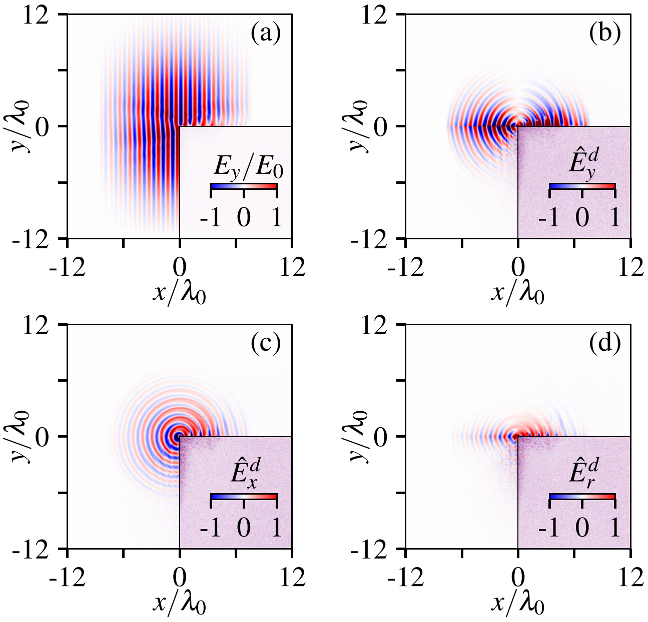

FIG. 4. Fields extracted from the 3D PIC simulation at $t = 0$: (a) total electric field E_y/E_0, (b) and (c) y and x components of the electric field associated to the diffracted wave, respectively, and (d) radial component of the electric field $\hat{E}_r^d$ associated to the diffracted wave.

or longitudinal electric field, maximum for diffraction angle $\theta \sim 0$, pointing along the target surface and thus efficiently accelerating particles in this direction. Unlike the SPW that is confined at the vacuum-target interface (within an evanescent length $\sim\lambda_0$), this longitudinal field of the diffracted wave extends over a few wavelengths in the ($x > 0, y > 0$) vacuum region. This property can be seen in Fig. 4, which reports different field components extracted from 3D PIC simulation for $a_0 = 5$ and $n = 100n_c$ at time $t = 0$ and for $z = 0$ (center of the laser pulse in the third dimension). Figure 4(a) depicts the total electric field E_y/E_0, (b) the E_y^d and (c) E_x^d components of the diffracted wave only, and (d) the radial component $E_r^d = \hat{E}_r^d\, e^{-i(\mathbf{k}.\mathbf{r}-\omega t)}$ of the diffracted wave, where $\hat{E}_r^d = \hat{E}_x^d(x/\sqrt{x^2+y^2}) + \hat{E}_y^d(y/\sqrt{x^2+y^2})$. All electric fields shown with a hat are reported in units of $m_e c\omega_0/e$.

To obtain the components of the diffracted field, we have run three different PIC simulations: (i) one in which the laser pulse is irradiated over the 3D plasma slab, resulting in the total field [Fig. 4(a)], (ii) one in which the laser pulse is irradiated over a plasma slab ($x > 0$ and $-\infty < y < \infty$) that blocks the whole laser beam and describes the reflected field, and (iii) one in which the laser pulse propagates in the free space and describes the incident wave. Then, for $y < 0$ ($y > 0$), we remove the incident (reflected) field from the total field. The field structures observed here are similar to those reported in the literature [35–37] considering the irradiation of a right-angled wedge by a plane wave. Our 3D PIC simulations confirm that even at relativistic intensities, and considering finite size and pulse duration, the diffracted field properties are preserved.

To perform parametric studies, we have considered a series of two-dimensional (2D) simulation at higher resolution (see details in Appendix A). The 2D simulations are representatives of the 3D fields at the center of the box (i.e., $z = 0$), and we found excellent agreement when benchmarking with the correspondent 3D cases (see Appendix B). For this reason, we will henceforth consider 2D PIC simulations in the following.

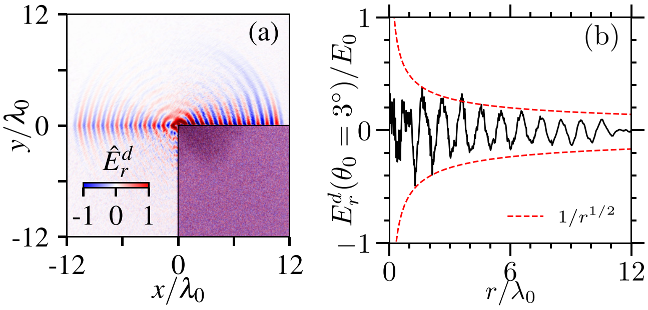

FIG. 5. 2D PIC simulation using a constant laser temporal profile. (a) Radial field $\hat{E}_r^d$ associated to the diffracted wave. (b) Line-out of $\hat{E}_r^d$ recorded at an angle $\theta_0 = 3°$ from the target surface.

We reproduce in Fig. 5 the radial field from a 2D PIC simulation for which the laser field amplitude was kept constant over the whole simulation duration. This allows us to highlight the decrease with the distance from the wedge of the longitudinal field E_r close to the surface. The longitudinal field of the diffracted wave $\hat{E}_r^d$ is reported in Fig. 5(a), while Fig. 5(b) shows a line-out of the field recorded at a small angle $\theta_0 = 3°$ with respect to the x direction (to remove noisy contributions at the surface location). The one-over-square-root dependence expected from Refs. [35–37] is recovered, and this slow decay can sustain the electron dynamics over long acceleration distances.

V. SCALING LAW FOR THE ELECTRON ACCELERATION

Because of the high directionality of the accelerated electrons reported in Fig. 3(b), we can consider the longitudinal electric field E_r of the diffracted wave, as the main driver for the electron acceleration, E_r is approximately equal to the E_x component. Based on these assumptions, a simple one-dimensional model can be derived to describe the electron acceleration process.

We consider that E_x decays in space as $1/\sqrt{k_0 x}$ from its maximum value ηE_0 ($\eta \lesssim 1$ being the ratio of the maximum amplitude of the diffracted and the laser field that can be extracted from the simulations). The wave envelope and carrier are determined by the finite laser pulse itself. As a result, the equation of motion of an electron in the resulting longitudinal field reads

$$m_e \frac{d}{dt}\gamma v_x = -e\,\eta E_0\, e^{-(t-x/c)^2/\tau^2}\, \frac{\sin(k_0 x - \omega_0 t)}{\sqrt{k_0 x}}, \qquad (1)$$

where $v_x = dx/dt$ is the electron velocity and $\gamma = (1 - v_x^2/c^2)^{-1/2}$ its Lorentz factor. Equation (1) can be solved numerically considering a given initial position $x_0 = x(t = 0)$ and zero initial velocity $v_x(t = 0) = 0$. This equation can also be solved analytically for an ultrarelativistic electron, where $dt \sim dx/c$. In this limit, considering a constant phase and the peak field $-\eta E_0$, Eq. (1) reduces to $k_0^{-1} d\gamma/dx = \eta\, a_0/\sqrt{k_0 x}$,

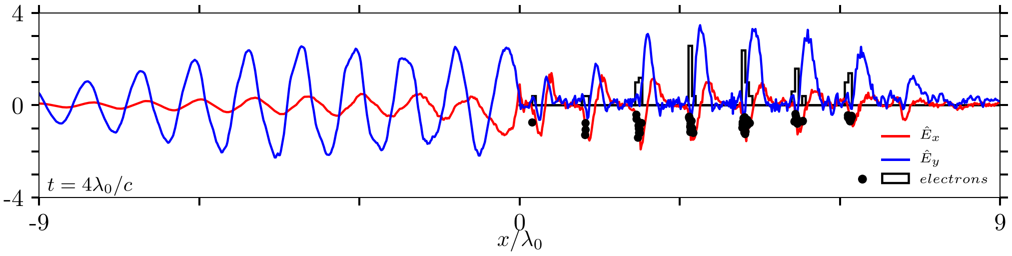

FIG. 6. Total transverse (blue) and longitudinal (red) electric fields at time $t = 4\lambda_0/c$ as extracted from a 2D simulation with $a_0 = 5$ and $n = 100n_c$. Black dots represent high energetic test electrons propagating with the wave and the solid black line is a histogram representing the number of accelerated electrons at a given position.

which leads to a scaling for the electron energy:

$$\gamma(t) \sim 2\eta a_0 \sqrt{\omega_0 t}. \tag{2}$$

This scaling is found to be in excellent agreement with the maximum electron energy reported in Fig. 3(a), leading to maximum energies of 34 MeV ($\gamma \sim 67$) for $t = 18\lambda_0/c$ and 59 MeV ($\gamma \sim 116$) for $t = 54\lambda_0/c$ when taking $a_0 = 5$ and $\eta = 0.63$, which are consistent with our simulations. The square-root dependence of the electron energy with time is key evidence that the acceleration takes place in the longitudinal field of the diffracted wave.

VI. ELECTRON'S INJECTION

For electrons to be accelerated by the diffracted wave, they first need to be extracted from the plasma, then injected in the wave with a (longitudinal) velocity close to c so they can phase lock with the accelerating field. This early stage predominantly occurs *at the target wedge*, close to $x = 0$, where the laser transverse electric field, E_y, can efficiently pull electrons out of the plasma. This happens whenever E_y assumes negative values so the electrons acquire a positive transverse velocity $v_y > 0$. The resulting v_yB_z contribution of the relativistic ($a_0 \gtrsim 1$) laser pulse together with the longitudinal $\sim E_x$ field of the diffracted wave can then bring the electron to near-relativistic longitudinal velocities ($v_x \sim c$) within less than an optical cycle. This happens above a threshold in the laser intensity ($a_0 > 1$) and inspection of particle orbits shows that, while both E_x and v_yB_z contribute to the injection and phase locking, the first term dominates in most cases. Moreover, phase locking requires that the electrons are generated (extracted than injected) in a region where the longitudinal electric field of the diffracted wave is negative.

It is to be noted that as reported by Karal and Karp [36], the diffracted wave is not in phase with the incident laser wave, but phase-shifted by $5\pi/4$ with respect to it. This is confirmed in our PIC simulations and is visible when reporting the (total) longitudinal and transverse electric fields measured at the plasma surface, $y/\lambda_0 = 0$, as shown in Fig. 6. Indeed, electrons are injected at the plasma wedge, $x = 0$, when both $\hat{E}_x$ (solid red line) and $\hat{E}_y$ (solid blue line) are negative. Because of a phase shift of $5\pi/4$ between the E_y and E_r components for $x > 0$, electrons are injected once per laser period as nanobunches accelerating in the region of negative $\hat{E}_x$ field. In Fig. 6, the black dots represent high energetic test electrons propagating with the electromagnetic wave. The solid black line is a histogram representing the number of electrons at a given position. Once the particles phase lock, the total force due to the transverse fields is ~ 0 and does not participate in the acceleration, as will be discussed more in detail in the following.

VII. VALIDATION OF THE SCALING LAW BY PIC SIMULATIONS

To confirm the validity of the model developed above and the interest of the proposed acceleration scheme, we report the results of a series of 2D PIC simulations in the x, y plane at longer timescales and for different laser intensities.

We first discuss in more detail the time evolution for our reference case $a_0 = 5$, whose results are summarized in Fig. 7. In Fig. 7(a), we report the temporal evolution of the Lorentz factor of three representative electrons (macroparticles) as they are accelerated in the diffracted wave. The Lorentz factor of the most energetic electron (red line) increases with time as predicted by our model (dashed line) [Eq. (1) using $\eta = 0.63$ and $x_0 = k_0^{-1}$], and shows strong evidence of the $\sqrt{\omega_0 t}$ time dependence. Note also that the Lorentz factor in this 2D simulation at times $t = 18\lambda_0/c$ ($\gamma \sim 65$) and $54\lambda_0/c$

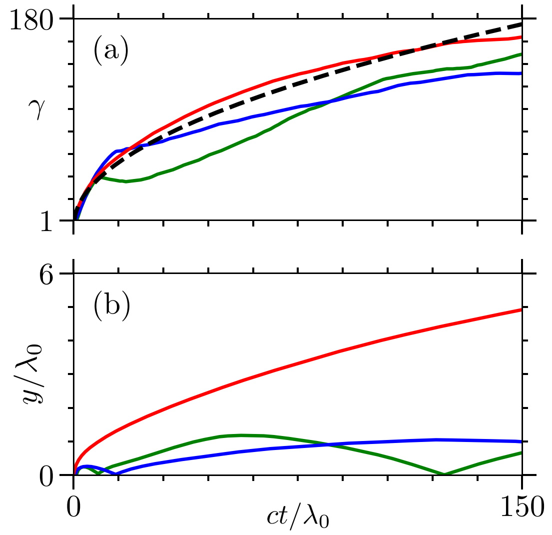

FIG. 7. (a) Temporal evolution of the Lorentz factor (γ) of three representative electrons extracted from 2D PIC simulations (with $a_0 = 5$ and $n = 100n_c$); the dashed black line is obtained by solving Eq. (1) numerically. (b) Transverse excursions of the three representative electrons shown in panel (a).

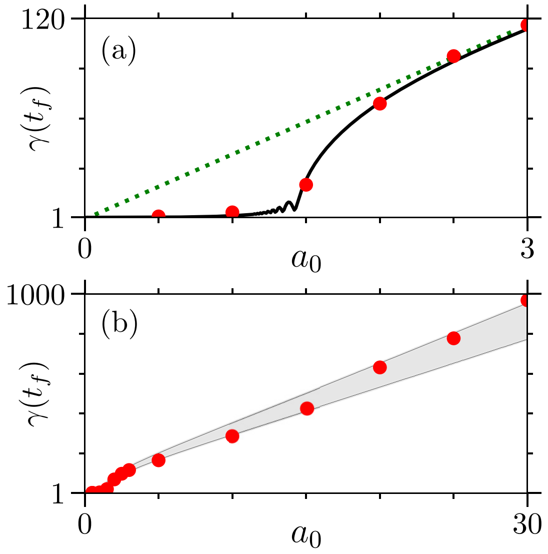

FIG. 8. Panels (a) and (b) report as red points the maximum Lorentz factor obtained in 2D PIC simulations at $t_f = 150\lambda_0/c$ as a function of a_0. In panel (a), the numerical integration of Eq. (1) is shown as a solid black line, and the prediction of Eq. (2) as a green dotted line (using $\eta = 0.63$). In panel (b), the grey region corresponds to the integration of Eq. (1) for $0.6 < \eta < 0.75$.

($\gamma \sim 110$) is the same as in the 3D simulation. The blue and green lines correspond to electrons for which phase locking was less efficient, but that can later be picked up by the wave and further accelerated to large energies. For all these representative particles, our model gives a good estimate for the maximum energy (Lorentz factor) the particle can get as a function of time. This 2D simulation also shows that the acceleration can be maintained over long times, allowing us to reach high energies, here of the order of 86 MeV ($\gamma \sim 170$) at $t = 150\lambda_0/c$ for the most energetic electron (red line). The acceleration can thus develop over long distances along the target surface. As shown in Fig. 7(b), where we reproduce the trajectory of the same test particles as in Fig. 7(a), the electrons have propagated over $\sim 150\lambda_0$ in the x direction, but only a few wavelengths in the y direction (note the scale difference).

We then perform a scan in peak intensity from $I\lambda_0^2 \simeq 5.35 \times 10^{17}$ to 1.92×10^{21} W/cm^2, corresponding to a_0 in between 0.5 and 30, and assuming $\lambda_0 = 0.8\,\mu$m, while keeping the remaining laser and plasma parameters unchanged.

The maximum Lorentz factors achieved by an electron at time $t = 150\lambda_0/c$ was extracted as a function of a_0 and reported in Figs. 8(a) and 8(b). Figure 8(a) shows the transition of nonrelativistic to mildly relativistic field strengths, $0.5 \leqslant a_0 \leqslant 3$, where a threshold is clearly observed for $a_0 \sim 1.5$ (correspondingly, $\eta a_0 \sim 1$). The threshold is well reproduced by the theoretical model when solving Eq. (1) numerically (solid black line). The electron energy scaling given by Eq. (2) ($\propto a_0$, dashed green line), found by considering highly relativistic particles, gives excellent agreement with the PIC results above threshold. As a_0 increases, the parameter η shows a weak dependence with $a_0\, n_c/n$. In the simulations, we find that η is equal to 0.75 for $a_0 = 30$. Indeed, as shown in Fig. 8(b), the energy scaling using $\eta = 0.75$ in Eq. (1) gives a better estimate at large a_0.

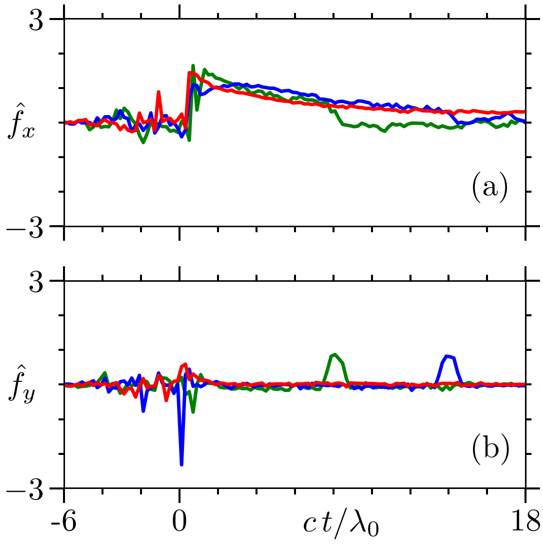

FIG. 9. Temporal evolution of (a) the parallel $\hat{f}_x = f_x/(m_e c\omega_0)$ and (b) the transverse $\hat{f}_y = f_y/(m_e c\omega_0)$ forces acting over the three electrons reported in Fig. 7.

The agreement between the simulations and our one-dimensional model can be understood by looking at the forces acting on the accelerated electrons. The longitudinal [$f_x = -e(E_x + v_y B_z)$] and perpendicular [$f_y = -e(E_y - v_x B_z)$] forces experienced by the three electrons discussed in Fig. 7 are reported in Figs. 9(a) and 9(b), respectively, for our reference case. For readability, only short times $t < 18\lambda_0/c$ are shown. The longitudinal force f_x in Fig. 9(a) clearly shows the $1/\sqrt{\omega_0 t}$ time dependence expected for acceleration in the longitudinal field of the diffracted wave (with $ct \sim x$). This confirms the dominant contribution of E_x compared to the magnetic force $v_y B_z$ (consistent with the fact that v_y stays small for the high-energy electrons and that the energy gain is due to the work of the longitudinal field only). From Fig. 9(b), we also see that the transverse force f_y experienced by the electron is always very small, which implies that the two contributions E_y and $v_x B_z$ compensate each other (which is possible for $v_x \to c$). The transverse force assumes non-negligible values only at the time of injection ($t \sim 0$) and for the electron represented by the green and blue lines, at times $t \sim 8\lambda_0/c$ and $15\lambda_0/c$, respectively. A closer look at the particle orbits shows that these times correspond to the moment when those particles are bouncing off the target surface. Indeed, at those times the electrons penetrate the plasma skin depth, experience a screened electric field ($E_y \to 0$), and are turned back by the strong $v_x B_z$ force (B_z is not screened). At those times, the electrons do not gain energy [see Fig. 7(a)], but they can re-enter the wave and get further accelerated.

VIII. PHASE LOCKING

The slow decrease ($\propto 1/\sqrt{k_0 x}$) of the longitudinal field of the diffracted wave along the target surface means that electrons can, in principle, remain in phase and be accelerated over distancesor times even longer that that considered so far.

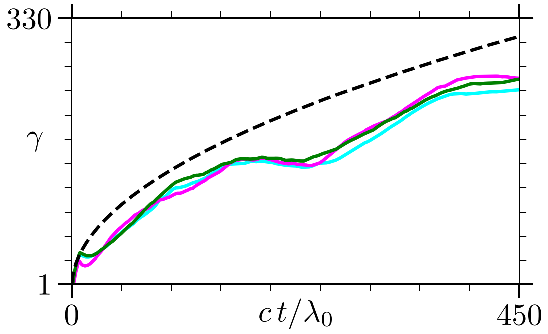

FIG. 10. Temporal evolution of the Lorentz factor (γ) of three electrons which are accelerated over a long time interval. The dashed black line is the result from the theoretical approach using $\eta = 0.63$. The green line represents the same particle in all panels. Here, $a_0 = 5$ and $n = 100n_c$.

This is confirmed in Fig. 10, where few selected high-energy electrons from our reference case were tracked over 450 optical cycles, propagating distances $\sim 450\lambda_0$ along the target surface and reaching energies of nearly 130 MeV ($\gamma \sim 260$).

To explain this, we examine the phase shift an electron acquires with respect to the accelerating wave:

$$\Delta\varphi = k_0 \int_{t_{\text{inj}}}^{t} (c - v_x)\, dt. \tag{3}$$

For relativistic electrons, $v_x(t)$ is well approximated by Eq. (2) [using $v_x = (1 - 1/\gamma^2)^{1/2}$]. In addition, if we assume that the electron energy at time t is much larger than that at the moment of injection [$\gamma(t) \gg \gamma(t_{\text{inj}})$], then we obtain that the phase shift $\Delta\varphi \sim (8\eta^2 a_0^2)^{-1} \ln 4\eta^2 a_0^2\, \omega_0 t$ increases logarithmically with time. Conversely, the dephasing time $\omega_0 t_d \propto \exp(8\pi\eta^2 a_0^2)$, at which $\Delta\varphi \sim \pi$, increases exponentially with $\eta^2 a_0^2$. This ensures that the electron can remain in phase with the accelerating field whenever $\eta a_0 > 1$.

Considering the forces in Figs. 9(a) and 9(b), the transverse motion in the complex field resulting from the superposition of the cylindrical diffracted wave and incident laser field can induce in some particles a temporary dephasing with respect to the accelerating field as they hit the surface. A similar effect can occur at much longer timescales, and it is at the origin of the fact that for a short amount of time the energy stops increasing, as visible in Fig. 10, but starts again after reinjection. Note also that 3D diffraction effects can set in over long distances and limit the acceleration.

IX. ROLE OF THE PLASMA DENSITY

As discussed earlier, we find a very weak dependence of the amplitude of the diffracted wave that is represented by the η parameter with $a_0 n_c/n$. Complementary simulations with different plasma densities also show that both the η parameter and the final electron acceleration are almost independent of n/n_c, as long as it is much larger than one. Moreover, the diffracted wave phase velocity should be independent of the plasma density. This is in contrast with SPWs, whose phase velocity, as predicted from the theory $v_{\text{ph}} \approx c(1 - n_c/2n)$ [8] depends on the parameter n/n_c and is subluminal. We exploited this result to show that, even if a surface plasma is present, the main contribution to acceleration comes from the diffracted wave.

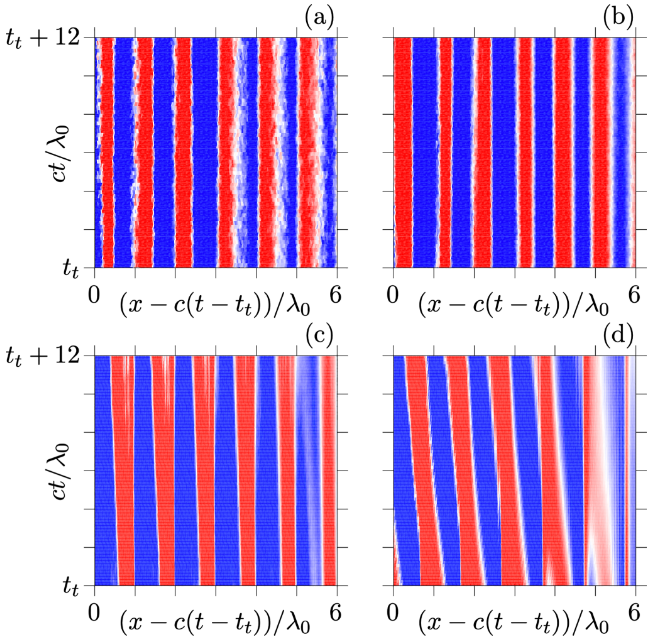

FIG. 11. Field phase velocity observed from two different setups: the one in the present paper, panels (a) and (b), and a setup involving resonant excitation of surface plasma waves, as in Ref. [12], with $\Delta\beta = 0$ and $\theta_{\text{inc}} = 31^\circ$, panels (c) and (d). In the figures, $a_0 = 5$ and $t_t = 30c/\lambda_0$ is much longer than the pulse duration.

We measured the temporal evolution of the longitudinal electric field amplitude (represented by the saturated colors) in our configuration in a frame that moves at the speed of light using a probe located on the plasma surface. The vertical lines indicate no variation in the phase velocity, both for the case the plasma density is $n = 100n_c$ in Fig. 11(a) and $n = 20n_c$ in Fig. 11(b). We then performed simulations where we resonantly excite SPWs (same arrangement as Ref. [12] with $\Delta\beta = 0$ and $\theta_{\text{inc}} = 31^\circ$). In contrast to the previous case, we observe with the same diagnostic that the wave phase velocity depends on the density: it is slightly less, but the same order than c for $n = 100n_c$ as shown in Fig. 11(c) and clearly smaller then the speed of light, $v_{\text{ph}} \approx 0.96c$, for the lower density case $n = 20n_c$, Fig. 11(d), as expected.

We also note that the excursion of the electrons shown in Fig. 7(b) show that efficient electron acceleration can happen at some wavelengths above the surface. This indicates that resonant SPWs are not at the origin of the particle acceleration as these waves are well localized at the target surface and decay exponentially with the distance from the surface over evanescent lengths of the order of λ_0.

X. DISCUSSION AND CONCLUSION

The robustness of the proposed acceleration mechanism was tested using complementary 2D PIC simulations (not shown). In these simulations, various parameters were changed, such as the shape of the target's corner or the roughness of the plasma surface. The presence of a small preplasma

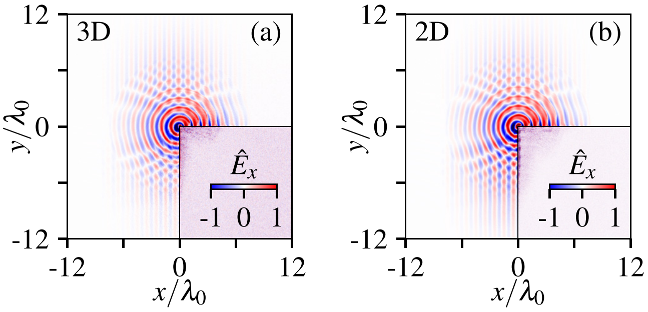

FIG. 12. Comparison of the total field $\hat{E}_x$ extracted from (a) 3D and (b) 2D simulations.

or a small misalignment of the laser were also considered (the laser impinging at an angle up to ±5° with respect to the surface, and with variations of the focus location of a few wavelengths in all directions). In all these complementary simulations, the parameter η and the electron acceleration was shown to be marginally impacted, suggesting that this acceleration scheme could be easily implemented in experiments aimed at demonstrating new energetic particle sources. Moreover, the laser transverse size and pulse duration can be used to control the total charge: the longer the pulse, the more electron bunches will be accelerated. We verified this trend by performing 3D PIC simulations increasing either the transverse size by one and a half or doubling the pulse duration. In the first case, we found an increase of 76% of the charge, and in the second case the doubling of the charge for the 30% fastest particles. However, the increase of the charge with the laser pulse will likely be limited by the plasma evolution for pulses above a few 100 fs range. A consequence of the robustness of this acceleration mechanism is that, even though it was never identified or discussed in previous works, acceleration in the field of the diffracted could develop in various laser-plasma interaction setups.

In conclusion, a unique mechanism of electron acceleration has been identified in the interaction of a relativistically intense laser pulse with an overdense plasma wedge. Both 3D and 2D PIC simulations have shown this mechanism to be robust and provide highly charged (nC), well-collimated electron bunches with energies of several tens to hundreds of MeV. A simple analytical model has been developed that shows that the maximum energy of the accelerated electrons scales linearly with the laser field strength parameter (a_0) and increases with the square root of time to values well beyond the ponderomotive scaling. From this model, we obtain that the particle energy gain can be controlled by the longitudinal target size and, in particular, that the maximum electron energy scales with the square root of this size. As for the total charge of the accelerated beam, it can be controlled by the laser transverse size and pulse duration.

Note added. Recently, we came across a study by Shen *et al.* [38,39] where the authors report on electron acceleration along a thin film irradiated at parallel incidence by an intense laser. While they attribute electron acceleration to the excitation of a SPW, our results suggest that they should also consider acceleration in the diffracted wave. A similar scheme was also proposed by Sarma *et al.* [40] with emphasis on SPW excitation.

ACKNOWLEDGMENTS

P.S.K. was supported by the CEA NUMERICS program, which has received funding from the European Union's Horizon 2020 research and innovation program under the Marie Sklodowska-Curie Grant Agreement No. 800945. Financial support from Grant No. ANR-11-IDEX-0004-02 Plas@Par is acknowledged. Simulations were performed on the Irene-SKL machine hosted at TGCC- France, using High Performance Computing resources from GENCI-TGCC (Grant No. 2021-x2016057678). The authors are grateful to F. Amiranoff, A. Grassi, F. Massimo, A. Mercuri, F. Pérez, L. Romagnani, and T. Vinci for fruitful discussions and to the SMILEI dev-team for technical support.

APPENDIX A: NUMERICAL SETUP

Simulations have been performed with the SMILEI PIC code [33]. The 3D simulation box is $72\lambda_0 \times 24\lambda_0 \times 24\lambda_0$ (in the x-y-z directions) and composed of $4608 \times 1536 \times 1536$ cells (spatial resolution $\Delta = \lambda_0/64$). The time resolution is $\Delta t = 0.95\Delta/(\sqrt{3}c)$. Electromagnetic field boundary conditions are injecting or absorbing in the x direction and absorbing in the y, z directions. Particle boundary conditions are either thermalizing at $y_{\min}$, $z_{\min}$, and $x_{\max}$ or absorbing in complementary directions. In each computational plasma cell, there are four macroelectrons and four macroions. The ion over electron mass ratio is given by $A\, m_p/Z = 1836\, m_e$, with A, Z, respectively, the atomic number and charge, and m_p the proton mass.

The 2D simulation box is $192\lambda_0 \times 36\lambda_0$ (in the x, y directions) and composed of 49152×9216 cells (spatial resolution $\Delta = \lambda_0/128$). The time resolution is $\Delta t = 0.95\Delta/(\sqrt{2}c)$. In each computational plasma cell, there are 32 macroelectrons and 32 macroions. The electromagnetic field and particle boundary conditions are the same as in the 3D simulation.

APPENDIX B: 2D AND 3D SIMULATION COMPARISON

The same electromagnetic field structures are recovered in 2D PIC simulations using the same physical (laser and plasma) parameters, but with higher resolution, box size, and duration of the simulation. A direct comparison of the $\hat{E}_x$ component of the electric field drawn from 3D and 2D PIC simulations is reported in Fig. 12. The two simulations show excellent agreement, and we verified that the same is true for the other fields. A 3D simulation with reduced resolution (not shown) also confirms that both the general electromagnetic field structure and the electron acceleration were correctly described in 2D simulations up to the maximum time accessible in the 3D simulation $t \sim 150\lambda_0/c$.

---

[1] D. C. Joy, and B. G. Frost, Scanning electron microscopy: Present capability, future improvements and potential replacements, AIP Conf. Proc. **550**, 561 (2001).

[2] S. V. Bulanov, J. J. Wilkens, T. Zh. Esirkepov, G. Korn, G. Kraft, S. D. Kraft, M. Molls, and V. S. Khoroshkov, Laser ion acceleration for hadron therapy, Phys. Usp. **57**, 1149 (2014).

[3] I. Levchenko, S. Xu, S. Mazouffre, D. Lev, D. Pedrini, D. Goebel, L. Garrigues, F. Taccogna, and K. Bazaka, Perspectives, frontiers, and new horizons for plasma-based space electric propulsion, Phys. Plasmas **27**, 020601 (2020).

[4] E. Esarey, C. B. Schroeder, and W. P. Leemans, Physics of laser-driven plasma-based electron accelerators, Rev. Mod. Phys. **81**, 1229 (2009).

[5] N. Naumova, I. Sokolov, J. Nees, A. Maksimchuk, V. Yanovsky, and G. Mourou, Attosecond Electron Bunches, Phys. Rev. Lett. **93**, 195003 (2004).

[6] N. Naumova, J. A. Nees, and G. A. Mourou, Relativistic attosecond physics, Phys. Plasmas **12**, 056707 (2005).

[7] M. Raynaud, J. Kupersztych, C. Riconda, J. C. Adam, and A. Heron, Strongly enhanced laser absorption and electron acceleration via resonant excitation of surface plasma waves, Phys. Plasmas **14**, 092702 (2007).

[8] C. Riconda, M. Raynaud, T. Vialis, and M. Grech, Simple scalings for various regimes of electron acceleration in surface plasma waves, Phys. Plasmas **22**, 073103 (2015).

[9] A. MacchiSurface plasmons in superintense laser-solid interactions, Phys. Plasmas **25**, 031906 (2018).

[10] G. Cantono, L. Fedeli, A. Sgattoni, A. Denoeud, L. Chopineau, F. Réau, T. Ceccotti, A. Macchi *et al.*, Extreme Ultraviolet Beam Enhancement by Relativistic Surface Plasmons, Phys. Rev. Lett. **120**, 264803 (2018).

[11] M. Raynaud, A. Heron, and J.-C. Adam, Excitation of surface plasma waves and fast electron generation in relativistic laser-plasma interaction, Sci. Rep. **10**, 13450 (2020).

[12] S. Marini, P. S. Kleij, F. Pisani, F. Amiranoff, M. Grech, A. Macchi, M. Raynaud, and C. Riconda, Ultrashort high energy electron bunches from tunable surface plasma waves driven with laser wavefront rotation, Phys. Rev. E **103**, L021201 (2021).

[13] S. Marini, P. S. Kleij, F. Amiranoff, M. Grech, C. Riconda, and M. Raynaud, Key parameters for surface plasma wave excitation in the ultra high intensity regime, Phys. Plasmas **28**, 073104 (2021).

[14] O. Lundh, J. Lim, C. Rechatin, L. Ammoura, A. Ben-Isma'l, X. Davoine, G. Gallot, J-P. Goddet, E. Lefebvre, V. Malka, and J. Faure, Few femtosecond, few kiloampere electron bunch produced by a laser-plasma accelerator, Nat. Phys. **7**, 219 (2011).

[15] M. Bailly-Grandvaux, D. Kawahito, C. McGuffey, J. Strehlow, B. Edghill, M. S. Wei, N. Alexander, A. Haid, C. Brabetz, V. Bagnoud, R. Hollinger, M. G. Capeluto, J. J. Rocca, and F. N. Beg, Ion acceleration from microstructured targets irradiated by high-intensity picosecond laser pulses, Phys. Rev. E **102**, 021201(R) (2020).

[16] A. R. Knyazev, Y. Zhang, and S. I. Krasheninnikov, Laser-driven electron acceleration in nanoplate array targets, Phys. Rev. E **103**, 013204 (2021).

[17] B. Quesnel and P. Mora, Theory and simulation of the interaction of ultraintense laser pulses with electrons in vacuum, Phys. Rev. E **58**, 3719 (1998).

[18] S. Marini, E. Peter, G. I. de Oliveira, and F. B. Rizzato, Breakdown of the ponderomotive approximation as an acceleration mechanism in wave-particle nonlinear dynamics, Phys. Plasmas **24**, 093113 (2017).

[19] M. Thévenet, A. Leblanc, S. Kahaly, H. Vincenti, A. Vernier, F. Quéré, and J. Faure, Vacuum laser acceleration of relativistic electrons using plasma mirror injectors, Nat. Phys. **12**, 355 (2016).

[20] C. Zhou, Y. Bai, L. Song, Y. Zeng, Y. Xu, D. Zhang, X. Lu, Y. Leng, J. Liu, Y. Tian, R. Li, and Z. Xu, Direct mapping of attosecond electron dynamics, Nat. Photonics **15**, 216 (2021).

[21] M. Wen, Y. I. Salamin, and C. H. Keitel, Electron Acceleration in Direct Laser-Solid Interactions Far Beyond the Ponderomotive Limit, Phys. Rev. Appl. **13**, 034001 (2020).

[22] A. V. Arefiev, A. P. L. Robinson, V. N. Khudik, Novel aspects of direct laser acceleration of relativistic electrons, J. Plasma Phys. **81**, 475810404 (2015).

[23] K. D. Xiao, T. W. Huang, L. B. Ju, R. Li, S. L. Yang, Y. C. Yang, S. Z. Wu, H. Zhang, B. Qiao, S. C. Ruan, C. T. Zhou, and X. T. He, Ion acceleration from microstructured targets irradiated by high-intensity picosecond laser pulses, Phys. Rev. E **93**, 043207 (2016).

[24] Z. Gong, A. P. L. Robinson, X. Q. Yan, and A. V. Arefiev, Highly collimated electron acceleration by longitudinal laser fields in a hollow-core target, Plasma Phys. Control. Fusion **61**, 035012 (2019).

[25] L. Willingale, A. G. R. Thomas, P. M. Nilson, H. Chen, J. Cobble, R. S. Craxton, A. Maksimchuk, P. A. Norreys, T. C. Sangster, R. H. H. Scott, C. Stoeckl, C. Zulick, and K. Krushelnick, Surface waves and electron acceleration from high-power, kilojoule-class laser interactions with underdense plasma, New J. Phys. **15**, 025023 (2013).

[26] L. Fedeli, A. Sgattoni, G. Cantono, D. Garzella, F. Réau, I. Prencipe, M. Passoni, M. Raynaud, M. Květoň, J. Proska, A. Macchi, T. Ceccotti, Electron Acceleration by Relativistic Surface Plasmons in Laser-Grating Interaction, Phys. Rev. Lett. **116**, 015001 (2016).

[27] E. Esarey, P. Sprangle, and J. Krall, Laser acceleration of electrons in vacuum, Phys. Rev. E **52**, 5443 (1995).

[28] F. Hartemann, S. Fochs, G. Le Sage, N. Luhmann, J. Woodworth, M. Perry, Y. Chen, and A. Kerman, Nonlinear ponderomotive scattering of relativistic electrons by an intense laser field at focus, Phys. Rev. E **51**, 4833 (1995).

[29] J. Pang, Y. K. Ho, X. Q. Yuan, N. Cao, Q. Kong, P. X. Wang, L. Shao, E. H. Esarey, and A. M. Sessler, Subluminous phase velocity of a focused laser beam and vacuum laser acceleration, Phys. Rev. E **66**, 066501 (2002).

[30] J. F. Hua, Y. Z. Lin, Ch. X. Tang, Y. K. Ho, and Q. Kong, Phase motion of accelerated electrons in vacuum laser acceleration, J. Appl. Phys. **101**, 023102 (2007).

[31] P. K. Singh, F.-Y. Li, C.-K. Huang, A. Moreau, R. Hollinger, A. Junghans, A. Favalli, C. Calvi, S. Wang, Y. Wang, H. Song, J. J. Rocca, R. E. Reinovsky and, S. Palaniyappan, Vacuum laser acceleration of super-ponderomotive electrons using relativistic transparency injection, Nat. Commun. **13**, 54 (2022).

[32] M. Jirka, M. Vranic, T. Grismayer, and L. O. Silva, Scaling laws for direct laser acceleration in a radiation-reaction dominated regime, New J. Phys. **22**, 083058 (2020).

[33] J. Derouillat, A. Beck, F. Pérez, T. Vinci, M. Chiaramello, A. Grassi, M. Flé, G. Bouchard, I. Plotnikov, N. Aunai, J. Dargent, C. Riconda, and M. Grech, Smilei: A collaborative, open-source, multi-purpose particle-in-cell code for plasma simulation, Comput. Phys. Commun. **222**, 351 (2018).

[34] M. Ferrario, *Injection, Extraction and Matching*, Proceedings of the CAS-CERN (CERN, Geneva, 2016).

[35] C. A. Balanis, *Advanced Engineering Electromagnetics*, 2nd ed. (John Wiley & Sons, Inc., Hoboken, NJ 07030, USA, 2012).

[36] F. C. Karal Jr., and S. N. Karp, Diffraction of a plane wave by a right angled wedge which sustains surface waves on one face, Quart. Appl. Math. **20**, 97 (1962).

[37] Y. Xi, Y. S. Jung, and H. K. Kim, Interaction of light with a metal wedge: The role of diffraction in shaping energy flow, Opt. Express **18**, 2588 (2010).

[38] X. F. Shen, A. M. Pukhov, S. E. Perevalov, and A. A. Soloviev, Electron acceleration in intense laser - solid interactions at parallel incidence, Quantum Electron. **51**, 833 (2021).

[39] X. F. Shen, A. Pukhov, and B. Qiao, Monoenergetic High-Energy Ion Source via Femtosecond Laser Interacting with a Microtape, Phys. Rev. X **11**, 041002 (2021).

[40] J. Sarma, A. McIlvenny, N. Das, M. Borghesi, and A Macchi, Surface plasmon-driven electron and proton acceleration without grating coupling, New J. Phys. **24**, 073023 (2022).

Correction: The affiliation indicators for the third, fourth, and fifth authors were incorrect and have been fixed.

Appendix B

Wave front rotation

Ultrashort pulses exhibit spatio-temporal coupling (STC) when their spatial and temporal properties are interdependent, *i.e.* their electric field $E(r,t) \neq E_1(r)E_2(t)$. Wavefront rotation is a type of STC where the wavefronts of a EM wave rotate in time. They are obtained by focusing a Pulse Front Tilt (PFT) which is a common spatio-temporal distortion in ultrafast optics [109] that can be introduced in the laser beam through a prism or a grating as illustrated in Fig.B.1. The propagation through a prism (see Fig.B.1a) induces angular dispersion and PFT. This is due to the fact that ultrashort pulse have a broad spectral bandwidth and therefore the different frequencies will be deflected at different angles with different propagation velocities when traveling through a prism. On the other hand, the different spectral components of the pulse impinge on different sides of the grating (see Fig.B.1b) causing different directions of propagation causing PFT.

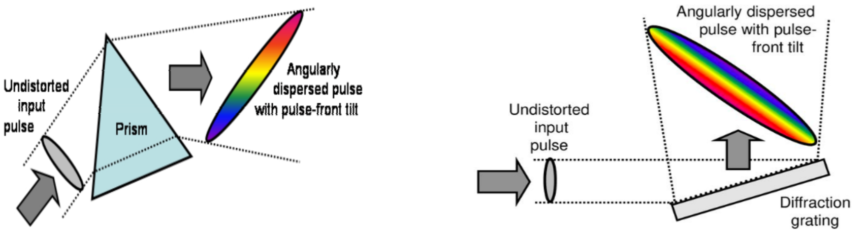

(a) Laser pulse traversing a prism. **(b)** Laser pulse impinging on a grating.

Figure B.1: Two sources of Pulse Front Tilt (PFT). Taken from [109].

Wavefront rotation can also occur by a misalignment of a grating, or prism, in the compressor of a chirped pulse amplification laser leading to pulse front tilt and spatial chirp. As shown in Fig.B.2, a spatially chirped pulse traverses a dispersive medium where the longer wavelengths will travel faster than the shorter wavelength resulting in a wavefront with PFT. This pulse is then focused with a lens and the upper part of the pulse will intersect the lens before the lower part. As a consequence, each part of the pulse will reach the focus point at different times, with the upper part reaching it before the lower part. Each part of the pulse will then propagate at different directions resulting in different wave vectors in the focus. The PFT before focusing turns into a rotation of pulse's propagation direction at focus leading therefore to a WFR at focus.

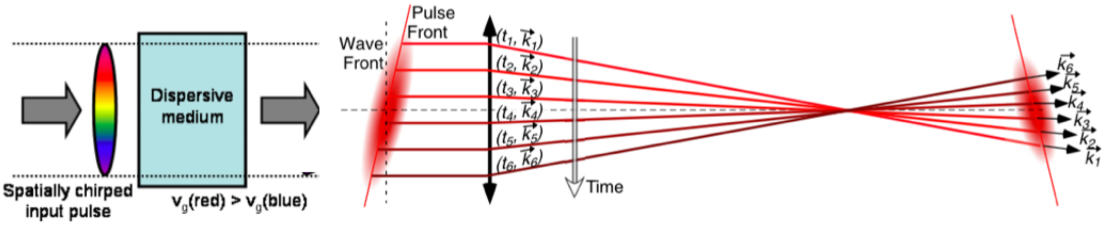

Figure B.2: Illustration showing an ultrashort laser pulse with PFT prior to focusing by a lens, leading to a WFR once the beam is focused. Adapted from [109, 140].

This phenomenon can arise as a side effect, hence viewed as undesirable, and is carefully avoided in some experiments because it decreases the peak intensity at focus. However, it can be greatly beneficial for other experiments given that it represents a controllable pulse beam parameter that can be exploited to generate ultra-short SPWs. Indeed, the use of WFR implies that only a fraction of the laser pulse will satisfy the resonance condition, and thus generate a SPW. As a consequence, the excited SPW will only be a fraction of the laser pulse duration.

Appendix C

Test particle code

```
import numpy as np
import math as m
import matplotlib.pyplot as plt
import scipy
from scipy.interpolate import interp1d
from tqdm import tqdm
import scipy.integrate as integrate
import scipy.special as special
from numpy import linalg as LA

#### Definition of the parameters
### laser (plane wave)
a0     = 3
g0     = m.sqrt(1.+0.5*a0**2)
delta  = 0. #1./m.sqrt(2.)  # linear polarization if delta=0. , circular if 1/sqrt(2)
phase  = 0 #m.pi/4 #0.


### particle
g00 = 1. #  initial energy
n_part = 1
charge_over_mass = -1.

## Parameters for the single particle trajectory
t0 = 2.*m.pi
n_loop = 10 #(3*a0**2 /4)/a0**2
res = 1000.
dt     = t0/res
t_end  = n_loop * t0
n_timestep = int(t_end/dt+1.)
time = np.linspace(0., t_end, n_timestep)

#PIC
x    = np.zeros(n_timestep) ## position
y    = np.zeros(n_timestep)
z    = np.zeros(n_timestep)
umx  = np.zeros(n_timestep) ## momentum (u = p/m)
umy  = np.zeros(n_timestep)
umz  = np.zeros(n_timestep)

pxsm  = np.zeros(n_timestep) ## momentum (u = p/m)
pysm  = np.zeros(n_timestep)
pzsm  = np.zeros(n_timestep)
ts2 = 0.5*dt
```

```
charge_over_mass_dt   = charge_over_mass*dt
charge_over_mass_dts2 = charge_over_mass*dts2

# Plane wave
Kx = 1.
Ky = 0.
Kz = 0.

phi = np.zeros(n_timestep)
phi[0]=0.

x[0] = 0.#a0**2/4.* ( phi[0] + (2*delta*delta -1.)/2.*np.sin(2*phi[0]))
y[0] = 0.#a0*delta*np.sin(phi[0])
z[0] = -a0

Ex = 0.
Ey = a0*delta*m.sin(phi[0])
Ez = -a0*m.sqrt(1.- delta*delta)*m.cos(phi[0])
umx[0] = -g00*np.sqrt(1.-1./g00**2)
umy[0] = 0.
umz[0] = 0.

## half a timestep pusher back in time
umx[0] -=  charge_over_mass_dts2*Ex
umy[0] -=  charge_over_mass_dts2*Ey
umz[0] -=  charge_over_mass_dts2*Ez

for it in range(n_timestep-1):

    phi[it] = time[it] - (Kx*x[it]+Ky*y[it]+Kz*z[it]) + phase

    # Plane wave
    Ex = 0.
    Ey = a0*delta*m.sin(phi[it])
    Ez = -a0*m.sqrt(1.- delta*delta)*m.cos(phi[it])

    Bx = Ky*Ez-Kz*Ey
    By = -Kx*Ez+Kz*Ex
    Bz = Kx*Ey-Ky*Ex

    invgf = 1./m.sqrt(1.0 + umx[it]**2+umy[it]**2+umz[it]**2)

    #### VAY PUSHER
    #u1/2  + add half electric field
    upmx = umx[it] + charge_over_mass_dts2*Ex
    upmy = umy[it] + charge_over_mass_dts2*Ey
    upmz = umz[it] + charge_over_mass_dts2*Ez

    ## magnetic field
    Taux = charge_over_mass_dts2*Bx
    Tauy = charge_over_mass_dts2*By
    Tauz = charge_over_mass_dts2*Bz

    upmx += invgf * (umy[it]*Tauz - umz[it]*Tauy)
    upmy += invgf * (umz[it]*Taux - umx[it]*Tauz)
    upmz += invgf * (umx[it]*Tauy - umy[it]*Taux)

    #complete u prime
    upx = upmx + charge_over_mass_dts2*Ex
    upy = upmy + charge_over_mass_dts2*Ey
    upz = upmz + charge_over_mass_dts2*Ez
```

```
    Tau2 = Taux*Taux + Tauy*Tauy + Tauz*Tauz

    alpha = 1. + upx*upx + upy*upy + upz*upz
    sigma = alpha - Tau2
    ust   = upx*Taux + upy*Tauy + upz*Tauz

    alphasq = 2./(sigma+ m.sqrt(sigma*sigma + 4.*(Tau2 + ust*ust)))
    alpha_gf = m.sqrt(alphasq)

    tx = Taux*alpha_gf
    ty = Tauy*alpha_gf
    tz = Tauz*alpha_gf
    t2 = tx*tx + ty*ty + tz*tz

    s = 1./(1.+ t2)
    upt = upx*tx + upy*ty + upz*tz

    umx[it+1] = s*(upx + upt*tx + tz*upy - ty*upz)
    umy[it+1] = s*(upy + upt*ty + tx*upz - tz*upx)
    umz[it+1] = s*(upz + upt*tz + ty*upx - tx*upy)

    invgf = 1./m.sqrt(1.0 + umx[it+1]*umx[it+1] + umy[it+1]*umy[it+1] + umz[it+1]*umz[it+1])

    #position
    x[it+1] = x[it] + dt*umx[it+1]*invgf
    y[it+1] = y[it] + dt*umy[it+1]*invgf
    z[it+1] = z[it] + dt*umz[it+1]*invgf

### Emitted radiation
#Direction of detection
theta_det     = m.pi/2.
phi_det       = 0  #m.pi/2.
distance_det  = 1.e3

#Position of the detector
Xd        = distance_det*np.cos(theta_det)*np.sin(phi_det)
Yd        = distance_det*np.sin(theta_det)*np.sin(phi_det)
Zd        = distance_det*np.cos(phi_det)

gamma_r = np.sqrt(1.+umx*umx + umy*umy +umz*umz )
inv_gamma = 1./gamma_r

# velocity
bx = umx*inv_gamma
by = umy*inv_gamma
bz = umz*inv_gamma
dt = time[1]-time[0]

# p'
upx   = np.diff(umx)/dt; upx.resize(umx.size)
upy   = np.diff(umy)/dt; upy.resize(umx.size)
upz   = np.diff(umz)/dt; upz.resize(umx.size)

gamma_p = np.diff(gamma_r)/dt ; gamma_p.resize(gamma_r.size)

bprx = inv_gamma*(upx-inv_gamma*gamma_p*umx)
bpry = inv_gamma*(upy-inv_gamma*gamma_p*umy)
bprz = inv_gamma*(upz-inv_gamma*gamma_p*umz)

#retarded time
```

```
nx   = Xd - x
ny   = Yd - y
nz   = Zd - z
R    = np.sqrt(nx**2+ny**2+nz**2)
nx  /= R
ny  /= R
nz  /= R
Td   = time + R

# Electric field components
Ex_d   = ny*bpry*nx - ny*bpry*bx - bprx*ny**2 + ny*bprx*by - bprx*nz**2 + nz*bprx*bz + nz*bprz*nx - nz*bprz*bx
Ey_d   = nz*bprz*ny - nz*bprz*by - bpry*nz**2 + nz*bpry*bz - bpry*nx**2 + nx*bpry*bx + nx*bprx*ny - nx*bprx*by
Ez_d   = nx*bprx*nz - nx*bprx*bz - bprz*nx**2 + nx*bprz*bx - bprz*ny**2 + ny*bprz*by + ny*bpry*nz - ny*bpry*bz

factor = (1. - nx*bx - ny*by - nz*bz)**3
Ex_d = Ex_d/factor
Ey_d = Ey_d/factor
Ez_d = Ez_d/factor

### METHOD 1 ###

# High-rate interpolation, because Td = time at the detector, it is not uniformely spaced
Td = Td-Td[0]
dtmin = (np.diff(Td)).min();
Nt_int = int(Td[-1]/dtmin);
#print('I need to interpolate if they are different: ',len(Td),Nt)

Td_int = np.linspace(Td[0],Td[-1],Nt_int)
Ex_int = np.interp(Td_int,Td,Ex_d)
Ey_int = np.interp(Td_int,Td,Ey_d)
Ez_int = np.interp(Td_int,Td,Ez_d)

# Fourier transform (over the full trajectory)
Ex_F = np.fft.rfft(Ex_int)
Ey_F = np.fft.rfft(Ey_int)
Ez_F = np.fft.rfft(Ez_int)
Freq_   = np.fft.rfftfreq(len(Td_int),np.diff(Td_int)[0]) * 2.*np.pi

### METHOD 2 ###
Nt_det = n_timestep

Tdet   = time + R
Td_det = np.linspace(Tdet[0],Tdet[-1],Nt_det)
tdmin_det  = np.min(Td_det)
Freq_det  = np.fft.rfftfreq(len(Tdet),np.diff(Tdet)[0]) * 2.*np.pi

nw = 5001
freq = np.linspace(np.min(Freq_det),np.max(Freq_det),nw)

print(np.shape(Freq_))
print('min f =', np.min(Freq_))
print('max f =', np.max(Freq_))
print('min f =', np.min(Freq_det))
print('max f =', np.max(Freq_det))
print(np.shape(freq))

SumEx = np.zeros(nw,dtype=complex)
SumEy = np.zeros(nw,dtype=complex)
SumEz = np.zeros(nw,dtype=complex)
```

```
for iw in range(nw):
    SumEx[iw] = sum(Ex_d[it]*np.exp(1j*freq[iw]*Tdet[it]) for it in range(0,Nt_det ))
    SumEy[iw] = sum(Ey_d[it]*np.exp(1j*freq[iw]*Tdet[it]) for it in range(0,Nt_det))
    SumEz[iw] = sum(Ez_d[it]*np.exp(1j*freq[iw]*Tdet[it]) for it in range(0,Nt_det))

#### Fields:
plt.figure(figsize=(17,4))
plt.subplot(1,3,1) # Ex
plt.loglog(abs(Freq_)  , abs(Ex_F)**2)
plt.loglog( abs(freq), np.abs(SumEx)**2, 'r--')
plt.xlabel("$\omega$")
#plt.show()


plt.subplot(1,3,2)# Ey
plt.plot(abs(Freq_)  , abs(Ey_F)**2)
plt.plot( abs(freq), abs(SumEy)**2, 'r--')
plt.xscale('log')
#plt.yscale('log')
plt.xlabel("$\omega$")

plt.subplot(1,3,3)# Ez
plt.loglog(abs(Freq_)  , abs(Ez_F)**2)
plt.loglog( abs(freq), abs(SumEz)**2, 'r--')
plt.xlabel("$\omega$")
```

Bibliography

[1] H. Raether, *Surface Plasmons on Smooth and Rough Surfaces and on Gratings*. Springer-Verlag, 1988.

[2] A. D. W. L. Barnes and T. W. Ebbesen, “Surface plasmon subwavelength optics,” *Nature*, vol. 424, pp. pp. 824–830, 2003.

[3] S. A. Maier, *Plasmonics: Fundamentals and Applications*. Springer, 2007.

[4] J. Pitarke, V. Silkin, E. Chulkov, and P. Echenique, “Theory of surface plasmons and surface-plasmon polaritons,” *Reports on Progress in Physics*, vol. 70, 11 2006.

[5] J. Homola, “Surface plasmon resonance sensors for detection of chemical and biological species,” *Chemical reviews*, vol. 108, pp. 462–93, 03 2008.

[6] K. Huang, M.-K. Seo, T. Sarmiento, Y. Huo, J. Harris, and M. L. Brongersma, “Electrically driven subwavelength optical nanocircuits,” *Nature Photonics*, no. 8, pp. 244–249, 2014.

[7] R. Zhang, Y. Zhang, Z. Dong, S. Jiang, C. Zhang, L. Chen, L. Zhang, Y. Liao, J. Aizpurua, Y. Luo, J. Yang, and J. Hou, “Chemical mapping of a single molecule by plasmon-enhanced raman scattering,” *Nature*, vol. 498, pp. 82–86, 06 2013.

[8] A. Meola, J. Rao, N. Chaudhary, M. Sharma, and S. Chang, “Gold nanoparticles for brain tumor imaging: A systematic review,” *Front. Neurol.*, vol. 9, 05 2018.

[9] M. Bocková, J. Slabý, T. Špringer, and J. Homola, “Advances in surface plasmon resonance imaging and microscopy and their biological applications,” *Annual Review of Analytical Chemistry*, vol. 12, 06 2019.

[10] Y. Wu, M. Ali, K. Chen, N. Fang, and M. El-Sayed, “Gold nanoparticles in biological optical imaging,” *Nano Today*, vol. 24, 02 2019.

[11] H. A. Atwater and A. Polman, “Plasmonics for improved photovoltaic devices,” *Nature Materials*, vol. 9, pp. 205–213, 2010.

[12] F. Enrichi, A. Quandt, and G. Righini, “Plasmonic enhanced solar cells: Summary of possible strategies and recent results,” *Renewable and Sustainable Energy Reviews*, vol. 82, 09 2017.

[13] E. Ozbay, “Plasmonics: Merging photonics and electronics at nanoscale dimensions,” *Science*, vol. 311, pp. 189 – 193, 2006.

[14] T. Chung, S.-Y. Lee, E. Song, and B. Chun, H.G.and Lee, “Plasmonic nanostructures for nano-scale bio-sensing,” *Sensors*, vol. 11, pp. 10907–10929, 2011.

[15] M. I. S. e. al, “Roadmap on plasmonics,” *Journal of Optics*, no. 20, p. 043001, 2018.

[16] R. H. Ritchie, “Plasma losses by fast electrons in thin films,” *Phys. Rev.*, vol. 106, pp. 874–881, 1957.

[17] R. W. Wood, “On a remarkable case of uneven distribution of light in a diffraction grating spectrum,” *Physical Society of London*, vol. 18, p. 269, 1902.

[18] T. H. Maiman, “Stimulated optical radiation in ruby,” *Nature*, vol. 187, pp. 493–494, 1960.

[19] D. Strickland and G. Mourou, “Compression of amplified chirped optical pulses,” *Optics Communications*, vol. 55, pp. 219–221, 1985.

[20] G. A. Mourou, T. Tajima, and S. V. Bulanov, “Optics in the relativistic regime,” *Rev. Mod. Phys.*, vol. 78, pp. 309–371, Apr 2006.

[21] T. Kluge, S. Gaillard, K. Flippo, T. Burris-Mog, W. Enghardt, B. Gall, M. Geissel, A. Helm, S. Kraft, T. Lockard, J. Metzkes, D. Offermann, M. Schollmeier, U. Schramm, K. Zeil, M. Bussmann, and T. Cowan *New Journal of Physics*, vol. 14, p. 023038, 2012.

[22] S. Jiang, A. G. Krygier, D. W. Schumacher, K. U. Akli, and R. R. Freeman *Physical Review E.*, vol. 89, p. 013106, 2014.

[23] P. K. Kaw and J. B. McBride *Physics of Fluids*, vol. 13, p. 1784, 1970.

[24] S. H. Zaidi, M. Yousaf, and S. R. J. Brueck, “Grating coupling to surface plasma waves. i. first-order coupling,” *J. Opt. Soc. Am. B*, vol. 8, pp. 770–779, Apr 1991.

[25] A. Bigongiari, M. Raynaud, C. Riconda, A. Héron, and A. Macchi, "Efficient laser-overdense plasma coupling via surface plasma waves and steady magnetic field generation," *Physics of Plasmas*, vol. 18, no. 10, p. 102701, 2011-10.

[26] G. Agarwal and S. Jha, "Theory of second harmonic generation at a metal surface with surface plasmon excitation," *Solid State Communications*, vol. 41, no. 6, pp. 499–501, 1982.

[27] J. L. Coutaz and R. Reinisch, "Groove depth dependence of surface plasmon luminescence from bare silver gratings: experimental study," *Computer Physics Communications*, vol. 56, no. 6, pp. 545–548, 1985.

[28] P. Jatav and J. Parashar, "Second harmonic generation by crossed surface plasma waves over a metallic surface," *Physics of Plasmas*, vol. 26, no. 2, p. 022301, 2019.

[29] J. Kupersztych, P. Monchicourt, and M. Raynaud, "Ponderomotive acceleration of photoelectrons in surface-plasmon-assisted multiphoton photoelectric emission," *Phys. Rev. Lett.*, vol. 86, pp. 5180–5183, May 2001.

[30] J. Zawadzka, D. A. Jaroszynski, J. J. Carey, and K. Wynne, "Evanescent-wave acceleration of ultrashort electron pulses," *Applied Physics Letters*, vol. 79, no. 14, pp. 2130–2132, 2001.

[31] S. C. Wilks, W. L. Kruer, M. Tabak, and A. B. Langdon *Physical Review Letter*, vol. 69, p. 1383, 1992.

[32] S. Wilks and W. Kruer *IEEE J. Quantum Electron*, vol. 33, p. 1954, 1997.

[33] W. L. Kruer and K. Estabrook *Phys. Fluids*, vol. 28, p. 430, 1985.

[34] F. Brunel, "Not-so-resonant, resonant absorption," *Phys. Rev. Lett.*, vol. 59, pp. 52–55, Jul 1987.

[35] F. Brunel *Physics of Fluids*, vol. 31, p. 2714, 1988.

[36] C. Ren *Physics of Plasmas*, vol. 13, p. 056308, 2006.

[37] F. N. C. Beg *Physics of Plasmas*, vol. 4, p. 47, 1997.

[38] C. Riconda, M. Raynaud, T. Vialis, and M. Grech, "Simple scalings for various regimes of electron acceleration in surface plasma waves," *Physics of Plasmas*, vol. 22, no. 7, p. 073103, 2015-07.

[39] D. Naseri, D. Pesme, and W. Rozmus *Physics of Plasmas*, vol. 20, p. 103121, 2013.

[40] P. M. Willingale, A. G. R. Nilson, R. S. Thomas, J. Cobble, A. Craxton, P. A. Maksimchuk, T. C. Norreys, R. H. H. Sangster, R. H. H. Scott, C. Stoeckl, C. Zulick, and K. Krushelnick *Physical Review Letters*, vol. 106, p. 105002, 2011.

[41] P. M. Willingale, A. G. R. Nilson, R. S. Thomas, J. Cobble, A. Craxton, P. A. Maksimchuk, T. C. Norreys, R. H. H. Sangster, R. H. H. Scott, C. Stoeckl, C. Zulick, and K. Krushelnick *New Journal of Physics*, vol. 15, p. 025023, 2013.

[42] L. Fedeli, A. Sgattoni, G. Cantono, D. Garzella, F. Réau, I. Prencipe, M. Passoni, M. Raynaud, M. Květoň, J. Proska, A. Macchi, and T. Ceccotti, "Electron acceleration by relativistic surface plasmons in laser-grating interaction," *Phys. Rev. Lett.*, vol. 116, no. 1, p. 015001, 2016-01-07.

[43] G. Cantono, A. Sgattoni, L. Fedeli, D. Garzella, F. Réau, C. Riconda, A. Macchi, and T. Ceccotti, "Extensive study of electron acceleration by relativistic surface plasmons," *Physics of Plasmas*, vol. 25, no. 3, p. 031907, 2018-03.

[44] M. Raynaud, A. Héron, and J.-C. Adam, "Excitation of surface plasma waves and fast electron generation in relativistic laser–plasma interaction," *Sci Rep*, vol. 10, no. 1, p. 13450, 2020-12.

[45] X. M. Zhu, R. Prasad, M. Swantusch, B. Aurand, A. A. Andreev, O. Willi, and M. Cerchez, "Relativistic electron acceleration by surface plasma waves excited with high intensity laser pulses," *High Power Laser Science and Engineering*, vol. 8, 2020. Publisher: Cambridge University Press.

[46] S. Marini, P. S. Kleij, F. Pisani, F. Amiranoff, M. Grech, M. Raynaud, A. Macchi, and C. Riconda, "Kultrashort high energy electron bunches from tunable surface plasma waves driven with laser wavefront rotation," *Physical Review E*, vol. 103, p. 21201, 2021.

[47] G. Cantono, "Relativistic plasmonics for ultra-short radiation sources," 2017.

[48] B. Le Garrec, D. Papadopoulos, C. Le Blanc, J.-P. Zou, A. Fréneaux, L. Martin, N. Lebas, A. Beluze, F. Mathieu, P. Audebert, G. Cheriaux, P. Georges, and F. Druon, "Design update and recent results of the apollon 10 pw facility," p. SF1K.3, 01 2017.

[49] everyone you know, "Mp3 multi-petawatt physics prioritization workshop report," 2022.

[50] Y. Azamoum, V. Tcheremiskine, V. Clady, A. Ferré, L. Charmasson, O. Utéza, and M. Sentis, "Impact of the pulse contrast ratio on molybdenum k_α generation by ultrahigh intensity femtosecond laser solid interaction," *Sci. Rep.*, vol. 8, p. 4119, 2018.

[51] J. Liu, C. Xia, W. Wang, H. Lu, C. Wang, A. H. Deng, W. T. Li, H. Zhang, X. Liang, Y. X. Leng, X. M. Lu, C. Wang, J. Z. Wang, K. Nakajima, R. X. Li, and Z. Z. Xu, "All-optical cascaded laser wakefield accelerator using ionization-induced injection," *Physical Review Letter*, vol. 107, p. 035001, 2011.

[52] S. Tokita, M. Hashida, S. Inoue, T. Nishoji, K. Otani, and S. Sakabe, "Single-shot ultrafast electron diffraction with a laser-accelerated sub-mev electron pulse," *Physical Review Letter*, vol. 105, p. 2015004, 2010.

[53] "Lupetti, m. and hengster, j. and uphues, t. and scrinzi, a.," *Physical Review Letter*, vol. 113, p. 013903, 2014.

[54] S. Marini, P. S. Kleij, F. Amiranoff, M. Grech, C. Riconda, and M. Raynaud, "Key parameters for surface plasma wave excitation in the ultra-high intensity regime," *Physics of Plasmas*, vol. 28, no. 7, p. 073104, 2021-07.

[55] J. Derouillat, A. Beck, F. Pérez, T. Vinci, M. Chiaramello, A. Grassi, M. Flé, G. Bouchard, I. Plotnikov, N. Aunai, J. Dargent, C. Riconda, and M. Grech, "Smilei : A collaborative, open-source, multi-purpose particle-in-cell code for plasma simulation," *Computer Physics Communications*, vol. 222, pp. 351–373, 2018-01.

[56] L. D. Landau and E. M. Lifshitz, *The Classical Theory of Fields*. Elsevier, 2 ed., 1975.

[57] P. Gibbon, *Short Pulse Laser Interactions with Matter: An Introduction*. 09 2005.

[58] A. Macchi, *A Superintense Laser-Plasma Interaction Theory Primer.* SpringerBriefs in Physics, Springer Netherlands, 2013.

[59] P. Mora, *Plasmas crées par laser. Géneralités et applications choisis.* EDP Sciences / CNRS Editions, 2021.

[60] D. Bauer, P. Mulser, and W. H. Steeb, "Relativistic ponderomotive force, uphill acceleration, and transition to chaos," *Phys. Rev. Lett.*, vol. 75, pp. 4622–4625, Dec 1995.

[61] B. Quesnel and P. Mora, "Theory and simulation of the interaction of ultraintense laser pulses with electrons in vacuum," *Phys. Rev. E*, vol. 58, pp. 3719–3732, Sep 1998.

[62] W. Kruer, *The Physics Of Laser Plasma Interactions (1st ed.).* CRC Press, 2003.

[63] A. I. Akhiezer and R. V. Polovin, "Theory of wave motion of an electron plasma," *Soviet Phys. JETP*, vol. 3, 1956.

[64] A. Macchi, F. Cornolti, F. Pegoraro, T. V. Liseikina, H. Ruhl, and V. A. Vshivkov, "Surface oscillations in overdense plasmas irradiated by ultrashort laser pulses," *Phys. Rev. Lett.*, vol. 87, no. 20, p. 205004, 2001-10-29. Publisher: American Physical Society.

[65] E. Siminos, M. Grech, S. Skupin, T. Schlegel, and V. T. Tikhonchuk, "Effect of electron heating on self-induced transparency in relativistic-intensity laser-plasma interactions," *Phys. Rev. E*, vol. 86, no. 5, p. 056404, 2012-11-09.

[66] M. Raynaud, A. Héron, and J.-C. Adam, "High intensity surface plasma waves, theory and PIC simulations," *Plasma Phys. Control. Fusion*, vol. 60, no. 1, p. 014021, 2018-01-01.

[67] A. Macchi, "Surface plasmons in superintense laser-solid interactions," *Physics of Plasmas*, vol. 25, p. 031906, 2018.

[68] S. Palaniyappan, B. Hegelich, H. Wu, D. Jung, D. Gautier, L. Yin, B. Albright, R. Johnson, T. Shimada, S. Letzring, D. Offermann, J. Ren, C.-K. Huang, R. Hörlein, B. Dromey, J. Fernandez, and R. Shah, "Dynamics of relativistic transparency and optical shuttering in expanding overdense plasmas," *Nat. Phys.*, vol. 8, pp. 763–769, 08 2012.

[69] A. Bigongiari, "High intensity laser-plasma grating interaction:surface wave excitation and particle acceleration," 2012.

[70] F. Brunel *Physical Review Letter*, vol. 59, p. 52, 1987.

[71] A. Otto, "Excitation of nonradiative surface plasma waves in silver by the method of frustated total reflection," *Zeitschrift für Physik*, vol. 216, no. 4, pp. pp. 398–410, 1968.

[72] E. Kretschmann and H. Raether, "Radiative decay of non radiative surface plasmons excited by light," *Zeitschrift Naturforsch*, vol. 23, no. 2135, pp. pp. 2135–2136, 1968.

[73] L. Fedeli, "High field plasmonics," 2016.

[74] W. L. Barnes, T. W. Preist, S. C. Kitson, and J. R. Sambles, "Physical origin of photonic energy gaps in the propagation of surface plasmons on gratings," *Phys. Rev. B*, vol. 54, no. 9, p. 6227, 1996.

[75] C. P. et al., *Diffraction Grating Handbook*. Newport Corporation, 6 ed., 2005.

[76] B. N. and J. Neauport, "Diffraction gratings: from principles to applications in high-intensity lasers," *Advances in Optics and Photonics*, vol. 8, no. 1, pp. 156–199, 2016.

[77] M. N. E. G. Loewen and D. Maystre, "Grating efficiency theory as it applies to blazed and holographic gratings," *Applied Optics*, vol. 16, pp. 2711–2721, 1977.

[78] Shimadzu, "Shimadzu diffraction gratings," 2019.

[79] Y. M. M. Memarian1, X. Li and T. Itoh, "Wide-band/angle blazed surfaces using multiple coupled blazing resonances," *Scientific Reports*, vol. 7, no. 1, p. 42286, 2017.

[80] N. Bonod, L. Popov, E. Li, and B. Chernov, "Unidirectional excitation of surface plasmons by slanted gratings," *Optics Express*, vol. 15, pp. 11427–11432, 2007.

[81] Thorlabs, "Gratings tutorial," 2019. Published: https://www.thorlabs.com/tutorials.cfm?tabID=0CA9A8BD-2332-48F8-B01A-7F8BF0C03D4E.

[82] Dynasil, "Definitive guide to diffraction grating," 2019.

[83] A. Macchi, G. Cantono, L. Fedeli, F. Pisani, and T. Ceccotti, "Extreme high field plasmonics: Electron acceleration and XUV harmonic generation from ultrashort surface plasmons," *Physics of Plasmas*, vol. 26, p. 042114, 2019.

[84] F. Niel, *Classical and Quantum Description of Plasma and Radiation in Strong Fields.* Springer Theses, Springer International Publishing, 2021.

[85] J. D. Jackson, *Classical Electrodynamics.* Wiley, 1962.

[86] R. Pausch, "Electromagnetic radiation from relativistic electrons as characteristic signature of their dynamics," 2012-12-13. Publisher: Zenodo.

[87] M. Tamburini, F. Pegoraro, A. Di Piazza, C. H. Keitel, and A. Macchi, "Radiation reaction effects on radiation pressure acceleration," *New J. Phys.*, vol. 12, no. 12, p. 123005, 2010-12-07.

[88] A. Di Piazza, K. Z. Hatsagortsyan, and C. H. Keitel *Phys. Rev. Lett.*, no. 102, p. 254802, 2009.

[89] J. L. Martins, M. Vranic, T. Grismayer, J. Vieira, R. A. Fonseca, and L. O. Silva, "Modelling radiation emission in the transition from the classical to the quantum regime," *Plasma Phys. Control. Fusion*, vol. 58, no. 1, p. 014035, 2016-01-01.

[90] A. Di Piazza, C. Müller, K. Z. Hatsagortsyan, and C. H. Keitel, "Extremely high-intensity laser interactions with fundamental quantum systems," *Rev. Mod. Phys.*, vol. 84, pp. 1177–1228, Aug 2012.

[91] T. Tajima and J. M. Dawson *Physical Review Letter*, vol. 43, p. 267, 1979.

[92] C. K. Birdsall and A. B. Langdoni, *Plasma Physics via Computer Simulation.* Springer, 1991.

[93] K. Yee, "Numerical solution of initial boundary value problems involving maxwell's equations in isotropic media," *IEEE Transactions on Antennas and Propagation*, vol. 14, pp. 302 – 307, 1966.

[94] C. K. Birdsall and A. B. Langdon, *Plasma physics via Computer Simulation.* Taylor & Francis, 2004.

[95] B. Ripperda, F. Bacchini, J. Teunissen, C. Xia, O. Porth, L. Sironi, G. Lapenta, and R. Keppens, "A comprehensive comparison of relativistic particle integrators," *ApJS*, vol. 235, no. 1, p. 21, 2018-03-15.

[96] J. L. Vay, "Simulation of beams or plasmas crossing at relativistic velocity," *Physics of Plasmas*, vol. 15, pp. 056701–056701, 02 2008.

[97] "Exact charge conservation scheme for Particle-in-Cell simulation with an arbitrary form-factor," *Computer Physics Communications*, vol. 135, pp. 144–153, Apr. 2001.

[98] A. Gonoskov, S. Bastrakov, E. Efimenko, A. Ilderton, M. Marklund, I. Meyerov, A. Muraviev, A. Sergeev, I. Surmin, and E. Wallin, "Extended particle-in-cell schemes for physics in ultrastrong laser fields: Review and developments," *Physical Review E*, vol. 92, p. 023305, Aug. 2015.

[99] F. Niel, C. Riconda, F. Amiranoff, M. Lobet, J. Derouillat, F. Pérez, T. Vinci, and M. Grech, "From quantum to classical modeling of radiation reaction: a focus on the radiation spectrum," *Plasma Phys. Control. Fusion*, vol. 60, no. 9, p. 094002, 2018-09-01.

[100] M. Lobet, "Effets radiatifs et d'électrodynamique quantique dans l'interaction laser-matière ultra-relativiste," 2015.

[101] H. Burau, R. Widera, W. Hoenig, G. Juckeland, A. Debus, T. Kluge, U. Schramm, T. Cowan, R. Sauerbrey, and M. Bussmann, "Picongpu: A fully relativistic particle-in-cell code for a gpu cluster," *Plasma Science, IEEE Transactions on*, vol. 38, pp. 2831 – 2839, 11 2010.

[102] R. Fonseca, L. Silva, F. Tsung, V. Decyk, W. Lu, C. Ren, W. Mori, S. Deng, S. Lee, T. Katsouleas, and J. Adam, "Osiris: A three-dimensional, fully relativistic particle in cell code for modeling plasma based accelerators," pp. 342–351, 04 2002.

[103] R. Pausch, A. Debus, A. Huebl, U. Schramm, K. Steiniger, R. Widera, and M. Bussmann, "Quantitatively consistent computation of coherent and incoherent radiation in particle-in-cell codes—a general form factor formalism for macro-particles," *Nuclear Instruments and Methods in Physics Research Section A: Accelerators, Spectrometers, Detectors and Associated Equipment*, vol. 909, pp. 419–422, 2018-11.

[104] J. L. Martins, S. F. Martins, R. A. Fonseca, L. O. Silva, S. H. Gold, and G. S. Nusinovich, "Radiation in 1.5 GeV and 12 GeV laser wakefield acceleration stages from PIC simulations," pp. 191–196, 2010.

[105] M. Pardal, A. Sainte-Marie, A. Reboul-Salze, R. Fonseca, and J. Vieira, “Radio: An efficient spatiotemporal radiation diagnostic for particle-in-cell codes,” *Computer Physics Communications*, vol. 285, p. 108634, 2023.

[106] R. Nuter, M. Grech, P. Gonzalez de Alaiza Martinez, G. Bonnaud, and E. d’Humières *Eur. Phys. J. D*, vol. 68, p. 177, 2014.

[107] “Study of grating target and rotation wave front for high field plasmonics.”

[108] F. Quere and H. Vincenti, “Attosecond lighthouses: How to use spatiotemporatlly coupled light fields to generate isolated attosecond pulses,” *PRL*, no. 108, p. 113904, 2012.

[109] X. Gu, S. Akturk, and R. Trebino *Optical Society of America*, vol. 02003, pp. 0332–0430, 2004.

[110] F. Pisani, “Ultrashort surface plasmon generation by rotating wavefronts,” 2016.

[111] F. P. L. Fedeli and A. Macchi, “Few-cycle surface plasmon polariton generation by rotating wavefront pulses,” *ACS Photonics*, vol. 5, pp. 1068–1073, 2017.

[112] P. Mora and F. Amiranoff *Journal Applied Physics*, vol. 66, p. 3476, 1989.

[113] P. Mora *Physics of Fluids*, vol. 4, p. 1630, 1992.

[114] A. J. Gonsalves, K. Nakamura, J. Daniels, C. Benedetti, C. Pieronek, T. C. H. de Raadt, S. Steinke, J. H. Bin, S. S. Bulanov, J. van Tilborg, C. G. R. Geddes, C. B. Schroeder, C. Tóth, E. Esarey, K. Swanson, L. Fan-Chiang, G. Bagdasarov, N. Bobrova, V. Gasilov, G. Korn, P. Sasorov, and W. P. Leemans, “Petawatt laser guiding and electron beam acceleration to 8 gev in a laser-heated capillary discharge waveguide,” *Phys. Rev. Lett.*, vol. 122, p. 084801, Feb 2019.

[115] O. Lundh, J. Lim, C. Rechatin, L. Ammoura, A. Ben-Ismaïl, X. Davoine, G. Gallot, J.-P. Goddet, E. Lefebvre, V. Malka, and J. Faure, “Few femtosecond, few kiloampere electron bunch produced by a laser–plasma accelerator,” *Nature Phys*, vol. 7, no. 3, pp. 219–222, 2011-03.

[116] E. Brunetti, R. Shanks, G. Manahan, M. Islam, B. Ersfeld, M. P. Anania, S. Cipiccia, R. Issac, G. Raj, G. Vieux, G. Welsh, S. Wiggins, and D. Jaroszynski, "Low emittance, high brilliance relativistic electron beams from a laser-plasma accelerator," *Physical review letters*, vol. 105, p. 215007, 11 2010.

[117] S. Kneip, C. McGuffey, J. L. Martins, M. S. Bloom, V. Chvykov, F. Dollar, R. Fonseca, S. Jolly, G. Kalintchenko, K. Krushelnick, A. Maksimchuk, S. P. D. Mangles, Z. Najmudin, C. A. J. Palmer, K. T. Phuoc, W. Schumaker, L. O. Silva, J. Vieira, V. Yanovsky, and A. G. R. Thomas, "Characterization of transverse beam emittance of electrons from a laser-plasma wakefield accelerator in the bubble regime using betatron x-ray radiation," *Phys. Rev. ST Accel. Beams*, vol. 15, p. 021302, Feb 2012.

[118] G. R. Plateau, C. G. R. Geddes, D. B. Thorn, M. Chen, C. Benedetti, E. Esarey, A. J. Gonsalves, N. H. Matlis, K. Nakamura, C. B. Schroeder, S. Shiraishi, T. Sokollik, J. van Tilborg, C. Toth, S. Trotsenko, T. S. Kim, M. Battaglia, T. Stöhlker, and W. P. Leemans, "Low-emittance electron bunches from a laser-plasma accelerator measured using single-shot x-ray spectroscopy," *Phys. Rev. Lett.*, vol. 109, p. 064802, Aug 2012.

[119] D. Turnbull, S. Bucht, A. Davies, D. Haberberger, T. Kessler, J. L. Shaw, and D. H. Froula, "Raman amplification with a flying focus," *Physical Review Letters*, vol. 120, p. 024801, Jan 2018.

[120] T. T. Simpson, D. Ramsey, P. Frank, K. Weichman, M. V. Ambat, D. Turnbull, D. H. Froula, and J. P. Palastro, "Spatiotemporal control of laser intensity through cross-phase modulation," *Optical Express*, vol. 30, pp. 9878–9891, 2022.

[121] N. Smijesh *Optics Letters*, vol. 44, p. 4028, 2019.

[122] T. M. Jeong and J. Lee *Ann. Phys.*, no. 526, p. 157, 2014.

[123] M. Raynaud, J. Kupersztych, C. Riconda, A. Héron, and J. Adam *Physics of Plasmas*, vol. 14, p. 092702, 2007.

[124] M. C. Hutley and D. Maystre *Optics Communications*, no. 19, p. 43, 1976.

[125] A. Héron, J. C. Adam, and P. Mora *Physics of Plasmas*, vol. 27, p. 013103, 2020.

[126] L. L. Ji, A. Pukhov, E. N. Nerush, I. Y. Kostyukov, B. F. Shen, and K. U. Akli, “Energy partition, γ-ray emission, and radiation reaction in the near-quantum electrodynamical regime of laser-plasma interaction,” *Physics of Plasmas*, vol. 21, no. 2, p. 023109, 2014.

[127] S. Corde, K. Ta Phuoc, G. Lambert, R. Fitour, V. Malka, A. Rousse, A. Beck, and E. Lefebvre, “Femtosecond x rays from laser-plasma accelerators,” *Rev. Mod. Phys.*, vol. 85, pp. 1–48, Jan 2013.

[128] F. Albert, M. Couprie, A. Debus, M. Downer, J. Faure, A. Flacco, L. Gizzi, T. Grismayer, A. Huebl, C. Joshi, M. Labat, W. Leemans, A. Maier, S. Mangles, P. Mason, F. Mathieu, P. Muggli, M. Nishiuchi, J. Osterhoff, and K. Zeil, “2020 roadmap on plasma accelerators,” *New Journal of Physics*, vol. 23, 03 2021.

[129] C. N. Harvey, A. Gonoskov, A. Ilderton, and M. Marklund, “Quantum quenching of radiation losses in short laser pulses,” *Phys. Rev. Lett.*, vol. 118, p. 105004, Mar 2017.

[130] A. B. Borisov, A. V. Borovskiy, O. B. Shiryaev, V. V. Korobkin, A. M. Prokhorov, J. C. Solem, T. S. Luk, K. Boyer, and C. K. Rhodes, “Relativistic and charge-displacement self-channeling of intense ultrashort laser pulses in plasmas,” *Phys. Rev. A*, vol. 45, pp. 5830–5845, Apr 1992.

[131] C. P. Ridgers, C. S. Brady, R. Duclous, J. G. Kirk, K. Bennett, T. D. Arber, A. P. L. Robinson, and A. R. Bell, “Dense electron-positron plasmas and ultraintense γ rays from laser-irradiated solids,” *Phys. Rev. Lett.*, vol. 108, p. 165006, Apr 2012.

[132] M. Vranic, T. Grismayer, R. A. Fonseca, and L. O. Silva, “Quantum radiation reaction in head-on laser-electron beam interaction,” *New J. Phys.*, vol. 18, no. 7, p. 073035, 2016-07-18.

[133] T. G. Blackburn, “Radiation reaction in electron–beam interactions with high-intensity lasers,” *Rev. Mod. Plasma Phys.*, vol. 4, no. 1, p. 5, 2020-12.

[134] A. di Piazza, K. Hatsagortsyan, and C. Keitel, “Quantum radiation reaction effects in multiphoton compton scattering,” *Physical review letters*, vol. 105, p. 220403, 11 2010.

[135] M. Jirka, M. Vranic, T. Grismayer, and L. O. Silva, “Scaling laws for direct laser acceleration in a radiation-reaction dominated regime,” *New J. Phys.*, vol. 22, no. 8, p. 083058, 2020-08-20.

[136] F. Niel, “Classical and quantum description of plasma and radiation in strong fields,” 2019.

[137] A. Mercuri-Baron, M. Grech, F. Niel, A. Grassi, M. Lobet, A. Di Piazza, and C. Riconda, “Impact of the laser spatio-temporal shape on breit–wheeler pair production,” *New Journal of Physics*, vol. 23, no. 8, p. 085006, 2021.

[138] Y.-J. Gu, M. Jirka, O. Klimo, and S. Weber, “Gamma photons and electron-positron pairs from ultra-intense laser-matter interaction: A comparative study of proposed configurations,” *Matter and Radiation at Extremes*, vol. 4, no. 6, p. 064403, 2019.

[139] M. Jirka, O. Klimo, Y. Gu, and S. Weber, “Enhanced photon emission from a double-layer target at moderate laser intensities,” *Scientific Reports*, vol. 10, p. 8887, 06 2020.

[140] F. Quere, “Applications of ultrafast wavefront rotation in highly nonlinear optics,” *Phys. B: At. Mol. Opt. Phys.*, no. 47, p. 124004, 2014.

ECOLE
DOCTORALE

Titre : Plasmonique en régime ultra relativiste

Mots clés : plasma, simulation, onde de surface, rayonnement

Résumé : Le travail analytique et numérique présenté dans cette thèse a été motivé par les capacités actuelles et la mise à niveau des installations laser multi-PW existantes, telles qu'Apollon et ELI en Europe, avec des lasers atteignant des intensités supérieures à 10^{21} W/cm^2. L'extension de l'étude de la physique plasmonique relativiste vers des régimes d'intensité plus élevés, où les effets non linéaires et relativistes vont jouer un rôle prépondérant, sont d'un intérêt fondamental pour la physique des plasmas sur-denses relativistes. Dans ce travail, nous explorons la génération de faisceaux d'électrons rapides dans l'interaction laser-solide via l'excitation dans des cibles pré-structurées d'ondes plasma de surface (SPW) ou de modes électromagnétiques localisés. Comme les SPW présentent déjà des propriétés intéressantes dans le régime de faible intensité, la manipulation et l'exploitation des phénomènes plasmoniques dans le régime ultra-relativiste révèlent des perspectives prometteuses d'utilisation des SPW pour l'obtention de sources de particules et de rayonnement de haute énergie en utilisant la prochaine génération de lasers multi-PW. Grâce à des simulations réalisées avec le code open-source SMILEI (Particle-In-Cell), nous prouvons que dans ce régime, l'utilisation d'un réseau résonant pour la génération de SPW améliore l'accélération et l'émission des électrons le long de la surface. En effet, les paquets d'électrons relativistes de haute charge, produits par le SPW, subissent une forte accélération, émettant ainsi de grandes quantités de rayonnement électromagnétique avec des caractéristiques intéressantes. Ce schéma représente une alternative intéressante de source de lumière car l'énergie perdue par les électrons en raison de l'émission de rayonnement est transférée à des photons de haute énergie. En outre, nous présentons un schéma inédit permettant de piloter la durée et l'intensité du SPW et par conséquent les caractéristiques du faisceau d'électrons; obtenant ainsi des paquets d'électrons ultracourts (quelques fs) ayant une charge de quelques dizaines de pC à des énergies de plusieurs dizaines de MeV dans le régime relativiste et des paquets d'électrons plus énergétiques et collimatés, ainsi qu'une émission améliorée de photons, dans le régime ultra-relativiste de l'interaction. L'ensemble de ces résultats ouvre de nouvelles perspectives pour le développement de sources compactes de particules et de rayonnement énergétiques.

Title : Plasmonics in ultra relativistic regime

Keywords : plasma, simulation, surface wave, radiation

Abstract : The analytical and numerical work presented in this thesis has been motivated by the current capabilities and upgrade of existing multi-PW laser facilities, such as Apollon and ELI in Europe, with lasers reaching intensities beyond 10^{21} W/cm^2. Extending the study of Relativistic Plasmonics physics toward higher intensity regimes, where nonlinear and relativistic effects play a major role, is of fundamental interest to the physics of relativistic plasmas. In this work, we explore the generation of fast electron beams in relativistic laser-solid interaction by using properly-structured targets whose surface characteristics allow surface plasma wave (SPW) excitation or local electromagnetic modes. Since SPW already exhibit interesting properties in the low-intensity regime, manipulating and harnessing plasmonic phenomena in the ultra-relativistic regime reveal promising prospects of using SPW for the obtention of high-energy particle and radiation sources using the next generation of multi-PW lasers. Through simulations performed with the open-source Particle-In-Cell (PIC) code SMILEI, we prove that in this regime, the use of a solid resonant grating for SPW generation enhances the acceleration and emission of the electrons along the surface. Indeed, the relativistic high-charge electron bunches produced by SPW, experience strong acceleration, therefore emitting large amounts of electromagnetic radiation with interesting characteristics. This scheme represents an interesting alternative of light source as the energy lost by electrons due to radiation emission is transferred to high-energy photons. In addition, we proposed a novel scheme to control the duration and intensity of the SPW and consequently the characteristics of the electron beam; thus obtaining ultrashort (few fs) electron packets with a charge of a few tens of pC at energies of several tens of MeV in the relativistic regime and more energetic and collimated electron bunches, as well as improved photon emission, in the ultra-relativistic regime of interaction. All these results open up new perspectives for the development of compact sources of energetic particles and radiation.

Institut Polytechnique de Paris
91120 Palaiseau, France